Surface Science Reports 8 (1988) 211–357
North-Holland, Amsterdam

SURFACE INFRARED SPECTROSCOPY

Y.J. CHABAL

AT&T Bell Laboratories, Murray Hill, NJ 07974, USA

Manuscript received in final form 25 January 1988

Infrared spectroscopy has become a useful tool to investigate surfaces. The theoretical and experimental foundation of surface IR spectroscopy is described and selected examples are presented to illustrate the kind of information derived in several important areas of surface science such as chemistry, structure, dynamics and kinetics at surfaces.

Contents

1. Introduction

Among the various classes of techniques utilized to probe solid surfaces, surface vibrational spectroscopy (SVS) has gained wide recognition for its ability to determine the chemical nature of surfaces and adsorbates. Such information is not readily available by electron or photoelectron spectroscopies such as Auger electron spectroscopy (AES), ultraviolet or X-ray photoelectron spectroscopies (UPS or XPS), and not as directly accessible by surface extended X-ray absorption fine structure (SEXAFS) spectroscopy. In addition, SVS has been instrumental to determine bonding sites and adsorbate geometry through symmetry analysis. When used in conjunction with diffraction techniques such as low-energy electron or X-ray diffraction and with first principle calculations, quantitative structural interpretation of SV spectra can be achieved for adsorbates on single crystal surfaces. Furthermore, the potential to measure dynamics at surfaces, directly from time-resolved laser experiments or indirectly from line shape analysis, is attractive to study surface-confined processes, i.e. relaxation, reaction, diffusion. Such information would complement dynamic measurements of gas–surface interactions such as those carried out with beam scattering techniques. Finally, recent applications of real-time SVS to surface kinetics indicate that such microscopic phenomena are accessible experimentally with SVS [1–3].

The investigation of a particular surface vibrational phenomenon usually requires a specific SVS technique. Surface infrared spectroscopy (SIRS) is only one of many probes of vibrational and low energy ($< 10\,000\ \mathrm{cm}^{-1}$) electronic excitations at surfaces. The most popular methods are electron energy loss spectroscopy (EELS), inelastic atom beam scattering (IABS) and Raman scattering. Others include inelastic tunneling and inelastic neutron scattering spectroscopies. Each of these techniques possesses definite attributes that render them particularly suitable to probe different aspects of vibrational and electronic properties of surfaces. For that reason, rather than emphasizing sensitivity figures that can be misleading, table 1 summarizes the strengths and weaknesses of each technique. Prototypical experiments are then described that highlight those attributes of each spectroscopy.

For instance, the class of experiments that can be tackled most successfully by IR spectroscopy are those that require high resolution, strict polarization rules, time resolution or high pressures. Investigation of the adsorption and decomposition of complex organometallic molecules on a semiconductor surface in real time at low and high pressures combines most of these properties. The spectral resolution makes it possible to resolve the closely spaced normal modes associated with the hydrocarbon stretch; the sensitivity to both parallel and perpendicular components of the modes is key to the mode assignment and structure determination; and the time resolution (~ 1 s) is compatible with kinetics taking place as the pressure or the temperature is

Table 1
List of surface vibrational spectroscopies

	EELS	SIRS	SRS	IABS	IETS	INS
Probe	Low energy electrons (~ 5 eV)	Photons	Photons	Thermal atoms (~ 0.04 eV)	Electrons	Neutrons
Mechanism	Inelastic	Resonant	Inelastic	Inelastic	Resonant contr. to inelastic channel	Inelastic
Analysis	Electrostatic analyzer	Grating or interferometer spectrometers	Grating spectrometer	Time of flight	Voltage–current differentiation	Grating or time of flight
Advantages	Sensitive (dipole and non-dipole modes) Broadband (10–1000 meV) Momentum transfer (~ $Å^{-1}$) Time resolution < 1 s	High resolution (< 1 cm^{-1}) Selection rules Low and high pressures Electric and magnetic fields Time resolution < 1 s	Good resolution (~ 1 cm^{-1}) Selection rules Low and high pressures Electric and magnetic fields	High resolution (< 1 cm^{-1}) Low frequency (< 400 cm^{-1}) Large momentum transfer (~ $Å^{-1}$) Surface sensitive	Broadband Potentially local probe (STM)	Broadband (> 3000 cm^{-1}) Sensitive to H Quantitive measure of all normal modes
Disad-vantages	Low resolution (~ 30 cm^{-1}) Requires vacuum (10^{-4} Torr) Reflectivity strongly depends on surface order	Current detectors and radiation sources limit sensitivity at low frequencies (< 600 cm^{-1})	Very insensitive except resonant or enhanced SRS	Restricted to low frequencies (< 400 cm^{-1}) to avoid multi-phonon effects Requires long-range substrate order (> 50 Å)	ILL characterized surfaces or very insensitive (STM)	Requires high surface area Only sensitive to H
Prototypical experiments	Identifying all H normal modes at surfaces Mapping surface phonon spectra	Identifying all dipole modes of complex molecules at all pressures Monitoring kinetics	Identifying chemical (e.g. charge transfer) mechanisms at surfaces	Mapping surface phonon dispersion Probing atom–potential (bound state resonances)	Modes of molecules in Al_2O_3 layers	Quantifying H sites in high area metal supported particles

EELS = electron energy loss spectroscopy; SIRS = surface infrared spectroscopy; SRS = surface Raman scattering; IABS = inelastic atom beam scattering; IETS = inelastic electron tunneling spectroscopy; INS = inelastic neutron scattering.

Table 2
List of techniques for surface infrared spectroscopy

Technique	Source	Spectrometer	Attributes
RAS	Globar [a]	Grating	Narrow spectral range (~ 10 cm^{-1}), moderate resolution (~ 2 cm^{-1}), kinetics (10^{-4} s)
		Interferometer	Broad spectral range, high resolution (< 1 cm^{-1}), kinetics (10^{-1} s)
	Laser	No	Narrow spectral range (~ 500 cm^{-1}), dynamics (10^{-12} s), non-linear phenomena
SEWS	Laser [b]	No [c]	Narrow spectral range (~ 100 cm^{-1}), substrate electronic absorption, metal substrates *only*
ES	Sample	Grating	Low frequency region (~ 400 cm^{-1}), high sample temperature (> 250 K)
		Interferometer	Same as for grating
PAS	Laser [b]	No [c]	Best on transparent substrates for high frequency modes (> 1000 cm^{-1})
PTDS	Laser [b]	No [c]	Best on transparent substrates for electronic absorption measurements at high frequency (> 1000 cm^{-1})

[a] Or synchrotron radiation.
[b] Globar can also be used.
[c] Interferometer or grating spectrometers of broadband source is used.

varied, even under conditions when electron spectroscopies are inoperable.

An appreciation of SIRS is further gained by noting that there are several ways to carry it out as summarized in table 2. Each technique requires a different configuration so that very few laboratories use more than one. In order to make the classification relevant to experimentalists, we discuss table 2 in terms of instrumentation. With a grating instrument and an array detector, sensitivity in a small frequency range (~ 10 cm^{-1}) is achieved with good time resolution (~ 10^{-4} s for strong absorptions). This approach is justified to monitor a narrow band that does not shift appreciably in frequency. If the instrument is immersed in liquid N_2 or He or if hot samples are studied, then emission spectroscopy can be performed with proper shielding [4]. Gratings are, however, badly suited to record changes in the broadband absorption, to measure broad or rapidly dispersing modes, or to detect simultaneously vibrational modes that are widely separated in frequency.

Interferometers alleviate the above-mentioned problems since the complete spectrum (typically 500–5000 cm^{-1}) is obtained at once (< 0.1 s). In most

cases, they are superior to grating instruments, particularly when high resolution (< 1 cm^{-1}) is necessary (section 3.3.2). They can also be cooled to cryogenic temperatures for emission spectroscopy [5]. However, interferometers have not yet been used with ms time resolution. Both gratings and interferometers have been used with broadband sources to study semiconductor surfaces with multiple internal reflections [6,7], metal surfaces with a single grazing incidence reflection [8,9], with surface electromagnetic waves (SEW) [10], or with emission [4,11], and to investigate kinetic phenomena [3]. Lasers, however, are better suited as sources for SEW excitations [12] or for photoacoustic [13] and photothermal displacement spectroscopies [14].

Since all the various surface IR techniques are subject to the same basic principles governing the strength of the probing electric field at the surface, general considerations based on Maxwell's equations at the ambient/substrate interface and boundary conditions are first presented (section 2.1) in the theory section (section 2). Such simple considerations are in fact sufficient to choose the best geometry for a desired measurement. A macroscopic theory, treating the absorbing layer explicitly and assuming sharp boundary conditions is then summarized (section 2.2). This description in terms of dielectric functions is adequate for quantitative analysis of most IR data, as long as a proper connection (e.g., the Lorentz oscillator model for vibrational modes) is made to the relevant microscopic parameters (section 2.3.1). Section 2.3.2 briefly discusses the difficulties associated with the assumption of sharp boundary conditions in evaluating the electric field at the position of the dipole or electronic state under study. The rest of section 2 describes the current theoretical effort to predict vibrational spectra of adsorbates on metal and semiconductor surfaces from first principle calculations (section 2.4) and to understand the dynamics of adsorbates from trajectory and phenomenological calculations (section 2.5). These theoretical developments which have taken place mostly in the last couple of years, constitute an important stepping stone for SVS and are a strong motivation for expanding the experimental data base on simple adsorbates (e.g. H) with more careful experimental line shape analysis of their vibrational spectra.

The experimental section (3) describes and analyzes the different ways to perform SIRS. For metal surfaces (section 3.1), infrared reflection–absorption spectroscopy (IRRAS) has been used most successfully (section 3.1.1). Surface electromagnetic wave (SEW) and emission spectroscopies, which have not been applied as widely as IRRAS, are important complements and will be described in sections 3.1.2 and 3.1.3, respectively. Semiconductors and insulator surfaces are probed most sensitively by means of a multiple internal reflection (MIR) geometry whenever possible (section 3.2.1) although external reflection is also useful (section 3.2.2). Photoacoustic and photothermal displacement spectroscopies, although infrequently used so far, may be very powerful tools for studying the electronic absorption of inhomogeneous

surfaces (sections 3.2.3 and 3.2.4). Ultimately, the choice between various techniques always rests on their relative sensitivity to monolayers of the adsorbate modes or the electronic absorption of interest. Sensitivity problems (section 3.3) associated with each technique can be alleviated by improving sources (section 3.3.1), spectrometers (section 3.3.2) or detectors (section 3.3.3), depending on the requirements of the particular technique.

With these important considerations in mind, this article will review work performed with SIRS that has contributed to several areas of surface science: chemistry and structure of adsorbates at surfaces (section 4.1), surface electronic structure (section 4.2), dynamics at surfaces (section 4.3), and kinetics of molecules at surfaces (section 4.4). Emphasis will be given to results that could not have been obtained by other spectroscopies (such as EELS), because of either intrinsic or practical experimental reasons, and to recent work which was not reported in previous reviews. Notably Hoffmann [15] and Hollins and Pritchard [16] have given an excellent account of IRRAS of adsorbed molecules, emphasizing results on CO adsorption and dipole–dipole interactions. More recently, Hayden [17] and Bradshaw and Schweizer [18] have reviewed the latest developments of IRRAS spectroscopy mostly for metal surfaces and Ueba [19] and Tobin [20] the problems associated with vibrational line shape analysis. Finally, Richardson and Sheppard [21] have nicely described the concept of normal modes and symmetries at surfaces. Consequently, the present article will describe some studies of adsorbates at semiconductor surfaces, of the electronic adsorption at both semiconductor and metal surfaces and of the *experimental* considerations for line shape analysis. Although this review is not exhaustive, it will attempt to reference recent and representative SIRS work dealing with single crystal or well defined surfaces. No mention will be made of the pioneering and still very active work on supported metal catalysts [22–24]. It should be recognized, however, that the latter was directly responsible for the development of SIRS on single crystal surfaces.

2. Theory

A necessary condition to probe vibrational modes at surfaces is that the local field, i.e. the exciting electric field, evaluated at the position of the absorbing dipole or electronic transition, be large. In this section, classical electromagnetism is used to estimate the electric field on the vacuum side of a vacuum/substrate interface. The implicit assumptions are that: (1) the adsorbate vibrational absorption occurs outside the substrate, (2) the interface response is sharp on the atomic scale, and (3) the presence of the adsorbate does not substantially modify the local electric field. These simple considerations help understand the choice of geometries for SIRS to study adsorbate

monolayers on a variety of substrates (metals, semiconductors, insulators). A more rigorous treatment, including the electromagnetic response of the adsorbate layer itself, will be given in section 2.2.

2.1. Basic principles

The macroscopic response of a solid to electromagnetic radiation is often expressed as a dielectric function, $\epsilon(\omega)$, the proportionality factor between the displacement vector $\boldsymbol{D}$ and the electric vector $\boldsymbol{E}$ [25]. In the local limit, the constitutive relation defining $\epsilon(\omega)$ is:

$$D_i = \sum_j \epsilon_{ij} E_j, \tag{2.1}$$

where i, j represent the coordinate indices (e.g., x, y, z). For high symmetry systems, axes can be defined so that ϵ_{ij} is diagonal. For an isotropic medium, of course, all the diagonal terms are equal. In general, the dielectric function is complex, $\tilde{\epsilon} = \epsilon' + i\epsilon''$, and the imaginary part ϵ'' represents the absorption of the medium.

At an interface, the fields are calculated by solving Maxwell's equations subject to the boundary conditions (for non-magnetic media):

D_{normal} continuous (no surface free charge), (2.2a)

$E_{\text{tangential}}$ continuous, (2.2b)

$B = H$ continuous (non-magnetic media). (2.2c)

These boundary conditions, together with the knowledge of ϵ for various substrates (see fig. 1), make it possible to evaluate the components of the electric field at the position of the adsorbate (i.e., on the vacuum side of the interface), and thus to determine the optimal geometry.

2.1.1. Absorbing substrates: external reflection

Condition (2.2a) states that, given a substrate characterized by a large dielectric function $|\tilde{\epsilon}| \gg 1$, the normal component of the electric field on the vacuum side of the interface is much larger than that on the substrate side since $E_z^{\text{vacuum}}(z=0) = \tilde{\epsilon} E_z^{\text{substrate}}(z=0)$. In fact, it is usually of the order of the incident external field, E^0. This is not the case for the tangential component of the field, which is small on both sides of the interface. The above statements are quantified by expressing the *amplitude* of the electric field components at the surface ($z=0$), on the vacuum side of the vacuum/substrate interface, for

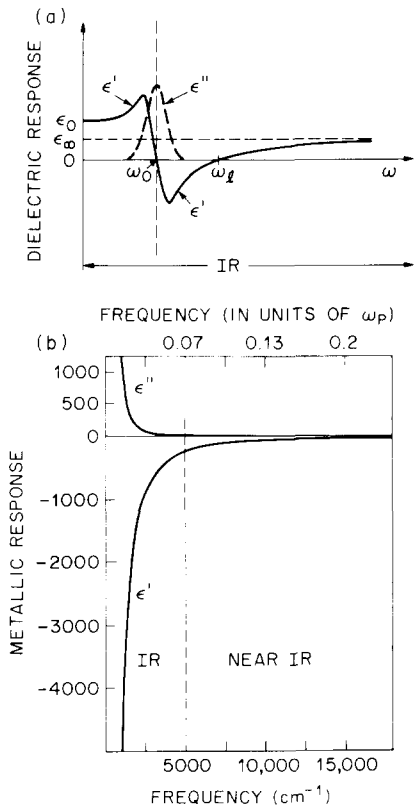

Fig. 1. Schematic plot of the dielectric response $\tilde{\epsilon} = \epsilon' + i\epsilon''$ of (a) a dielectric solid in the infrared region (100–5000 cm^{-1}), and (b) a metallic solid in the infrared and near-infrared region. In curve (a), ω_0 is the resonant frequency of the ions. For N such ionic oscillators per unit volume, with effective mass M^* and charge e^*, the longitudinal mode frequency is $\omega_l = (\omega_0^2 + 4\pi Ne^{*2}/M^*)^{1/2}$ and the DC dielectric response is $\epsilon_0 = \epsilon_\infty + 4\pi Ne^{*2}/(M^*\omega_0^2)$. The full width at half maximum of the imaginary part of $\tilde{\epsilon}$ is the distance between the two inflection points of ϵ'. In curve (b), the real part of $\tilde{\epsilon}$ (large and negative in the IR) becomes zero at the electronic plasma frequency ω_p and approaches +1 asymptotically above ω_p.

a plane wave externally incident at an angle θ, $\boldsymbol{E}(\boldsymbol{r}, t) = \boldsymbol{E}^0 e^{i\boldsymbol{k}\cdot\boldsymbol{r} - i\omega t}$. The geometry for the two possible polarizations is shown in fig. 2. For s-polarization (E-field parallel to the surface, i.e. along y):

$$E_y^{\text{vacuum}}(z=0) = \left[1 - \frac{(\tilde{\epsilon} - \sin^2\theta)^{1/2} - \cos\theta}{(\tilde{\epsilon} - \sin^2\theta)^{1/2} + \cos\theta}\right] E^0. \tag{2.3}$$

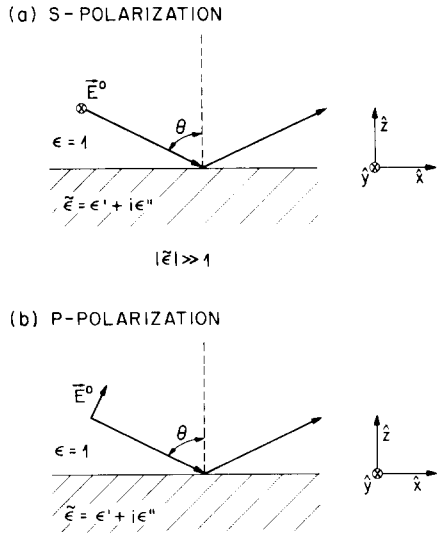

Fig. 2. Schematic representation of a plane wave beam of radiation incident at an angle θ onto a metallic or strongly absorbing substrate for the two polarizations of interest. Note that the symbol used to represent $\boldsymbol{E}$ in (a) [and $\hat{y}$ in both (a) and (b)] indicates a vector pointing into the plane of the figure.

For p-polarization (E-field in plane of incidence, i.e. in the xz plane):

$$E_z^{\text{vacuum}}(z=0) = \left[1 + \frac{\tilde{\epsilon}\cos\theta - (\tilde{\epsilon} - \sin^2\theta)^{1/2}}{\tilde{\epsilon}\cos\theta + (\tilde{\epsilon} - \sin^2\theta)^{1/2}}\right](\sin\theta\, E^0), \tag{2.4}$$

$$E_x^{\text{vacuum}}(z=0) = \left[1 - \frac{\tilde{\epsilon}\cos\theta - (\tilde{\epsilon} - \sin^2\theta)^{1/2}}{\tilde{\epsilon}\cos\theta + (\tilde{\epsilon} - \sin^2\theta)^{1/2}}\right](\cos\theta\, E^0), \tag{2.5}$$

The physics of the process is explicit in the way eqs. (2.3)–(2.5) are written. For large ϵ, the tangential components of the reflected field amplitudes (E_x, E_y) are close in magnitude but opposite in sign (phase shifted by π) to the incident field, represented by the factor 1 in the terms in brackets. A node is set up at the surface, resulting in a net amplitude of order $E^0/\sqrt{|\tilde{\epsilon}|}$. In contrast, the normal component of the electric field (E_z for p-polarization) does not suffer a π phase shift and the reflected field adds constructively to the incident field. Hence, only E_z can be large, i.e. of order E^0.

Practical ways to establish a large E_z^{vacuum} at *metal* surfaces are: (1) launching and detecting surface electromagnetic waves (SEW's) shown schematically in fig. 3a and discussed in section 3.1.2, or (2) reflecting p-polarized radiation at grazing incidence (fig. 3b and section 3.1.1). The condition for SEW excitation is obtained from eq. (2.4) by requiring that the reflected

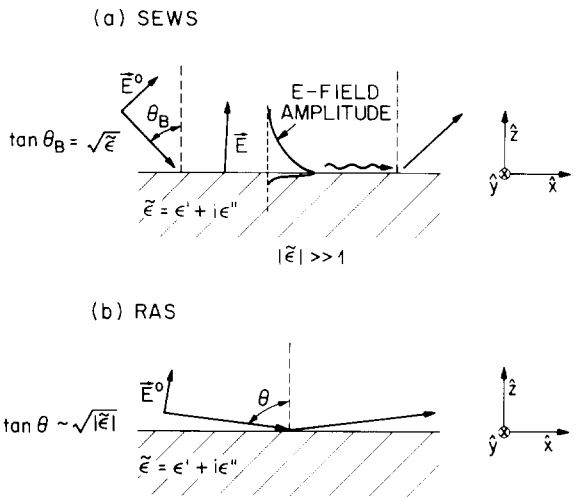

Fig. 3. Schematic representation of the two optical configurations: (a) for surface electromagnetic wave spectroscopy where the SEW's are trapped on the surface and propagate with $k_{x_{SEW}} = (\omega/c)[\epsilon/(1+\epsilon)]^{1/2} > \omega/c$, and (b) for reflection–absorption spectroscopy. The means of achieving a complex angle θ_B are discussed in section 3.1.2.

amplitude of the electric field be zero. This defines the Brewster angle, $\tan\theta_B = \sqrt{\tilde{\epsilon}}$. However, since $\tilde{\epsilon}$ is complex for metals (fig. 1), no real angle of incidence can satisfy the Brewster condition. In section 3.1.2, simple means of producing a complex angle of incidence will be presented, which approximately satisfy the Brewster condition. When this condition is satisfied, the electromagnetic radiation is trapped at the surface and propagates along the surface with a large $E_z^{\text{vacuum}}(z=0)$ component. It can therefore interact with adsorbed molecules for an absorption length (~ 1 cm) before being decoupled and detected. For a standard external reflection, however, the angle of incidence is real and the reflected amplitude is finite. The reflected field intensity is minimized (for p-polarization) for $\tan\theta = \sqrt{|\tilde{\epsilon}|}$. This defines the pseudo-Brewster angle for which the maximum amount of electromagnetic energy is imparted to the metallic substrate. It will be shown in sections 2.2.1 and 3.1.1 that this angle and polarization give the highest sensitivity to the surface electronic absorption of the substrate.

2.1.2. Non-absorbing substrates: internal reflection

If the substrate is *non-absorbing* (ϵ real) but still characterized by a high index ($\epsilon \gg 1$), as is the case for a number of semiconductors (Ge, Si, GaAs), it is possible to consider radiation internally incident on the interface. For angles of incidence greater than the critical angle, $\theta > \theta_c \equiv \sin^{-1}(1/\sqrt{\epsilon})$, radiation is totally internally reflected (fig. 4). The fields of interest are now the "trans-

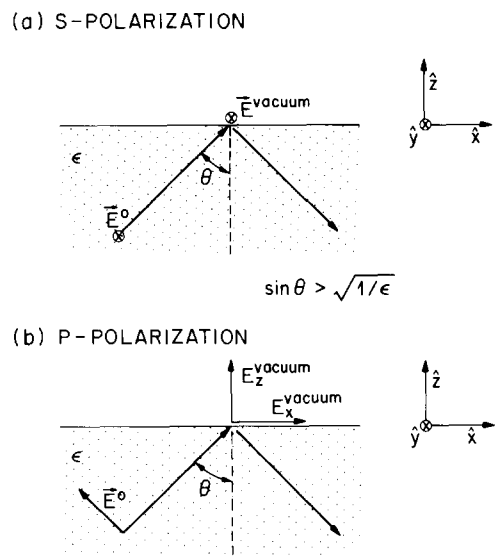

Fig. 4. Schematic representation of the internal reflection configuration for the two polarizations of interest. Note that all the components of the fields on the vacuum side of the interface are evanescent, i.e. their amplitude decays exponentially into the vacuum ($z > 0$). For $\epsilon \gg 1$, $|E_i^{vacuum}| \sim 2(\cos\theta)E^0$ for $i = x, y, z$.

mitted" fields that are actually evanescent. This is due to the fact that the propagation vector normal to the surface, $(\omega/c)\sqrt{1 - \epsilon \sin^2\theta}$, is now purely imaginary since $\sin\theta > 1/\sqrt{\epsilon}$. In the field equations, (2.3)–(2.5), the amplitude of the evanescent tangential fields at $z \gtrsim 0$ can be obtained by replacing $\epsilon/1$ by $1/\epsilon$ and $(1 - \epsilon \sin^2\theta)^{1/2}$ by $i(\epsilon \sin^2\theta - 1)^{1/2}$. For the evanescent normal field at $z \gtrsim 0$, E_z^{vacuum}, condition (2.2a) requires its amplitude to be scaled by ϵ. The results are for s-polarization:

$$|E_y^{vacuum}(z = 0)| = \frac{2\cos\theta}{(1 - 1/\epsilon)^{1/2}} E^0, \tag{2.6}$$

and for p-polarization:

$$|E_z^{vacuum}(z = 0)| = \frac{2\cos\theta}{(1 - 1/\epsilon)^{1/2}\left[(1 + 1/\epsilon)\sin^2\theta - 1/\epsilon\right]^{1/2}} (\sin\theta\, E^0), \tag{2.7}$$

$$|E_x^{vacuum}(z = 0)| = \frac{2(\sin^2\theta - 1/\epsilon)^{1/2}}{(1 - 1/\epsilon)^{1/2}\left[(1 + 1/\epsilon)\sin^2\theta - 1/\epsilon\right]^{1/2}} (\cos\theta\, E^0). \tag{2.8}$$

The above equations (2.6)–(2.8) show a property of internal reflection which is of practical importance: for $\epsilon \gg 1$, all the field components have roughly

equal amplitude, $(2 \cos \theta)E^0$. All components of a surface dipole can therefore be probed *with equal sensitivity*.

This is not the case for external reflection for which the tangential components are attenuated by approximately $1/\sqrt{\epsilon}$. The sensitivity to dipoles parallel to the surface is therefore ϵ times weaker than to perpendicular dipoles since the absorption is proportional to the square of the electric field. This observation is also important when comparing EELS and MIR SIRS because specular EELS corresponds to an *external* incidence geometry with consequently lower sensitivity to the tangential components.

For completeness, we note that for $\theta < \theta_c$, the tangential component of the field in an internal incidence configuration is still large on the vacuum side. For example, at normal incidence:

$$E^{\text{vacuum}}(z = 0) = \frac{2}{1 + 1/\sqrt{\epsilon}} E^0, \tag{2.9}$$

in contrast to external reflection, where:

$$E^{\text{vacuum}}(z = 0) = \frac{2}{\sqrt{\epsilon} + 1} E^0. \tag{2.10}$$

If the source could be located either inside or outside the high index material, internal transmission would therefore be more sensitive to tangential modes than external reflection.

In the case of transparent materials with low index of refraction (e.g. $1 < \epsilon < 3$), the difference between external and internal reflection is not as large. Specific constraints such as sample size and critical angle, and requirements such as polarization of the modes under study become important factors in the choice of an optimal geometry.

In this section, the essence of SIRS was outlined in a qualitative way. The sensitivity to adsorbates was assumed to be proportional to the electric field intensity on the vacuum side of the interface. As a first approximation, the response of the adsorbate was neglected in the calculations of the field amplitudes, which were then solely dependent on the substrate response, $\epsilon(\omega)$. While proper sensitivity analysis (taking into account the adsorbate layer response) will be presented in section 3, the main ideas can be summarized here. For adsorbates on metal substrates, *grazing* incidence reflection (section 3.1.1), SEW launching and detecting (section 3.1.2), or emission at grazing incidence (section 3.1.3) should be used in order to *maximize* the normal component of the electric field. Tangential components are always weak on metals. For adsorbates on transparent substrates (semiconductors or insulators), total internal reflection is preferable, particularly for high index materials (section 3.2.1). For mildly absorbing or low index materials, external reflection should also be considered (section 3.2.2).

2.2. Three-layer model

For a quantitative analysis of the infrared reflection spectra of adsorbates at surfaces, a microscopic theory of the surface optical response is required. Only in rare cases, however, can the response of a substrate/adsorbate system to plane electromagnetic waves be calculated from first principles (section 2.4.1). Usually, the *local* surface polarizability $\alpha(\omega)$ is computed from cluster calculations or expressed phenomenologically. Evaluation of the local field, including adsorbate–adsorbate interactions and non-local effects, becomes then very important. This can be seen by considering the change in reflectivity $\Delta R/R \equiv (R^0 - R)/R^0$ arising from the presence of an absorbing "surface" layer of polarizability $\alpha(\omega)$. R and R^0 are the reflectivities of the substrate with and without the "surface" layer, respectively. In general,

$$\Delta R/R = 4\pi(\omega/c)\ F(\theta)\ N_s\ \mathrm{Im}\ \alpha(\omega), \tag{2.11}$$

where ω is the circular frequency $\omega = 2\pi c\tilde{\nu}$, N_s is the number of adsorbates characterized by $\alpha(\omega)$ per unit area (coverage), and $F(\theta)$ is a function of the polarization (s or p), the angle of incidence θ and the dielectric response of the system. If $\alpha(\omega)$ is the *local* polarizability, then $F(\theta)$ contains all the local field complexity.

A simple macroscopic model [8,26,27] has therefore been introduced to calculate the local fields by describing the system in terms of three media separated by sharp boundaries: (1) the substrate characterized by its bulk dielectric function, (2) the surface layer characterized by a dielectric function $\tilde{\epsilon}$ and an "effective" thickness d, and (3) the vacuum. Within this macroscopic description, all the physics is buried in the two parameters $\tilde{\epsilon}$ and d. These parameters are required inputs for the three-layer model and are not independent. In the local limit, they are defined by:

$$\sum_j \tilde{\Lambda}_{ij} = \sum_j (\tilde{\epsilon}_{ij} - 1) d_{ij} = 4\pi (N_s)_i \alpha_i, \quad i, j = x, y, z. \tag{2.12}$$

The quantity $(N_s)_i$ is the number of centers per unit area contributing to the ith component of the polarizability, α_i. N_s is therefore the same quantity appearing in eq. (2.11). The functional form of Λ_{ij} is defined only by the microscopic quantities of the adsorbate. In the three-layer model, the separation of $\tilde{\Lambda}$ into $\tilde{\epsilon}$ and d is done to give the conventional *macroscopic* picture. There is no macroscopic meaning to d, except that it provides the proper relationship between the two-dimensional macroscopic response $\tilde{\Lambda}$ and the three-dimensional macroscopic response $\tilde{\epsilon}$. For an anisotropic layer, a different d is in general associated with each component of the dielectric tensor.

The model shown in fig. 5 was first introduced by Francis and Ellison [8] and worked out by Greenler [26]. To make it more relevant, the most

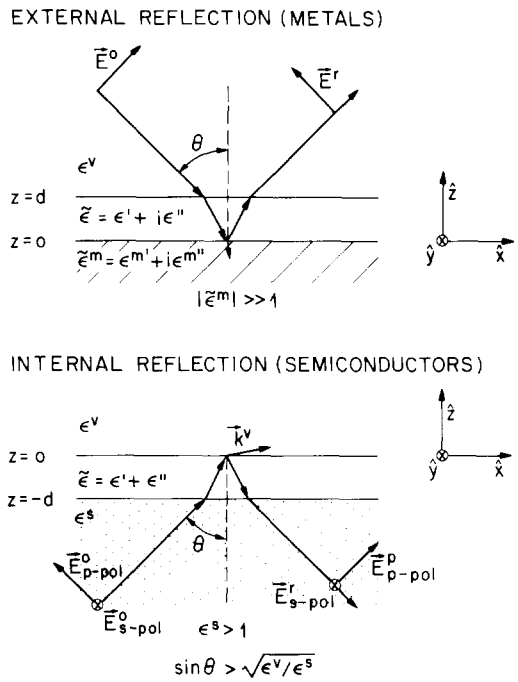

Fig. 5. Schematic representation of the three-layer model to treat (a) external reflection on metal substrates, and (b) internal reflection at a semiconductor/vacuum interface. Note that the propagation vector k^v in (b) has a purely imaginary z-component for total internal reflection (evanescent field) and a real z-component for external reflection (propagating transmitted radiation).

commonly used geometries are shown: (a) external reflection for metals (fig. 5a), characterized by a complex $\tilde{\epsilon}^m$, and (b) internal reflection for transparent substrates (fig. 5b), characterized by a real ϵ^s. However, to be applicable to cases where the ambient is not vacuum, we keep the response of the vacuum as a variable, ϵ^v. The present derivation follows the work of McIntyre and Aspnes [27]. Since we are interested in submonolayer coverages of atoms or molecules *oriented* on the surface, we follow Dignam and Moskovits [28,29] by assuming that the active adsorbate layer is characterized by an anisotropic response but with principal axes along x, y and z. The dielectric tensors are therefore diagonal with principal values $\tilde{\epsilon}_x$, $\tilde{\epsilon}_y$, $\tilde{\epsilon}_z$ and d_x, d_y, d_z. The media are assumed nonmagnetic.

The essence of the derivation, reported in ref. [30], is to solve Maxwell's equations subject to the boundary conditions (2.2) at each interface and to use a linear approximation when expanding in powers of d/λ: $\exp(ik_z d) \approx 1 + ik_z d$. This assumption is excellent since the layer effective thickness (~ 1 Å) is much smaller than the infrared wavelengths ($\sim 100\,000$ Å).

2.2.1. Metallic substrates

The quantities calculated are the Fresnel coefficients, $r = E^r/E^0$ in the presence of an adsorbate layer of thickness d (see fig. 5a), and $r^0 \equiv r(d=0)$ without such a layer. Experimentally, the reflectivities of the clean $R^0 = |r^0|^2$ and adsorbate covered $R = |r|^2$ surfaces are recorded, from which the reflectance, R/R^0, is obtained. The absorption associated with the adsorbate layer is best expressed as $\Delta R/R = 1 - |r/r^0|^2$. For an anisotropic metal substrate characterized by $\tilde{\epsilon}_x^m$, $\tilde{\epsilon}_y^m$, $\tilde{\epsilon}_z^m$, and d_x, d_y, d_z, the absorption for s-polarization (s-pol) is:

$$[\Delta R/R]_{\text{s-pol}} = 8\pi\tilde{\nu}\sqrt{\epsilon^v}\, d_y \cos\theta \,\operatorname{Im}\left[\frac{\tilde{\epsilon}_y^m - \tilde{\epsilon}_y}{\tilde{\epsilon}_y^m - \epsilon^v}\right], \tag{2.13}$$

where $\tilde{\nu}$ is the vibrational frequency in cm^{-1} ($\omega = 2\pi c\tilde{\nu}$); and for p-polarization (p-pol):

$$[\Delta R/R]_{\text{p-pol}} = 8\pi\tilde{\nu}\sqrt{\epsilon^v}\cos\theta \,\operatorname{Im}\left[\frac{(\tilde{\epsilon}_x^m - \tilde{\epsilon}_x)d_x - ((\tilde{\epsilon}_x^m/\tilde{\epsilon}_z)d_z - (\tilde{\epsilon}_x/\tilde{\epsilon}_z^m)d_x)\epsilon^v \sin^2\theta}{(\tilde{\epsilon}_x^m - \epsilon^v) - ((\tilde{\epsilon}_x^m/\epsilon^v) - (\epsilon^v/\tilde{\epsilon}_z^m))\epsilon^v \sin^2\theta}\right]. \tag{2.14}$$

Eqs. (2.13) and (2.14) can be simplified for the two cases of interest: the vibrational spectrum of an adsorbed monolayer (weak absorber) and the electronic spectrum of a surface state excitation. The adsorbate layer is characterized by a dielectric function of order one with a small absorption term. In contrast, the electronic absorption occurs inside the medium with a large dielectric function ($\tilde{\epsilon} \approx \tilde{\epsilon}^m$).

We first consider the vibrational absorption of an adsorbed layer (outside the metal). Using $|\tilde{\epsilon}^m| \gg \epsilon^v \approx 1$, eq. (2.13) becomes, to order ϵ^v/ϵ^m:

$$[\Delta R/R]_{\text{s-pol}} \approx 8\pi\tilde{\nu}\sqrt{\epsilon^v}\, d_y \cos\theta \,\operatorname{Im}\left[\frac{\epsilon^v - \tilde{\epsilon}_y}{\tilde{\epsilon}_y^m}\right]. \tag{2.15}$$

In eq. (2.15), the term $\operatorname{Im}[(\epsilon^v - \tilde{\epsilon}_y)/\tilde{\epsilon}_y^m] = [\epsilon_y^{m''}(\epsilon_y' - \epsilon^v) - \epsilon^{m'}\epsilon_y'']/|\tilde{\epsilon}^m|^2$ explicitly shows that any finite surface absorption ($\epsilon_y'' > 0$) leads to a positive value of $\Delta R/R$ ("positive" absorption) because $\epsilon^{m'} < 0$ for metals (see fig. 1b). This is not the case for a dielectric substrate since $\epsilon^{s'} > 0$ as will be shown in section 2.2.2. Note that the magnitude of $\Delta R/R$ is scaled by $1/|\tilde{\epsilon}^m|$, and is therefore small.

With the additional simplifying assumption that the metal substrate is isotropic ($\tilde{\epsilon}_x^m = \tilde{\epsilon}_z^m = \tilde{\epsilon}^m$), eq. (2.14) becomes, to order ϵ^v/ϵ^m:

$$[\Delta R/R]_{\text{p-pol}} \approx 8\pi\tilde{\nu}\sqrt{\epsilon^v}\,\operatorname{Im}\left[\frac{-(\epsilon^v/\tilde{\epsilon}_z)d_z \sin^2\theta + ((\epsilon^v - \tilde{\epsilon}_x)/\tilde{\epsilon}^m)d_x}{\cos\theta\,(1 - (\epsilon^v/\tilde{\epsilon}^m)\tan^2\theta)}\right]. \tag{2.16}$$

The leading term of eq. (2.16) is:

$$[\Delta R/R]_{\text{p-pol}} \simeq 8\pi\tilde{\nu}\epsilon^{\text{v}}\sqrt{\epsilon^{\text{v}}}\, d_z \frac{\sin^2\theta}{\cos\theta} \operatorname{Im}\left[\frac{-1/\tilde{\epsilon}_z}{1-(\epsilon^{\text{v}}/\tilde{\epsilon}^{\text{m}})\tan^2\theta}\right]. \tag{2.17}$$

To an excellent approximation, the optimum angle (i.e. yielding the largest $\Delta R/R$ for a given $\tilde{\epsilon}_z$) can be obtained by minimizing the denominator

$$\cos\theta\,|1-(\epsilon^{\text{v}}/\tilde{\epsilon}^{\text{m}})\tan^2\theta\,|^2, \tag{2.18}$$

giving $\tan^2\theta = (|\tilde{\epsilon}^{\text{m}}|/\epsilon^{\text{v}})(\sqrt{3} - \epsilon^{\text{m}'}/|\tilde{\epsilon}^{\text{m}}|)^{-1}$. If we assume that $\text{Re}(\tilde{\epsilon}^{\text{m}}) \equiv \epsilon^{\text{m}'} \ll |\tilde{\epsilon}^{\text{m}}|$ as was done by Ibach and Mills [31], the optimum angle is then given by $\tan\theta \approx \sqrt{|\tilde{\epsilon}^{m}|/3^{1/2}\epsilon^{\text{v}}}$. By evaluating eq. (2.16) numerically, Greenler has calculated the optimum angles for a number of metallic substrates [32]. For each substrate, the optimum angle is slightly less than the pseudo-Brewster angle defined by $\tan\theta = \sqrt{|\tilde{\epsilon}^{m}|/\epsilon^{\text{v}}}$, as expected from the above estimates. In practice, however, experiments are carried out with $85° \lesssim \theta < 80°$ for which $\tan^2\theta < |\tilde{\epsilon}^{\text{m}}|/\epsilon^{\text{v}}$. Therefore, for practical applications, a useful approximate form of eq. (2.17) is:

$$[\Delta R/R]_{\text{p-pol}} \approx 8\pi\tilde{\nu}\epsilon^{\text{v}}\sqrt{\epsilon^{\text{v}}}\, d_z(\sin^2\theta/\cos\theta)\,\operatorname{Im}(-1/\tilde{\epsilon}_z). \tag{2.19}$$

We now consider the case of an electronic absorption taking place *inside* the high index metal, the dielectric function of the active layer is now large ($|\tilde{\epsilon}| \approx |\tilde{\epsilon}^{\text{m}}| \gg \epsilon^{\text{v}} \approx 1$). For s-polarization, eq. (2.13) becomes:

$$[\Delta R/R]_{\text{s-pol}} \approx 8\pi\tilde{\nu}\sqrt{\epsilon^{\text{v}}}\, d_y \cos\theta\, \operatorname{Im}\left[\frac{-\tilde{\epsilon}_y}{\tilde{\epsilon}_y^{\text{m}}}\right], \tag{2.20}$$

and, for p-polarization, eq. (2.14) becomes (for $\theta \leq 85°$):

$$[\Delta R/R]_{\text{p-pol}} \approx 8\pi\tilde{\nu}\sqrt{\epsilon^{\text{v}}}\, d_x \frac{1}{\cos\theta} \operatorname{Im}\left[\frac{-\tilde{\epsilon}_x}{\tilde{\epsilon}_x^{\text{m}}}\right]. \tag{2.21}$$

The important observation here is that all the terms involving $\tilde{\epsilon}_z$ and d_z are small and can be neglected, leaving only the tangential components. Apart from the angular dependence representing the strength of the parallel component of the electric field inside the high index layer (see discussion at the end of section 3.1.1), eqs. (2.20) and (2.21) are identical. Physically, they emphasize that the radiation is so strongly refracted within the substrate that it only probes sensitively the tangential component of the dielectric function.

2.2.2. Semiconductor and insulator substrates

Since we have already argued in section 2.1.2 that internal reflection is more favorable when the substrates are transparent, we present the results of the three-layer model for internal reflection (see fig. 5b) where ϵ^{s} and ϵ^{v} are real and *isotropic*. In the following equations, ϵ^{s} and ϵ^{v} can be simply interchanged

to describe the case of external reflection. With these definitions (fig. 5b) and assumptions, eqs. (2.13) and (2.14) become:

$$[\Delta R/R]_{\text{s-pol}} = \frac{2\pi\tilde{\nu}}{\sqrt{\epsilon^{\text{s}}}\cos\theta} I_y(\epsilon_y'' d_y), \tag{2.22}$$

$$[\Delta R/R]_{\text{p-pol}} = \frac{2\pi\tilde{\nu}}{\sqrt{\epsilon^{\text{s}}}\cos\theta}\left[I_x(\epsilon_x'' d_x) + I_z \frac{\epsilon^{\text{v}2}}{\epsilon_z'^2 + \epsilon_z''^2}(\epsilon_z'' d_z)\right], \tag{2.23}$$

where the quantities I_i are the components of the field *intensities* derived in section 2.1.2 (eqs. (2.6)–(2.8)), namely:

$$I_y = \frac{4\epsilon^{\text{s}}\cos^2\theta}{\epsilon^{\text{s}} - \epsilon^{\text{v}}}, \tag{2.24}$$

$$I_z = \frac{4\epsilon^{\text{s}}\cos^2\theta}{\epsilon^{\text{s}} - \epsilon^{\text{v}}} \frac{(\epsilon^{\text{s}}/\epsilon^{\text{v}})\sin^2\theta}{\left[((\epsilon^{\text{s}} + \epsilon^{\text{v}})/\epsilon^{\text{v}})\sin^2\theta - 1\right]}, \tag{2.25}$$

$$I_x = \frac{4\epsilon^{\text{s}}\cos^2\theta}{\epsilon^{\text{s}} - \epsilon^{\text{v}}} \frac{\left[(\epsilon^{\text{s}}/\epsilon^{\text{v}})\sin^2\theta - 1\right]}{\left[((\epsilon^{\text{s}} + \epsilon^{\text{v}})/\epsilon^{\text{v}})\sin^2\theta - 1\right]}. \tag{2.26}$$

In eqs. (2.22) and (2.23), the factor $1/(\cos\theta)$ represents the increase in sampling area as the angle of incidence is increased and the factor $1/\sqrt{\epsilon^{\text{s}}}$ reflects the index matching role of the active layer [33]. Therefore, because the substrate and vacuum do not absorb, these expressions only involve the factors $\text{Im}(\epsilon_y d_y)$, $\text{Im}(\epsilon_x d_x)$ and $\text{Im}(-1/\epsilon_z)d_z$ to represent the absorption of the active layer. The next section provides a microscopic description of this absorption. In closing, we note that for external reflection [$\epsilon^{\text{s}} \to \epsilon^{\text{v}}$ and $\epsilon^{\text{v}} \to \epsilon^{\text{s}}$ in eqs. (2.22)–(2.25)], the quantities I_x and I_y are negative whereas I_z remain positive. This implies that, on a dielectric substrate ($\epsilon^{\text{s}'} > 0$), any finite tangential absorption ($\epsilon_{\parallel}'' > 0$) leads to a negative value of $\Delta R/R$ ("negative" absorption). In other words, an absorbing layer acts as a reflection coating for tangential fields, in contrast to metallic substrates.

2.3. *Microscopic considerations*

2.3.1. *Lorentz oscillator model*

The previous macroscopic description is only useful if $\tilde{\epsilon}$ can be expressed in terms of meaningful microscopic quantities such as the local polarizability α and ultimately the dynamic charge of the adsorbate mode and the electronic screening within the adsorbate layer. Since ab-initio calculations are in general difficult, a Lorentz oscillator parametrization of an adsorbate layer has been used extensively [34]. The equations of motion of a layer of dipoles, subject to

damping, are solved to obtain the vibrational part of the polarizability. The generalized polarizability is then written:

$$\alpha_i(\omega) = \alpha_{e_i} + \alpha_{v_i}(\omega) = \alpha_{e_i} + \frac{e_i^{*2}/m_i^*}{(\omega_0)_i^2 - \omega^2 - i\gamma_i\omega}, \quad i = x, y, z, \tag{2.27}$$

where α_e is the electronic component of the polarizability including the contribution from valence and core electrons (usually constant at the frequency of interest) and also possible resonant electronic levels which can interact with the atomic motion (see section 2.5.2). The oscillator parameters are ω_0 the resonant frequency, γ the natural line width, e^* the effective dynamic charge and m^* the effective mass. The dielectric function is defined by eq. (2.12) and assumed diagonal:

$$\tilde{\epsilon}_i(\omega) = 1 + 4\pi\frac{(N_s)_i}{d_i}\alpha_i(\omega) = (\epsilon_\infty)_i + \frac{(\omega_p)_i^2}{(\omega_0)_i^2 - \omega^2 - i\gamma_i\omega}, \tag{2.28}$$

where $(\epsilon_\infty)_i = 1 + 4\pi[(N_s)_i/d_i]\alpha_{e_i}$ represents the electronic part of the dielectric function and $(\omega_p)_i = [4\pi[(N_s)_i/d_i]e_i^{*2}/m_i^*]^{1/2}$ is the plasma frequency associated with the adsorbate layer. For reference purposes, eq. (2.28) is rewritten in terms of the frequency in cm^{-1}, $\tilde{\nu} = (2\pi c)^{-1}\omega$, and dropping the cumbersome index i:

$$\tilde{\epsilon}(\tilde{\nu}) = \left(1 + 4\pi\frac{N_s}{d}\alpha_e\right) + \frac{(N_s/d)e^{*2}/\pi m^* c^2}{\tilde{\nu}_0^2 - \tilde{\nu}^2 - i\Gamma\tilde{\nu}}, \tag{2.29}$$

where $\tilde{\nu}_0$ is the resonant frequency (in cm^{-1}) and $\Gamma = (2\pi c)^{-1}\gamma$ the natural line width (in cm^{-1}).

Note that the definition of $\tilde{\epsilon}$ is correct only to the extent that the right physics is put into d. The Lorentz oscillator model for the vibrational response of the layer gives a particularly simple expression for d, consistent with eqs. (2.12), (2.27) and (2.28):

$$d = 4\pi N_s / \sum_{n \neq m} (1/r_{nm})^3, \tag{2.30}$$

where r_{nm} is the distance between the nth and mth dipoles. The quantity $U_0 \equiv \sum_{n \neq m}(1/r_{nm})^3$ can in general be written $CN_s^{3/2}$ where C is a constant (close to 10) that depends on the specific arrangement of the dipoles at the surface [35,36]. Clearly, d does not represent a physical distance but rather a length scale over which the adsorbate layer, described by $\tilde{\epsilon}$, responds to the electromagnetic radiation. To illustrate how the three-layer model complements the general expression given in eq. (2.11), $F(\theta)$ is written out explicitly for the cases derived in the previous section.

For external reflection at a *metal* surface ($|\tilde{\epsilon}^{m}| \gg \epsilon^{v} \approx 1$), eqs. (2.19) and (2.11) yield:

$$F(\theta) = 4\epsilon^{v}\sqrt{\epsilon^{v}}\,\frac{\sin^2\theta}{\cos\theta}\,|\tilde{\epsilon}_z|^{-2}. \tag{2.31}$$

For internal reflection at the surface of a transparent substrate (ϵ^{s} real), eqs. (2.11) and (2.22) yield (s-polarization):

$$F(\theta)|_y = I_y/(\sqrt{\epsilon^{s}}\cos\theta) = \frac{4\sqrt{\epsilon^{s}}\cos\theta}{\epsilon^{s}-\epsilon^{v}}, \tag{2.32}$$

and eqs. (2.11) and (2.23) yield (p-polarization):

$$F(\theta)|_z = \frac{I_z}{\sqrt{\epsilon^{s}}\cos\theta}\left(\frac{\epsilon^{v}}{|\epsilon_z|}\right)^2 = \frac{4\sqrt{\epsilon^{s}}(\epsilon^{s}\epsilon^{v})\cos\theta\,\sin^2\theta}{(\epsilon^{s}-\epsilon^{v})\left[((\epsilon^{s}+\epsilon^{v})/\epsilon^{v})\,\sin^2\theta-1\right]}\,|\tilde{\epsilon}_z|^{-2}, \tag{2.33}$$

$$F(\theta)|_x = \frac{I_x}{\sqrt{\epsilon^{s}}\cos\theta} = \frac{4\sqrt{\epsilon^{s}}\cos\theta\left[(\epsilon^{s}/\epsilon^{v})\,\sin^2\theta-1\right]}{(\epsilon^{s}-\epsilon^{v})\left[((\epsilon^{s}+\epsilon^{v})/\epsilon^{v})\,\sin^2\theta-1\right]}. \tag{2.34}$$

Recall, for completeness, that the case of external reflection for non-absorbing substrates is recovered by interchanging ϵ^{v} and ϵ^{s} in eqs. (2.32)–(2.34). With these explicit expressions for $F(\theta)$, the change in reflectivity is written:

$$\Delta R/R|_i = 2\pi\tilde{\nu}\,F(\theta)|_i\,\mathrm{Im}(\epsilon_i d_i), \tag{2.35}$$

where d_i and ϵ_i must satisfy eq. (2.12), i.e. $\mathrm{Im}(\epsilon_i d_i) = 4\pi(N_s)_i\,\mathrm{Im}(\alpha_i)$ is independent of d_i. This reflects the fact that the absorption involving the parallel components (x and y) of the layer dielectric function does not involve electronic screening or dipole–dipole interactions, and thus does not involve d. The absorption normal to the surface, however, involves $\mathrm{Im}(-1/\tilde{\epsilon}_z)d_z$, reflected in the factor $|\tilde{\epsilon}_z|^{-2}$ in eqs. (2.13) and (2.33). Using eqs. (2.27) and (2.29), this function can be written explicitly:

$$\mathrm{Im}\left[\frac{-1}{\tilde{\epsilon}_z}\right]d_z = N_s\,\frac{\Gamma\tilde{\nu}\nu_0^2}{\left(\tilde{\nu}_0^2+\tilde{\nu}_p^2/\epsilon_\infty-\tilde{\nu}^2\right)^2+\Gamma^2\tilde{\nu}^2}\left(\frac{4\pi\alpha_v(0)}{\epsilon_\infty^2}\right), \tag{2.36}$$

where $\alpha_v(0) = (e^{*2}/m^*)/4\pi^2c^2\nu_0^2 = e^{*2}/m^*\omega_0^2$ and $4\pi^2c^2\tilde{\nu}_p^2 = \omega_p^2 = (4\pi N_s/d)(e^{*2}/m^*) = U_0(e^{*2}/m^*)$. It is apparent that the resonance now occurs at:

$$\tilde{\nu} = \sqrt{\tilde{\nu}_0^2+\tilde{\nu}_p^2/\epsilon_\infty} = \tilde{\nu}_0\left[1+\frac{U_0\alpha_v(0)}{1+U_0\alpha_e}\right]^{1/2}, \tag{2.37}$$

and the intensity of the mode is attenuated:

$$\int(\Delta R/R)\,\mathrm{d}\tilde{\nu} \propto \epsilon_z'' d_z/\epsilon_\infty^2 \propto \frac{\alpha_v(0)}{(1+U_0\alpha_e)^2}. \tag{2.38}$$

The explicit expression for a metallic substrate is, using eqs. (2.31) and (2.35):

$$\int (\Delta R/R)\, \mathrm{d}\tilde{\nu} = 4\pi\epsilon^{\mathrm{v}}\sqrt{\epsilon^{\mathrm{v}}}\,\frac{\sin^2\theta}{\cos\theta} N_{\mathrm{s}}\left(e^{*2}/m^{*}c^{2}\right)\left(1/\epsilon_{\infty}^{2}\right). \tag{2.38a}$$

In summary, for a homogeneous adsorbate layer of coverage N_{s} described by a Lorentz oscillator model, the three-layer model describes the dynamical interactions in terms of d, defined by eq. (2.30), and $\epsilon_{\infty} = 1 + U_0\alpha_{\mathrm{e}}$.

The problem is more complicated when the active layer is used to describe surface electronic, rather than vibrational absorption. Although, the layer is still modelled by a dielectric function $\tilde{\epsilon}$ and a thickness d, the interpretation of these quantities is different. The thickness is viewed as a real space distance over which the electronic absorption occurs and ϵ is calculated independently. Extensive modelling of $\tilde{\epsilon}$ has been done in the case of electronic surface state absorption at semiconductor surfaces [37] and will be discussed in section 4. The next section will give a flavor of the possible expression for d.

2.3.2. Assumption of sharp boundaries and non-locality problem

Feibelman has pointed out that the underlying assumption of a step function discontinuity in ϵ at an interface meets serious fundamental problems [38]. First, Poisson's equation identifies the source of the discontinuity for the normal component of the electric field as an induced surface charge density:

$$\rho(\boldsymbol{r}) = (1/\pi)\left[E_{\perp}(\mathrm{out}) - E_{\perp}(\mathrm{in})\right]\, \delta(z). \tag{2.39}$$

Physically, the extent of this charge density must be of order Å, i.e. a screening length or Fermi wavelength, rather than a delta function. Second, Feibelman argues that the hypothetized optical excitation by a discontinuous field would lead to an overestimate of the momentum imparted in the excitation process. Therefore, the region over which E_z varies must be finite (of order Å). It then becomes critical to ascertain the exact position (i.e. to determine the local field) where the optical excitation of adsorbate vibrational modes or electric states takes place.

Furthermore, apart from the problems associated with a discontinuous dielectric function $\tilde{\epsilon}$, the *local* constitutive relation for $\tilde{\epsilon}$ given in eq. (2.1) is not valid because the electric field varies rapidly on the atomic scale. The rigorous relation should be:

$$D_i(\boldsymbol{r}, t) = \sum_j \int \mathrm{d}t' \int \mathrm{d}^3 r'\, \tilde{\epsilon}_{ij}(\boldsymbol{r}, \boldsymbol{r}', t, t')\, E_j(\boldsymbol{r}', t'). \tag{2.40}$$

For the tangential components ($j = x, y$), the boundary condition (2.2b) states that the electric fields are continuous. Therefore, the local relation (2.1) is accurate as long as the off-diagonal elements of $\tilde{\epsilon}$ are much smaller than $\tilde{\epsilon}_{zz}$. For the normal component ($j = z$), however, the variation of the electric field

is large on the scale of the lattice spacing a. The Taylor expansion for $\boldsymbol{E}(\boldsymbol{r}', t')$ about $\boldsymbol{r}$,

$$\boldsymbol{E}(\boldsymbol{r}', t') = \boldsymbol{E}(\boldsymbol{r}, t') + (\boldsymbol{r}' - \boldsymbol{r}) \cdot \nabla \boldsymbol{E}(\boldsymbol{r}, t') + \ldots \tag{2.41}$$

contains terms, such as $\partial E_z(\boldsymbol{r}, t')/\partial z$, that are comparable to $E(\boldsymbol{r}, t')/a$, i.e. not negligible compared to the zeroth-order term.

To deal with the non-local response of the surface to rapidly varying electric fields normal to the surface, Feibelman defined a *surface* response function, $d_\perp(\omega)$. For infrared frequencies, i.e. well below the plasma frequency, the integro-differential equation is:

$$d_\perp(\omega) = \frac{1}{\tilde{\epsilon}^{\mathrm{m}}/\epsilon^{\mathrm{v}} - 1} \int_{z^{\mathrm{m}}}^{z^{\mathrm{v}}} \mathrm{d}z'\, z' \frac{\mathrm{d}}{\mathrm{d}z'} \tilde{\epsilon}_z(z'), \tag{2.42}$$

where $\epsilon_z(z') = E_z^{\mathrm{m}}(z')/E_z^{\mathrm{v}}(z')$ and $z \lesssim 0$ in the metal substrate ($z^{\mathrm{m}} \leq 0$). The limits of integration, z^{m} and z^{v}, are chosen such that *all* the surface absorption occurs between these two values. For instance, if we make the same assumptions as in the three-layer model described in section 2.2, i.e. all the absorption occurs between $z = 0$ and $z = d$, then eq. (2.42) becomes:

$$d_\perp(\omega) = \frac{1/\epsilon^{\mathrm{v}} - 1/\tilde{\epsilon}_z}{1/\epsilon^{\mathrm{v}} - 1/\tilde{\epsilon}^{\mathrm{m}}} d. \tag{2.43}$$

Note that $d_\perp(\omega) = 0$ if $\tilde{\epsilon}_z = \epsilon^{\mathrm{v}}$ or $d = 0$ (i.e. $\tilde{\epsilon}_z = \tilde{\epsilon}^{\mathrm{m}}$). The physical meaning of $d_\perp(\omega)$ is discussed by Feibelman. The centroid of the *surface* "position", i.e. of the induced charge responsible for the surface absorption, is given by $\mathrm{Re}[d_\perp(\omega)]$. Moreover, if the substrate does not have any bulk absorption (ϵ^{m} or ϵ^{s} real) as is the case for semiconductors in the gap, then $\mathrm{Im}[d_\perp(\omega)]$ is the *surface* power absorption.

Alternatively, Bagchi et al. [39,40] have described the surface by a diagonal tensor $\Delta\epsilon_{ii}$ ($i = x, y, z$) defined by

$$\Delta\epsilon_{ij}(z, z')\ \delta_{ij} = \epsilon_{ij}(z - z') - \delta_{ij}\ \delta(z - z')\ \epsilon^0(z), \tag{2.44}$$

where the first term in the rhs of eq. (2.44) is the true response and the second is the Fresnel-like response ($\epsilon^0 = \tilde{\epsilon}^{\mathrm{m}}/\epsilon^{\mathrm{v}}$ or $\epsilon^{\mathrm{s}}/\epsilon^{\mathrm{v}}$) with a known solution to Maxwell's equation. The field components are then expressed in terms of this known solution for $\Delta\epsilon = 0$ and an integral over $\Delta\epsilon$ using the Green function approach. The integro-differential equations can be solved with the Born approximation and using E_x, E_y and D_z (instead of E_z) since all three quantities are continuous at the interface. The definition of D_z is:

$$E_z(z) = \int \mathrm{d}z'\, \epsilon_{zz}^{-1}(z, z')\ D_z(z'), \tag{2.45}$$

where ϵ^{-1} is the matrix inverse of ϵ, namely:

$$\int \epsilon_{zz}(z, z')\ \epsilon_{zz}^{-1}(z', z'')\ \mathrm{d}z' = \delta(z - z''). \tag{2.46}$$

The equations are now local, since all the fields are continuous at the interface. The solutions can again be compared to the results of the three-layer model (assuming an isotropic surface layer) for p-polarization:

$$\overline{\Delta\epsilon_{xx}} \equiv \int \mathrm{d}z\, \mathrm{d}z'\, \Delta\epsilon_{xx}(z, z') = d(\tilde{\epsilon}_x - \tilde{\epsilon}^{\mathrm{m}})/\epsilon^{\mathrm{v}}, \tag{2.47}$$

$$\overline{\Delta\epsilon_{zz}} \equiv \int \mathrm{d}z\, \mathrm{d}z' \left[\epsilon_{zz}^{-1}(z, z') - \frac{\delta(z - z')}{\epsilon^{0}(z)}\right] = d\left(\tilde{\epsilon}_z^{-1} - \tilde{\epsilon}^{\mathrm{m}\,-1}\right)\epsilon^{\mathrm{v}}. \tag{2.48}$$

In summary, the three-layer model is useful to calculate the surface absorption. When sharp boundaries and non-local effects are considered in detail, it appears that the model is in fact quite accurate for vibrational absorption of monolayers located outside the substrate. The local fields can be calculated by treating the dipoles correctly and defining d according to eq. (2.30).

The situation is more difficult for the interpretation of surface electronic absorption, especially when the substrate is absorbing. Computational efforts, based on the Born approximation, are now in progress to average the non-local dielectric function as realistically as possible [37,41–44]. However, no theory can yet account for all the aspects of the surface response when both the substrate and the surface layer have electronic absorption. For instance, recent calculations neglect local field effects [42,43] or simplify the problem by assuming that the electronic polarizability at the surface is the same as that in the bulk [44]. Nevertheless, such calculations have been very useful to interpret the measured surface electronic absorption such as that of Si(111)-(2 × 1) for instance, as reviewed by Chiaradia [37] and Olmstead [41].

2.4. First principle calculations

In section 2.3.2, we concluded that the three-layer model was useful to evaluate the *vibrational* absorption of an *adsorbate* layer described by a Lorentz oscillator model. That is the local field at the position of the vibrational dipoles could be calculated reasonably well within this model. In section 2.3.1, we gave a relationship between the macroscopic quantity $\tilde{\epsilon}$ and microscopic parameters e^*, m^*, α_e. In section 4, we will show that a thorough infrared study, including isotopic mixture experiments, can provide a measure of the natural frequencies and effective charges of the oscillators, *and* of the electronic screening as well. When such measurements are possible, then first principle calculations of the *local* polarizability are sufficient. Otherwise, the *extended* polarizability of the surface layer must be calculated.

In general, first principle calculations are difficult because they require an accurate enough computation of the surface total energy to yield reliable changes due to small displacements of the atoms about their equilibrium positions. However, two different approaches have been successful in many

cases. The first involves self-consistent *slab* calculations, the second ab-initio *cluster* calculations. In a slab calculation, the full periodicity of the surface is maintained whereas in a cluster calculation, a *finite* size cluster (usually a unit cell) represents the surface. As a result, the slab calculation yields directly the fully renormalized normal mode frequencies, including adsorbate–adsorbate dynamical interactions such as the dipole shift $\tilde{\nu}_p^2/2\epsilon_\infty\tilde{\nu}_0$, and the screened effective charge, e^*/ϵ^∞ (see end of section 2.3.1). In contrast, the cluster calculations give the local polarizability (within the cluster) so that the interactions involving adsorbates outside the cluster, such as adsorbate–adsorbate dynamical interactions and electronic screening, must be determined experimentally.

2.4.1. Slab calculations

The slab calculations are based on the local density functional (LDF) method where the total energy of the system is expressed as a function of the electron charge density [45,46]. The LDF equations are then solved self-consistently by appropriate band structure techniques. For instance, the linear augmented plane wave (LAPW) method [47,48] divides space into three kinds of disjoint regions, "muffin-tin" spheres centered on each atom, interstitial regions between these spheres but in the slab (typically 3 to 4 atomic layers thick), and vacuum. Alternatively, the pseudopotential method handles the orthogonalization of the valence electron wavefunctions with those of the core electrons by introducing an effective potential around the core [49]. In all cases, the slabs are then repeated periodically in the z-direction. This introduces a unit cell normal to the slab direction and allows the introduction of Bloch wavefunctions. In the interstitial region, a plane wave basis set is used. The Schrödinger equation, obtained variationally, is then solved self-consistently [50].

The evaluation of the vibrational frequencies first requires the determination of the binding site. This is done by minimizing the total energy with respect to the adsorbate position and repeating such a procedure for all possible binding sites. Then, the adsorbate atom is moved along the direction of a particular normal mode (e.g. perpendicular to the surface for a symmetric stretch) and the binding energy evaluated for each new position. A least-squares fit of several polynomials to these results determines the curvature of the binding energy versus distance curve, from which the vibrational frequency is derived [50]. Note that if the adsorbate mass is comparable to that of the substrate atoms, the motion of substrate atoms cannot be neglected and the situation is much more complicated.

Such calculations are well suited for treating an ordered adlayer, preferably atomic and light, with a small unit cell. There is no restriction on the size of the electronic wavefunctions so that metal slabs, with delocalized wavefunctions, can be handled well. It is therefore natural that this approach has been

Table 3
List of systems studied with slab calculations

Surface	Adsorbate	Site (Coverage)	Modes	Theory (meV)	Experiment (meV)
Si(111)	H	Atop	ss	265 [a]	260 [b]
Ru(0001)	H	3-fold	as	100 [c]	138 [d], 102 [e]
		fcc	ss	140 [c]	105 [d], 141 [e]
W(001)	H	Bridge	Wag	77 [f]	80 [h],[i]
		2 ML	as	169 [f]	160 [j],[h], 118 [i]
			ss	141 [f], 133 [g]	130 [j],[h],[i], 133 [k]
			Opt	150 [f]	118 [i]
Pt(111)	H	3-fold	as	114 [l]	152 [m], 67 [n]
		fcc	ss	166 [l]	68 [m], 112 [n], 155 [o]
Rh(001)	H	4-fold	as	67 [p]	138 [q]
			ss	92 [p]	82 [q]
			Mix	142 [p]	
			Mix	148 [p]	152 [q]
Pd(001)	H	4-fold (hollow) $\theta = 1$	ss	77 [r]	64 [s]
		Bridge $\theta = 2$	ss	165 [r]	–
Ni(001)	H	4-fold (hollow)	ss	82 [t], 90 [u]	74 [v]
Fe(001)	O	4-fold	ss	71 [w]	–
Cu(111)	H	3-fold fcc	ss	120 [x]	–
Cu/Ru(0001)	H	3-fold fcc	ss	130 [x]	–
Ni/W(001)	H	Bridge	ss	67 [y]	–

[a] Appelbaum and Hamann [51].
[b] Backes and Ibach [53].
[c] Feibelman and Hamann [54].
[d] Barteau et al. [55].
[e] Conrad et al. [56].
[f] Biswas and Hamann [57].
[g] Weinert et al. [58].
[h] Barnes and Willis [59].
[i] Woods and Erskine [60].
[j] Ho et al. [61].
[k] Chabal [62].
[l] Feibelman and Hamann [63].
[m] Baró et al. [64].
[n] Richter and Ho [65].
[o] Reutt et al. [66].
[p] Hamann and Feibelman [67].
[q] Richter and Ho [68].
[r] Tománek et al. [69].
[s] Nyberg and Tengstal [70].
[t] Weinert and Davenport [71].
[u] Umrigar and Wilkins [72].
[v] Andersson [73].
[w] Chubb and Pickett [74].
[x] Feibelman and Hamann [75].
[y] Feibelman and Hamann [76].

Key to symbols: ss = symmetric stretch, as = asymmetric stretch, Opt = optical mode.

used extensively and very successfully for H adsorbed on a number of transition and noble metals [51–76] as summarized in table 3. Self-consistent slab calculations have not been used for semiconductor surfaces, with the exception of an early study of H on unreconstructed Si(111) surface [51], mostly because the unit cells tend to be larger than on metals (reconstruction) and cluster calculations are well justified for these more localized surfaces. A new technique, combining density functional and scattering theory, is being developed to tackle the case of *isolated* molecules at surfaces [52].

2.4.2. Cluster calculations

Cluster calculations, on the other hand, utilize the smallest possible number of substrate atoms that can represent the surface accurately. Practically, a unit cell with up to 4 atomic layers is considered. The surface is covered by the atom or molecule under study. The subsurface dangling bonds are made chemically equivalent to the bulk environment by attaching hydrogen or methyl groups [77]. The symmetry of the bulk and surface (for ordered overlayers) is used to fix the atoms within certain planes or along certain axes, thus reducing the number of possible degrees of freedom for atomic motion. Again minimization of the total energy with respect to all atomic motions, constrained to the possible degrees of freedom, is used to determine the equilibrium geometry.

The success of such calculations depends on the choice of basis set (or basis functions) to represent the relevant electronic wavefunctions. The basis set typically consists of s-, p- and d-type atomic orbitals on each center. The number of such functions necessary to reproduce molecular geometries reliably has been well documented for a wide variety of systems [78]. The effects of larger basis sets on the calculated geometries can usually be checked by using smaller clusters. Electron correlation effects are usually considered by means of configuration interaction or by perturbation theory though their effects on molecular geometries of systems such as H on Si(100) are small [79]. Once the geometry has been determined and if the substrate atom motion can be neglected, the complete force field and vibrational frequencies are evaluated using a smaller cluster but with a larger basis set. The complete quadratic force field is usually evaluated easily and cubic or higher order terms can also be computed if necessary. Such calculations were done for H on Si(100) using efficient analytical gradient techniques. In general, the absolute calculated frequencies are about 10% higher than experimentally measured [80]. However, in a systematic study of gas-phase molecules, Raghavachari was able to establish that the *frequency splitting* among the modes involving a similar motion (e.g. symmetric and antisymmetric stretches) could be reproduced reliably [81]. In particular, in the case of the monohydride structure for H on Si(100) such a frequency splitting was found to be remarkably independent of the basis set or the level of theory used [79].

Finally, the dynamic dipole moments, μ, for the various normal modes can be computed using as large a basis set as possible and including electron correlation effects. For H on Si(100), the correlation was introduced by means of Moller–Plesset perturbation theory carried out to fourth order [82]. The changes in the dipole moments are evaluated by taking finite steps, Δd, along the direction of the normal mode under study and calculating the resulting dipole moments. A linear fit of the data about the equilibrium position yields the value $\Delta\mu/\Delta d$. The ratio of the dynamic dipole moments associated with modes that are close in energy can thus be obtained accurately [79]. The absolute dynamic dipole moment can also be extracted by multiplying the quantity $\Delta\dot{\mu}/\Delta d$ by the extremum of the atomic displacements for the mode under study.

The capability of computing reliably such quantities as frequency splittings and relative dynamic dipole moments is essential to the understanding of vibrational spectra of adsorbate–substrate modes. In contrast to adsorbate *internal modes*, these modes have no gas-phase equivalent because the surface cannot be well described by one or two atoms. The importance of ab initio calculations will be revealed in the study of H on Si(100) described in section 4.1.5.

Although cluster calculations are best suited for semiconductor substrates, with well-localized electronic wavefunctions, they have also been applied to adsorbates on metallic substrates [83,84]. For instance, they have been instrumental in understanding the origin of the coverage-dependent vibrational shifts of O and S on Ni(100) [85,86]. In order to model the $p(2\times 2)$ and $c(2\times 2)$ ordered O and S structures, a cluster of 25 Ni atoms (4×4 in top layer and 3×3 in second layer) was used, assuming no relaxation or reconstruction of the substrate.

Batra et al. have also used a combination of cluster calculations and self-consistent slab simulations to investigate the dissociative chemisorption of oxygen on Si(100) and estimate the symmetric stretch frequencies at different binding sites [87]. Since the vibrational frequencies were obtained keeping the Si lattice rigid, however, it is likely that errors arising from the neglect of the Si atom motion are large, particularly for the high coordination sites.

2.4.3. The effective medium theory

The effective medium theory (EMT) emphasizes the adsorbate interaction with the substrate *delocalized* electrons [88–90]. It assumes that, to leading order, the energy gain associated with moving an adatom from infinity to a position $\boldsymbol{r}$ at the surface is equal to the energy gained by placing the atom in an infinite homogeneous electron gas (the effective medium) of density $\bar{n}(\boldsymbol{r})$, where $\bar{n}(\boldsymbol{r})$ is an average of the substrate electron density over the region of the adsorbate [90]. This assumption is optimum for isolated small atoms such as H adsorbed on free electron metals. To describe the surface corrugation, a

covalent correction is introduced to first order, which involves tabulated constants [90,91] and provides the site specificity.

The EMT has the advantage of allowing very simple predictions. To lowest order, the adsorbate position will be where the average substrate electron density has the preferred infinite jellium value of $0.01e/a_B^3$ where e is an electron charge and a_B is the Bohr radius. Again, to lowest order, the symmetric stretch frequency of an adatom scales with the density gradient $\partial\bar{n}(\boldsymbol{r})/\partial z$ at the binding site. Since the parallel mode frequency is determined by the covalent correction term only, large errors are expected in the determination of such frequencies.

An intriguing aspect of the EMT is the ability to describe the delocalized quantum adsorption of H on close-packed metal surfaces [92]; an observation of such quantum effect has been claimed by Mate and Somorjai [93]. However, the calculations have dealt mostly with an isolated adatom, while experiments are typically done at saturation coverage. The recent extension of the theory to saturated coverages does show, in fact, that delocalization effects can be dramatically reduced at such coverages [94].

The bonding of an adatom can also be investigated using the embedded atom method (EAM) that is closely related to EMT, as was done for H on Ni(100) by Daw and Baskes [95]. A program is also under way to combine the self-consistent embedding scheme of Gunnarsson and Hjelmberg [96], the EMT described above, and the Newns–Anderson model [97] to determine the geometry and vibrational frequencies of *molecules* such as OH on transition metal surfaces [98].

2.5. Theoretical treatment of dynamics

Surface infrared data give not only the wavenumbers and oscillator strengths of vibrational modes but also their line shapes. All these quantities can vary as a function of temperature, coverage adlayer composition, etc. Except for possible effects of inhomogeneous broadening, these variations are due to dynamical mechanisms. So far, first principle calculations have kept the substrate fixed (frozen-lattice calculations), thus evaluating only the wavenumbers and strengths of the modes. One must therefore go beyond these calculations by taking into account the substrate dynamics and the adsorbate–substrate dynamical (possibly non-adiabatic) coupling. A number of simplifying assumptions and parameters have to be introduced in order to carry out such calculations. Two main approaches have been developed, molecular dynamics simulations based on stochastic trajectory methods and purely phenomenological descriptions of the adsorbate polarizability.

2.5.1. Molecular dynamics simulations

Stochastic trajectory techniques have been developed to simulate dynamical events that are imbedded in large systems [99–102]. They are useful to

simulate adsorption, molecular dissociation, surface diffusion, recombination and desorption, as well as vibrational motion. However, classical mechanics is not particularly well suited to simulate vibrational properties because most experimental measurements of infrared line shapes and vibrational lifetimes are carried out under conditions for which $\hbar\omega \gtrsim kT_s$ where ω is the adsorbate or phonon frequency and T_s the surface temperature. Thus the validity of classical mechanics is in question. Fortunately, in many cases quantum effects (zero-point motion) can be introduced into an otherwise completely classical stochastic trajectory method to achieve accurate simulations [103].

The essence of the stochastic trajectory method is to partition the system into a local zone of a few atoms (primary zone) and the remaining surrounding atoms (secondary zone), and to assume that interactions involving secondary atoms are harmonic. The resulting Hamilton equations of motion can be solved for the secondary atom positions and recast as a set of coupled Langevin equations of motion involving *only* the primary atoms plus a friction term and a fluctuating force. The friction accounts for the dissipation of energy from the primary zone to the secondary lattice. The fluctuating force accounts for impulses to the primary zone from thermal fluctuations of the secondary atoms. Various approximations are used to evaluate these two terms adequately [104].

The *lifetime* of an excited vibrational mode of an adsorbate can be computed directly by the stochastic trajectory technique. Initial conditions are chosen for each trajectory corresponding to the desired excitation in the designated mode, and random thermal populations in all other adsorbate and surface modes. A large ensemble of such trajectories are computed, and the average loss of energy from the designated mode follows directly as a function of time. As long as the time scale for energy relaxation is not longer than 10 ns or so, this procedure is computationally feasible.

The infrared absorption intensity at frequency ω is given by the Fourier transform of the dipole moment autocorrelation function:

$$I(\omega) \propto \int \langle \mu(t)\, \mu(0) \rangle\, e^{-i\omega t}\, dt, \tag{2.49}$$

where $\mu(t) = e^{iHt}\, \mu\, e^{-iHt}$ is the dipole moment of the system at time t, the brackets indicate ensemble average over many trajectories and H is the Hamiltonian of the complete system (Heisenberg representation). This expression is exact, within linear response theory, if the exact quantum mechanical dipole moment autocorrelation function is employed. Approximation of the dipole moment function by its classical mechanical value, computed by molecular dynamics, has proved to be a valuable technique for determining line positions [105–107].

The stochastic trajectory method provides a way to extend this technique to calculation of homogeneous line widths and line shapes, including contributions from dephasing adsorbate–adsorbate interactions. A "quantum" fluctua-

tion–dissipation theorem can be devised to approximate the correct quantum-mechanical distributions [108], which is a requirement for obtaining the correct Arrhenius-type temperature dependence of pure dephasing line widths.

Application of the stochastic trajectory method of infrared line shapes for an adlayer of hydrogen on Si(100) has been carried out by Tully et al. [108]. In that case, the interaction potentials, anharmonic terms and dipole moment functions had been computed by *ab initio* quantum electronic structure methods. Thus the calculations were completely *a priori*, and in full dimensionality (a 32 atom Si slab, with 16 H atoms). Quantitative agreement between calculated and measured line widths for the H–Si stretch as a function of temperature were obtained, and the major broadening mechanism identified as dephasing via the H–Si bending vibration (see section 4.3.1.2). The lifetime of the H–Si stretch was also computed by the method described above. The resulting values of $\sim 10^{-9}$ s for D–Si and $\geq 2 \times 10^{-8}$ s for H–Si are much longer than typically assumed for adsorbate vibrations. Lifetime contribution to the line width is therefore negligible in this case (see section 4.3.1.2).

The coupling to electron–hole pairs can also be described by this method. Although the electron motion participating in this non-adiabatic process is quantal, an effective classical degree of freedom can be constructed to introduce electronic coupling [109]. An approximation is then used to evaluate the non-adiabatic electronic matrix element [104] and generalized Langevin techniques are again applied to reduce the electronic interactions to additional friction and fluctuating forces. This approach has been used to calculate the quenching of a vibrationally excited NO molecule upon collision with a Ag(111) surface [104] and should prove useful for modelling vibrational line shapes reflecting electron–hole pair excitation.

In closing, we note that a *quantum* molecular dynamics simulation of the motion of hydrogen and its isotopes on Ni(001) has been performed using effective medium potentials [110]. The results show that quantum effects are important even at room temperature. This approach may be valuable to simulate the vibrational spectra of H at metal surfaces.

2.5.2. Phenomenological description

The simplest approach to quantify surface vibrational spectra is the phenomenology developed in sections 2.1–2.3. To treat dynamical effects, most workers start from eq. (2.11):

$$\Delta R/R \sim \tilde{\nu} N_s \, \mathrm{Im}[\alpha(\tilde{\nu})], \tag{2.50}$$

where $\alpha(\tilde{\nu}) = \alpha_e + \alpha_v(\tilde{\nu})$ is the local polarizability associated with an adsorbate mode and defined in eq. (2.27):

$$\alpha_v(\tilde{\nu}) = \frac{e^{*2}/(4\pi^2 m^* c^2)}{\tilde{\nu}_0^2 - \tilde{\nu}^2 - i\Gamma\tilde{\nu}}. \tag{2.51}$$

2.5.2.1. Vibrational energy relaxation. Historically, it was first believed that the line width Γ in eq. (2.51) was due to the damping of the vibrational mode at $\tilde{\nu}_0$ (T_1 process) [20,111–114]. Assuming that inhomogeneous broadening was negligible, the vibrational lifetime could simply be derived from the measured Lorentzian full width at half maximum (FWHM) via:

$$\tau = (\pi c \Gamma)^{-1}, \tag{2.52}$$

where τ is in s, Γ in cm^{-1} and c the speed of light (in cm/s). Two mechanisms have been considered: decay via (1) electron–hole pair excitation, and (2) multiphonon generation. Experimentally, a lack of temperature dependence was taken as a signature of the former [112,115–118] and proximity to the phonon band as an indication of the latter [119,120]. Theoretically, calculations of Γ were carried out from first principles assuming a free electron substrate or within other approximations [111,113,121–129].

In the past few years, however, several difficulties associated with lifetime measurements have become apparent [20,114]:

(1) It is extremely difficult to measure experimentally the magnitude of inhomogeneous broadening. For example, the widths of the C–H stretching modes in adsorbed CH_3O on Cu(100) were first believed to be dominated by lifetime broadening because the expected $1/m^*$ dependence for electron–hole pair excitation was observed in isotopic substitution experiments [112,115]. However, more careful experiments showed that inhomogeneous broadening in fact dominates in this system [116]. Alternatively, Ryberg has argued that the observation of a Lorentzian line shape guarantees that inhomogeneous broadening is negligible [118]. In section 4, it will be apparent that this criterion is in fact not sufficient [20].

(2) Vibrational *phase* relaxation (dephasing), which does not involve energy relaxation, may dominate the line width and will be discussed in section 2.5.2.2.

(3) If the non-adiabatic coupling between the adsorbate vibration and the substrate electrons does account for the width Γ, then the dynamic dipole moment, $\mu = e^*/\sqrt{2m^*\omega_0}$, has two components $\mu = \mu^{\mathrm{i}} + \mu^{\mathrm{e}}$, the nuclei (ion) contribution μ^{i} and the electron contribution μ^{e}. Langreth [130] has pointed out that the very process that allows a non-zero Γ also ensures that μ^{e} has an imaginary part since the electronic response is in general out of phase with that of the nuclei. Thus, $\mu = \mu' + \mathrm{i}\mu'' \equiv \mu'(1 + \mathrm{i}\omega\tau)$ and the resulting line shape of $\Delta R/R$ is asymmetric. The asymmetry parameter, $\omega\tau \equiv \mu''/\mu'$, is a measure of the *phase* lag between the response of the electrons and nuclei. Note that the *intensity* of the mode, μ'^2, is enhanced over the purely adiabatic vibrational value $(\mu^{\mathrm{i}'})^2$. Explicitly, the generalized polarizability has the form [131]:

$$\alpha(\omega) = \alpha_{\mathrm{c}} + \left(\frac{\mu^{\mathrm{e}'}}{\mu'} + \mathrm{i}\omega\tau\right)\frac{2\mu'^2\omega_0\tau}{\Gamma} - 2\mu'^2\omega_0\frac{(1 + \mathrm{i}\omega\tau)^2}{\omega^2 - \omega_0^2 + \mathrm{i}\Gamma\omega}, \tag{2.53}$$

where α_c is the usual electronic polarizability describing the contribution from core and valence electrons. The line shape is obtained from eq. (2.11) and (2.50) with:

$$\mathrm{Im}[\alpha(\omega)] = 2\omega_0\mu'^2\left[\frac{\omega\tau^2}{\Gamma} + \frac{\omega\Gamma(1-\omega^2\tau^2) - 2\omega\tau(\omega^2-\omega_0^2)}{(\omega^2-\omega_0^2)^2 + \Gamma^2\omega^2}\right]. \tag{2.54}$$

(4) Sorbello [132] pointed out that asymmetric line shapes could also result from adiabatic mechanisms such as the coupling of an adsorbate mode to the phonon continuum of the substrate. Such a mechanism, of course, requires that the local oscillator (adsorbate) frequency be below the top of the substrate phonon density of state, ω_{Debye}, and is therefore only relevant for low frequency modes. Sorbello also derived an intensity sum rule in the limit of a vanishing coupling between the phonons (including adsorbate and substrate motion) and the electron–hole pair excitation continuum. In such a limit, this sum rule is violated for any non-adiabatic interaction giving rise to an asymmetry as is apparent in Langreth's formalism: $\mu' = \mu^{i'} + \mu^{e'} > \mu^{i'}$.

(5) Morawitz [133] recently conjectured that the vibrational phase relaxation (dephasing) by the electron–hole pair continuum may also be important. A *strong temperature dependence* of the line width would then also be expected for this purely electronic phenomenon. Specifically, Morawitz finds:

$$\Gamma_{e-h} \sim T^3, \tag{2.55}$$

where the proportionality factor depends on a number of parameters, including the adsorbate-orbital-projected-single particle density of state at the Fermi level, $\rho(E_F)$. For CO on Ni(111), Morawitz estimates this factor to be 0.6×10^{-6} cm^{-1}/K^3, yielding ~ 15 cm^{-1} increase of the CO stretch line width between 100 and 300 K. However, $\rho(E_F)$ is calculated using a standard Newns–Anderson model and a simple two-level system to represent the diatomic molecule. Since Γ depends on $\rho(E_p)^4$, small errors in the estimate of ρ may result in large variations in the calculated Γ.

All the above phenomenological considerations make it very clear that vibrational lifetime can usually not be simply derived from experimentally measured line widths. A number of *different* mechanisms can produce temperature, coverage and isotopic dependences of the line widths and affect the line shape in a complicated fashion. For instance, T dependence may be present in inhomogeneous line widths for systems with small energy difference between several possible adsorption sites, for modes dephased by phonons (or possibly by electrons), and for modes that decay at least partially into phonons. Coverage and isotopic dependence may be due to inhomogeneities and dipole–dipole, or more generally adsorbate–adsorbate dynamical interactions, as well as dephasing and electron–hole pair mechanisms (see section 4). In summary, estimating the vibrational lifetime from line width measurements is

extremely difficult, even if inhomogeneous broadening is negligible or independently known. So far, it appears that dephasing may often obscure lifetime effects.

2.5.2.2. Vibrational phase relaxation (dephasing). Dephasing has been discussed at length in a number of reviews [114,18–20] and recent papers [134]. A clear pictorial description, borrowed from Gadzuk and Luntz [114], is reproduced in fig. 6. When an adsorbate mode is coupled anharmonically to nearby lower frequency modes (adsorbate or substrate), the transient excitation or de-excitation of the latter will cause the phase of the former to fluctuate, without any damping. Recalling that the infrared spectrum can be expressed in terms of the autocorrelation function of the dynamic dipole moment (eq. (2.49)), the dephasing process can be described phenomenologically by considering the model Hamiltonian, obtained by expanding the interaction energy

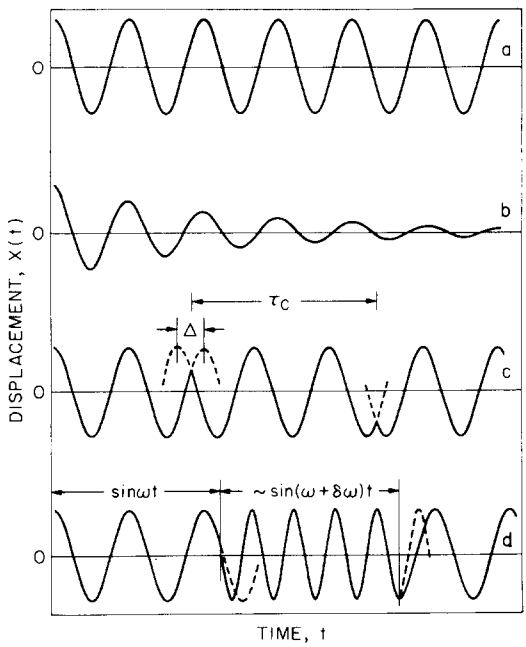

Fig. 6. Schematic representation of the displacement of an oscillator as a function of time, t, for (a) an undamped harmonic oscillator (Lorentzian line), and (c) an harmonic oscillator showing two simple dephasing events (Δ phase change) and giving rise to a symmetric broadening with half width $(\tau_c)^{-1}$ if τ_c is the mean time between events. Dephasing usually arises from anharmonic coupling to a low frequency mode (see text). The thermal-induced occupation of this mode gives rise to a frequency change $\delta\omega$ of the mode under investigation as depicted in (d) (with permission from ref. [114]).

$E(u-v)$ in powers of $(u-v)$ [135] (u and v are the displacements of the adatom of mass M and of the substrate of mass m, respectively):

$$H = H_0 + H_1, \tag{2.56}$$

where

$$H_0 = \hbar\Omega_0 b^+ b + \sum_\kappa \hbar\omega_\kappa b_\kappa^+ b_\kappa + M\Omega_0^2\left(v^2/2 - uv\right), \tag{2.57}$$

$$H_1 = Auv^2 + Buv^3 + Cu^2v^2 + Du^2v. \tag{2.58}$$

The first two terms of H_1 give rise to the decay of the localized oscillator. The last two terms give rise to dephasing. While only the first dephasing term, with coefficient C, has been usually considered, Zhang and Langreth [136] have recently argued that the last term, with coefficient D, should also be included if $\boldsymbol{u}\cdot\boldsymbol{v} \neq 0$. That is, except for the special cases when D is zero by symmetry [e.g bridge-bonded CO stretch coupled to a hindered rotation or translation on Ni(111)], Zhang and Langreth show that the cubic term (u^2v) makes a contribution to the pure dephasing line width which is roughly equal to the contribution made by the quartic term (u^2v^2).

Classically, the above description can be seen as introducing an anharmonic effective coupling constant $\phi_{\text{eff}} \simeq M\Omega_0^2 + KV$, where V is the normal coordinate of the dominant low frequency mode. For adiabatic variations in V, ϕ_{eff} gives an effective frequency [137]:

$$\Omega_{\text{eff}} = \left(\Omega_0^2 + \frac{KV}{M}\right)^{1/2} \approx \Omega_0\left(1 + \frac{KV}{2M\Omega_0^2} - \frac{K^2V^2}{8M^2\Omega_0^2}\right). \tag{2.59}$$

Using Persson's notation [135], i.e. $a \equiv -K^2/8M^2\Omega_0^2$, and neglecting the linear term for now, the equations of motions are in terms of the normal coordinate of the high frequency localized mode, U:

$$M\ddot{U} + M\left(\Omega_0^2 + aV^2\right)U = 0, \tag{2.60}$$

and for the dominant low frequency mode:

$$m\ddot{V} + m\omega_0^2 V + m\eta\dot{V} + MaU^2V = f(t), \tag{2.61}$$

where η is the friction coefficient (damping term) for the low frequency mode of resonant frequency ω_0. The random force $f(t)$ is introduced to take into account the thermal excitation of that mode and satisfies the fluctuation–dissipation theorem:

$$\langle f(t)\, f(0)\rangle = 2\eta m k_{\text{B}} T\, \delta(t). \tag{2.62}$$

The infrared spectrum, eq. (2.49), can be written down analytically for the high and low temperature limits ($k_B T \gg \hbar\omega_0$ or $k_B T \ll \hbar\omega_0$). At high T:

$$I(\omega) \sim \frac{\Gamma/2}{(\omega - \Omega_0 - \Delta\Omega)^2 + (\Gamma/2)^2}. \tag{2.63}$$

where

$$\Gamma = \frac{2}{\eta}\left(\frac{\hbar a}{2m\Omega_0\omega_0}\right)^2\left(\frac{k_B T}{\omega_0}\right)^2 = \frac{2}{\eta}(\delta\omega)^2\left(\frac{k_B T}{\omega_0}\right)^2. \tag{2.64}$$

$$\Delta\Omega = \left(\frac{\hbar a}{2m\Omega_0\omega_0}\right)\left(\frac{k_B T}{\omega_0}\right) = (\delta\omega)\left(\frac{k_B T}{\omega_0}\right). \tag{2.65}$$

At low T, $I(\omega)$ is again approximately a Lorentzian with

$$\Gamma = 2\frac{(\delta\omega)^2}{(\delta\omega)^2 + \eta^2}\eta\, e^{-\hbar\omega_0/k_B T}, \tag{2.66}$$

$$\Delta\Omega = \frac{\eta^2}{(\delta\omega)^2 + \eta^2}(\delta\omega)\, e^{-\hbar\omega_0/k_B T}. \tag{2.67}$$

Introduction of the cubic term ($u^2 v$), i.e. the linear term in eq. (2.59), as advocated by Zhang and Langreth [136], results in the production of sidebands in the vibrational spectrum. More explicitly, if the continuum spectral density of the substrate contains a rather sharp peak at frequency ω_m, or if the dephasing is essentially due to a low-lying adsorbate mode, the cubic term not only gives a dephasing contribution to the central peak at frequency Ω, but also produces satellites at $\Omega \pm \omega_m$, $\Omega \pm 2\omega_m$, $\cdots$. The strength of the first satellites (the most important) relative to the central peak at Ω, defined as f_{+1} and f_{-1}, is:

$$(f_{\pm 1})^2 = (0.0731)\left(\frac{n+1}{n}\right)^{\pm 1}\left(\frac{\Omega}{\omega_m}\right)^2\left(\frac{\Gamma}{\omega_m}\right)\left(\frac{\gamma}{\omega_m}\right), \tag{2.68}$$

where Γ is the total dephasing contribution to the FWHM (including quartic and cubic terms) of the central peak at Ω, and γ the width of the lower frequency vibrational mode or resonant state responsible for the dephasing. The quantity n is the Planck factor, $n^{-1} = e^{\hbar\omega_m/k_B T} - 1$. The exact magnitude of the prefactor, 0.0731, depends on the shape (not the strength) of the adsorbate–substrate interaction potential and the shape (not the strength) of the low frequency mode density of state near ω_m. The numerical prefactor in eq. (2.68) is given for a Morse potential and a Lorentzian line shape. It applies in particular to terminal bonding where both the modes at Ω and at ω_m have parallel polarization vectors.

In summary, line shape analysis involves the understanding and quantifica-

tion of a number of mechanisms. From an experimentalist point of view, therefore, the spectroscopy has reached a sophisticated level where claims of a dominant mechanism cannot be made hastily [20]. Well defined tests must be performed, including a careful measure of *line shape* and *line strength* as a function of temperature, coverage and isotopic concentration over an extended range. The beginnings of such studies will be discussed in section 4.3.

3. Experimental

The purpose of this section is to summarize and evaluate the most important considerations for the choice of a particular technique and the design and execution of the measurements. An effort is made to contrast the physical quantities that are measured by each technique. To this end, some expressions presented in the previous section are used whenever appropriate and new derivations or results derived elsewhere are outlined as required.

3.1. Metal surfaces

3.1.1. Reflection–absorption spectroscopy (RAS)

The study of the *vibrational* spectrum of an adsorbed monolayer is first considered. For this case, Francis and Ellison [8] first recognized that p-polarized radiation at a large angle of incidence was necessary to enhance the sensitivity. The theory of reflection at metal surfaces was later developed by Greenler [26,138,139]. For an adsorbed layer, the expressions for $\Delta R/R \equiv (R^0 - R_{\text{layer}})/R^0$ are given in eqs. (2.15)–(2.19); $\Delta R/R$ is largest at θ_{opt} given in eq. (2.18). Multiple reflections with $\theta = \theta_{\text{opt}}$ could therefore enhance the signal. However, Greenler pointed out that, θ_{opt} was close to the metal pseudo-Brewster angle at which the metal substrate absorbs substantially ($\sim 30\%$). Therefore, for experiments relying on conventional thermal sources (low signal regime), the signal-to-noise ratio S/N is limited by the detector noise and is proportional to the total intensity. The optimum number of reflections is therefore obtained by maximizing $\Delta R(\theta_{\text{opt}})$. In the usual limit of a weak absorption, the optimum number of reflections N_{opt} is the closest integer that reduces the incident intensity by a factor e, that is:

$$N_{\text{opt}} = \text{int}\left[-1/\ln(R^0)\right]. \tag{3.1}$$

The results (θ_{opt}, N_{opt}) for a number of substrates are summarized in table 4 [32].

Experimentally, the selection of θ and the geometry depend also on the infrared source aperture, the beam convergence at the sample, the sample size and the radiation strength. For relatively large UHV chambers (30 cm diameter), the last focussing mirror before the sample is usually 30–40 cm away from the sample. Since typical interferometer beams are ~ 5 cm in

Table 4
Optimum angle of incidence and corresponding reflectance change for various metal substrates using a single external reflection (from ref. [32])

Substrate	Resonance at 500 cm^{-1}			Resonance at 2100 cm^{-1}		
	θ_{opt} (deg)	$\Delta R(\theta_{opt}) \times 10^4$	$\Delta R(85°) \times 10^4$	θ_{opt} (deg)	$\Delta R(\theta_{opt}) \times 10^4$	$\Delta R(85°) \times 10^4$
Al	89.2	9.8	3.4	88.2	14.5	10.5
Cr	87.6	3.0	2.4	85.8	6.3	6.2
Co	89.0	7.3	3.4	86.0	7.0	6.8
Cu	89.3	9.0	3.4	88.0	16.4	12.2
Au	89.0	7.1	3.1	87.8	14.5	11.5
Hf	87.8	2.8	2.2	83.0	4.0	3.8
Fe	88.3	4.4	2.8	85.4	5.8	5.7
Mg	~ 83.5	1.0	0.9	~ 78.0	1.8	0.9
Mo	88.2	3.6	2.5	86.7	8.2	7.7
Ni	88.9	6.3	3.1	86.2	7.5	7.1
Nb	88.2	3.7	2.6	86.2	7.3	7.1
Pd	89.0	6.2	3.0	85.0	5.1	5.1
Pt	88.5	5.0	2.9	86.7	8.7	8.1
Ag	89.6	12.5	3.4	87.2	19.0	12.3
Ta	87.7	2.8	2.3	84.3	4.0	4.0
Ti	86.2	1.6	1.5	81.5	3.2	3.0
W	88.5	4.7	2.9	85.8	7.0	6.9
V	88.3	3.9	2.8	86.5	7.5	7.2
Zr	87.8	2.9	2.3	83.0	3.5	3.2

The active layer is characterized by $\epsilon' = 1.68$, $\epsilon''_{max} = 0.26$ and $d = 3$ Å (see ref. [32]). The optical constants of the metals, listed in ref. [32], were calculated from data in: A.P. Lenham and D.M. Trenherne, J. Opt. Soc. Am. 56 (1966) 583, 752, 1137 and in Proceedings of the International Colloquium on Optical Properties of Metals and Metal Alloys (North-Holland, Amsterdam, 1966) p. 196.

diameter, the full beam convergence is $\pm 4°$, assuming that the IR window diameter is not restricting the field of view. Therefore, an optimum geometry would be, based on the requirement of table 4, to use 86° incidence with a *3 cm long sample* for a typical source aperture of 2 mm. A possible set-up is shown in fig. 7 [14]. Alternatively, faster optics [141] can be used for small UHV chambers (< 10 cm diameter) [142,143]. Typically, such chambers are mounted above a larger UHV vessel and a long vertical translation manipulator takes the sample from the infrared cell to the larger vessel where all the conventional surface analyses can be performed. In this case, full beam convergence can be as large as $\pm 10°$, leading to the natural choice of $\theta = 80°$. This geometry is particularly appropriate to study smaller samples (≤ 1 cm) with high dynamic-range detectors (away from the saturation region). An example of this second configuration is shown in fig. 8 [143].

For interferometer set-ups utilizing the moving mirror as the sole means of modulation, the spectrometer position with respect to the sample and detector

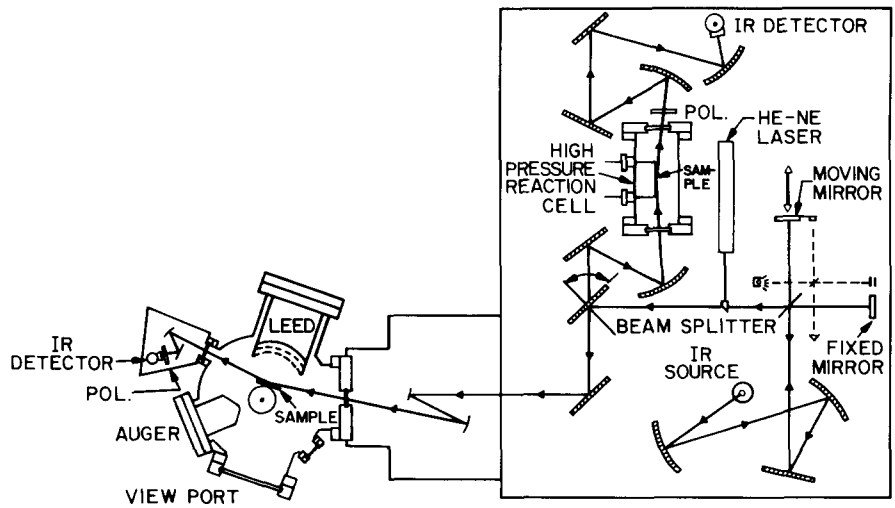

Fig. 7. Possible configuration to perform RAS on single crystal samples in UHV with slow optics ($f = 7$). A separate cell can be added to the interferometer bench to perform RAS at high pressures with faster optics ($f \simeq 5$). In both cases, the polarizer (POL.) is placed between the sample and the detector and the optics are purged with dry N_2 (from ref. [140]).

is important, particularly for the study of *low frequency* modes ($< 1200\ cm^{-1}$) when the emission from the spectrometer and the optics can interfere with the source signal. If the sample is placed *before* the spectrometer and detector assembly, then the emission from the sample and optics is modulated by the spectrometer and interferes directly with the absorption signal as was apparent in the O–O spectrum on Pt [144]. The sample should always be *after* the spectrometer, right before the detector. Even so, part of the emitted radiation that is modulated by the interferometer travels back towards the detector. For low frequency work (or for hot samples), it is therefore important to measure the emission contribution by simply turning off the source. This problem does not exist if there is a chopper to modulate the source radiation before the sample.

Another aspect, common to all designs, is the sealing of IR windows for UHV conditions, i.e. requiring 150 °C baking. There have been a large number of possible designs in the literature [145–158]. The most widely used method is that of Hollins and Pritchard [156] utilizing a double O-ring seal with differential pumping. A recent modification, requiring an additional aluminum disk eliminates the need for differential pumping [158].

Historically, there have been many proposals for more sophisticated geometries with multiple reflections. For example, the use of a flat mirror after the

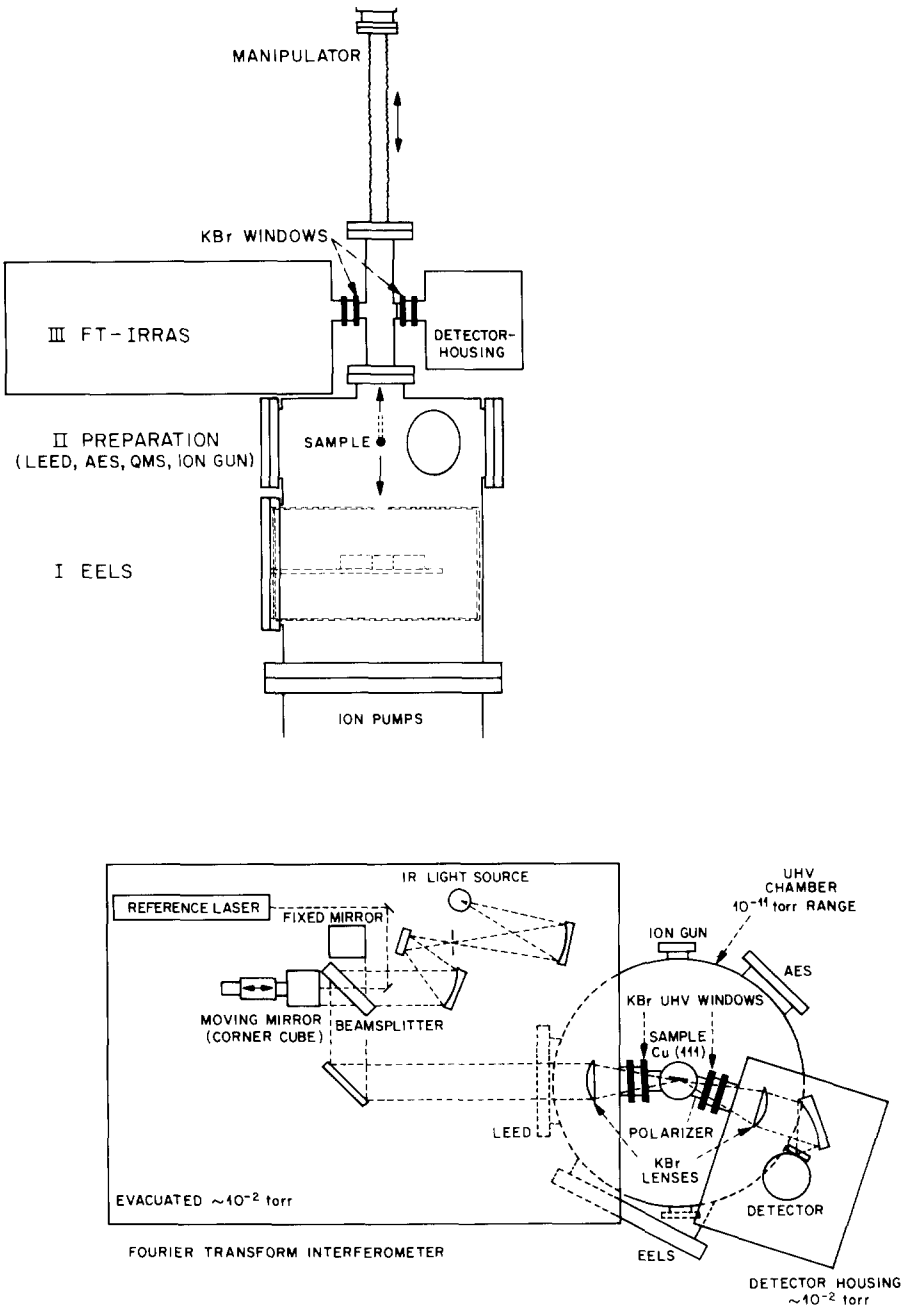

Fig. 8. Possible configuration to perform RAS on single crystal in UHV with fast optics ($f \simeq 3$) designed by Erley [143]. This configuration, with a small infrared chamber, a preparation area and EELS spectrometer, is also used by Hoffmann and Robbins [142]. The present set-up maintains all the optics under vacuum, a clear advantage for the far-infrared, the 1500 cm^{-1} region and other regions where atmospheric gas-phase absorption is important (with permission from ref. [143]).

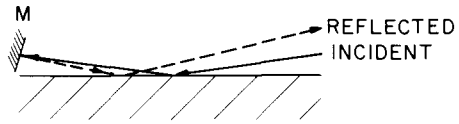

Fig. 9. A flat mirror (M) can be used to reflect the infrared radiation back onto the sample for a second pass. Note that the second reflection does not overlap the first so that the reflected beam can be separated from the incident beam.

sample (see fig. 9) would provide two grazing incidence reflections (closer to the optimum number of reflections) and require only one infrared window. However, the separation of the incident and reflected beam outside the UHV chamber is difficult. In general, most set-ups with a conventional source, and carried out in UHV with a number of other surface probes, use only one grazing incidence reflection. For stronger sources such as lasers, the situation can be quite different. The high collimation and intensity of laser beams make some of the multiple reflection geometries more attractive.

For more details on the vibrational RAS of adsorbates at metal surfaces, we refer the reader to a large number of excellent reviews. Historical perspective can be found in the works of Tompkins [159], Pritchard [160] and Pritchard and Catterick [161]. More recent perspectives are given by Ryberg [162], Hoffmann [15], Hollins and Pritchard [16], Hayden [17], and Bradshaw and Schweizer [18].

The study of the *electronic* absorption of metallic surfaces is now considered. As mentioned above, such absorption is large in typical RAS experiment performed at $\theta = \theta_{opt}$. Furthermore, important differences exist between RAS and SEWS (next section) that require a summary of the effects of electronic absorption in RAS. In section 2.2.1, the quantity $\Delta R/R = 1 - |\tilde{r}/\tilde{r}^0|^2$ was derived for both polarizations. The expressions for $\tilde{r}^0$ are (using the definitions in fig. 5a, and the fact that $|\tilde{\epsilon}_i^m| \gg \epsilon^v \approx 1$) for s-polarization:

$$\tilde{r}^0_{\text{s-pol}} = \frac{\sqrt{\epsilon^v}\cos\theta - \left(\tilde{\epsilon}_y^m - \epsilon^v \sin^2\theta\right)^{1/2}}{\sqrt{\epsilon^v}\cos\theta + \left(\tilde{\epsilon}_y^m - \epsilon^v \sin^2\theta\right)^{1/2}} \tag{3.2}$$

$$\approx \frac{\sqrt{\epsilon^v}\cos\theta - \sqrt{\tilde{\epsilon}_y^m}}{\sqrt{\epsilon^v}\cos\theta + \sqrt{\tilde{\epsilon}_y^m}}, \tag{3.3}$$

and, for p-polarization:

$$\tilde{r}^0_{\text{p-pol}} = \frac{\tilde{\epsilon}_x^m\sqrt{\epsilon^v}\cos\theta - \epsilon^v\left[\tilde{\epsilon}_x^m\left(1 - (\epsilon^v/\tilde{\epsilon}_z^m)\sin^2\theta\right)\right]^{1/2}}{\tilde{\epsilon}_x^m\sqrt{\epsilon^v}\cos\theta + \epsilon^v\left[\tilde{\epsilon}_x^m\left(1 - (\epsilon^v/\tilde{\epsilon}_z^m)\sin^2\theta\right)\right]^{1/2}} \tag{3.4}$$

$$\approx \frac{\sqrt{\tilde{\epsilon}_x^m}\cos\theta - \sqrt{\epsilon^v}}{\sqrt{\tilde{\epsilon}_x^m}\cos\theta + \sqrt{\epsilon^v}}. \tag{3.5}$$

At this point, it is useful to define a quantity $Z_i \equiv (\tilde{\epsilon}_i^{\,m})^{-1/2}$ ($i = y$ or x for s- or p-polarization) which is actually the normalized surface impedance of the metal substrate [163,164]. In particular, for a Drude metal in the local limit [164,165]:

$$Z(\omega) \equiv R(\omega) + iX(\omega) = (1+i)\left(\omega/2\omega_p^2\tau\right)^{1/2}(1+i\omega\tau)^{1/2}. \tag{3.6}$$

With this definition, it is straightforward to express the reflected intensity $R^0 = |\tilde{r}^0|^2$ in terms of Z, in the limit $|\tilde{\epsilon}^m| = |Z|^{-2} \gg \epsilon^v \approx 1$:

$$R^0_{s\text{-pol}} \approx \frac{\left(R_y^2 + X_y^2\right)\cos^2\theta - 2\left(R_y/\sqrt{\epsilon^v}\right)\cos\theta + (1/\epsilon^v)}{\left(R_y^2 + X_y^2\right)\cos^2\theta + 2\left(R_y/\sqrt{\epsilon^v}\right)\cos\theta + (1/\epsilon^v)}, \tag{3.7}$$

$$R^0_{p\text{-pol}} \approx \frac{R_x^2 + X_x^2 - 2\left(R_x/\sqrt{\epsilon^v}\right)\cos\theta + \cos^2\theta/\epsilon^v}{R_x^2 + X_x^2 + 2\left(R_x/\sqrt{\epsilon^v}\right)\cos\theta + \cos^2\theta/\epsilon^v}. \tag{3.8}$$

Note that $R^0_{s\text{-pol}}$ is largest for $\cos\theta = 1$, whereas $R^0_{p\text{-pol}}$ is largest for $\cos\theta = \sqrt{\epsilon^v}\,|Z_x| = \sqrt{\epsilon^v/|\tilde{\epsilon}_x^m|}$. The latter is the pseudo-Brewster angle, falling between 88° and 89° for most metals. Practically, however, all RAS experiments are performed with $\theta \leq 85°$, that is for $\cos^2\theta \gg |Z|^2 = (R^2 + X^2)$. Therefore, eqs. (3.7) and (3.8) reduce to:

$$R^0_{s\text{-pol}} \approx 1 - 4R_y\sqrt{\epsilon^v}\cos\theta, \tag{3.9}$$

$$R^0_{p\text{-pol}} \approx 1 - 4R_x\sqrt{\epsilon^v}/\cos\theta, \tag{3.10}$$

yielding for the corresponding substrate *absorption*, $A \equiv 1 - R^0$:

$$A_{s\text{-pol}} \approx 4R_y\sqrt{\epsilon^v}\cos\theta, \tag{3.11}$$

$$A_{p\text{-pol}} \approx 4R_x\sqrt{\epsilon^v}/\cos\theta. \tag{3.12}$$

In the above equations the quantity R_i is well described for metals by the Drude model (in the local limit):

$$R_i = \left[\omega/2(\omega_p)_i\tau_i\right]^{1/2}\left[-\omega\tau_i + \sqrt{1+\omega^2\tau_i^2}\right]^{1/2}. \tag{3.13}$$

The two Drude parameters, the plasma frequency ω_p and the electron relaxation time τ, appear as a product. Therefore, they cannot be separated in any limit such as in the non-relaxation $[(\omega\tau)^2 \ll 1]$ and the extreme relaxation $[(\omega\tau)^2 \gg 1]$ regions.

In closing, we highlight an interesting property associated with the grazing incidence geometry. Eqs. (2.20) and (2.21) describing the *surface* electronic absorption or eqs. (3.11) and (3.12) describing the total *substrate* electronic absorption show that s- and p-polarizations have the factor $\cos\theta$ and $1/(\cos\theta)$, respectively, multiplying the *normal incidence* value. For $\theta = 85°$, this means that the measured signal is $\sim \frac{1}{10}$ and ~ 10, respectively, times that

measured at normal incidence. Consequently, grazing incidence *p-polarization* is over two orders of magnitude more sensitive to the *tangential* component of the surface or substrate electronic response than grazing incidence s-polarization. The physical reason for this enhancement is the large penetration of both the tangential and normal components of the incident electric field into the metal as the pseudo-Brewster angle is approached. Once in the metal, the radiation is strongly refracted resulting in a much stronger ($\sim \sqrt{|\tilde{\epsilon}^m|}$) tangential component than normal component.

3.1.2. Surface electromagnetic wave spectroscopy (SEWS)

Surface electromagnetic waves (SEW's) have been known since the time of Zenneck [166] and Sommerfeld [167] to constitute a class of inhomogeneous wave solutions to Maxwell's equations at a metal/air interface. These waves are transverse magnetic (H field parallel to surface), propagate along the metal surface and have an exponentially decaying amplitude away from the surface both in the air and in the metal [168–170]. The parallel component of their propagation wave vector is (see fig. 3a):

$$k_{x_{\mathrm{SEW}}} \equiv k'_{x_{\mathrm{SEW}}} + \mathrm{i}k''_{x_{\mathrm{SEW}}} = \left(\frac{\omega}{c}\right)\left[\frac{\epsilon^{\mathrm{v}}\tilde{\epsilon}^{\mathrm{m}}_x}{\epsilon^{\mathrm{v}} + \tilde{\epsilon}^{\mathrm{m}}_x}\right]^{1/2}, \tag{3.14}$$

where ϵ^{v} and $\tilde{\epsilon}^{\mathrm{m}}$ are the dielectric functions of the ambient ($\epsilon^{\mathrm{v}} \approx 1$) and the metal substrate, respectively. Since the real part of the metal dielectric function, $\epsilon^{\mathrm{m}'}$, is large and negative (see fig. 1b), the real part of k_x is always larger than ω/c, i.e. the SEW dispersion curve lies below the light line in the ω–k plane. As a result, SEW's cannot be excited directly by plane waves incident on a flat metal surface.

The earliest indication that SEW's could be excited by plane waves on a modified surface came from the explanation of Wood's anomalies [171] by Fano [172] and later by Ritchie et al. [173]. An anomalous absorption was observed when radiation was incident onto a metal *grating* at specific angles. At a grating, the radiation dispersion is modified as follows (fig. 10a):

$$k_x = (\omega/c)\sin\theta \pm n(2\pi/a), \tag{3.15}$$

where a is the grating spacing, n the diffraction order and θ the angle of incidence. By choosing θ and a appropriately, the parallel component of the radiation wave vector k_x can be made equal to $k'_{x_{\mathrm{SEW}}}$, and coupling occurs.

In 1968, Otto [174] realized that the phenomenon of total internal reflection could also be used to match $k'_{x_{\mathrm{SEW}}}$. When light is incident from a high index material ($n = \sqrt{\epsilon^{\mathrm{s}}}$) onto a vacuum interface (fig. 4), the parallel component of the wave vector is

$$k_x = (\omega/c)\sqrt{\epsilon^{\mathrm{s}}}\sin\theta, \tag{3.16}$$

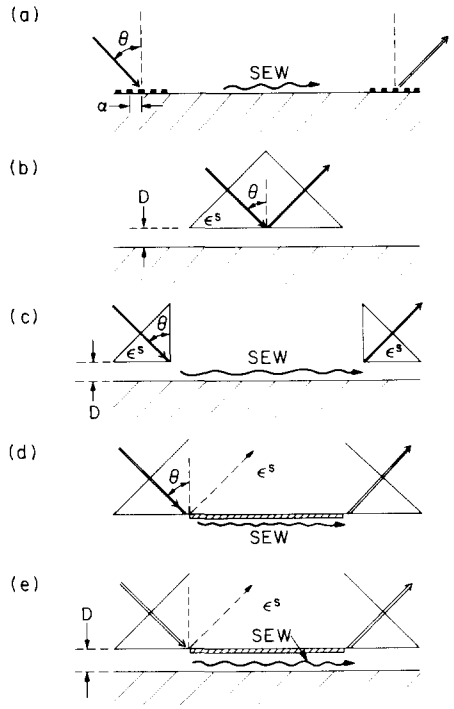

Fig. 10. Various schemes to launch and detect surface electromagnetic waves (SEW's) represented by the wavy arrows: (a) grating coupler where grooves are etched in single crystal samples; (b) single-prism coupler (Otto's geometry [174]) to launch and detect SEW's without substantial propagation; (c) two-prism coupler (Schoenwald et al. [177]) for substantial SEW propagation before decoupling; (d) edge coupler where the metal substrate (~ 1 μm thick) is evaporated onto the base of the prism and the reflected beam (dotted line) can be well separated from the decoupled beam [187], (e) hybrid configuration that combines edge and prism couplers. SEW's propagate both on the evaporated film and on the single crystal surface separated by the gap D [189]. In (b), (c) and (e), the magnitude of the gap is on the order of a few wavelengths.

where θ is the internal angle of incidence. Again, θ can be chosen so that $k_x = \mathrm{Re}(k_{x_{\mathrm{SEW}}})$. The refracted wave, however, is now evanescent since k_z is purely imaginary. If a metal surface is brought close to the high index dielectric/vacuum interface (within a decay length), then SEW's can be excited on the metal surface (fig. 10b). An extension of this technique, devised by Kretschmann and Raether [175] is only applicable above 3500 cm^{-1} and will not be considered here. The reader is referred to excellent reviews [12,168–170,176].

A modification of the single prism technique was suggested by Schoenwald et al. [177] whereby the SEW's could be launched and detected separately (fig.

10c). By varying the distance between the input and output prism couplers, the SEW absorption coefficient:

$$\alpha_{SEW} \equiv 2k''_{x_{SEW}} \tag{3.17}$$

could be measured. It was found that the absorption length $l \equiv \alpha_{SEW}^{-1}$ was on the order of 1 cm at 1000 cm^{-1} on most metals.

Although the absorption of dielectric films could be measured in this fashion [12,178–186] several features of this configuration were undesirable: (1) low throughput ($\sim 0.1\%$ of incident radiation detected), (2) unwanted scattered radiation at the corner of the input prism, and (3) a strong dependence on the distance between the prism base and the metal, D. Most of these problems were eliminated by the "edge coupling" configuration shown in fig. 10d [187]. A thin metal film (~ 1 μm) is evaporated on a dielectric surface. The thickness is not critical as long as it is much larger than the relevant skin depth (~ 200 Å) and much smaller than the decay length of the evanescent field (~ 100 μm). The overall throughput is roughly 15 times better than for the two-prism coupler, mostly due to a better match of the spatial profile of the evanescent field and the SEW's. The part of the radiation that does not excite SEW's is totally internally reflected and can be easily blocked (see fig. 10d).

The edge coupler can also be used to measure the absorption of a second metal surface as shown in fig. 10e. This configuration makes use of both the prism–gap–metal coupling and the prism–metal edge coupling. The electric field component of the SEW is maximum at the two metal surface and minimum in between [188,189].

Although SEW's had only been excited by laser radiation, Schlesinger and Sievers [10] succeeded in exciting and detecting broadband SEW's (600–1800 cm^{-1}). They used the edge coupling geometry and a dispersion compensation technique to take into account the frequency dependence of the coupling angle. Later, Chesters et al. [190] used an aperture excitation geometry to excite SEW's in the region 570–2200 cm^{-1}.

There is, however, a fundamental problem associated with SEWS, particularly severe for the configuration shown in fig. 10e, and for measurements at long wavelength (100 μm) as noted by Schlesinger et al. [191] and Koteles and McNeill [192]. Because of mismatch between the SEW field profile and the evanescent exciting fields, radiative plane electromagnetic waves (PEW's) are generated at the input coupling position. Neglect of those PEW's has led to the inference of anomalously high absorption coefficient α_{SEW} [193,194] and to spurious results in the study of H vibration on W(100) [189,195,196]. PEW's and SEW's travel parallel to the surface at different speeds, PEW's at the speed of light (no interaction with surface) and SEW's at the phase velocity:

$$v = c\ \mathrm{Re}(1/\tilde{\epsilon}_x^m + 1/\epsilon^v)^{1/2} \tag{3.18}$$

and can therefore interfere at the output coupler used for SEW (and neces-

sarily PEW) detection. In elegant experiments, Schlesinger and Sievers [197] demonstrated this interference phenomenon by recording the SEW transmission intensity for different lengths of a thin Ge overlayer on a Ag film. PEW's were generated from SEW's at the Ge edge and recoupled to SEW's at the other Ge edge. This interference phenomenon was also later observed by Yakovlev et al. [198] in the far-field pattern of SEW's decoupled at the edge of the metal substrate.

We now summarize how this interference phenomenon can be used to advantage to determine uniquely the *electronic* response of the metal surface and then summarize the status of SEWS as a probe of adsorbate *vibrational* modes. In the case of clean surfaces, Hanssen et al. [199] have shown that PEW's generated at the input coupler can interfere with SEW's at the output coupler. The resultant intensity at the detector can be written:

$$I = I_{\mathrm{SEW}} + I_{\mathrm{PEW}} + 2\left(I_{\mathrm{SEW}} I_{\mathrm{PEW}}\right)^{1/2} \cos\phi, \tag{3.19}$$

where the phase is, in general:

$$\phi = \left(k'_{x_{\mathrm{SEW}}} - k_{x_{\mathrm{PEW}}}\right) L + \phi^0; \tag{3.20}$$

L is the propagation distance (length between input and output couplers), $k'_{x_{\mathrm{SEW}}}$ is the real part of the SEW wave vector (eq. (3.14)), $k_{x_{\mathrm{PEW}}} = \omega/c$ and ϕ^0 the phase shift between the two waves. The magnitude of ϕ^0 arises from the details of coupling and decoupling and was assumed constant over the frequency range considered by Hanssen et al. [199].

To highlight the implications of the above statements, we consider the case of a clean metal in vacuum ($\epsilon^{\mathrm{v}} = 1$) and well-described by the Drude theory. Defining the surface impedance for SEW's [200]:

$$Z^{\mathrm{SEW}}(\omega) \equiv R^{\mathrm{SEW}}(\omega) + \mathrm{i}\, X^{\mathrm{SEW}}(\omega) = \left[\epsilon^{\mathrm{v}} + \tilde{\epsilon}^{\mathrm{m}}_x(\omega)\right]^{-1/2} \tag{3.21}$$

the dispersion relation (eq. (3.14)) becomes:

$$k_{x_{\mathrm{SEW}}} = (\omega/c)\sqrt{\epsilon^{\mathrm{v}}}\left[1 - \epsilon^{\mathrm{v}}\left(Z^{\mathrm{SEW}}\right)^2\right]^{1/2}. \tag{3.22}$$

Note that, since $|\tilde{\epsilon}^{\mathrm{m}}_x| \gg \epsilon^{\mathrm{v}}$, the functional form of $Z^{\mathrm{SEW}}(\omega)$ is:

$$Z^{\mathrm{SEW}}(\omega) \approx Z(\omega)\left(\equiv \left(\tilde{\epsilon}^{\mathrm{m}}\right)^{-1/2}\right) = (1 + \mathrm{i})\left(\omega/2\omega_{\mathrm{p}}^2\tau\right)^{1/2}(1 + \mathrm{i}\omega\tau)^{1/2}. \tag{3.23}$$

The SEW absorption coefficient is (eq. (3.17)):

$$\alpha_{\mathrm{SEW}}(\omega) \equiv \left(2k''_{x_{\mathrm{SEW}}}\right) = 2(\omega/c)\epsilon^{\mathrm{v}}\sqrt{\epsilon^{\mathrm{v}}}\, R_x X_x, \tag{3.24}$$

and the SEW phase is obtained from

$$k'_{x_{\mathrm{SEW}}} = (\omega/c)\sqrt{\epsilon^{\mathrm{v}}}\left[1 - \epsilon^{\mathrm{v}}\left(R_{\mathrm{n}}^2 - X_{\mathrm{n}}^2\right)\right]. \tag{3.25}$$

For a Drude metal and $\epsilon^{v} = 1$, we have:

$$\alpha_{SEW}(\omega) = \left(\frac{\omega}{\omega_p}\right)^2 \frac{1}{c\tau} = \frac{\omega^2}{4\pi c}\rho(T), \tag{3.26}$$

where ρ is the DC resistivity, and

$$k'_{x_{SEW}} \approx (\omega/c)\left(1 + \omega^2/2\omega_p^2\right). \tag{3.27}$$

The phase difference, given in eq. (3.20), for a Drude metal is

$$\phi \approx (\omega L/c)\left(\omega^2/2\omega_p^2\right) + \phi^0. \tag{3.28}$$

Experimentally, ϕ can be measured by using eq. (3.19) with $I_{SEW} = I_{0\,SEW} \times e^{-\alpha_{SEW} L}$ and $I_{PEW} = I_{0\,PEW} f(R)$ where R is the real part of the normalized surface impedance. The function $f(R)$ is independent of T and is determined in ref. [199] to fit the measured $I(T)$. From a plot of ϕ versus ω^3 the slope gives, according to eq. (3.28), the value of $L/2c\omega_p^2$ and the intercept gives ϕ^0.

In summary, interference measurements between SEW's and PEW's provide a unique measure of ω_p for Drude metals. By measuring k'_x and k''_x for SEW's, one can determine independently ω_p and τ at each frequency. In contrast, these parameters are only obtainable with Kramers–Kronig analysis in RAS measurements. Such analysis eliminates any possibility of discovering any interesting frequency dependence to these parameters which may arise from, say, electron–phonon coupling. SEW spectroscopy is therefore better suited to the determination of the substrate Drude parameters than RAS.

On the other hand, vibrational spectroscopy of adsorbed molecules can only be done if the intensity of the PEW's is negligible compared to the measured changes in SEW intensity. Practically, this requirement eliminates the use of the convenient hybrid configuration shown in fig. 10e because the intensity of the waveguide PEW's is large and at best comparable to that of the SEW's. It also invalidates most SEW absorption measurements performed with varying the distance between the two prisms in the configuration shown in fig. 10c unless the contribution of PEW's is determined at each spacing. In careful experiments using the fact that I_{SEW} has a strong temperature dependence, Riffe et al. [196] have used grating couplers to measure the weak vibrational absorption of the H symmetric stretch. However, the restricted spectral range and lower signal-to-noise ratio than in standard RAS measurements [196,62] is not encouraging for purely *vibrational* spectroscopy of adsorbates at surfaces. This conclusion is all the more disappointing since the sensitivity, or contrast, of the technique is higher than that of RAS. That is, for a given adsorbate on a metal surface, $\Delta I/I\,|_{SEW}$ obtained after probing a length $L \approx (\alpha_{SEW})^{-1}$ is larger than $\Delta R/R\,|_{RAS}$ obtained after one grazing incidence at $\theta \approx \theta_{opt}$ by at least a factor of ten, the exact value depending on the metal dielectric constant [10]. With conventional sources (Globar) or

present laser sources (lower stability), the S/N achieved in SEWS experiments is lower than with RAS experiments. The situation may change if stronger broadband sources or more stable lasers are used.

3.1.3. Emission spectroscopy (ES)

The idea of using infrared emission spectroscopy was first implemented by Low and Coleman [201,202] to study multilayer films on metals slightly above room temperature. Griffiths [302] has reviewed the work done with ES prior to to 1975. Metallic oxides have also been studied by ES [204–206]. Blanke and Overend [207] achieved better sensitivity by using multiple reflections for a nine-layer Langmuir–Blodgett film. However, detection of a monolayer at room temperature requires low temperature detectors and careful shielding of all room-temperature radiation (except for the sample). Durana and McDonald [5] developed a method to cool a fast-scanning interferometer (He gas bearing) to liquid N_2 temperature to study emission from room-temperature samples. With such an instrument, the emission spectrum of a monolayer of chemisorbed p-nitrobenzoic acid on evaporated copper at 300 K was measured [11]. The vibrational spectrum of a molecule–adsorbate mode was first measured by Chiang et al. with a He-cooled grating spectrometer shown in fig. 11 [119]. This system has been the most successful so far and estimates and results by this group are given below.

Emission spectroscopy addresses three fundamental limitations of RAS:
(1) The dynamic range problem arising from the large background signal R^0 and the relatively small adsorbate induced absorption $\Delta R = R^0 - R$. Ultimately, the signal-to-noise ratio in an RAS experiment is limited by the finite signal-averaging time available (mostly limited by drifts in the system) and by the dynamic range of the detector and A/D convertor. High-frequency polarization modulation can alleviate this problem and will be discussed in section 3.3.2.
(2) Because of geometric constraints (sample size and beam divergence), RAS is performed at $\theta \leq 85°$, i.e. away from $\theta_{\text{pseudo-Brewster}}$. As a result, the reflected intensity R^0 is large ($> 90\%$ of the incident intensity) and the recorded ΔR is small ($\theta < \theta_{\text{opt}}$), particularly for low frequency modes (see table 4).
(3) Broadband RAS using conventional thermal sources is severely limited in the far-infrared (50–600 cm^{-1}) by the relatively strong room temperature background. For instance, at 600 cm^{-1} (peak of the room-temperature black body), a 1200 K Globar is only ~ 20 times brighter than the background radiation. Therefore, after typical losses associated with the spectrometer, mirrors and polarizers are taken into account, the Globar signal is only ~ 5 times stronger than the background radiation. Even with modulation techniques, this situation adversely affects the S/N.

In ES, the surface vibrational signal $\Delta E/E$ is measured. Here $\Delta E(\theta) \equiv E(\theta) - E^0(\theta)$ is equal to $\Delta R(\theta)$ and $E^0(\theta) = 1 - R^0(\theta)$. For typical angles

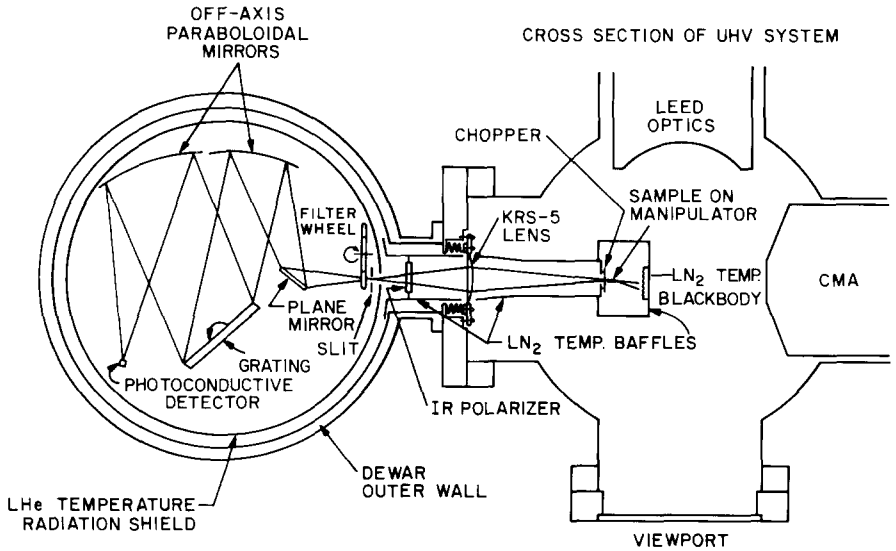

Fig. 11. Optical layout of the infrared emission spectrometer designed by Chiang et al. [119]. The grating spectrometer on the left is cooled with liquid He (4.2 K). The UHV chamber on the right is at room temperature except for a liquid N_2-cooled black body behind the sample and liquid N_2-cooled baffles around the polarizer, KRS-5 window/lens and sample. The sample temperature is regulated to within 0.04 K using a thermocouple spot-welded to its back. The copper consists of a metal vane coated with gold black, attached to a torsion bar and driven to oscillate at 20 Hz by magnetic coils. The cooled filter wheel is necessary to eliminate the strong low frequency radiation ($\sim 500\ cm^{-1}$) when measurements are performed at 2000 cm^{-1} (with permission from ref. [4]).

between 80° and 85°, for example, eq. (3.12) gives $A = E \approx 4R_{\nu}/(\cos\theta)$ for p-polarized radiation. This value is 10%–20% for most metals around 1000 cm^{-1}. Fig. 12 shows two extremes with Cu and Ni. Therefore $\Delta R/R \approx (0.1 \text{ to } 0.25) \times (\Delta E/E)$. Furthermore, the function $\Delta E/E(\theta) = [\Delta R/(1 - R^0)](\theta)$ is maximum for $\theta \approx 80°$ for most metals. As a result, a larger solid angle (e.g. $90° \leq \theta \leq 70°$) can be used. For a room temperature sample, most emitted energy is in the range 300–650 cm^{-1}. Emission spectroscopy is therefore best to look at low frequency modes.

The ultimate S/N achievable with ES is limited by the photon noise. However, to reach this limit, shielding has to be good enough that fluctuations in the background are negligible. The temperature of the sample also must be controlled well enough over the data acquisition time. Finally, the detector and preamplifier noise must be lower than the photon noise for typical photon rates of 10^9–10^{11} photons/s (i.e., very low signal regime). Commercial cooled preamplifiers can be found with noise levels equivalent to the photon fluctuation noise for 10^8 photons/s at 10 Hz modulation [4], and IR detectors (e.g. Si : As) have been developed with photon noise limits in this region [208].

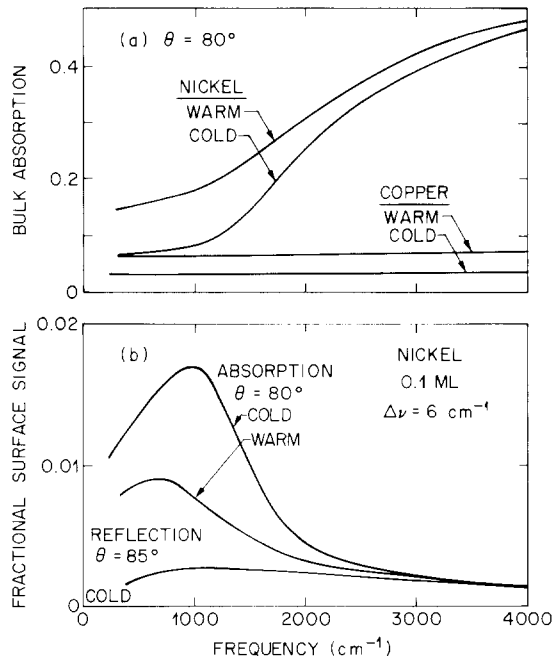

Fig. 12. Bulk and surface signals as a function of frequency in the far- and mid-infrared for nickel and copper. The bulk absorption is evaluated using the measured optical constants including interband transitions. The surface signal is calculated for 0.1 ML of a molecule on nickel with the same parameters as CO (width = 6 cm^{-1}) except for its resonant frequency. Note that the fractional surface emission (absorption) of a molecule on a nickel substrate has a strong frequency dependence related to the frequency dependence of the nickel emission. In addition, the fractional surface emission is larger (although the absolute emission is weaker) at lower temperatures (from R.B. Bailey's PhD Thesis, University of California, Berkeley (1978)).

Thus, in principle, the photon noise limit can be reached in ES. In fig. 13, this theoretical limit has been marked by solid lines for a nickel surface ($E^0 \approx 0.1$) and the geometry used by Chiang et al. [119], i.e. $65° \leq \theta \leq 85°$. Each curve is obtained for a specific grating and indicates the minimum adsorbate signal, expressed as $\Delta E/E$, that could be measured with a S/N of unity in 1 Hz band width. The calculations of the detection limit use the actual resolution of the spectrometer with each grating, which varies from ~ 1 cm^{-1} for the lowest frequencies to > 20 cm^{-1} for the highest. Note that approximately the same fractional signal sensitivity is expected with a cooled interferometer since the detector noise usually remains below the photon noise level in this higher signal regime. The dashed line represents the sensitivity achieved so far. The main causes of the present limit are the fluctuations of the stray radiation that enters the spectrometer.

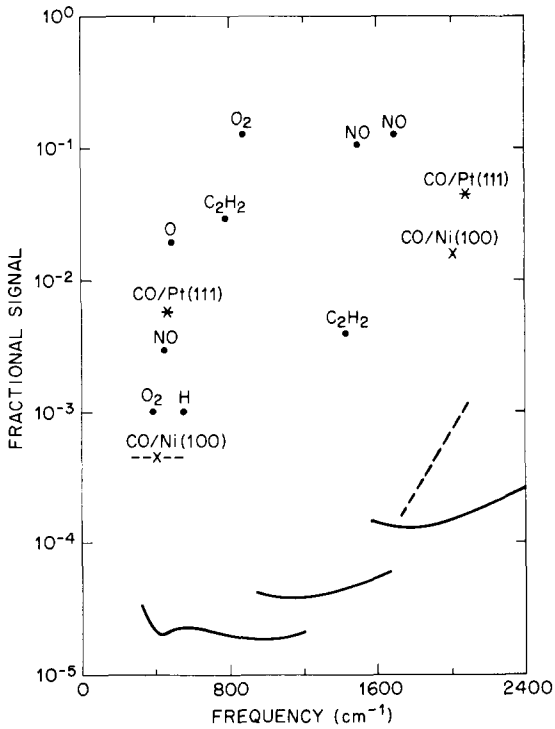

Fig. 13. Ratio of adsorbate vibrational emission to metallic substrate emission (fractional signal) in the far- and mid-infrared for a number of systems. The solid curves show the detection threshold calculated for the apparatus shown in fig. 11, assuming a substrate emissivity of 0.1 and a temperature of 300 K and using measured values of the spectrometer efficiency and detector quantum efficiency, *assuming a photon noise limit*. The dashed lines show the experimental sensitivity experimentally achieved without modulation. The ×'s are the measured surface signals for both CO modes on Ni(100). The dots and chemical symbols indicate the signal levels to be expected from a monolayer coverage of various adsorbates on Pt(111) (with permission from ref. [4]).

The dots in fig. 13 represent the expected fractional signal due to a saturation coverage of various adsorbates on Pt(111). The values were estimated from published EELS spectra, using Ibach's comparison of infrared reflection and EELS cross sections [209] assuming a nominal 10 cm^{-1} line width for these modes. The ×'s show the measured signal levels for the two observable modes of CO on Ni(100) [119] and the *'s that of CO on Pt(111) [20,210,211].

The advantage of the emission technique is apparent for the low frequency modes (~ 500 cm^{-1}). The sensitivity at high frequencies degrades very rapidly as the sample is cooled (and improves if the sample is heated above room temperature), while frequencies near or below the black body peak are less

strongly affected. The lowest measured fractional signals are therefore obtained at these low frequencies for room temperature samples. Furthermore, for a given dynamic dipole moment, the fractional signal $\Delta E/E$ is largest for $\theta \approx 80°$, compared to a $\Delta R/R$ measurement at $\theta \approx 85°$, for a mode at low frequencies (see fig. 12b). This point is emphasized if the peak absorption $\Delta R/R|_{peak}$ is estimated for the Ni–CO mode for $\theta \simeq 85°$. From the measured value $\Delta E/E|_{peak} \approx 4 \times 10^{-4}$ shown in fig. 13, $\Delta R/R|_{peak} \approx 0.18 \Delta E/E$ is obtained from fig. 12. This value $\Delta R/R|_{peak} \approx 7 \times 10^{-5}$ cannot be measured with conventional RAS *at 500 cm*$^{-1}$, although $\Delta R/R|_{peak} \approx 5 \times 10^{-5}$ has been measured for H on Pt(111) *at 1200 cm*$^{-1}$ [66]. For CO on Pt(111), detection of the Pt–CO mode, with $\Delta R/R \approx 1 \times 10^{-3}$ [obtained from $\Delta E/E|_{peak} \simeq 4 \times 10^{-3}$, and $\Delta R/R(85°) \simeq 0.25 \Delta E/E(80°)$], may still be very marginal.

3.2. Semiconductor and insulator surfaces

3.2.1. Multiple internal reflection (MIR)

For transparent substrates, Harrick [212] and Fahrenfort [213] were the first to demonstrate that the absorption spectrum of adsorbed layers could be measured using *internal* reflection. Although a large number of publications exploiting internal reflection ensued [33,214–216] only few dealt with chemisorbed atoms or molecules at surfaces. In 1963, Becker and Gobeli [6] were able to observe the weak Si–H stretch modes of H chemisorbed on Si. Later, Harrick [217] showed the presence of OH and CH groups on an oxidized Si surface and Beckmann [218] determined the composition of the surface film produced on Ge and Si in different etchants. Beckmann and Harrick [219] subsequently determined the hydride and hydroxyl content of anodically and thermally grown SiO_2 films on Si.

The full power of the technique was not appreciated for a long time. In particular, it took twenty years after the original proposal [220] before the quantized electronic states in the semiconductor space charge region were measured [221]. It took also that long after the pioneering work of Becker and Gobeli [6] before the study of H adsorption on *well-characterized* semiconductor surfaces was undertaken [7]. With the increasing interest in processing of semiconductor surfaces, however, MIR is again used extensively. Some of the work will be reviewed in section 4.

The power of MIR spectroscopy comes from the fact that, apart from the reflection losses at the input and output faces of the sample, all the absorption occurs at the surface of the internal plate. Moreover, as mentioned in section 2.2.2, the sensitivity to all the components of surface dipoles is higher than for external reflection. This last statement is quantified by first considering a single reflection and then the complete MIR system. For the usual situation of weak signal limit, it is proper to compare the quantity $\Delta R \equiv R^0 - R$ rather

than $\Delta R/R \equiv (R^0 - R)/R^0$. For internal reflection (ϵ^s real and isotropic), eqs. (2.22) and (2.23) are:

$$\Delta R\,|_{\text{s-pol}} = \frac{2\pi\tilde{\nu}}{\sqrt{\epsilon^s}\cos\theta}\left|\tilde{r}^0_{\text{s-pol}}\right|^2 I_y(\epsilon''_y d_y), \tag{3.29}$$

$$\Delta R\,|_{\text{p-pol}} = \frac{2\pi\tilde{\nu}}{\sqrt{\epsilon^s}\cos\theta}\left|\tilde{r}^0_{\text{p-pol}}\right|^2\left[I_x(\epsilon''_x d_x) + I_z\frac{\epsilon^{v^2}}{\epsilon'^2_z + \epsilon''^2_z}(\epsilon''_z d_z)\right], \tag{3.30}$$

where I_y, I_z and I_x are given in eqs. (2.24), (2.25) and (2.26), respectively, and

$$\tilde{r}^0_{\text{s-pol}} = \frac{\sqrt{\epsilon^s}\cos\theta - \sqrt{\epsilon^v_y - \epsilon^s\sin^2\theta}}{\sqrt{\epsilon^s}\cos\theta + \sqrt{\epsilon^v_y - \epsilon^s\sin^2\theta}} \tag{3.31}$$

and

$$\tilde{r}^0_{\text{p-pol}} = \frac{\epsilon^v_x\sqrt{\epsilon^s}\cos\theta - \epsilon^s\left[\epsilon^v_x\left(1 - (\epsilon^s/\epsilon^v_z)\sin^2\theta\right)\right]^{1/2}}{\epsilon^v_x\sqrt{\epsilon^s}\cos\theta + \epsilon^s\left[\epsilon^v_x\left(1 - (\epsilon^s/\epsilon^v_z)\sin^2\theta\right)\right]^{1/2}}, \tag{3.32}$$

where $\epsilon^v_x = \epsilon^v_y = \epsilon^v_z = 1$ for internal reflection at a vacuum/semiconductor interface. Note that $|\tilde{r}^0|^2 = 1$ for both polarizations in the case of total *internal* reflection, i.e. for $\theta \geq \sin^{-1}(\sqrt{\epsilon^v/\epsilon^s})$. For external reflection ($\epsilon^s = 1$ and $\epsilon^v_x = \epsilon^v_y = \epsilon^z_x$ = substrate dielectric function), $|\tilde{r}^0|^2$ is always smaller than 1.

For the purpose of estimating the sensitivity of both geometries (internal and external), we assume that the active layer is isotropic with the following parameters, typical of H on Si surfaces: the coverage $N_s = 5 \times 10^{14}$ cm^{-2}, the mode frequency $\tilde{\nu}_0 = 2100$ cm^{-1}, the line width $\Gamma = 5$ cm^{-1}, the strength $(e^*/e)/(m^*/m)^{1/2} = 0.05$ and the electronic screening $\epsilon_{\infty z} = 1.3$. The substrate is silicon ($\epsilon^s = 11.7$) and the incidence angle $\theta = 45°$. The results for both polarizations are shown in fig. 14a for *internal* reflection and in fig. 14b for *external* reflection. Note that the change in reflectivity ΔR is of order 10^{-4} for internal reflection and 10^{-5} for external reflection. The case of a strong absorber is then modelled by increasing the value of the dipole moment to $(e^*/e)/(m^*/m)^{1/2} = 0.5$ while keeping all the other parameters constant. The results, shown in figs. 15a and 15b, differ qualitatively from those of fig. 14 only in the positive frequency shift of the tangential component of the absorption function. This shift results from dynamical interactions between the dipoles (depolarization) as discussed in section 2.3.1 [see eq. (2.37)]. Fig. 15 shows that two vibrational lines can be observed with p-polarization for an *isotropic* layer with a *unique* resonant frequency $\tilde{\nu}_0$.

The first conclusion to draw from examining figs. 14 and 15 is that internal reflection gives a factor of 2 to 10 better S/N than external reflection

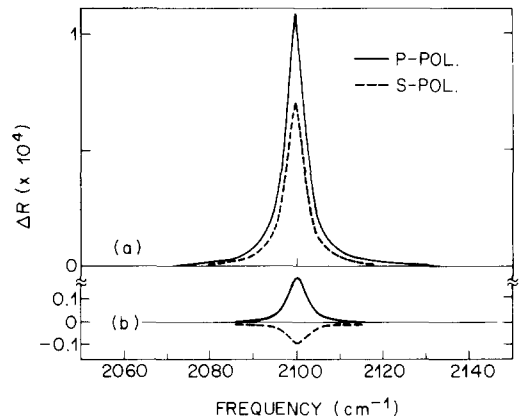

Fig. 14. Model calculations of $\Delta R = R(0) - R(d)$ in the case of (a) *internal* reflection, and (b) *external* reflection for both p- and s-polarizations. The parameters used are $\epsilon^{v} = 1$, $\epsilon^{s} = 11.7$, $\tilde{\nu}_{0x} = \tilde{\nu}_{0y} = \tilde{\nu}_{0z} = 2100\ \mathrm{cm}^{-1}$, $\Gamma_x = \Gamma_y = \Gamma_z = 5\ \mathrm{cm}^{-1}$, $N_{sx} = N_{sy} = N_{sz} = 5 \times 10^{14}\ \mathrm{cm}^{-2}$, $m_x^* = m_y^* = m_z^* = 1$ amu, $(e^*/e)_x = (e^*/e)_y = (e^*/e)_z = 0.05$, $\epsilon_{\infty z} = 1.3$, $\theta = 45°$. This represents the case of a weakly absorbing, isotropic monolayer (from ref. [30]).

depending on polarization and substrate-and-layer dielectric functions. Second, the external reflection spectrum is more complex due to interference between the negative x and positive z components in p-polarized spectra. The physical interpretation of these changes of sign is that, for external reflection, the thin active layer can act either as a reflection or anti-reflection coating depending on polarization, angle of incidence and layer optical responses.

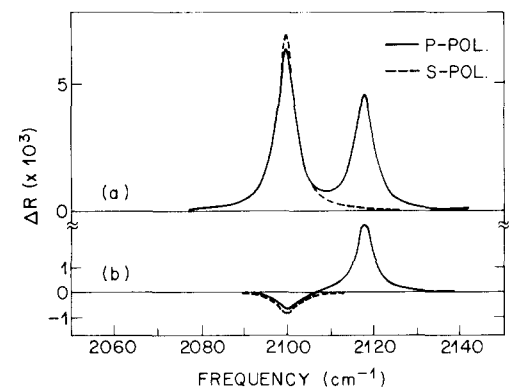

Fig. 15. Model calculation of ΔR in the case of (a) *internal* reflection, and (b) *external* reflection for both polarizations. The parameters used are identical to those used for fig. 14 except that $(e^*/e)_x = (e^*/e)_y = (e^*/e)_z = 0.5$. This represents the case of a strongly absorbing isotropic monolayer (from ref. [30]).

Similar calculations of ΔR for a range of angles of incidence and substrate dielectric functions show that: (1) a single internal reflection always gives a better S/N than a single external reflection by a factor 2 to over 10; (2) the spectrum obtained by internal reflection is simple (I_x, I_y and I_z are positive), and (3) I_x, I_y, I_z are close in magnitude for a wide range of angles. As a result, all the components of vibrational modes can be probed with equal sensitivity and quantitative analysis of the data is possible even for highly diverging radiation and poor knowledge of the angle of incidence. This is not true of external reflection for which positive or negative contributions can occur and where the parallel components are *always* small.

To estimate the sensitivity of *multiple* internal reflection, a thin plate (0.05 cm thick and 5 cm long) with bevelled edges is used. In practice, only a fraction of the incident radiation, f, couples because the spot size at the focus is usually larger than the coupling edge. In addition, there are reflection losses at the input and output edges, so that only a fraction, T_0, of the radiation intensity reaches the detector. As a result, the measured ΔR for N reflections is:

$$\Delta R(N) = fT_0 N \Delta R(1), \tag{3.33}$$

where $\Delta R(1)$ is given by eqs. (3.29) or (3.30). For a 5 mm diameter spot size and a Si plate ($\epsilon^s = 11.7$), $\Delta R(50 \text{ refl.}) = 6.25 \Delta R(1)$. Since $\Delta R(1)$ is between a factor of two and over an order of magnitude larger than that for external reflection, this MIR geometry gives one to two orders of magnitude better S/N than an external reflection. Having established this point, we refer the reader to Harricks' book for a review of experimental MIR geometries [33].

Although the above analysis was done for an adsorbed layer, probed by the evanescent refracted fields, similar conclusions are reached for electronic transitions in the surface region of the substrate, probed by the propagating fields. All the field components are roughly equal so that equal sensitivity to all components of the dielectric function is achieved.

3.2.2. External reflection (ER)

If the semiconductor substrate absorbs, even weakly ($\alpha \approx 0.5 \text{ cm}^{-1}$), then MIR spectroscopy is not possible, leaving external reflection or transmission as the only alternatives. For external reflection, it is possible to calculate the expected $\Delta R/R$ from eqs. (2.13) and (2.14) where $\tilde{\epsilon}^s = \tilde{\epsilon}^m$ is complex. Unfortunately, there are no simple explicit expressions corresponding to eqs. (2.22) and (2.23). The optimum parameters (e.g. angle of incidence) depend strongly on the substrate medium and the nature of the overlayer. They can be determined numerically. In practice, *normal* reflection or transmission have been used for which the equations are greatly simplified and the sensitivity to tangential absorption is large, as reviewed by Chiaradia [37] and Olmstead [41].

Some physical intuition is gained by working out two limits of very weakly and very strongly absorbing substrates. For the weakly absorbing substrates, the equations derived in section 2.22 are approximately valid and it is found that the largest $\Delta R \mid_{\text{p-pol}}$ is obtained for grazing incidence (e.g. $80° < \phi < 87°$ for a silicon substrate). Note however, that at these large angles of incidence ΔR is negative even for the z-component and that the x and y components are small. The latter components are best probed near normal incidence, either by reflection or transmission through a thin sample.

For the other limit ($|\tilde{\epsilon}^{\circ}| \gg 1$), the equations derived for a metal substrate in section 2.2.1 are valid. In particular, only the z-component of a weakly absorbing adsorbate layer can be probed with grazing incidence (p-polarization) reflection. The general conclusion is that, for absorbing substrates, external reflection must be used. For this configuration the sensitivity to modes parallel to the surface is substantially reduced and the maximum sensitivity to modes perpendicular to the surface is achieved by grazing incidence. Transmission is best for modes parallel to the surface on a weakly absorbing substrate.

As a result, one may want to investigate alternatives depending on the particular system under study. For instance, if the Si–O modes are of interest on a silicon substrate, standard multiple internal reflection on a Si plate is ill advised since the modes under study occur at a frequency (~ 900 cm^{-1}) where the Si substrate absorbs. However, epitaxial Si can be grown on Ge single crystals with are transparent above 800 cm^{-1}. Multiple internal reflection using a Ge plate with a thin (~ 100 Å) Si layer is particularly attractive if modes parallel to the surface need to be studied [222]. Alternatively, a single internal reflection can be used through a very thin Si prism. The small path length through the bulk Si gives an easily detectable reflected intensity and the internal reflection gives a better sensitivity to both the parallel and perpendicular modes.

It is clear that, depending on the particular system under study, a variety of approaches are possible. A quantitative estimate of the sensitivity of the various approaches can be done by means of eqs. (2.29) and (2.30) for transparent or weakly absorbing substrates or of eqs. (2.13) and (2.14) in general.

3.2.3. Photoacoustic spectroscopy (PAS)

Photoacoustic spectroscopy (PAS) has gained importance in the past 10–15 years because the measurements are reasonably simple and can be performed on samples that scatter radiation. The spectroscopy of condensed matter has been reviewed by Patel and Tam [13] for pulsed PAS and in a book edited by Mandelis [223] for general PAS. The basic process involves the absorption of electromagnetic radiation by a solid, the conversion of the heat into acoustic waves and the detection of such waves with piezoelectric transducers (PZT)

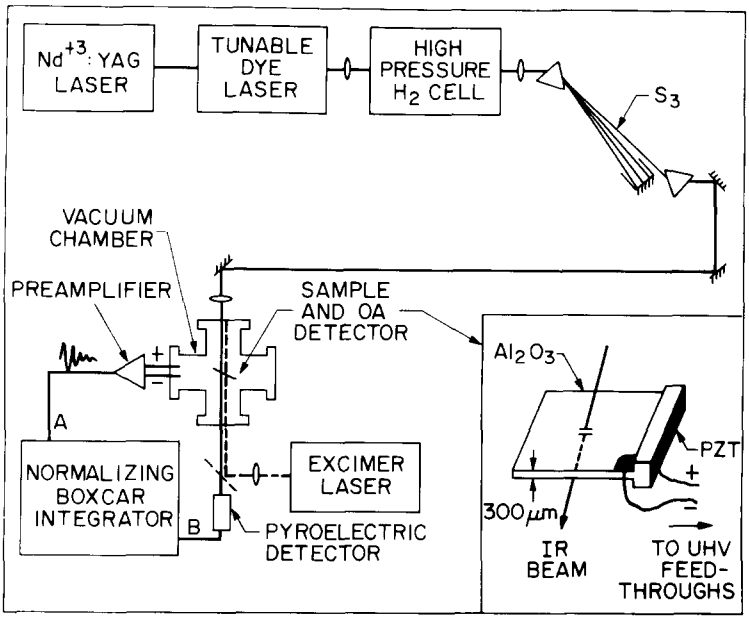

Fig. 16. Schematic of the pulsed optoacoustic apparatus used by Higashi and Rothberg [226]. The source of tunable infrared radiation is based on a visible dye laser pumped by a pulsed Nd^{+3}:YAG laser. Approximately 50–90 mJ of red light in 8 ns pulses induce stimulated Raman scattering in the high pressure H_2 cell (350 psi). 300 μJ of third Stokes radiation is separated at 2.9 μm, spanning 2800–3800 cm^{-1}. The sample consists of a piece of $1\bar{1}02$ sapphire to which a piezo-electric slab (LTZ-2) is edge-bonded with silver epoxy, and suspended from a vacuum flange with electrical feedthroughs.

that are in contact with the solid. The success of the technique is due in part to the good acoustic impedance matching between a solid and the attached piezoelectric detector ($\sim$ 50%).

The technique was extended to surfaces by Brueck et al. [224] who measured the electronic absorption of rhodamine-590 dye physisorbed on crystal quartz with a pulsed laser and an edge-bonded $LiNbO_3$ transducer; and by Träger et al. [225] who coated the piezoelectric detector with a thin silver film ($\sim$ 1 μm) and monitored the strong vibrational absorption of physisorbed SF_6. More recently, Higashi and Rothberg [226] used pulsed PAS to monitor adsorbate chemistry of monolayers of organoaluminum complexes adsorbed on sapphire. The schematic of their experimental apparatus is shown in fig. 16. With a ceramic piezoelectric transducer glued to the sapphire sample, they were able to monitor the weak vibrational bands of adsorbed OH and hydrocarbons as photochemistry was induced by excimer lasers (KrF: 248 nm; ArF: 193 nm).

The main advantage of the technique stems from its measurement of the surface absorption instead of surface reflection. The latter is clearly inadequate for samples that scatter radiation, a common state of affairs in semiconductor surfaces that have been annealed close to the melting point. Absorption measurements are also valuable when "reference" spectra (necessary for RAS) cannot be easily obtained, as is common for chemically treated surfaces at atmospheric pressure. The main disadvantage for UHV studies is the difficulty in attaching the PZT to the sample after the high temperature flashes in vacuum required to clean the sample. If this difficulty is solved, however, pulsed PAS may be useful for real-time measurements of vibrational lifetime τ at surfaces. Indeed, Rothberg et al. [227,228] have argued that in a pump–probe experiment of a vibrational mode, the ratio of the signal due to the probe to the signal due to the pump is essentially of order unity for small delay times ($t \ll \tau$) and is independent of both transient concentration and pump power. The technique was tested in the study of Langmuir–Blodgett film melting [228] and should be contrasted with the pump–probe RAS technique developed by Cavanagh et al. [229] and discussed in section 5. In the latter, the probe-to-pump signal ratio depends directly on the transient concentration and pump power and is typically much smaller than 1. On the other hand, the pump–probe technique is not hindered by substrate absorption and has been used successfully for adsorbates on supported metal surfaces.

3.2.4. Photothermal displacement spectroscopy (PTDS)

The photoinduced thermal displacement of a sample surface was first investigated by Ameri et al. [230] using an interferometer. As in all photothermal techniques, both the thermal and optical properties of the sample can be determined. If the thermal properties are known, then PTDS measures the surface absorption by detecting the thermal expansion of the sample upon optical heating. The idea of monitoring the change of slope of the sample due to the *local* expansion of the surface by measuring the deflection of a smaller probe beam reflected from the sample was first implemented by Olmstead et al. [14,231]. As in the case of PAS, only the energy absorbed by the sample gives rise to a signal. If there is little or no bulk absorption, then the PTD signal is directly proportional to the surface absorption. Otherwise, a modulation technique is used to separate the surface and the bulk signals [231,232]. The theory of PTDS has been recently reviewed by Olmstead [41].

The schematic of the set-up used by Olmstead and Amer [233] is shown in fig. 17. It was used to study the surface electronic absorption of cleaved Si(111) as detailed in section 4.2.1. After cleavage, the sample is illuminated by two laser beams. The pump beam is focussed by a non-birefringent (e.g. CaF_2) lens onto the sample at normal incidence. The polarization can be varied with a rotatable polarizer. The HeNe probe beam is focussed onto the same point of the sample and the reflected beam detected by a position-sensitive split

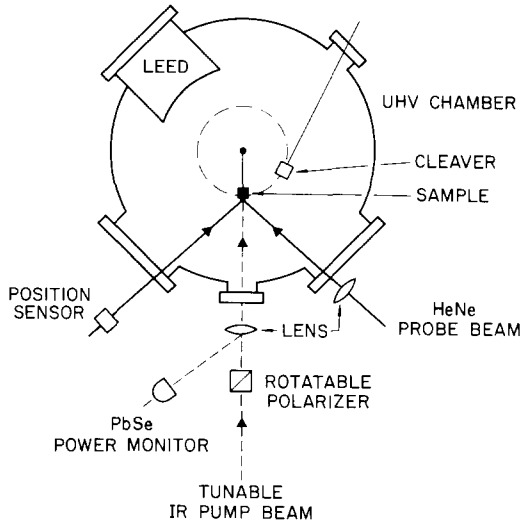

Fig. 17. Schematic of the photothermal displacement surface apparatus used by Olmstead and Amer [231]. The sample can be oriented in both azimuths but is mounted securely to avoid vibrations. After cleavage, the sample is illuminated by two laser beams. The pump laser is focused normal to the sample by a CaF_2 lens and its polarization can be continuously varied. The probe HeNe laser is focused at 45° incidence on the same spot and its reflection collected by a position sensitive detector (with permission from ref. [41]).

photocell. The deflection signal is amplified by a phase-sensitive lock-in amplifier, referenced to the modulation of the pump beam. It should be emphasized that conventional broadband sources can also be used as pump radiation. For such sources, the modulation is provided by the mirror motion of an interferometer [234] or by an external chopper with a grating spectrometer.

The technique is relatively recent and has not been used to measure vibrational spectra of adsorbed molecules. It is therefore too early to assess its full usefulness. Some of the results presented in section 7 should give, however, a good indication of the versatility of the technique.

3.3. Sensitivity problems and solutions

As is the case of all optical spectroscopies, infrared spectroscopy is intrinsically not sensitive to surfaces. To investigate how the S/N can be improved, each part of the experimental set-up must be considered. We outline below some possibilities that have been discussed and proposed. In particular, we examine in order the sources available for SIRS, the spectrometers and modulation techniques, and the detectors.

3.3.1. Sources

3.3.1.1. Broadband sources. The conventional sources are Globars and Nernst glowers, i.e. black body sources. The energy radiated per unit area at a wavelength λ in an interval $\Delta\lambda$ is given by the Planck radiation law:

$$E_{bb}\,\Delta\lambda = \epsilon(\lambda)\frac{2\pi hc^2}{\lambda^4}\left[\exp\left(\frac{hc}{\lambda kT}\right) - 1\right]^{-1}\frac{\Delta\lambda}{\lambda}, \tag{3.34}$$

where $\epsilon(\lambda)$ is the emissivity and T the source temperature. Note that in the far-infrared (large λ), this expression becomes:

$$E_{bb}\,\Delta\lambda \approx 2\pi c\,\epsilon(\lambda)\frac{kT}{\lambda^3}\frac{\Delta\lambda}{\lambda}, \tag{3.35}$$

emphasizing that the energy radiated is linear in T and proportional to λ^{-3} (per spectral resolution element $\Delta\lambda/\lambda$).

In 1973, Stevenson et al. [235] pointed out that synchrotron radiation could be useful for the far-infrared region because of its weaker dependence on wavelength than the black body. More explicitly, they and later others [236–239] used the theory of Schwinger [240] and of Sokolov and Ternov [241] to derive the power radiated per unit angle of the orbit and integrated over the out of plane angle):

$$E_{sr}\,\Delta\lambda \approx CIR^{1/3}\lambda^{-4/3}\frac{\Delta\lambda}{\lambda}, \tag{3.36}$$

where I is the electron current, R the radius of curvature and λ the wavelength of emitted radiation. The constant $C = 8.64 \times 10^{-13}$ W cm^2/mA if E_{sr} is expressed in W. This expression, only valid for the long wavelength region, shows that the amount of energy radiation falls off more slowly that for the black body as the wavelength increases, that is $E_{sr}/E_{bb} \sim \lambda^{5/3}$ in the 100 to 1000 cm^{-1} region [239].

Several aspects of synchrotron radiation are appealing for surface studies: (1) the small source size and the small divergence make it a bright source. The out-of-plane divergence goes as $\lambda^{1/3}$ and is approximately 35 mrad (2°) at 100 μm. (2) The radiation is polarized (in the plane of the orbit). (3) The relative stability of the radiation is better than that of a black body.

All these feature have been quantified in a number of papers [235–239] and reviews [15–18] that are not reproduced here. The essence of the calculations is to consider a practical system with a $\sim$ 1 cm long sample and an optimum incidence angle θ_{opt} in order to define the useable solid angle. The smaller the required solid angle, the better synchrotron radiation fares since it is a brighter and better polarized source. In addition, the smaller the solid angle into the far-infrared detector, the lower the background detector noise since a cold shield can be inserted to screen out more effectively the room temperature

radiation. As a result, the background noise is lower than for a black body source. It is believed that the combination of a brighter source and a lower detector noise operation will give an order of magnitude better S/N in the 300–500 cm^{-1} region than achievable with a Globar source, for UV rings such as at BESSY or Brookhaven.

Experimental flux comparisons of synchrotron radiation and thermal sources have been performed by Yarwood et al. [242] and Schweizer et al. [243], as reviewed by Bradshaw and Schweizer [18]. The results of the latter confirm that, for a 100 mA electron current ($R = 183$ cm and $E = 0.8$ GeV), synchrotron radiation becomes more intense than black body radiation below 1000 cm^{-1}. In the 200–500 cm^{-1} region, the intensity is only a factor of 3 to 4 better. However, only ± 15 mrad were accepted both in the out-of-plane and in-plane direction in this experiment, reducing the available radiation and enhancing diffraction losses for wavelengths above 10 μm. An effort is therefore under way at the UV ring of Brookhaven National Laboratories ($R = 191$ cm, $E = 0.75$ GeV, $I \approx 800$ mA) to extract 90 mrad (± 45 mrad) both out-of-plane and along the orbit. Preliminary results show that the synchrotron radiation (4 mm^2 source size, $\Omega \approx 0.01$ radian) is more intense than the unpolarized black body radiation from a 1000 K Globar (68 mm^2 source size, $\Omega \approx 0.2$ radian) below 200 cm^{-1}. For equivalent source size and solid angle, the synchrotron radiation is ~ 50 times stronger in the 200–400 cm^{-1} region.

The time structure of synchrotron radiation is becoming more interesting with the advent of avalanche periodic photodetectors (APP). For example, 0.2 ns electron bunches at the UV ring of BNL are separated by ~ 20 ns. The APP's have ps response times and could in principle operate over the range 200–1000 cm^{-1}. With gating techniques, time-resolved studies with ns resolution appear possible in the 500 cm^{-1} region. This is an exciting prospect as this may be the right time scale for vibrational lifetime of adsorbate on semiconductor surfaces. The distinct advantages of synchrotron radiation over lasers for time-resolved linear spectroscopy rests on the stability of the radiation pulses. Indeed, the same electron bunch can be used for signal averaging purposes which would substantially enhance the S/N.

3.3.1.2. Lasers. Lasers are an important class of sources for SIRS, particularly for the low frequency region and time-resolved spectroscopy. For example, diode lasers can span the whole range of interest (300 to 3000 cm^{-1}), each laser with a tunability that can exceed 200 cm^{-1}. Usually, frequency scans are achieved by temperature tuning, although current tuning can also be used. Such lasers have recently been used by Bermudez et al. [244] to study the vibrational spectrum of oxygen chemisorbed on Al(111). Their experimental set-up is shown in fig. 18 and described in detail in ref. [245]. The key elements are a chopper (rotating at ω_c) placed before the sample and a ZnSe (piezobi-

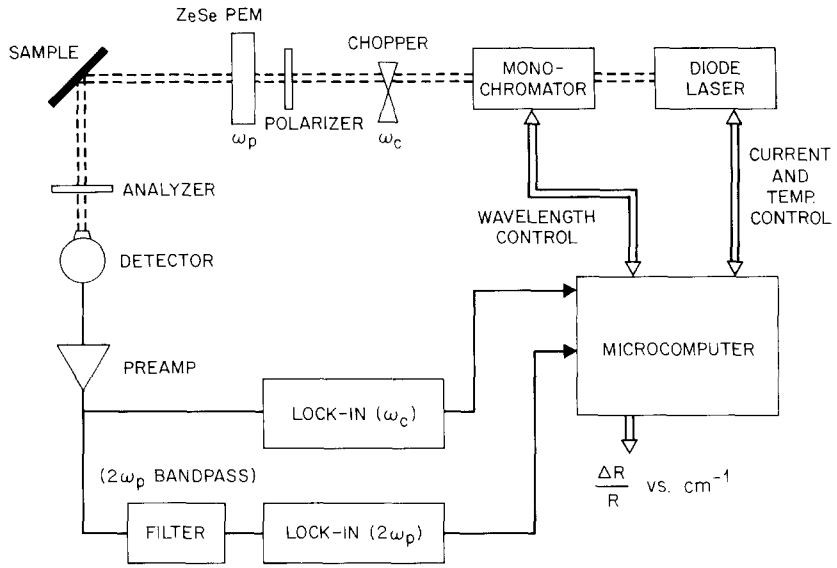

Fig. 18. Schematic diagram of the diode laser IRRAS optical system used by Bermudez et al. [245]. Not shown are the steering and focusing mirrors, the UHV chamber with differentially pumped KBr windows, the photoelastic modulator (PEM) electronics and lock-in reference inputs. For a metallic sample, the angle of incidence is actually about 86°. Typical values for the chopper (ω_c) and PEM (ω_p) frequencies are 800 Hz and 32 kHz, respectively. In practice, the monochromator is usually bypassed and spectra are obtained by controlling the laser current and/or temperature. The final polarizer is used to null $\Delta R/R$ for the clean surface (with permission from ref. [245]).

refringent) photoelastic modulator (PEM) providing polarization modulation and operating at a frequency $\omega_p \gg \omega_c$, typically ~ 50 kHz. The ~ 1 mW output of the diode laser makes it possible to use a HgCdTe detector with a good response at low frequencies. This double modulation makes it possible to measure simultaneously $R_p - R_s$ and $R_p + R_s$, yielding $\Delta R/R = (R_p - R_s)/(R_p + R_s)$ [246]. With proper gating techniques, noise levels between 0.01% and 0.03% have been achieved in the range 600–1020 cm^{-1} (using two diode lasers), sufficient to detect the weak Al–O stretch modes. Without a monochromator, the resolution of such a technique is defined by the energy range over which the multi-mode laser emission occurs at a given laser temperature and current, resulting in 10 to 20 cm^{-1} resolution. The noise level obtained with such a diode laser configuration is about an order of magnitude better than what has been achieved so far with conventional thermal sources and bolometer detectors. Moreover, a large incidence angle ($\theta = 86°$) can be used using RAS, so that a good surface sensitivity is attained for the 500 cm^{-1} region. Since other promising results are appearing elsewhere [247], it is likely that the utilization of diode lasers will become a very attractive alternative to

emission spectroscopy (and possibly to synchrotron radiation as well) for the investigation of low frequency modes. Higher resolution IRRAS with diode lasers in conjunction with a monochromator has been performed by Bermudez et al. but presents serious S/N limitations. Diode lasers have also been used in a single mode operation ($\sim 10^{-6}$ cm^{-1} resolution) to measure the first-order Stark shift of chemisorbed CO on Ni(110) [248] and Ni(100) [249]. The technique has been reviewed by Lambert [250].

Other tunable lasers using parametric oscillators or stimulated Raman scattering cells are important sources for SIRS. For instance, Hoffmann et al. [251] have recorded the spectrum of CO on Ru(001) with higher order Stokes radiation from a multipass high pressure Raman cell. Such a system can operate over a wide frequency region including the 500–700 cm^{-1} [252] and 900–10 000 cm^{-1}. Although the S/N achieved in this experiment is not higher than what can be done conventionally, the continuous tunability, high resolution (0.2 cm^{-1}) and short pulse width (< 10 ns) of this source make it a good candidate for investigating dynamics of molecules at surfaces.

In fact, the very recent development of the sum frequency generation technique [253–255] may enhance the performance of tunable infrared lasers for surface vibrational spectroscopy. Indeed, since this technique measures the nonlinear susceptibility, it is intrinsically surface sensitive for centro-symmetric substrates. Briefly, both infrared (ω_{ir}) and visible (ω_{vis}) laser beams mix at the surface via the second-order susceptibility and the reflected radiation is detected at $\omega_{sum} = \omega_{ir} + \omega_{vis}$, as the IR frequency is tuned. In the dipole approximation, the reflected intensity is:

$$S = C(U_{vis}U_{ir}/AT)\left|\chi^{(2)}_{sum}\right|^2, \tag{3.37}$$

where U_{vis} and U_{ir} are the incident pulse energies, A the overlap area, T the pulse length and $\chi^{(2)}_{sum} = \chi^{(2)}_{resonant} + \chi^{(2)}_{non\text{-}resonant}$ the second-order susceptibility tensor. The constant C depends on the substrate material and the incidence angle.

The sum frequency selection rules, recently demonstrated by Harris et al. [256], can be understood by considering the resonant part of the second-order susceptibility:

$$\left(\chi^{(2)}_{resonant}\right)_{lmn} = \frac{NA_nM_{lm}\,\Delta p}{\hbar(\omega_{ir} - \omega_{vib} + i\Gamma_{vib})}, \tag{3.38}$$

where N is the coverage, A_n the transition dipole matrix element $[\langle q \mid er_n \mid v\rangle]$ and Δp the population difference between the ground and excited vibrational states, $\langle q \mid$ and $\mid v\rangle$, ω_{vib} and Γ_{vib} the vibrational frequency and line width, and

$$M_{lmn} = \sum_{\substack{\text{all intermediate}\\ \text{states } s}} \left[\frac{\langle v \mid er_m \mid s\rangle\langle s \mid er_l \mid q\rangle}{\hbar(\omega_{sum} - \omega_{sq})} - \frac{\langle v \mid e_l \mid s\rangle\langle s \mid er_m \mid q\rangle}{\hbar(\omega_{sum} - \omega_{sv})}\right]. \tag{3.39}$$

Thus, the resonance occurs at $\omega_{ir} = \omega_{vib}$ and the strength of the resonance is proportional to both A_μ, the vibrational dipole moment, and M_{lm}, the *Raman* susceptibility. In the dipole approximation, therefore, the mode must be both infrared and Raman active to give a resonance in the sum frequency spectrum. Moreover, $\chi^{(2)}_{resonant}$ is proportional to the vibrational population difference (eq. (3.38)) and inversely proportional to the pulse length, for fixed frequency (eq. (3.37)). These two features make sum frequency generation well suited for vibrational lifetime studies.

In closing, it is important to stress that all the non-linear laser spectroscopies require large amounts of power at the surface, leading to possible disturbance of the system under study. This general limitation must be kept in mind.

3.3.2. Spectrometers and modulation

Comparison of the theoretical and practical performance of dispersive spectrometers and interferometers for conventional spectroscopy has been reported by several workers [257–263] and nicely summarized by Griffiths and de Haseth [264]. The fundamentals of interferometry have been well laid out by Steel [265], Bell [266] and Chamberlain et al. [267]. Dignam and Baker have proposed and analyzed the performance of a polarizing Michelson interferometer [268]. Very recently, Bradshaw and Schweizer [18] have given a practical viewpoint of interferometric versus dispersive instrumentation in their review of IRRAS. In this section, therefore, only a succinct summary of these discussions is presented and some qualitative conclusions are drawn.

The main difference between *surface* infrared spectroscopy and conventional spectroscopy of *bulk* samples is the requirement of the former for a small image size and solid angle at the sample position. Indeed, whether external or internal reflections are used, the sample is the throughput-limiting element of the optical system. Thus, Jacquinot's advantage (or throughput advantage) for interferometers does not play as important a role in SIRS as it does in conventional spectroscopy where the spectrometer is the throughput-limiting element. In any case, Jacquinot's advantage is only sizable at high resolution ($\Delta\tilde{\nu} < 4$ cm^{-1}).

The Felgett advantage (or multiplex advantage) of interferometers is also diminished in cases where a single, narrow vibrational band is of interest and the rest of the spectral region accessible to the detector does not contain any useful information. Moreover, the Felgett advantage is usually derived assuming that the detector noise dominates. However, in the case of systems limited by the source photon noise, the Felgett advantage disappears because the noise associated with each data point of the interferogram is the sum of all the noise associated with each spectral element measured with a dispersive instrument. While the photon noise limit has not yet been achieved, it is in principle possible.

The ability to record a large spectral region much faster than a conventional dispersive instrument is in fact the most useful aspect of interferometers for SIRS. To take full advantage of fast-scanning instruments, however, detectors with high frequency response, low noise and large dynamic range are required. The development of HgCdTe alloys and InSb crystals for the 700–5000 cm^{-1} region has been critical for surface interferometry, precisely because they combine high operating frequencies (~ 10 kHz) and large dynamic ranges. The dynamic range is defined as the ratio of the total signal achievable without saturation or strong non-linearity to the RMS noise for a given band width as discussed in the next section (3.3.3).

The choice between a dispersive spectrometer and interferometer for SIRS depends therefore critically on the specific experiments. For the sake of discussion, we consider first broadband experiments, then narrow band experiments. When information is sought over a large spectral range, interferometers are better, as long as conditions are such that a similar experiment performed with a dispersive instrument is not in the photon noise limit. Since detector noise or system instabilities are usually the dominant sources of noise, interferometers are superior particularly for high resolution runs.

The main difficulty for interferometers using state-of-the-art detectors is the dynamic range problem. With present analog-to-digital converters (ADC's), 16 bits are available (15 bits + sign) so that the ultimate dynamic range (for one scan) is 32768 (2^{15}). However, since the last bit must be random for successful signal averaging, the practical limit is $2^{14} = 16384$. For a spectrum measured between 400 and 4000 cm^{-1} at 4 cm^{-1} resolution ($M = 900$ spectral elements), the best spectral S/N achievable is $16384/\sqrt{900} = 546$ (~ 0.2% noise level). Possible ways to improve this figure when using high dynamic range detectors are:

(1) Using gain-ranging amplifiers that increase the gain on either side of the interferogram center burst. Since the amplitude of the interferogram decreases rapidly on either side of the center burst, most of the interferogram (containing information on sharp spectral features) is measured with increased gain [269]. Gain-ranging is only useful when the detector dynamic range exceeds that of the ADC.

(2) Eliminating the center burst by recording directly a *difference* spectrum such as in polarization modulation or optical subtraction. With photoelastic modulators (PEM's), the polarization is modulated at a frequency (~ 50 kHz) higher than the data-taking rate and the difference signal is demodulated with a lock-in amplifier *before* digitization [262,270–272]. Optical subtraction is usually performed in a dual beam arrangement [273–275] and will not be discussed here because it has hardly been applied to SIRS.

(3) Reducing the signal level by increasing the interaction with the surface. For example, multiple reflections or more grazing incidence on metal surfaces increase the contrast $\Delta R/R$ and decrease the magnitude of R. The use of

thinner ATR plates for MIR experiments increases the number of reflections while rejecting more radiation at the input edge for a given sample length.
(4) Reducing the spectral range to the utmost by inserting appropriate optical filters into the beam. Filtering out the high frequency end of the spectrum is particularly important with interferometers because it makes it possible to increase the minimum sample spacing required (i.e. to decrease the number of points necessary for a fixed resolution).

For narrow band experiments, such as the monitoring of the sharp CO stretch mode or of a very low frequency mode (~ 300 cm^{-1}), dispersive spectrometers may in fact be better. Indeed, for a high frequency mode, HgCdTe and InSb array detectors are commercially available so that the whole (narrow) spectrum can be recorded simultaneously with a dispersive element (no scanning necessary). With a high frequency modulation (~ 1 kHz), spectra can be accumulated continuously without "dead time" as for the interferometer (turn around time between data acquisition), resulting in superior S/N. Such a configuration would give high time resolution for kinetic experiments, limited only by the chopping frequency and the S/N of the feature under study. For a broad mode at low frequencies (< 600 cm^{-1}), both the throughput and multiplex advantages are very reduced for interferometers. That is, low resolution spectra can be obtained by dispersive instruments with comparable S/N.

In summary, the choice of a spectrometer to perform conventional SIRS with thermal sources depends a great deal on the particular experiment under consideration. While dispersive instruments equipped with array detectors are clearly better for time-resolved studies in a *narrow* spectral region, interferometers are preferable whenever broadband information is needed. As will be apparent in section 4, the understanding of most physical processes benefits greatly from data acquired over a broad spectral range. As a result, interferometers are being more widely used. In section 4.4.2, the possible extension of the interferometric time-resolved technique developed for gas-phase spectroscopy by Mantz [276] to the study of *repetitive* processes at surfaces will be suggested as a means to acquire a full spectrum in 10–100 μs.

Signal modulation in SIRS spectroscopy is necessary because infrared detectors operate by sensing a *change* in temperature or conductivity upon irradiation. Conventionally, a chopper modulates the radiation in a dispersive or step-and-integrate instrument and the moving mirror in a continuous scan interferometer. However, several other modulation schemes have been developed to improve the S/N of various experiments, as previously reviewed by Hoffmann [15]. For example, double-beam and polarization modulations help eliminate gas-phase absorption and wavelength modulation enhances the detection of *sharp* absorption lines. To choose between various modulation schemes, it is of paramount importance to understand what limits the S/N of the experiments under consideration. In general, this is a difficult task because

several sources of noise may give comparable contributions. A technical discussion on such an endeavor is beyond the scope of this review.

Often, the use of modulation results in a trade-off. For example, polarization modulation only works over a limited spectral region because the transmission function of the complete optical system has a polarization dependence that is frequency dependent. Below 700 cm^{-1}, photoelastic modulators (PEM) cannot be used and the use of a rotating polarizer leads to large quadrature signals that adversely affects the signal upon small lock-in drifts. Moreover, polarization modulation cannot be used for semiconductor or insulator surfaces studied with MIR because all components of the vibrational absorption are probed with equal sensitivity, leading to a potential cancellation at a given frequency. Wavelength modulation can only record sharp spectral lines. Its use for general line shape analysis and broadband electronic absorption is not possible. As a result, many of the schemes developed earlier are not widely used at present, particularly with interferometers.

3.3.3. Detectors

Infrared detectors have been the subject of several reviews [4,277–279]. They are usually classified into thermal detectors (e.g. Goley cell, pyroelectric bolometers, semiconductor bolometers) and quantum detectors (e.g. HgCdTe, InSb, PbS photoconductors). Thermal detectors tend to operate best in a low background radiation regime and are slower than quantum detectors because their response time is limited by the macroscopic element thermal relaxation time.

The most widely used detectors for the mid-infrared region (800–5000 cm^{-1}) are the liquid nitrogen cooled HgCdTe alloys and InSb crystals because their performance (detectivity) is close to the theoretical background limit (due to background photon noise). Their detector noise does not increase with spectral band width, making them ideal for broadband interferometric studies. Moreover, the InSb crystals remain remarkably linear and do not saturate up to a photon induced current of 3 mA. Such a photon flux is at least a factor of two higher than the maximum flux collectable from a thermal source.

The band gap of HgCdTe alloys can be continuously changed by varying the composition of HgTe and CdTe mixture. However, the smaller the band gap (the longer the wavelength response), the worse the detectivity. The highest detectivity HgCdTe elements have the worst linearity, which may be a problem for the measurements of strong absorption bands. Fortunately, non-linear effects are not a problem with dispersive instruments and only affect the center burst of interferograms. Non-linear effects do not, therefore, hinder significantly the measurement of sharp spectral lines.

In the far-infrared (< 700 cm^{-1}), the detectors of choice are either semiconductor bolometers operating around 1.5 K or high performance photoconductive detector operating at 4.2 K and listed in table 5. Bolometers are slower

Table 5
List of detectors most commonly available for surface infrared spectroscopy

Detector material	Low frequency cut-off (cm^{-1})
InSb	1820
Si : In	1400
HgCdTe (narrow)	1000
HgCdTe (broad)	650
Si : Bi	625
Si : Ga	555
Si : As	370
Si : Sb	330
Ge : Cu	320
Ge : Zn	250
Ge : Be	175
Ge : Ga	83
Stressed Ge : Ga	50

and more sensitive in low backgrounds, thus better suited for dispersive spectrometry using cold spectrometers. The photoconductors are in general better suited to interferometry.

4. Selected examples

The purpose of this section is to illustrate the type of information that can be extracted from SIRS using a few examples selected for their tutorial value. An effort is made not to duplicate any of the previous reviews on the subject [15–21] and to emphasize the methods developed to obtain the data and the information derived from the data. Generalizations are made whenever possible in an attempt to define SIRS with respect to other surface techniques. Four general areas are considered sequentially: (1) the chemical nature and geometry of adsorbates at surfaces (section 4.1), (2) surface electronic absorption (section 4.2), (3) dynamical effects involving the coupling of vibrational modes to other vibrational modes or to the substrate electronic excitations (section 4.3), and (4) kinetics at surfaces such as adsorbate diffusion or the effect of gas-phase and bulk transport phenomena on surface reactions (section 4.4).

4.1. Chemistry and structure

The understanding of any surface phenomenon requires the knowledge of the chemical nature of the substrate outer layer and the adsorbates attached to it. Among various vibrational spectroscopies, infrared spectroscopy is particularly useful to decipher between different chemical entities because it can

resolve modes that are separated by a few cm^{-1} (e.g. in the CH stretch region of hydrocarbons) and determine unambiguously their dipole activity. The chemical composition of the *substrate* surface can be probed by titration of the outer layer by a simple atom, such as H, and subsequent measurements of the "substrate-atom/adsorbed-atom" stretch mode. The characteristic frequencies are usually straightforward to interpret because they are well separated [280]. The chemical arrangement of *adsorbates* is inferred from the analysis of their *internal* vibrational modes.

The process of chemical identification by spectral analysis is, however, intimately linked to structural questions such as the nature of the adsorption sites and the adsorbate orientation, particularly for adsorbate–substrate modes. Therefore, this section discusses both the chemical and structural information that is directly obtained by SIRS. In general, SIRS is a structural tool complementary to (i.e. to be used with) other structural techniques, particularly when structural features of *clean* surfaces are of interest. Indeed, when the reconstruction involves large displacements and rearrangement of the surface atoms, such as the Si(111)-(7 × 7), titration with a very low coverage (~ 5% ML) of hydrogen can give qualitative information. For example, the adsorption of one H per 7 × 7 unit cell in a special site (distinguishable by the different Si–H stretch frequency) with a mode polarized normal to the surface gave a strong clue that a dangling bond was present at the bottom of the large corner holes [281,282]. In general, however, the adsorbates produce structural changes of the outer layer and cannot be used as non-destructive structural probes.

4.1.1. Ethylidyne on Pt(111)

We first consider the adsorption of ethylene ($H_2C{=}CH_2$) on Pt(111) because it exemplifies how SIRS can complement other vibrational techniques and because it has not been discussed at any length in previous reviews. Other important studies involving adsorbed hydrocarbons (e.g. formate and methoxy adsorbed at metal surfaces) were reviewed by Bradshaw and Schweizer [18] and will only be mentioned briefly.

At low temperatures (< 220 K), EELS data have indicated that ethylene is di-σ bonded at a bridge position on Pt(111) via the two carbon atoms, i.e. lies with its molecular axis parallel to the surface [283]. At room temperature, however, the adsorption is dissociative resulting in the formation of ethylidyne ($\equiv C{-}CH_3$) bonded with its molecular axis normal to the surface [284]. Early LEED investigations had shown that ethylidyne was adsorbed at a three-fold site [285] as was later confirmed by ARUPS [286] and NEXAFS [287]. The proposed structure is shown in fig. 19. The assignment of the later EELS spectra supported this structure, relying heavily on the combined infrared and Raman characterization of a model compound, $(CH_3C)CO_3(CO)_9$, containing an ethylidyne ligand [288] as summarized in table 6.

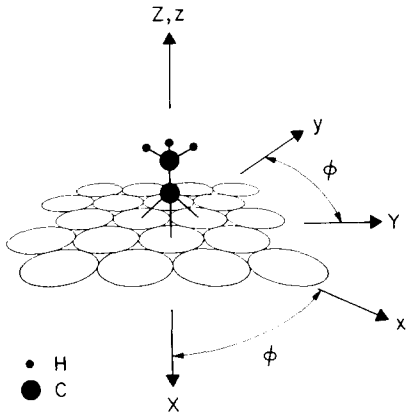

Fig. 19. Structure of ethylidyne on Pt(111) consistent with all experimental observations and originally proposed by Kesmodel et al. [285]. The space-fixed axes are X, Y and Z. The methyl group-fixed axes, x and y, can rotate about its z-axis, making an angle ϕ with respect to X and Y (with permission from ref. [291]).

Although the intensity of the EELS losses at 430, 1130 and 1350 cm^{-1} show an angular dependence characteristic of dipole scattering and consistent with the geometry of fig. 19, the $\nu_s(CH_3)$ mode at 2890 cm^{-1} is very weak, with comparable intensity to that of the non-dipole $\nu_{as}(CH_3)$ at 2950 cm^{-1}, and becomes relatively more intense off specular, unexpected for a dipole mode [289]. Furthermore, a loss peak at 900 cm^{-1} persists in all EEL spectra and cannot be assigned to ethylidyne. Finally, a number of loss features associated with non-dipole modes are present in the specular EEL spectra.

Recent IRRAS investigations have helped clarify these problems and confirm the model in fig. 19 [290,291]. Only three absorption bands were

Table 6
Assignment and observed wavenumbers for ethylidyne ($C-CH_3$) on Pt(111) and for the gas-phase model organometallic compound $(CH_3)CO_3(CO)_9$

Assignment	Symmetry	EELS [a]	SIRS [b,c]	$[(CH_3C)CO_3(CO_9)]$ [d] IR and Raman
ν_s(Pt–C)	A_1	430		401
ν_{as}(Pt–C)	E	~ 600		~ 600
$\rho(CH_3)$	E	980		1004
ν(C–C)	A_1	1130	1124 [b], 1118 [c]	1163
$\delta_s(CH_3)$	A_1	1350	1341 [b], 1339 [c]	1356
$\delta_{as}(CH_3)$	E	1420		1420
$\nu_s(CH_3)$	A_1	2890	2884 [b], 2884 [c]	2888
$\nu_{as}(CH_3)$	E	2950		2930

[a] Ref. [284]. [b] Ref. [290]. [c] Ref. [291]. [d] Ref. [288].

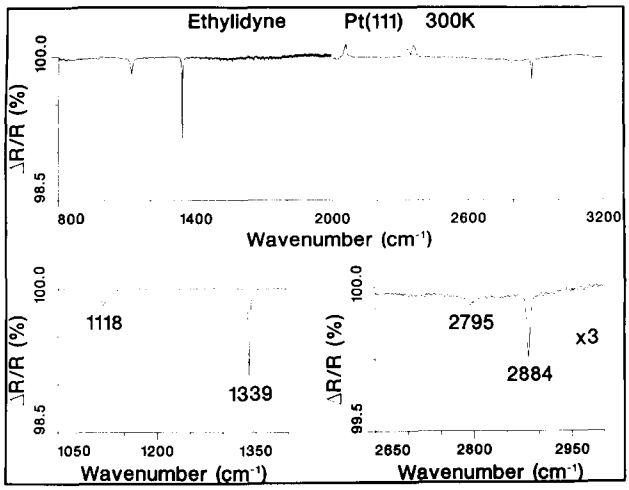

Fig. 20. IRRA spectrum of a saturation coverage of ethylidyne (3 L ethylene exposure at 350 K) on Pt(111), taken at 300 K using clean Pt(111) as a reference. The spectral region from 800 to 2000 cm^{-1} was obtained with a narrow-band HgCdTe detector and the region above 2000 cm^{-1} with an InSb detector. The radiation is p-polarized and the resolution 2 cm^{-1} (triangular apodization). Inadequate purging is responsible for the CO_2 band at 2336 cm^{-1} and $\lesssim 0.01$ ML adsorbed CO for the feature at 2030 cm^{-1}. The four other bands at 1118, 1339, 2795 and 2884 cm^{-1} are discussed in the text. The band at 1339 cm^{-1} was studied as a function of temperature with 0.5 cm^{-1} resolution (with permission from ref. [291]).

observed in the region 1000–3000 cm^{-1} corresponding to the three dipole-active modes ν(C–C), $\delta_s(CH_3)$ and $\nu_s(CH_3)$ as shown in fig. 20 and summarized in table 6. The discrepancies in the reported wavenumbers, in particular of the ν(C–C) mode, between the two IRRAS investigations (see table 6) are primarily due to the temperature dependence of the mode. Chesters and McCash [290] acquired their spectra at 94 K (8 cm^{-1} resolution) and Malik et al. [291] at room temperature (2 and 0.5 cm^{-1} resolution). The strong absorptions of the dipole allowed (A_1) modes and the lack of any detectable absorption for the dipole forbidden (E) modes (at 980, 1420 and 2980 cm^{-1}) beautifully confirm that ethylidyne has C_{3v} symmetry with its axis normal to the surface. In particular, the $\nu_s(CH_3)$ mode is clearly dipole allowed, although weaker than the other two modes, and the $\nu_{as}(CH_3)$ is clearly dipole forbidden. Furthermore, there is no detectable absorption around 900 cm^{-1}, indicating that, whatever impurity contributes to the EEL spectra, its mode is not dipole allowed.

Beyond the mode assignment, however, the IRRA spectrum of fig. 20 displays two interesting features, a weak band at 2795 cm^{-1} and a remarkably narrow $\nu_s(CH_3)$ band (2 cm^{-1} at 300 K). The weak band is assigned to the first overtone of the asymmetric CH_3 bend, $\delta_{as}(CH_3)$. While the fundamental

mode is dipole forbidden (E symmetry), its first overtone has A_1 symmetry and is in Fermi resonance with $\nu_s(CH_3)$, also with A_1 symmetry. Such a Fermi resonance has been observed for many molecules containing the methyl group [292]. The main result is an increase of the splitting and sharing of the intensity, accounting for the enhanced intensity of the overtone. The observation of this overtone, undetected in all previous EELS investigations, may be a fine measure of adsorbate–adsorbate interactions. Indeed, since the Fermi resonance depends critically on the force fields of the CH_3 group, any interaction with neighboring CH_3, with other adsorbates or with the substrate may modify the degree of the Fermi resonance, resulting in detectable changes in the strength and position of the modes.

The observation of overtones and combination bands in SIRS experiments is always very useful because it requires the participation of specific mechanisms to enhance the absorption of these weak modes, such as Fermi resonances. Unraveling those mechanisms helps understand the adsorbate structure better. For instance, in a careful study, Hayden et al. [293] showed that the combination band of two forbidden bands (B_1 symmetry) of the formate molecule

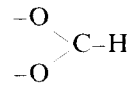

displayed a relatively strong absorption when absorbed on Cu(110) with C_{2v} symmetry [18]. They demonstrated that the combination of the antisymmetric C–O stretch, $\nu_{as}(CO)$, and the CH wagging mode, $\delta(CH)$, is indeed dipole allowed (A_1 symmetry) for the proposed structure and derives its intensity from a Fermi resonance mechanism. Another example of overtone detection due to a Fermi resonance is encountered for methoxy (CH_3O–) on Cu(100) [294–925] where two bands at 2882 and 2918 cm^{-1} are assigned to the overtones of the methoxy deformation modes in Fermi resonance with $\nu_s(CH)$ for an adsorption site with C_{3v} symmetry [295]. These studies have been discussed thoroughly by Bradshaw and Schweizer [18].

We return to the second interesting feature of the ethylidyne spectrum in fig. 20, the *sharp* umbrella mode, $\delta_s(CH_3)$, at 1339 cm^{-1}. The narrow line width (1.9 ± 0.3 cm^{-1} at 300 K, 1.2 ± 0.3 cm^{-1} at 82 K) stimulated Malik et al. [291] to investigate the possible observation of rotational sidebands. Indeed, the methyl group of ethylidyne (fig. 19) can rotate about the C–C bond (angular momentum along the z axis) with a rotational constant $A = h/8\pi^2 c I_{CH_3} \approx 5$ cm^{-1} (I_{CH_3} is the moment of inertia about the C–C axis). Unfortunately, however, the rotational transitions *cannot* be excited in this case because the electric field is perfectly aligned with the molecular rotational axis (Z in fig. 19) leading to the $\Delta K = 0$ selection rule. The observation of rotational–vibrational transitions for the methyl group aligned as such is therefore forbidden on metal surfaces. Rotational fine structure could only be

observed if this molecule were adsorbed on a transparent substrate (e.g. semiconductor) because non-normal fields can be set up (see section 3.2.1).

Malik et al. noted, however, that rotational motion could be manifested in the temperature dependence of the line width and wavenumber of the vibrational mode for strong enough vibration–rotation interactions. Such interactions lead to slightly different rotational constants for the ground (A_0) and first excited (A_1) vibrational levels, i.e. $A_1 - A_0 \neq 0$. The transition energy from an excited rotational level ($K \neq 0$) in the ground vibrational state ($v = 0$) to the *same* rotational level ($\Delta K = 0$) in the excited vibrational state ($v = 1$) is therefore slightly different from that of the $v = 0$ ($K = 0$) to $v = 1$ ($K = 0$) transition. For a symmetric top, such as the methyl group in fig. 19, the resulting vibration–transition frequency is [296]:

$$\omega = \omega_0 + (A_1 - A_0)K^2, \tag{4.1}$$

where ω_0 corresponds to the transition from $v = 0$ ($K = 0$) to $v = 1$ ($K = 0$) and K is the rotational label. As the thermal population of the higher rotational levels is increased, the vibrational band shifts and broadens. However, this effect could not account unambiguously for the observed line shift and broadening with temperature, leading Malik et al. to conclude that the IRRAS results alone do not disprove the existence of free rotation. They are, however, able to rule out free rotation of the methyl group for ethylidyne on Pt/Al_2O_3 samples from the lack of rotational structure in the (E) symmetry vibrational bands which are dipole allowed on small metal particles. This conclusion is supported by recent inelastic neutron scattering data [297] showing a CH_3 torsion mode with finite frequency (383 cm^{-1}). The observed temperature effects on Pt(111) are therefore most likely due to dephasing (section 4.3.1).

It is clear, however, that molecular rotation could be investigated for a number of systems where the dephasing contribution is small and rotational sidebands are allowed. This section has shown how SIRS goes beyond the assignment of adsorbate vibrational modes (often well carried out with EELS) to give structural and symmetry as well as rotational information. In addition, SIRS can also give a precise measure of the interaction between non-bonded atoms in an adsorbed molecule, as was recently done in high resolution studies of isotopic acetonitrile ($^{12}CH_3{}^{12}CN$ and $^{13}CH_3{}^{13}CN$) by Erley [143].

4.1.2. Water on Si(100)

The determination of the chemical arrangement of adsorbates by spectral analysis is made easier when the substrate is transparent, such as semiconductors, because all the components of the modes can be probed with similar sensitivity (see section 3.2.1). In particular, the intensity of each component of the absorption can be measured directly using p- and s-polarizations on surfaces with two-fold symmetry. For instance, the Si(100) surface displays only one orientation of the 2×1 reconstruction if it is cut a few degrees

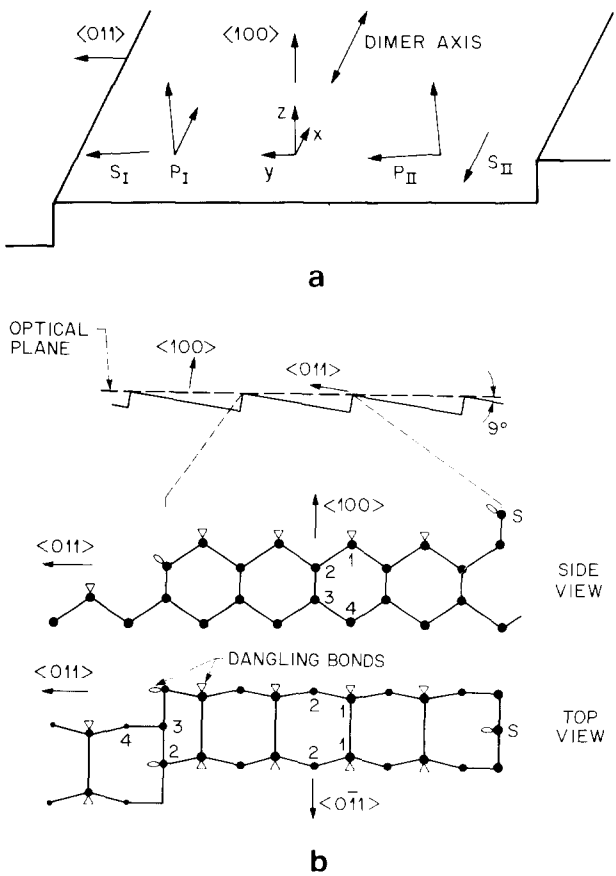

Fig. 21. (a) Schematic representation of the vicinal surface with indication of the (100) terrace, the surface dimer orientation, and the electric field components for configurations I and II (both polarizations). Note that the field vectors are decomposed with respect to the optical axis that is tilted with respect to the (100) plane. (b) Atomic representation of the vicinal surface for 9° inclination. The optical plane, to which the electric field vectors are referenced, is 9° from the (100) plane as shown at the top. The projection of the dangling bonds is shown schematically. Note that the step dangling bonds are oriented close to the $\langle 011 \rangle$ axis (from ref. [308]).

vicinal to the (100) plane about the $\langle 0\bar{1}1 \rangle$ axis [298]. Analysis of the LEED beam intensity shows in fact that the exposed plane is made up of a uniform array of double-layer steps separating the (100) terraces as shown in fig. 21. Fig. 21a clarifies how the use of p- and s-polarizations in two orthogonal configurations (I and II) makes it possible to extract each component (x, y, z) of the absorption spectrum, even if their frequency is the same. Furthermore, fig. 21b shows that the dangling bonds associated with the step atoms are oriented close to the $\langle 011 \rangle$ axis, i.e. parallel to the surface and orthogonal to

the step edge. In contrast, the terrace dangling bonds are contained within the (011) plane, orthogonal to the ⟨011⟩ axis.

The findings of SIRS for H_2O adsorption on Si(100) give an example of its contribution to the understanding of simple chemistry at semiconductor surfaces. Indeed, conflicting interpretations for this system were the motivation for this study. The original picture of Meyer [299] involving complete dissociation was first questioned by Fujiwara and Ogata [300] on the basis of three prominent features in the UPS spectrum assigned to the $1b_1$, $2a_1$, and $1b_2$ orbitals of the free H_2O molecule. This conclusion was challenged by Ibach et al. [301] who only observed in their EEL spectra the stretching modes associated with Si–H, Si–OH and O–H. In particular, they saw no evidence for the H_2O scissor mode at 1670 cm^{-1}. Shortly thereafter, Ciraci and Wagner [302] used a semi-empirical approach to show that molecularly adsorbed water would exhibit an unstable electronic configuration. Instead, they found that dissociated water was quite stable, and reinterpreted Fujiwara's data in terms of dissociative adsorption. However, in 1983, Schmeisser, Himpsel, and Hollinger [303] reported that new UPS data and photostimulated desorption (PDS) results could not be reconciled with dissociative adsorption. From their UPS data, which were distinctly different from Fujiwara's data, they suggested that H_2O was chemisorbed with its oxygen end toward the surface and argued that, since these conclusions were inconsistent with the EELS observation of the Si–H stretching mode, dissociation induced by low-energy electrons or by rough surface (with steps and defects) might account for the EELS results of Ibach et al. They also pointed out that the coexistence of molecular and dissociated water could not be ruled out for certain temperature and surface conditions. Finally, more recent UPS work indicated that water is molecularly physisorbed at 100 K and remains undissociated up to 600 K [304], while other EELS studies have found dissociative adsorption for water on all Si faces [305].

In view of these conflicting results it was critical to establish unambiguously whether and under which conditions water dissociates on Si(100). The use of high-resolution infrared spectroscopy was best suited for such investigations since it is sensitive enough to detect weak vibrations such as SiH without the possibility of probe-induced dissociation; further, the symmetry of the modes can be measured from polarization studies. Water adsorption was therefore investigated by SIRS in the temperature range 80 to 500 K on flat and vicinal Si(100)-(2 × 1) surfaces [306–308]. Fig. 22 shows that the Si–H and O–H modes of dissociated water are clearly observed upon exposure at room temperature. In fact, molecular water could only be observed by condensing water on an oxidized surface or on a layer with predissociated water. Even at 80 K, water was found to dissociate (i.e. yielded the same spectrum as in fig. 22a) as long as the Si(100) surface was clean [307]. Since all sources of electrons (gauges, etc.) were turned off during the experiment, the SIRS results

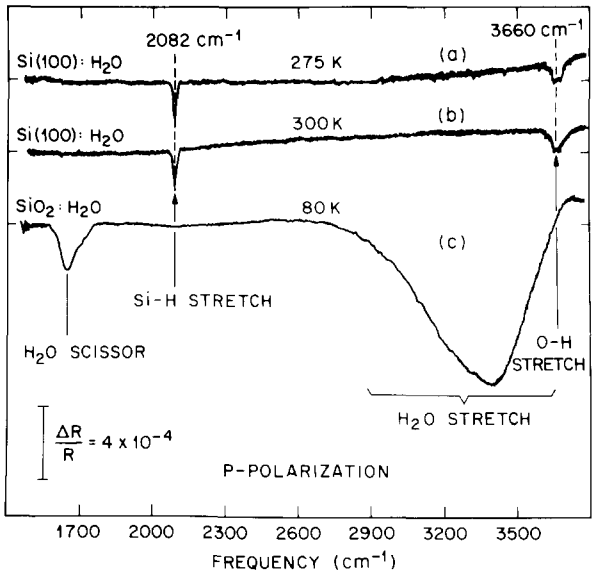

Fig. 22. Surface infrared spectra obtained upon exposure of clean Si(100)-(2×1) to (a) 0.5 L water at $T_s = 275$ K, and (b) 10 L water at $T_s = 300$ K. Curve (c) is obtained upon exposure of an oxidized Si(100) surface (native oxide) to 10 L water at $T_s = 80$ K. Data were taken at the exposure temperatures indicated next to each spectrum. The clean surface was used as a reference (from ref. [307]).

clearly showed that water dissociation is not induced by electron dissociation (either before or after adsorption), thus confirming the validity of the EELS data.

Moreover, the SIRS studies made it possible to assess the importance of steps and defects and to determine the molecular bond orientation. By using vicinal samples with steps along the $\langle 0\bar{1}1 \rangle$ direction as shown in fig. 21, the possible dissociation of water at steps could be investigated. Indeed the detection of Si–H modes polarized along the $\langle 011 \rangle$ direction would indicate the presence of H at steps. Although the data could not rule out the presence of some H at steps, they clearly showed that steps are not *saturated* with hydrogen [308]. Since the substrate temperature is too low for H to diffuse on the surface, it was therefore concluded that water dissociation must take place on the terraces themselves, probably on a single silicon dimer.

Furthermore, the observation of both normal and tangential components for the Si–H and O–H stretch modes indicates that these bonds are tilted with respect to the surface normal as shown schematically in fig. 23. While an attempt was made to determine the bond angles [306], the results must be viewed as only qualitative because, as explained in section 4.1.5.1, the IR measurements give the ratio of the components of the dipole moment compo-

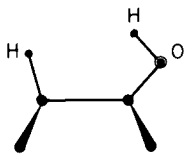

Fig. 23. Suggested arrangement of the dissociated H_2O molecule on Si(100). Note that the angles shown are approximate. In particular, recent ESDIAD work suggests that the OH is out of the H–Si–Si–O plane (from ref. [306]).

nents which can be very different from $\tan^2(\alpha)$, where α is the bond angle with respect to the surface normal. However, this work shows that systematic studies using both configurations I and II (see fig. 21a) and sophisticated cluster calculations (see section 2.4.2) could lead to a good structural determination, as was done for H on Si(100) in section 4.1.5.1. In particular, it could test the recent proposal, based on the interpretation of electron-stimulated-desorption-ion-angular-distribution (ESDIAD) data, that the OH bond is in the plane perpendicular to the Si dimer axis (fig. 23 shows the OH bond *in* the plane *containing* the dimer axis). The interested reader is referred to the recent and thorough review by Thiel and Madey [309] on the fundamental aspects of the interaction of water with solid surfaces.

4.1.3. CO on Pt(111) and Pt clusters

The dynamic dipole moment associated with the C–O stretching vibration of CO adsorbed on metallic substrates is very large ($e^*/e \simeq 0.5$–0.8) and the absorption line widths relatively narrow (5–10 cm^{-1}), making it an ideal candidate for surface infrared spectroscopy. Not surprisingly, CO on Pt(111) was one of the first systems studied by IRRAS [310] and has remained of current interest partly due to the challenge of separating the dipole–dipole from the chemical interactions. As a result, this system has been analyzed and summarized in every single review on surface infrared spectroscopy so far [15–20]. However, as pointed out by Bradshaw and Schweizer [18], many problems associated with the CO/Pt(111) system still remain unresolved despite all the extensive investigations by a variety of surface techniques. Furthermore, the large absorption strength of the CO stretch vibration makes it a molecule of choice for line shape analysis (section 4.3) and kinetic (time-resolved) measurements (section 4.4.2.2). Thus, although this system has been extensively discussed previously, it is considered here again but with a slightly different emphasis: The recent and outstanding problems associated with CO adsorption are first singled out and briefly discussed. Then, the adsorption of CO as a probe of surface *morphology* and electronic structure is examined in some detail.

Briefly, a single C–O stretch band is observed around 2100 cm^{-1}, corresponding to linearly bonded CO, for all coverages up to $\theta = 0.33$ ML ($\sim 5 \times 10^{14}$ CO/cm^2) at which a $(\sqrt{3} \times \sqrt{3})R30°$-like LEED pattern is observed

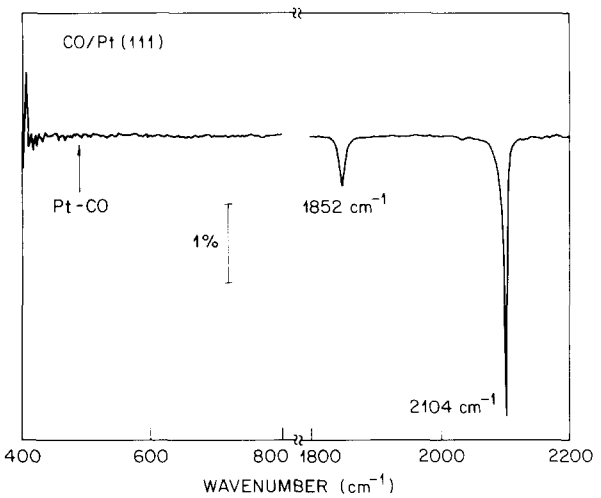

Fig. 24. IRRA spectrum of CO on Pt(111) at $\theta \approx 0.5$ ML obtained with a bolometer detector for the low frequency region (with permission from ref. [312]).

[311]. At $\theta = 0.5$ ML, a second C–O stretch band appears at 1850 cm^{-1}, corresponding to bridge-bonded CO, as a (4 × 2) LEED pattern is established. Further adsorption of CO at low temperature leads to the splitting of the (4 × 2) superlattice beams, forming a I(4 × 2) pattern at $\theta = 0.6$ ML (9×10^{14} CO/cm^2), the saturation coverage. A summary of the IRRAS data at $\theta = 0.5$ ML is shown in fig. 24.

The first outstanding problem is the failure to observe (see fig. 24) the low frequency Pt–CO stretch absorption band at 460 cm^{-1} by IRRAS [312] despite the good S/N in this spectral region ($\Delta R/R \mid_{\text{noise}} \approx 7 \times 10^{-4}$). Indeed, this band was measured in emission [211] to be, at saturation coverage, $\Delta E/E \mid_{\text{peak}} \approx 4.3 \times 10^{-3}$ or about an order of magnitude weaker than the measured $\Delta E/E \mid_{\text{peak}}$ for the C–O stretch [313]. In the IRRAS experiment, an upper limit for the Pt–CO mode absorption corresponding to $\Delta R/R \mid_{\text{peak}} < 7 \times 10^{-4}$ (i.e. over 50 times weaker than the measured C–O stretch intensity) was set using the 10 cm^{-1} width measured for this low frequency mode by high resolution (2.8 cm^{-1}) emission spectroscopy [211]. A possible resolution of this conflict is found at the end of section 3.1.3 where it is pointed out that $\Delta R/R \neq \Delta E/E$. Around 500 cm^{-1} for Pt, $\Delta R/R(85°) \approx 0.25 \Delta E/E(80°)$ because $R^0(85°)$ is much larger than $E^0(80°)$. Thus, using $\Delta E/E \mid_{\text{peak}} \approx 4.3 \times 10^{-3}$ measured by emission, we conclude that $\Delta R/R \mid_{\text{peak}}$ should be $\sim 1 \times 10^{-3}$ for this low frequency Pt–CO band. This level is marginal to be observed in the IRRAS experiment. The reason for $\Delta E/E \mid_{\text{peak}} \approx \Delta R/R \mid_{\text{peak}}$ for the high frequency C–O stretch band is two-fold: first, the resolution of the emission data (9.6 cm^{-1}) is much lower than that of the IRRAS data (2 cm^{-1})

reducing the $\Delta E/E|_{peak}$ because the line width is ~ 5 cm^{-1}. Second, the optical constants of Pt are such that $\Delta R/R(85°) \approx 0.5\Delta E/E(80°)$ around 2100 cm^{-1}. As a result, the ratio $(\Delta E/E|_{Pt-CO})/(\Delta E/E|_{C-O})$ cannot be carried over to $(\Delta R/R|_{Pt-CO})/(\Delta R/R|_{C-O})$ without correcting for the resolution and optical constants. Fig. 12b shows that the latter contribution can be substantial for metals like Ni with strong interband absorptions.

The second unresolved problem concerns the profile of the CO stretch band near the *bridge*-bonded CO band (~ 1850 cm^{-1}). In 1983, Hayden and Bradshaw [314] observed a lower frequency band at 1820 cm^{-1}, assigned to CO on a three-fold hollow site. The temperature dependence of the broadening, shift and intensity of the two bands at 1820 and 1850 cm^{-1} were accounted for by a relaxation dephasing mechanism at low temperatures (see section 2.5.2.2) and site exchange at higher temperatures. The latter dynamical effects were recently modelled by Gadzuk [315] and Jones et al. [316]. However, the lower frequency band (~ 1820 cm^{-1}), was not observed in more recent studies [312,313] on nominally flat Pt(111). It is possible, therefore, that the low frequency feature is due to CO adsorbed in a two-fold site at specific *defect* rather than in a three-fold site on (111) planes. Indeed, the spectral features of CO at steps is complex and has not yet been investigated exhaustively. For (100) steps one band is observed at 2064 cm^{-1}, assigned to CO linearly bonded at steps. For (111) steps, however, two bands at 2056 cm^{-1} and 2064 cm^{-1} are present, indicating two possible adsorption sites for linearly bonded CO. Furthermore, in the bridge-bonded CO region, another feature is apparent around 1870 cm^{-1} for surfaces with (111) steps. It is possible, therefore, that the 1820 cm^{-1} feature observed by Hayden and Bradshaw may in fact be due to CO adsorbed in a two-fold site at or near steps. Differences between different experimental groups would then arise from differences in the density of specific defects generated from miscuts and/or in the details of sample preparation (e.g. sputtering). More extensive investigations are necessary to resolve this problem.

A third aspect of interest (i.e. not thoroughly understood) is the temperature dependence of the IRRA spectra and LEED patterns for this system. On highly stepped crystals [e.g. (533) or (432) surfaces] the observed vibrational bands at low coverages for low T exposures (85 K) are all assigned to CO at steps [317–319] while only vibrational bands assigned to CO at terraces characterize lower step density crystals upon low T exposures (< 100 K). The step sites become completely populated upon annealing to 300 K for the latter case. Furthermore, sharp LEED patterns associated with well-defined CO ordering develop upon low exposures at low temperature (85 K). All these observations indicate that short-range motion, involving a couple lattice spacings, can occur at temperatures much lower than the temperature at which long-range motion (i.e. diffusion) is substantial on the (111) planes. Substantial diffusion from terrace sites to step sites was measured to be around 150 K

by analyzing the width of the (0, 0) helium diffraction beam [320]. Both the origin of the temperature dependence of the 1820 cm^{-1} band and the measure of the diffusion barrier on the (111) plane (see section 4.4.2) require the unravelling of complex kinetic behaviors taking place at the (111) surface.

We now turn to the use of CO as a probe of surface morphology and electronic structure. Indeed, studies of CO adsorbed on highly stepped crystals can help understand the CO adsorption on small catalysts (supported metal particles), in addition to providing good model systems for CO diffusion measurements (section 4.4.2). In a series of papers, Hayden, Greenler and co-workers [317–319] have investigated Pt(533) and Pt(432) surfaces corresponding to 4 atoms wide (111) terraces with (100) steps and 3 atoms wide terraces with (111) steps, respectively. This work has been reviewed by Bradshaw and Schweizer [18]. Briefly, CO adsorbed at steps is characterized by a stretch frequency 15 to 10 cm^{-1} lower than CO on (111) terraces (fig. 25). As a result, dynamical coupling between step and terrace CO rapidly becomes important as the coverage is increased, leading both to intensity borrowing and frequency shifts [16,321]. Consequently, the interpretation of IRRA spectra in terms of defect densities is difficult. This difficulty is partly responsible for the apparent lack of success in studying supported metal catalysts [322–324]. Nevertheless, is clear that high resolution studies at very low coverages ($< 2\%$) on very well-ordered stepped samples can alleviate some of the problems associated with dynamical interactions and be useful to characterize quantitatively defect morphology and density.

CO can also be useful to characterize the electronic structure and morphology of heterogeneous systems such as alkali-covered Pt(111) or Cu-covered Ru(001). For instance, the CO/K/Pt(111) system has been studied extensively [16,17,312], as reviewed by Bradshaw and Schweizer [18], yielding up to eight different C–O stretch frequencies in the range 1380–1800 cm^{-1} depending on the relative coverages of CO and K. While the general decrease of the C–O stretch frequency is due to the lowering of the $2\pi^*$ electronic level towards the Fermi level, it is difficult to account for all the discrete and relatively narrow bands.

Finally, CO has recently been used by Hoffmann and Paul to characterize the structural and electronic properties of Cu layers on Ru(001), and the dispersion of Cu on Ru(001) [325,326]. Although this work does not involve Pt(111), it illustrates beautifully the spirit of this section. Analysis of the CO stretch spectra indicates the formation of Cu islands for $0.25 < \theta_{Cu} < 1$ and chemical modification of the copper film by the underlying Ru, leading to increased Cu–CO back donation. For example, a weak chemical modification of the Cu films is still observed for a 3 ML thick Cu film, whereas 8 ML thick films exhibit all the CO adsorption properties of Cu(111), i.e. a coverage dependent red shift (2077–2075 cm^{-1}), a (1 × 1) LEED pattern and characteristic features of CO desorption. For high θ_{Cu}, strong vibrational coupling

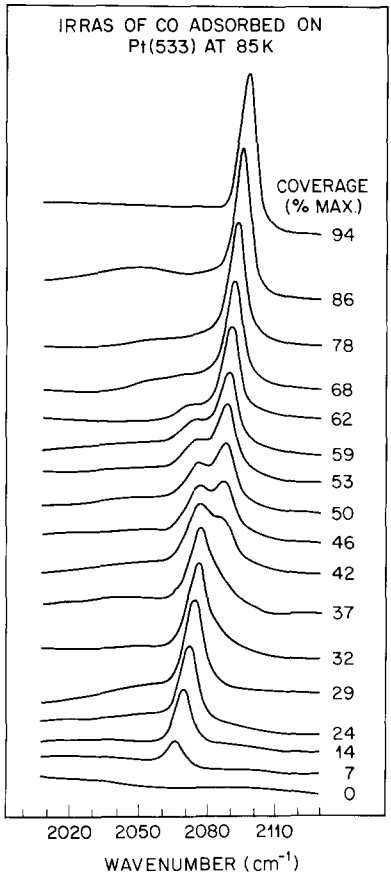

Fig. 25. IRRA spectrum of CO on Pt(533) as a function of increasing relative coverage (from ref. [317]).

between neighboring Cu–CO and Ru–CO leads to significant intensity transfer and frequency shifts. After characterizing the well-ordered epitaxial (annealed) Cu films, Hoffmann and Paul investigated the dispersion of Cu evaporated onto Ru(001) at 85 K. Analysis of the C–O stretch frequencies allows them to identify small copper clusters of 1–4 atoms (2138–2123 cm^{-1}), two-dimensional (2120–2110 cm^{-1}) and three-dimensional (2098 cm^{-1}) copper aggregates. They find that the formation of epitaxial monolayer or islands of copper (2082 cm^{-1}) requires the surprisingly low annealing temperature of 350 K. Annealing to 540 K results in a smooth copper layer with preferential (111) orientation (2075 cm^{-1}).

In summary, the molecule CO can be used to characterize the morphology and electronic structure of metal surfaces. The analysis, however, is com-

plicated by the strong dipole–dipole interaction between ad-molecules and the complex way in which the C–O vibration is chemically shifted. As described in the next two sections, the adsorption of hydrogen atoms to characterize the underlying structure is free of the above problems because the dipole–dipole interactions are negligible ($\lesssim 1$ cm^{-1} shift at saturation) and the charge transfer is small. Therefore, despite the difficulties to detect the weak H vibrations, several studies have now been completed [327].

4.1.4. H-induced reconstruction on W(100) and Mo(100)

Traditionally, SIRS has been applied to study surface phase diagrams involving the adsorbate long-range arrangement on an otherwise unreconstructed substrate. Examples of this kind include the extensive investigations of CO on Ru(001) [328], CO on Pd(100) [329] (see review by Hoffmann [15]) and the recent study of N_2 on Ni(110) [330]. For N_2 on Ni(110), the N–N internal mode at ~ 2200 cm^{-1} is monitored. Observation of subtle changes of the band shape are discussed within a phase diagram inferred from other studies [331]. However, just as for CO, the large dynamic dipole moment associated with the N–N stretching mode hinders the interpretation. In fact, Brubaker and Trenary [330], using isotopic mixtures, observe a strong intensity borrowing although the large dipole coupling is almost completely cancelled by a large chemical shift of opposite direction. The occurrence of such strong direct interactions makes it very difficult to interpret the spectra in terms of a detailed structural model.

In contrast, the H/W(100) and H/Mo(100) systems are particularly attractive because both the dynamical (e.g. dipole–dipole) and chemical interactions are small within a given substrate phase, leading to vibrational shifts that are smaller than 1 cm^{-1}. On the other hand, H induces a series of complicated *substrate* reconstructions [332]. Theoretically, the formation of these reconstructed phases has been modelled within the framework of adsorbate–adsorbate interactions, considering both direct interactions (Van der Waals, dipole–dipole and orbital overlap) and indirect interactions (mediated by the substrate electrons or phonons) [333]. For H/W(100) and H/Mo(100), the small dynamic dipole moment ($e^*/e \approx 0.05$) and small atomic radius associated with adsorbed H insures that direct interactions are negligible. Moreover, the adsorption site, determined by EELS for H/W(100), remains two-fold (bridge site) throughout the range of temperatures and coverages investigated (fig. 26c), greatly simplifying the spectral assignment. The strong H–substrate interaction, manifested by the large H induced substrate reconstruction, suggests that H–H effective interactions are indeed mediated by the substrate.

Since the reconstruction changes rapidly with coverage (see phase diagram for H/Mo(100) in fig. 26b) and the IR absorption is weak ($\Delta R/R \approx 10^{-4}$), two important aspects of the data acquisition must be mentioned. The first is the simultaneous LEED and IR monitoring. The second concerns the way the

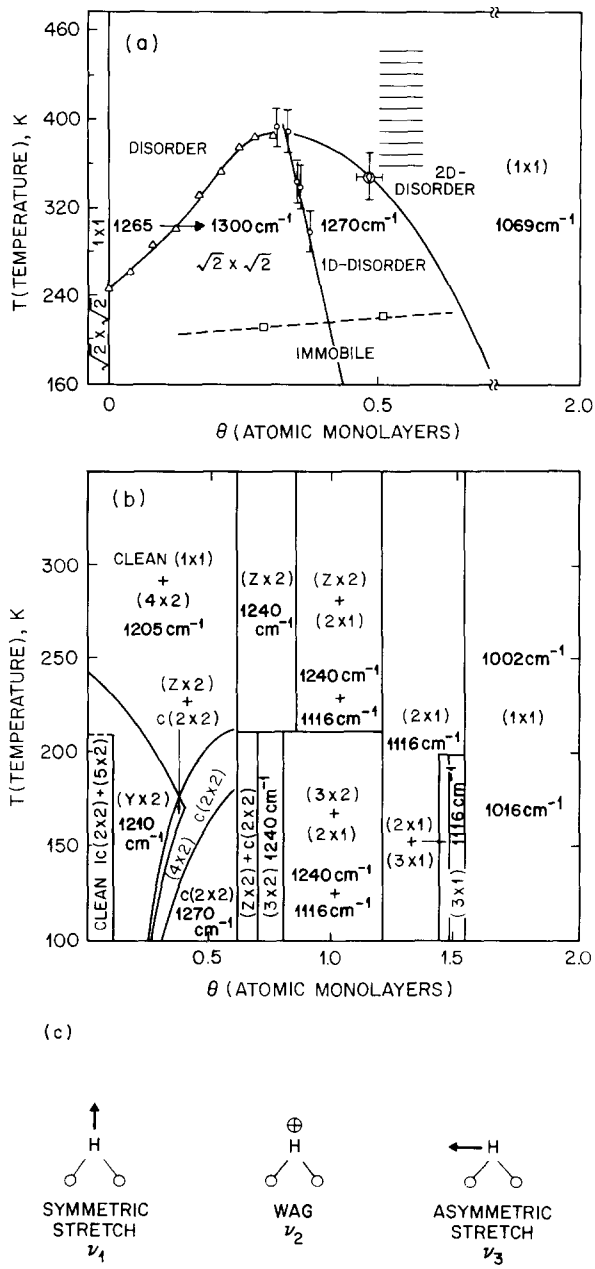

Fig. 26. Phase diagrams in $T-\theta$ for (a) H/W(100) and (b) H/Mo(100). The symmetric stretch mode (ν_1) shown in (c) is the only infrared allowed normal mode. Its wavenumber associated with each phase is shown in bold print in the two diagrams. Not included for the H/Mo(100) system are the lines at 1220 cm^{-1} for the $(5+2)+Ic(2\times2)$ region, 1210 and 1270 cm^{-1} for the $(4\times2)+c(2\times2)$ region, 1270 and 1240 cm^{-1} for the $c(2\times2)$ and $(z\times2)$ region, and 1116 and 1020 cm^{-1} for the $(2\times1)+(3\times1)$ region (with permission from ref. [335]).

IR spectra were recorded. After flash-cleaning of the sample, scans would be initiated as the sample cooled. Consecutive runs averaging 512 to 1024 scans (4 cm^{-1} resolution) would then be ratioed. When two consecutive ratios gave a flat baseline on the scale of interest ($< 10^{-4}$) over the frequency range 800–2000 cm^{-1}, an appropriate H_2 exposure was made to reach the desired coverage. Runs were then taken consecutively with the H coverage being incremented between each run. The resulting reflectivity spectra, R, were ratioed to a reference reflectivity spectrum, R^0. The reference surface could be the clean surface or a surface with a well defined H coverage. This procedure made it possible to measure changes of order $< 10^{-4}$ of the total reflectance spectrum, R/R^0. For Mo(100), the ratioing was frequently made between spectra for which the coverage did not vary greatly. This procedure minimized the noise arising from slow thermal drifts in the sample manipulator. In such cases, the two H-induced spectra were chosen so that the wavenumbers of the IR lines were far apart in frequency [334].

4.1.4.1. The phase diagrams. The H/W(100) phase diagram [332] can be described briefly as follows (fig. 26a): the very faint and broad $(\frac{1}{2},\frac{1}{2})$ feature of the clean reconstructed W(100) surface sharpens and becomes more intense as H is absorbed at room temperature up to $\theta = 0.30$. This phase has been named the commensurate $(\sqrt{2} \times \sqrt{2})R45°$ or $c(2 \times 2)$. From $\theta = 0.33$ to $\theta = 0.42$, the $(\frac{1}{2},\frac{1}{2})$ spot splits into four spots, forming the so-called "incommensurate" $I(\sqrt{2} \times \sqrt{2})$ phase. The spots then streak at $\theta = 0.48$ in the direction normal to the axis of the splitting, forming a 1D disordered phase. Faint $\frac{1}{5}$-order spots appear around $\theta = 0.9$. A disordered (1×1) pattern, characterized by strong diffuse scattering, can be seen at $\theta = 1.4$. As the saturation coverage is reached ($\theta = 2$), the diffuse scattering decreases and a well-ordered (1×1) pattern is established.

The phase diagram for the H/Mo(100) system is reproduced in fig. 26b and described in detail elsewhere [335]. Briefly, it comprises regions with one simple diffraction pattern such as (4×2), $(z \times 2)$, (2×1) and (1×1) above 220 K and $(y \times 2)$, $c(2 \times 2)$, (3×2), (3×1) and (1×1) below 220 K. Here y and z vary continuously with coverage from 5 to 4 and 4 to 2.75, respectively [335]. In between are regions characterized by a superposition of two diffraction patterns. This may be due either to first-order transitions wherein the coexistence of two distinct phases occurs or to second-order transitions where the intermediate regions consist of a single homogeneous structure with two distortion waves superimposed. The thrust of the infrared work is to use the complementarity of the IR data to infer the presence or absence of islands or other heterogeneous phases.

For both systems, the H-induced reconstruction is responsible for all changes observed in LEED [332,334–336]. Each of the clean surfaces also undergoes reconstruction spontaneously below room temperature, giving a

c(2 × 2) LEED pattern on W(100) and an Ic(2 × 2) on Mo(100). Upon H adsorption, a c(2 × 2) LEED pattern appears on both substrates for $\theta \approx 0.3$ to 0.5. However, for coverages both lower and higher than that corresponding to the H-induced c(2 × 2) LEED pattern, the long-range structures are very different: a remarkably large number of different phases occurs on Mo(100) whereas continuous phase transitions appear to set in on W(100) between zero and saturation coverage.

4.1.4.2. Interpretation of the ν_1 mode wavenumber. As discussed in detail in refs. [336,337], the wavenumber of the symmetric stretch mode (fig. 26c) depends on the local substrate arrangement, i.e. the W–W or Mo–Mo dimer length. Shifts associated with dipole interactions for $\theta = 2.0$ are less than 2 cm^{-1} for H/W and 1 cm^{-1} for H/Mo. Substrate mediated dynamical interactions are negligible on Mo and less than 10 cm^{-1} on W [336]. They are therefore negligible at low coverages.

In order to estimate changes in dimer length from frequency shifts, we summarize two crude approximations which give an upper and lower limit. The first is based on the central force spring model approximation, neglecting the wag force constant [338]. It is reasonably accurate for the reconstructed phases, for which the angle α between the W–H (or Mo–H) bond and the surface normal, is close to 45°. A small change, Δd, in the dimer length, d, leads to a frequency shift, $\Delta\tilde{\nu}$, given by:

$$\Delta\tilde{\nu} \equiv \tilde{\nu}(\alpha - \Delta\alpha) - \tilde{\nu}(\alpha) = \tilde{\nu}(\sin^2\alpha)\, \Delta d/d. \tag{4.2}$$

Note that the frequency increases as the dimer length decreases. An estimate of the smallest dimer length for W is $d = 2.74$ Å, yielding $\alpha = 45.8°$ [337] if the W–H bond length remains 1.91 Å [57]. Similar reasoning for Mo gives $d = 2.73$ Å and $\alpha \approx 45°$. In both cases, this geometry occurs in the c(2 × 2) phase.

Eq. (4.2) does not account for the observed shifts (230 cm^{-1} on W and 255 cm^{-1} on Mo) observed between the c(2 × 2) and 1 × 1 phases with $\Delta d = 0.42$ Å on W and Mo. This underestimate of $\Delta\tilde{\nu}$ is due to the neglect of the wag force constant and to the assumption of the spring model at saturation [57]. For these reasons, the second way of estimating $\Delta\tilde{\nu}$ is to assume that $\tilde{\nu}$ is simply inversely proportional to the dimer length over the whole range as was done by Arrecis et al. [337]. This will overestimate the frequency shift. The numerical expression for H/W(100) is:

$$\Delta\tilde{\nu} = 1.1\tilde{\nu}\, \Delta d/d. \tag{4.3}$$

In the next section, both ways of deriving Δd from $\Delta\tilde{\nu}$ are used to obtain a lower and upper limit.

4.1.4.3. Results for the low coverage region. The regions of interest are the transitions from (1) the $Ic(2 \times 2)_{clean}$ to the (5 × 2) on Mo(100) below 220 K,

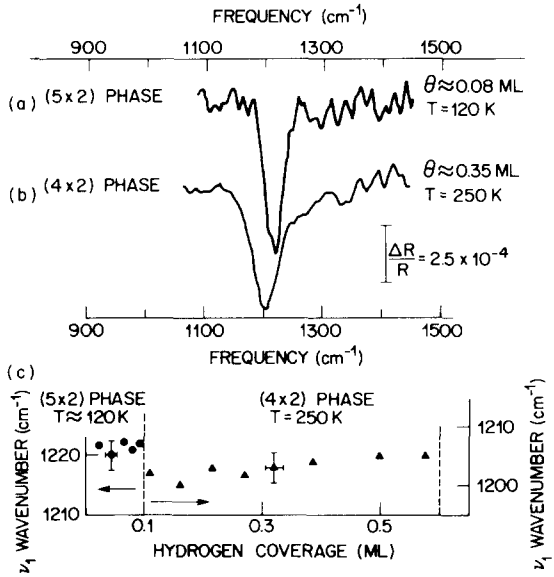

Fig. 27. IR absorption–reflection spectra associated with (a) the 5×2 phase with the reference phase taken at $\theta = 0.01$, and (b) the 4×2 phase with the reference phase taken at $\theta \approx 0.1$. The resolution is 8 cm^{-1}. Plot (c) summarizes the coverage dependence of the ν_1 wavenumber determined as described in the text (from ref. [336]).

(2) the $(1\times1)_{clean}$ to the (4×2) on Mo(100) above 220 K, and (3) the $(1\times1)_{clean}$ to the c(2×2) on W(100) at room temperature. Analysis of the diffraction beam intensities by Prybyla et al. [336] showed that, within the kinematical limit, the intermediate phase had to be made up of domains with Ic(2×2) and (5×2) symmetry. The range of coverages ($\theta = 0$ to 0.1) over which the (5×2) beams grow in intensity suggests that the H-induced structure maintains a local (island) coverage $\theta = 0.1$. This coverage region was carefully investigated by recording IR spectra every two minutes after flash-cleaning. The first run where the Ic(2×2) pattern appeared was used as reference for the subsequent runs (typically 3–4) obtained before the $(y\times2)$ pattern appeared. Fig. 27a shows a particularly good run taken at $\theta = 0.08$ and ratioed to $\theta = 0.01$. Background H_2 gas prevented more spectra to be accumulated in this region. Based on the ambient H_2 pressure and ambient exposure time, an estimate of the coverage could be derived. The mean and RMS error of the wavenumbers as a function of coverage, determined by a Lorentzian fit to the data, were obtained from a series of such runs and are plotted in fig. 27c (filled circles). It appears that there is no shift in frequency ($\Delta\tilde{\nu} < 2$ cm^{-1}) with coverage in this phase. Using eqs. (4.2) and (4.3), an upper limit between 0.01 and 0.004 Å can be placed on the local variation of the Mo–Mo dimer length. These observations are consistent with the formation of

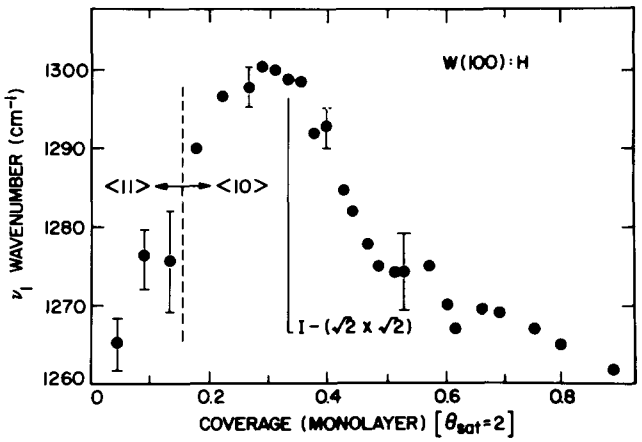

Fig. 28. ν_1 wavenumber as a function of coverage. Note that, above $\theta = 0.3$, a contribution around 1090 cm^{-1} is also present (not shown here). For $\theta > 1.0$, no ν_1 mode is detectable above 1200 cm^{-1}, i.e. the ν_1 mode of H on unreconstructed W(100) dominates the spectrum (from ref. [337]).

H-rich islands, giving rise to the (5 × 2) LEED pattern, on an otherwise almost clean Mo surface, giving rise to the Ic(2 × 2) pattern.

The same study was performed for the (4 × 2) region. Since the clean surface is characterized by a (1 × 1) pattern, LEED intensity measurements cannot determine whether or not islanding takes place in this region. LEED beams at the $\frac{1}{4}$-order position grow in and their intensity increases continuously with coverage. Either islands or a homogeneous surface can account for this observation. The latter case, however, requires that the Mo distortions (giving rise to the 4 × 2 pattern) be small initially and increase gradually with coverage. The IR data (e.g. fig. 27b), summarized in fig. 27c by the filled triangles, rule out this possibility. Indeed, the ν_1 wavenumber associated with the 4 × 2 phase does not change ($\Delta\tilde{\nu} < 2$ cm^{-1}) as the coverage increases from 0.1 to 0.6 ML. This observation strongly supports the formation of (4 × 2) islands in this region also. On Mo(100), therefore, the transition from the clean surface phase to the first H-stabilized phase is first order.

The situation is qualitatively different on W(100). At room temperature, the $\frac{1}{2}$-order beam, very faint and broad on the clean surface, sharpens rapidly and increases continuously in intensity as $\theta \rightarrow 0.28$. The ν_1 wavenumber undergoes a large and continuous frequency shift in this range from 1265 cm^{-1} at $\theta = 0.05$ to 1300 cm^{-1} at $\theta = 0.3$, as shown in fig. 28. A decrease of the dimer length of between 0.15 Å (eq. (4.2)) and 0.065 Å (eq. (4.3)) can therefore be inferred over this coverage range ($\Delta\theta = 0.25$). This observation is naturally reconciled with the $\frac{1}{2}$-order beam intensity measurements by invoking the formation of a homogeneous dilute H layer [336,337]. At very low coverages,

H polarizes the underlying W atoms along the ⟨10⟩ direction, leaving the rest of the surface displaced along the ⟨11⟩ direction. The strain field, developed around the W_2H moiety, affects the W–W dimer distance which depends therefore sensitively on the total H density. The observed frequency shift cannot be accounted for by the formation of constant density c(2 × 2) islands (with local coverage, say, $\theta = 0.5$) throughout the range $\theta = 0.05$ to 0.4, since there would be no mechanism to change the W–W dimer length with increasing coverage. If the H/W(100) is not perfectly homogeneous but contains clean and H-rich areas [339], then the H-rich domains must undergo a substantial and continuous local rearrangement (probably) due to large local coverage changes; such large local coverage changes, however, seem incompatible with island formation and growth.

Opting for the interpretation of a homogeneous surface, Prybyla et al. [336] propose that the difference in behavior of H on W(100) and Mo(100) is due to a difference in the substrate-mediated interaction. This interaction would arise from the coupling between substrate distortions induced by individual adatoms. The difference then would follow from the different elastic response of the two substrates. Comparison of surface phonon spectra, especially of the existence and location in k-space of soft phonons or near-instabilities for the clean surfaces, may help refine this picture.

4.1.4.4. Results for intermediate coverages. For the I($\sqrt{2} \times \sqrt{2}$) phase at $0.33 < \theta < 0.45$ on W(100), figs. 28 and 29 show that with increasing coverage the ν_1 mode around 1300 cm^{-1} shifts down in frequency and broadens while a new contribution around 1090 cm^{-1} appears (vertical arrow in fig. 29). This weak feature at 1090 cm^{-1}, already present at $\theta = 0.33$ (see fig. 4 of ref. [337]) and increasing in intensity in the $\theta = 0.35$ to 0.42 region, is attributed to H on unreconstructed parts of the W(100) surface. Of the various models proposed for the I($\sqrt{2} \times \sqrt{2}$) phase, the antiphase model with boundaries is the only one that can account for the presence of two distinct and rather sharp vibrational lines. The detection of the 1090 cm^{-1} line establishes that the antiphase boundaries are *unreconstructed* and of *finite size*. The continuous frequency shift and small broadening of the ν_1 mode around 1300 cm^{-1} indicate that the modulation is not a perfect square wave but incorporates a small relaxation of the dimer length at the edges of the reconstructed regions.

In contrast, for the ($y \times 2$) and ($z \times 2$) phases on Mo(100), a single absorption is observed. In the $y \times 2$ phase, the ν_1 wavenumber shifts continuously with coverage from 1220 cm^{-1} for $y = 5$ to 1210 cm^{-1} for $y = 4$, the width remaining constant and relatively sharp ($\sim$ 30 cm^{-1}). Since no other line is observed in this range, an upper limit of $\sim$ 10% of the total H coverage can be set for H adsorbed in a different local configuration (for a 30 cm^{-1} line width). Therefore, if an antiphase arrangement is operative, the boundaries are either infinitely narrow or little (< 10%) H adsorbs at these boundaries. In the

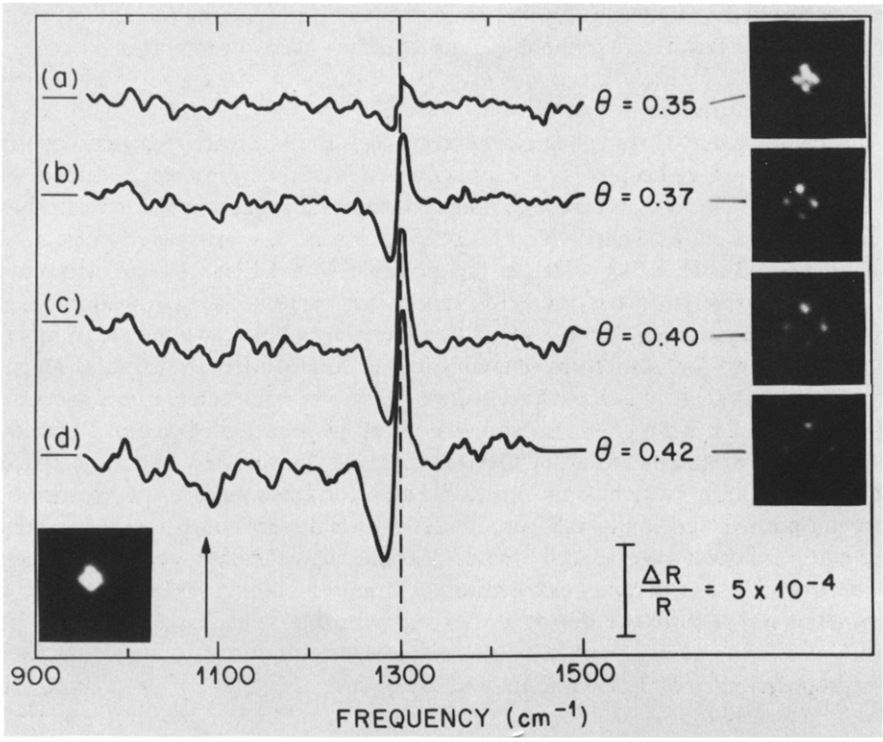

Fig. 29. Relative changes in the H-induced reflectance spectra, i.e. ratios of the reflectivity spectra obtained in the range $\theta = 0.35$ through 0.42 to that at $\theta = 0.33$. The $(\frac{1}{2},\frac{1}{2})$ beam of the reference surface ($\theta = 0.33$) is shown at the bottom left (note the beginning of the splitting). The $(\frac{1}{2},\frac{1}{2})$ LEED beams associated with each spectrum are shown on the right-hand side (from ref. [337]).

$c(2 \times 2) + (z \times 2)$ phase, the sharp line (~ 15 cm^{-1}) at 1270 cm^{-1} associated with the $c(2 \times 2)$ phase decreases in intensity with coverage, while a broader line (~ 30 cm^{-1}) moves continuously from 1245 cm^{-1} for $z = 2.75$ to 1236 cm^{-1} for $z = 3$. A number of mechanisms can account for these observations. At this time the available data cannot single out a particular mechanism.

In summary, this section has outlined the type of information that can be directly inferred from infrared absorption measurements of H on W(100) and Mo(100): H bonding configuration, estimate of W–W and Mo–Mo dimer-length variations, and surface homogeneity. Such knowledge is complementary to diffraction measurements (LEED, X-ray) which are not sensitive to H adatoms and from which the local atomic arrangement is not readily extracted. The present sensitivity of SIRS is adequate to detect weak vibrational modes associated with H on a number of metal surfaces. The level of information

obtained for the H/W and H/Mo systems is the best incentive to extend such studies to the far-infrared where heavier adatom–substrate vibrations occur.

4.1.5. Hydride phases on Si(100)

The study of hydrogen chemisorption on Si(100) by infrared spectroscopy is particularly useful because it exemplifies a number of important aspects of SIRS. First, it shows the power of polarized internal reflection spectroscopy to measure with equal sensitivity all components of the surface dipoles (see sections 2.2.2 and 3.2.1), which is not possible with EELS. Second, it points out that the line widths of the Si–H modes are narrower than for adsorbates on metals, requiring $\lesssim 1$ cm^{-1} resolution to resolve. Narrow lines are in fact a general feature for adsorbates on well-ordered semiconductor surfaces. Third, it emphasizes the necessity of accurate ab initio cluster calculations (section 2.4.2) to extract both chemical and structural information. Fourth, it beautifully demonstrates the value of SIRS to unravel complicated structures, such as hydride phases, which is an impossible task for other surface spectroscopies (including EELS). Finally, it is a reminder that H adsorption is the best model system because it can be well treated theoretically although it requires high experimental sensitivity (weak dynamic dipole moment). As such, it is a stringent test of both the theory and experiment that helps assess the value of both. All data analysis in this section is based on the derivations of, and uses the nomenclature of sections 2.1.2 and 2.2.2.

4.1.5.1. Structure of the Si(100)-(2×1)H surface. The exposure of the Si(100)-(2 × 1) surface to atomic hydrogen first leads to the development of a sharp, well-defined (2 × 1) LEED pattern before becoming a (1 × 1) pattern at saturation coverage. The general understanding of this phenomenon is that (a) the clean (100) surface reconstructs by forming dimers and (b) the addition of 1 monolayer of H saturates the dangling bonds of each dimer unit as shown in fig. 30. A (2 × 1) unit cell is maintained with one H per Si, i.e. 2 H per unit cell. There are therefore six vibrational modes associated with the structure, two of which involve the stretch of the Si–H bonds. Since the other four, involving the Si–H bend and frustrated translation, are too low in frequency to be detected with an internal reflection geometry, we focus on the two stretch modes occurring around 2100 cm^{-1}, from which accurate *structural* information can be learned [79].

A nominally flat Si(100) surface displays two domains rotated by 90° with (2 × 1) symmetry. Since the concentration of the two domains is equal, the surface is on average isotropic in two-dimensions and polarization studies cannot be performed efficiently. However, as pointed out in section 4.1.2 clean surfaces cut a few degrees off the (100) plane around the $\langle 0\bar{1}1\rangle$ axis give only one domain of (2 × 1) symmetry [298], as shown in fig. 21. Fig. 31 shows the resulting structure anticipated when H is added to such stepped surfaces. The

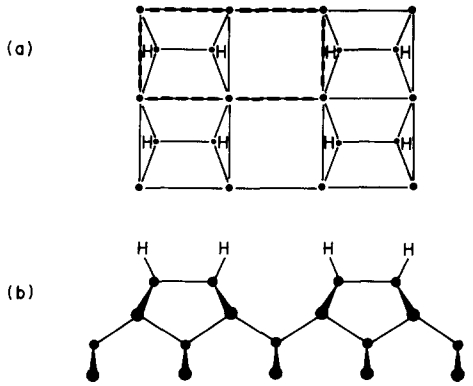

Fig. 30. (a) Top view and (b) side view of a portion of a uniform monohydride phase on Si(100) [or Ge(100)]. The resulting 2×1 unit cell is outlined in dashed lines. Dimerization of the top Si or Ge layer is depicted by reduction of the Si–Si (or Ge–Ge) distance (from ref. [30]).

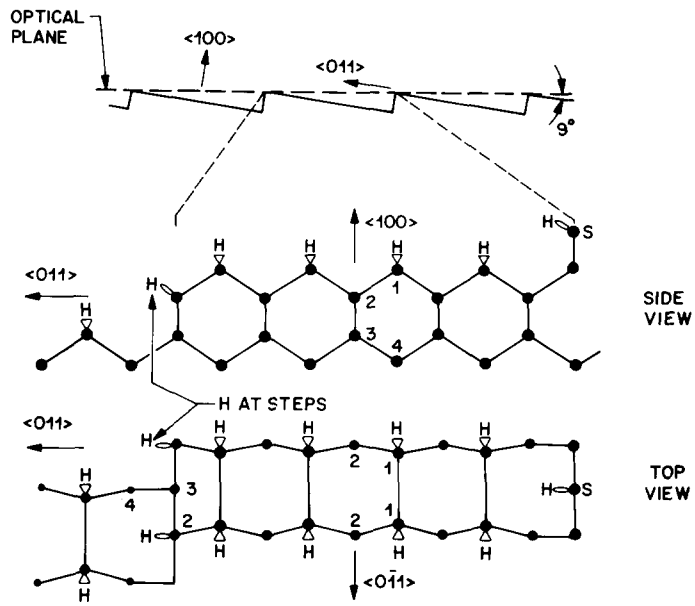

Fig. 31. Schematic representation of a vicinal surface cut at 9° from the (100) plane about the $\langle 0\bar{1}1\rangle$ axis, i.e. the optical plane with respect to which the probing electronic field vectors (E_x, E_y or E_z) are described makes a 9° angle with the (100) terraces. The atomic representation of the vicinal surface including one terrace and two steps is given below. The projection of H adsorbed at all available dangling bonds of the clean surface (assuming that the dimers are not broken) is also shown schematically (from refs. [79,308]).

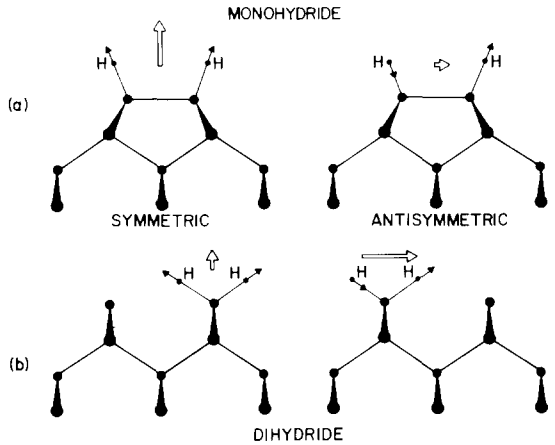

Fig. 32. Scale drawing of (a) the monohydride, and (b) the dihydride structures. The arrows (not to scale) represent the direction of H displacements (solid arrows) and the *polarization* (double arrows) of the two normal modes involving the stretching of Si–H bonds. The different magnitudes of the double arrows schematically indicate that the net dipole associated with each normal mode is different for the two structures, with $\mu_{\perp} < \mu_{\perp}$ for the monohydride and $\mu_{\parallel} > \mu_{\perp}$ for the dihydride (from ref. [30]).

importance of this geometry is that the components of the Si–H dielectric response can be associated with distinct modes: contributions to $\epsilon_{\langle 001 \rangle}$ come only from H adsorbed at steps while contributions to $\epsilon_{\langle 100 \rangle}$ and $\epsilon_{\langle 0\bar{1}1 \rangle}$ primarily come from perpendicular and parallel components of H adsorbed on terraces (see fig. 31). Fig. 32a shows that these modes are the symmetric (perpendicular to surface) and antisymmetric (parallel to surface) stretches of the "monohydride". Note that, unless the small perpendicular component of the mode associated with H at steps has a resonance at the same frequency as the symmetric stretch of the monohydride, its contribution to $\epsilon_{\langle 100 \rangle}$ can be sorted out. As shown in fig. 21a, the use of two samples oriented in orthogonal directions with respect to the probing radiation (cases I and II) makes it possible for s- and p-polarizations to probe (I) S_I: $\epsilon_{\langle 011 \rangle}$ and P_I: $\epsilon_{\langle 0\bar{1}1 \rangle}$ and $\epsilon_{\langle 100 \rangle}$, and (II) S_{II}: $\epsilon_{\langle 0\bar{1}1 \rangle}$ and P_{II}: $\epsilon_{\langle 011 \rangle}$ and $\epsilon_{\langle 100 \rangle}$. As a result, the three components of ϵ can be measured unambiguously.

Results of such measurements showed that the monohydride modes exhibit a resonance ($M_{\parallel}$) at 2087 cm^{-1} in $\epsilon_{\langle 0\bar{1}1 \rangle}$ and ($M_{\perp}$) at 2099 cm^{-1} in $\epsilon_{\langle 100 \rangle}$ at 300 K, while $\epsilon_{\langle 011 \rangle}$ is dominated by a strong resonance at 2087 cm^{-1} and much weaker contributions elsewhere in the spectrum [79]. Based on this knowledge, the data of fig. 33 show that, upon annealing to 625 K, *only* the resonances associated with the monohydride ($M_{\parallel}$ and $M_{\perp}$) on the terraces remain; all the resonances associated with H at steps disappear. To the extent that the monohydride, characterized only by two sharp modes with distinct

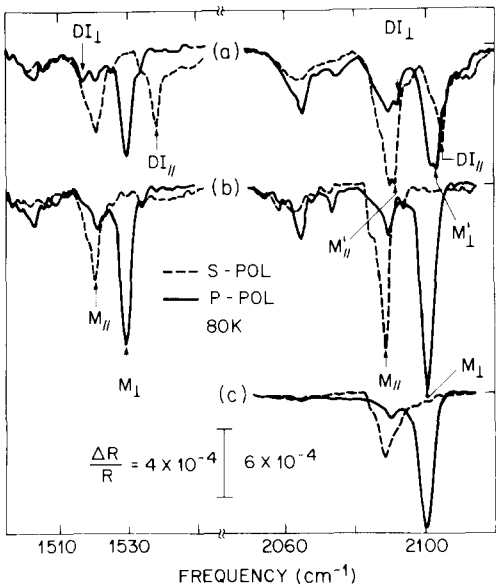

Fig. 33. Surface infrared spectra associated with (a) the (3×1) phase prepared by H saturation at 375 K, (b) the (2×1) phase obtained upon a 475 K anneal, and (c) the (2×1) phase obtained upon a 625 K anneal. On the left-hand side of the figure, spectra resulting from pure D exposures are shown. On the right-hand side of the figure, spectra resulting from pure H exposures are shown. The sample is cut 5° off the (100) plane. The s-polarization (dashed lines) has an electric field exactly along the $\langle 0\bar{1}1 \rangle$ axis. The p-polarization (solid lines) has components 5° off the $\langle 100 \rangle$ and $\langle 011 \rangle$ directions. The data are taken at 80 K resulting in narrower lines and a small (~ 3 cm^{-1}) blue shift from the room temperature frequencies (see section 4.3.1.2). The resolution is 0.5 cm^{-1} for the SiH region and 1 cm^{-1} for the SiD region (from ref. [341]).

frequencies and polarizations, is the most stable hydride on Si(100), it represents a *model* system which can be reproducibly prepared and for which a quantitative analysis is possible [7].

In this analysis, it is important to determine the origin of the frequency shift of the resonance in $\epsilon_z = \epsilon_{\langle 100 \rangle}$. As mentioned in section 2.3.1, it can arise from extended dynamical effects, i.e. inter-unit cell dynamical coupling. The resulting shift, $\Delta\tilde{\nu} \approx \tilde{\nu}_p^2/2\tilde{\nu}_0\epsilon_{\infty z}$ will be detected if it is larger than the spectral resolution, $\Delta\tilde{\nu} \gtrsim 0.5$ cm^{-1}. A shift between the antisymmetric (parallel) and symmetric (perpendicular) modes can also arise because of *local* dynamical effects. The latter phenomenon is sometimes referred to as "chemical" shift because it involves the coupling of normal modes *within* the unit cell and is therefore a signature of the particular chemical bonding within the cell. The two effects must be distinguished if, as is the case for this system, the data are compared to cluster calculations performed on a *single* unit cell.

Experimentally, the inter-unit cell dynamical coupling (extended) can be

measured by means of isotopic mixture experiments. As more D is substituted for H at constant coverage, the Si–H normal modes will approach their "isolated frequency" value, i.e. the value devoid of dynamical coupling. If all the splitting is due to extended coupling, then it should decrease to zero as the D concentration increases. If, on the other hand, it is due to local effects (intra-unit cell), the splitting will remain constant as long as enough unit cells are occupied purely by H. Then, as one of the H is replaced by D, the remaining H will be characterized by a new vibrational frequency, usually falling in between that of the two normal modes. Results of such isotopic mixture and coverage dependence experiments showed [79] that the extended dynamical coupling only accounts for $\sim 3\ \mathrm{cm}^{-1}$ for H and $\sim 2\ \mathrm{cm}^{-1}$ for D. The rest of the splitting, $9\ \mathrm{cm}^{-1}$ for H and $7.5\ \mathrm{cm}^{-1}$ for D, is due to local effects as confirmed by the appearance of a new isolated frequency for very low relative H concentration at $\sim 2092\ \mathrm{cm}^{-1}$ (i.e. in between the wavenumbers of the parallel and perpendicular components).

For a surface cut 9° from the (100) plane, the numbers of terrace and step sites are 5.4×10^{14} and $1.36 \times 10^{14}\ \mathrm{cm}^{-2}$, respectively. Since the Si–H effective mass ($m^* \approx 1$ amu) and the resonant frequencies ($\tilde{\nu}_{0\parallel} = 2087\ \mathrm{cm}^{-1}$, $\tilde{\nu}_{0z} = 2096\ \mathrm{cm}^{-1}$) are known, we are left with three unknowns: $e_\parallel^*$, $e_\perp^*$ and $\epsilon_{\infty z}$. The data provides us with three independently determined quantities:

$$\int \epsilon_{\langle 011\rangle}\, \mathrm{d}\tilde{\nu}$$

from s-polarization in configuration II,

$$\int \frac{\epsilon^{v^2}}{\epsilon'^2_{\langle 100\rangle} + \epsilon''^2_{\langle 100\rangle}} \epsilon''_{\langle 100\rangle}\, \mathrm{d}\tilde{\nu} \approx \frac{1}{\epsilon^2_{\infty z}} \int \epsilon''_{\langle 100\rangle}\, \mathrm{d}\tilde{\nu}$$

from p-polarization in configuration I, and $\Delta\tilde{\nu} \approx \tilde{\nu}_{\mathrm{p}}^2 / 2\tilde{\nu}_0 \epsilon_{\infty z}$ from isotopic mixture experiments. Fitting the data with the measured $\Delta\tilde{\nu} = 3\ \mathrm{cm}^{-1}$ yields $e_\parallel^*/e \approx 0.03$, $e_z^*/e \approx 0.05$ and $\epsilon_{\infty z} = 1.4$. The unscreened ratio

$$r \equiv \int \epsilon''_{\langle 0\bar{1}1\rangle}\, \mathrm{d}\tilde{\nu} \Big/ \int \epsilon''_{\langle 100\rangle}\, \mathrm{d}\tilde{\nu}$$

can then be obtained, $r \approx 0.35 \pm 0.1$. We note that the large error in r is due mostly to the uncertainty in $\epsilon_{\infty z}$. Here $\Delta\tilde{\nu}$ is used to determine $\epsilon_{\infty z}$. Because it is so small and known only within $0.5\ \mathrm{cm}^{-1}$, it leads to a $\pm 30\%$ error in r. In summary, the local (or "chemical") splitting is $+9\ \mathrm{cm}^{-1}$ for H, $7.5\ \mathrm{cm}^{-1}$ for D and the unscreened intensity ratio is $r = 0.35 \pm 0.1$.

In the cluster calculations (see section 2.4.2), a large cluster (Si_9H_{14}) was used to calculate the geometry by minimizing the cluster total energy with respect to bond lengths and bond angles, as shown in fig. 34a. From this geometry, the vibrational frequencies and intensities could be calculated using a smaller cluster (Si_2H_6), as shown in fig. 34b. Although the absolute value of

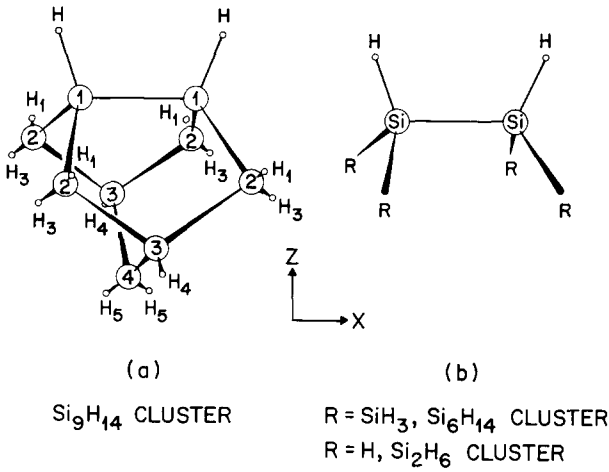

Fig. 34. Cluster models used to model the Si(100)-(2×1)H unit cell. The silicon atoms (large circles) and hydrogen atoms (small circles) are numbered according to the layer to which they belong. The twelve atoms representing the truncated cluster bonds in (a) are shown with shorter bond lengths for clarity. The details of the ab initio cluster calculations are given in section 2.4.2 (from ref. [79]).

vibrational frequencies is too high by about 10%, it was found that the splitting between similar normal modes (e.g. symmetric and antisymmetric stretch modes) could be calculated accurately (within a few cm^{-1}). The results for the monohydride and monodeuteride gave a symmetric stretch frequency 11 and 9 cm^{-1}, respectively, higher than the antisymmetric stretch frequency, in good agreement with the data. The calculated intensities associated with each normal mode gave the ratio:

$$\mu_{\parallel}/\mu_{\perp} = 0.59, \text{ i.e. } r = (0.59)^2 = 0.35,$$

again in good agreement with the data.

In closing, it is important to stress the limitations of SIRS if no theoretical input is available. For instance, if $\Delta\tilde{\nu}$ is too small to be observable, then $\epsilon_{\infty z}$ cannot be determined unless either $\mu_{\parallel}$ or $\mu_{\perp}$ is known independently. Unfortunately, the bare dipole moments are rarely accessible experimentally. As a result, the geometry (bond length and angle) cannot be obtained by SIRS experiments alone. In the case of the monohydride, the geometry was determined by cluster calculations and then used to evaluate quantities accessible to the experiment. In particular, the angle made by the Si–H bond with the surface normal was calculated to be $\alpha = 20°$. Such a value could *not* be obtained from the data alone, i.e. using $\tan\alpha = \mu_{\parallel}/\mu_{\perp}$, because the calculations showed that the back projections of $\mu_{\parallel}$ and $\mu_{\perp}$ along the Si–H bond do not give the *same* value for the two dynamic dipole moments. Experimentally,

we would have gotten $\tan \alpha = 0.59$ (i.e., $\alpha = 30°$) if we had assumed that the two normal modes had the same dynamic dipole moment.

4.1.5.2. Nature of the H-saturated Si(100) surfaces. Despite its limitations in determining precise adsorbate geometries, SIRS is a powerful tool to unravel complex structures at surfaces. The H-saturated phases on Si(100) [and Ge(100)] are good examples because both surfaces display a number of co-existing phases which cannot be detected by other probes such as EELS due to poor frequency resolution [340]. We refer the reader to refs. [7,341] for details of the summary presented here.

Let us consider the Si(100) [and Ge(100)] surface saturated with H atoms at room temperature. H/Si(100) displays a reasonably sharp (1×1) LEED pattern while H/Ge(100) displays weak $\frac{1}{2}$-order beams, remnant of a (2×1) LEED pattern. Prior to the SIRS work, the accepted view was that Si(100)-(1×1)H was made up of a uniform *dihydride* phase with all the dimers broken and that the Ge(100)-(2×1)H had only partial dihydride coverage. The initial key findings of SIRS were that at saturation (1) the strong modes ($M_{\parallel}$ and $M_{\perp}$ in fig. 33) characteristic of *monohydride* were still present among other absorption features and, (2) the Ge(100)-(2×1)H was characterized by a spectrum identical to that obtained for lower coverages for which a very sharp (2×1) pattern is present. Thus, it was apparent that the monohydride structure was an important part of the H-saturated Si(100) surface and the *dominant* part of the Ge(100) surface.

The next important observation was that a Si(100) surface saturated with H atoms while maintained at 380 K displayed a sharp (3×1) LEED pattern; yet it was characterized by an IR spectrum *identical* to that of the Si(100)-(1×1)H surface, prepared by H saturation at room temperature. These two observations pointed to the fact that the Si(100)-(1×1)H surface was in fact a phase with local (3×1) arrangement with no long-range order. The problem was then reduced to interpreting the SIR spectra associated with the well-ordered (3×1) phase only. As for the Si(100)-(2×1)H case, single domain structures could be prepared on crystals cut vicinal to the (100) plane; thus, polarized SIRS could be profitably used. The data in fig. 33 show the spectra associated with the (3×1) phase and phases obtained and upon annealing. They were taken on a sample at 80 K because the bands are sharper (see section 4.3.1.2) so that different spectral components could be better resolved.

Annealing the sample to 475 K (fig. 33b) produced two very well defined changes: (1) the LEED pattern changed from a (3×1) to a (2×1), and (2) the IR spectrum displayed the loss of two lines only, labelled $DI_{\perp}$ and $DI_{\parallel}$ in fig. 33a. Intermediate annealing confirmed that the intensity ratio of these two lines remained constant as they became weaker. Analysis of the data shows that: (1) the mode perpendicular to the surface is now at lower frequency than that parallel to the surface, i.e. $\Delta_H \equiv \tilde{\nu}^0_{\langle 100 \rangle} - \tilde{\nu}^0_{\langle 0\bar{1}1 \rangle} = -12.5\ \text{cm}^{-1}$ for H, (2)

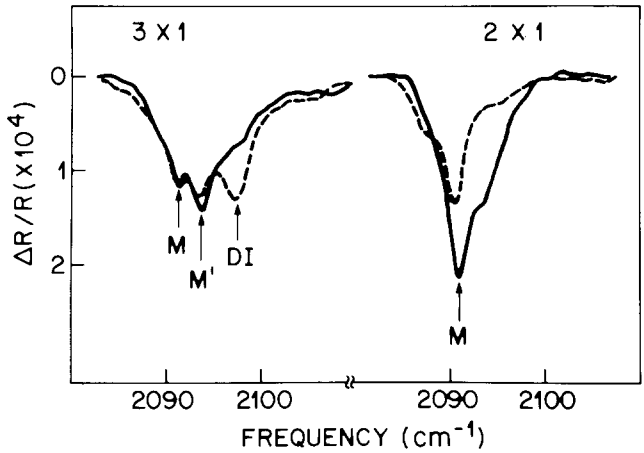

Fig. 35. Surface infrared spectra of the SiH stretch region obtained upon saturation exposure of an isotopic mixture at 375 K [(3×1) phase] and after a subsequent 475 K anneal [(2×1) phase]. Conditions are therefore identical to those yielding figs. 33a and 33b except that hydrogen represents only 7.5% of the total saturation coverage (measured from IR intensities). The data are taken at room temperature on a Si(100) 5° sample with the s-polarization (dashed lines) and p-polarization (solid lines) defined as in fig. 30. The resolution is 1 cm^{-1}. M, M′ and DI correspond to the isolated frequencies of pure monohydride, monohydride with a neighboring dihydride and dihydride, respectively (from ref. [341]).

The magnitude of the splitting between these two modes is larger for deuterium, i.e. $\Delta_D = -21$ cm^{-1}. (3) The intensity of $DI_{\parallel}$ is substantially larger than that of $D_{\perp}$, i.e. the unscreened ratio is $r \equiv I(DI_{\parallel})/I(DI_{\perp}) \approx 3$ assuming $\epsilon_{\infty z} \approx 1.4$. The unambiguous assignment of these lines to the dihydride structure (fig. 32b) relied again on cluster calculations [341] and isotopic mixture experiments. The theoretical predictions for the dihydride structure were $\Delta_H = -9$ cm^{-1}, $\Delta_D = -22$ cm^{-1} and $r \approx 3$. In addition, the calculations showed that the "isolated" frequency of the dihydride structure should be $+7$ cm^{-1} *higher* than the isolated frequency of the monohydride structure, and $+5$ cm^{-1} for the corresponding isolated deuterium modes. The results of isotopic mixture experiments fig. 35 clearly show that DI is 6.5 cm^{-1} higher in frequency than M. For this dilute H concentration, no lines were observed at $DI_{\parallel}$ and $DI_{\perp}$ or $M_{\parallel}$ and $M_{\perp}$; only the isolated frequencies remained, beautifully confirming that both the dihydride and monohydride structures are simultaneously present in the (3 × 1) phases.

The excellent resolution (1 cm^{-1}) and S/N of the data make it possible to resolve a small shift (~ 2 cm^{-1}) of the wavenumber of the monohydride modes whenever the dihydride is observed (see M′ in fig. 35 and $M'_{\perp}$ in fig. 33a). As discussed at the end of ref. [341], this small shift arises from small back-bond relaxation of the monohydride structure caused by the presence of

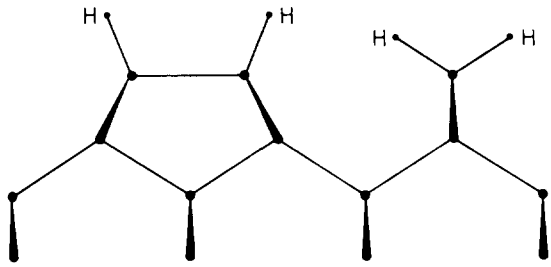

Fig. 36. Model (drawn to scale) of the 3×1 unit cell. The top layer Si and H atoms are all along the $\langle 0\bar{1}1\rangle$ axis, i.e. parallel to the step edges for the vicinal samples (from ref. [341]).

a neighboring dihydride. This observation is taken as supporting evidence that a dihydride structure always forms right next to a monohydride structure as shown in fig. 36. In fact, this model accounts for all observations to date, including the absolute coverage measurements of Feldman et al. [342].

The other unlabelled features in the spectra of figs. 33a and 33b were shown to arise from H (or D) at steps and defects. The presence of these features in Figs. 32a and 32b indicates that H is more strongly bound at steps and defects than in a dihydride configuration. However, the removal of these features upon annealing to 625 K shows that they are less stable than H in a monohydride configuration [7,308]. The results are summarized in table 7.

Based on the above semi-quantitative knowledge of the various hydride phases on Si(100) and their associated IR spectra, Chabal [7] carried out IR studies on the H/Ge(100) system for which no calculations were performed. Fig. 37 shows that the IR spectrum is dominated at all coverages (except for $\theta \lesssim 0.1$ ML) by two modes at 1979 and 1991 cm^{-1}, polarized parallel and perpendicular to the surface respectively. This observation, along with the (2×1) LEED pattern and *the absence of an absorption mode in the 750–1000 cm^{-1} region* (expected for the scissor mode of the dihydride structure) for all coverages investigated, indicates that the main hydride phase is monohydride, even at saturation coverage. Dihydride is *not* formed on Ge(100) for exposures up to ~ 5 L atomic hydrogen exposure, for samples maintained at tempera-

Table 7
H-stabilized phases on Si(100)

Formation temp. (K)	Desorption temp. (K)	LEED pattern	Structure
600	700	2×1	Monohydride (M)
450	500	2×1	M + H at steps
380	425	3×1 (ordered)	M + dihydride (D) + H at steps
300	425	1×1 (disordered)	M + D + H at steps

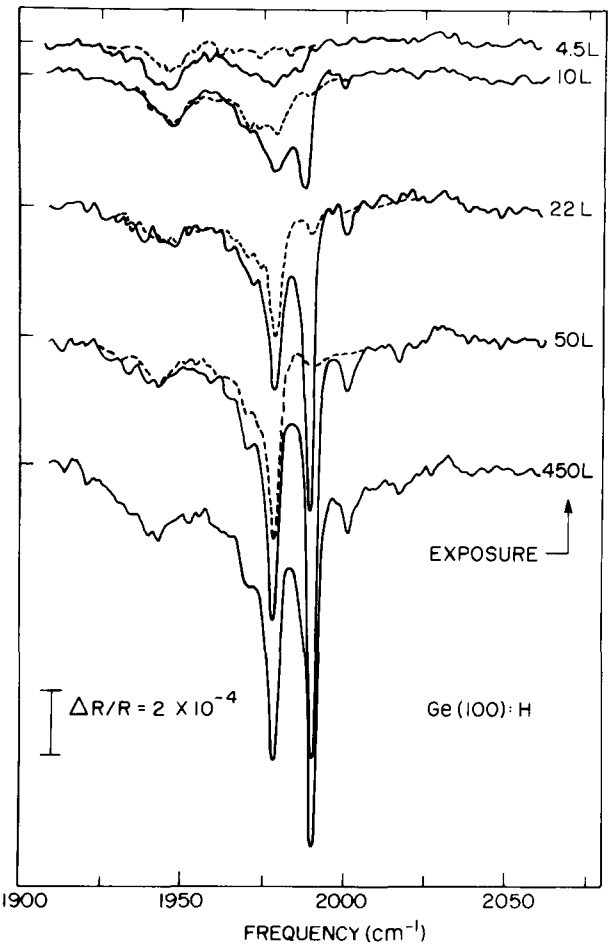

Fig. 37. Surface infrared spectra as a function of H coverage on a nominally flat Ge(100) surface at room temperature. The exposures are quoted in terms of *molecular* hydrogen exposures, using a 2000 K tungsten ribbon (1×2 cm^2) placed 4 cm in front of the sample to dissociate the molecular hydrogen. Atomic hydrogen exposures are approximately a factor of 100 lower. The dashed lines represent the results for s-polarization and the solid lines for p-polarization. The resolution is 2 cm^{-1}. There is not observed absorption for any exposure up to 450 L in the 750–1000 cm^{-1} region where the noise level is approximately 5×10^{-5} per reflection (from ref. [7]).

tures slightly above room temperature [343]. As expected, the faint (2×1) LEED pattern at saturation shows that the (2×1) unit cell has a poor *long-range* arrangement due to etching of the surface by H atoms.

For the purpose of this review, it is instructive to point out that although the splitting, $\Delta_H = 12$ cm^{-1}, observed on Ge is identical to that of the monohydride on Si(100), its origin is quite different. Isotopic mixture experi-

ments show that the two modes on Ge *continuously* shift with increasing D concentration at saturation coverage to the value of 1980.5 cm^{-1}. The extended dynamical interactions (inter-unit cell), therefore, appear to be dominant for this system [7], in contrast to Si(100)-(2 × 1)H.

4.2. Surface electronic absorption

Surface electronic absorption is an intrinsic part of SIRS because any change in electronic absorption between the reference surface and the surface under study will appear in the recorded SIR spectrum. For instance, any absorption arising from the presence of surface state on the clean surface and quenched by the adsorption of the molecule under study will manifest itself as a "negative absorption" feature in the $\Delta R/R$ spectrum (i.e. $R/R^0 > 1$ over the range of electronic absorption). Traditionally, such electronic absorption has been ignored in the vibrational studies because it is very broad compared to the sharp vibrational bands and often linear in the narrow frequency range of interest. Thus, a linear background subtraction is performed without even being mentioned in published papers. However, as briefly discussed at the end of section 2.2.1 for metals and in section 3.2.2 for semiconductors, any absorption arising from electronic transitions in the near-surface region of the substrate can be quantified as well as the vibrational absorption arising from molecules above the surface plane. In fact, the understanding of the broad-band electronic absorption is in many cases necessary to determine surface structures and adsorbate–substrate dynamics. It is therefore natural to discuss electronic absorption measurements between the sections on surface vibrational structures (section 4.1) and surface vibrational dynamics (section 4.3).

In this section, we present first the detailed studies of surface electronic absorption on the cleaved Si(111)-(2 × 1) surface that were a critical test of an unconventional new structural model for this surface. Although this work concentrates on the clean surface, using the adsorption of oxygen only to remove the clean surface electronic structure, it should be kept in mind that the electronic structure can be modified differently by different adsorbates. Therefore, careful monitoring of such absorption in all vibrational studies of semiconductor surfaces is required to gather additional information. We then summarize new SIRS results on the surface electronic absorption of the clean W(100) surface, which complement earlier photoemission and field emission studies, as well as theoretical calculations. Furthermore, these results are important to understand the dynamical results for W(100)-(1 × 1)H presented in section 4.3.2.2.

4.2.1. Semiconductors: clean Si(111)-(2×1)

The (111) surface of Si, obtained by cleaving, displays a sharp (2 × 1) LEED pattern [344], and has been studied intensively for more than two

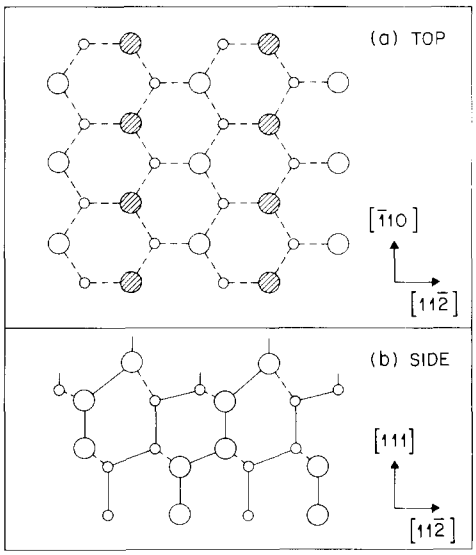

Fig. 38. Buckling model for the Si(111)-(2×1) surface. (a) Top (111) view with the hatched atoms raised. (b) Side ($\bar{1}$10) view (with permission from ref. [41]).

decades. The reader is referred to the review by Olmstead [41] for a history on this challenging surface. Briefly, an accepted model prior to 1981 was the "buckling model" [345] in which alternate rows of surface atoms are raised and lowered (fig. 38). In 1981, however, Pandey [346] suggested that the surface atoms could rearrange their bonding so that one half of the dangling bonds are effectively shifted to former second layer atoms, allowing dangling-bond orbitals to be located on nearest neighbors (fig. 39). This rearrangement allows the formation of π-bonds along the resultant chains of atoms, shown as a double line in fig. 39a. In this model, the gain in energy from delocalization of the dangling-bond orbitals (along the chains) is the dominant term stabilizing the surface reconstruction.

Interestingly, Pandey was led to re-examine the buckling model because he was not able to reconcile the finding of a semiconducting surface (0.45 eV excitation energy) by SIRS [347] with the features of surface-state energy bands observed by polarization-dependent angle-resolved photoemission [348]. Furthermore, later *polarization* dependent SIRS studies of the Si(111)-(2 × 1) surface were in fact key in ruling out the buckling model and confirming the π-bonded chain model. The series of these critical SIRS experiments is therefore summarized below.

Surface-state optical absorption by Si(111) and Ge(111) has been measured by many different techniques: internal [347,349–351] and external [352–356] reflection spectroscopy, ellipsometry [357–359], surface photovoltage [360],

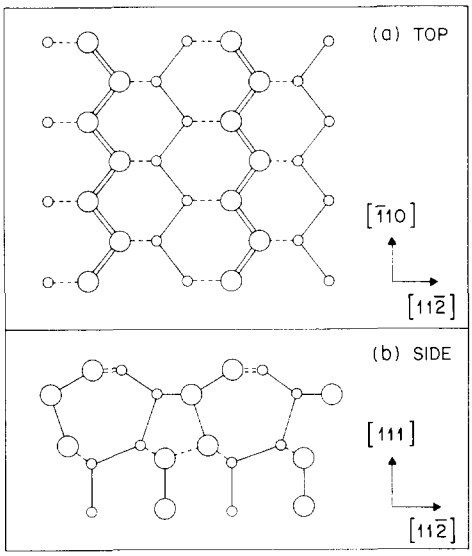

Fig. 39. π-bonded chain model for Si(111)-(2×1) surface. (a) Top (111) view. (b) Side ($\bar{1}$10) view. This figure does not include a possible dimerization or buckling of the chain (with permission from ref. [41]).

surface photoconductivity [361], photothermal displacement spectroscopy [232,233,362], and even non-linear laser spectroscopy [363]! The same optical transitions have also been excited by EELS [364]. We focus here on the reflection [347,350–356] and photothermal displacement [232,233,362] results on Si(111)-(2 × 1).

Using an MIR geometry, Chiarotti et al. [347] established early on the presence of a strong surface optical absorption at 0.45 eV. Later, by means of external reflection, they extended the range of this study to above the indirect gap, uncovering a broad and weaker surface absorption band between 1.0 and 3.5 eV [355]. Although these studies did not investigate the polarization dependence of the absorption, they were sufficient to cast doubts on the buckling model [346]. The motivation for polarized studies came from Del Sole and Selloni's prediction that, for the Pandey π-bonded chain model, the optical absorption arising from transitions between the bonding and anti-bonding orbitals of the π-bonded chains is strongest for light polarized *parallel* to the chains (i.e. along the $\langle\bar{1}10\rangle$ axis, see fig. 39) [365]. In contrast, the buckling model shown in fig. 38 would give a maximum absorption for light polarized *perpendicular* to the $\langle\bar{1}10\rangle$ axis.

Two studies were performed to test the model, an external reflection absorption experiment by Chiaradia et al. [354] and a photothermal displacement spectroscopy (PTDS) study by Olmstead and Amer [232,233]. The results are shown in figs. 40 and 41. In the reflection experiment, the radiation is

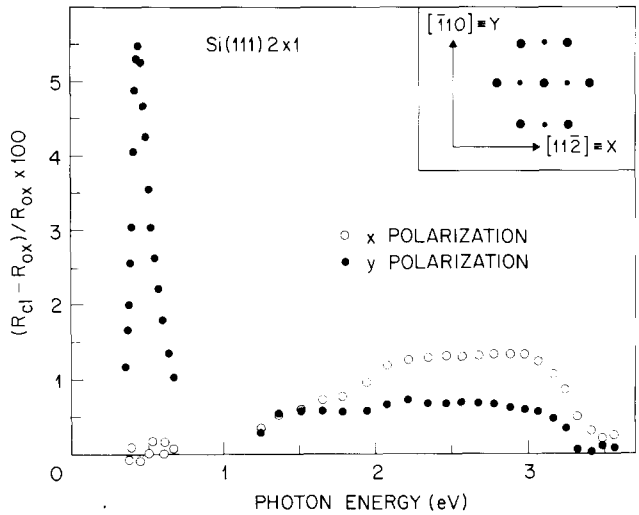

Fig. 40. Si(111)-(2×1) differential reflectance spectra taken at normal incidence with polarization parallel (solid circle) and perpendicular (open circle) to the reconstruction direction. The inset represents a sketch of the LEED pattern with integer and half-order beams and the main crystallographic directions in the (111) plane. The strong peak at 0.45 eV has a different dependence than the broad band centered at 2.5 eV (with permission from ref. [356]).

normally incident on the surface (i.e. E-field parallel to the surface) with the polarization continuously rotated from $\boldsymbol{E} \parallel \langle \bar{1}11 \rangle$ to $\boldsymbol{E} \parallel \langle 11\bar{2} \rangle$. In fig. 40, the differential reflectivity (reflectance) is plotted for the two extreme polarizations. The absorption at 0.45 eV is maximum for $\boldsymbol{E} \parallel \langle \bar{1}10 \rangle$ and falls to zero as $\boldsymbol{E}$ approaches the $\langle 11\bar{2} \rangle$ direction. The broad peak around 2.5 eV has a different polarization dependence than the strong peak at 0.45 eV. In the PTDS experiment, the absorption at 0.46 eV is again clearly maximum for $\boldsymbol{E} \parallel \langle \bar{1}10 \rangle$. Both techniques were able to produce a polar plot of the polarization dependence of this surface absorption band, an example of which is shown in fig. 42. A qualitative analysis of such a plot made it possible to support the Pandey model and rule out all the other models, particularly the buckling model. The weaker polarization dependence of the broad absorption band centered at 2.5 eV (opposite to that of the sharp peak at 0.45 eV) was also explained in the context of the π-bonded chain model [365]. Similar results and conclusions were obtained for the cleaved Ge(111)-(2 × 1) surface [347,349,355,232,233,362]. In both cases, the polarization capability of both reflection and photothermal deflection spectroscopies was crucial. These data constitute one of the strongest indications to date in favor of the π-bonded chain model. We refer the reader to sections 3 and 6.2 of Olmstead's review [41] for a thorough comparison of the polarization dependence with theory.

In closing, we point out that an analysis of the temperature dependence of

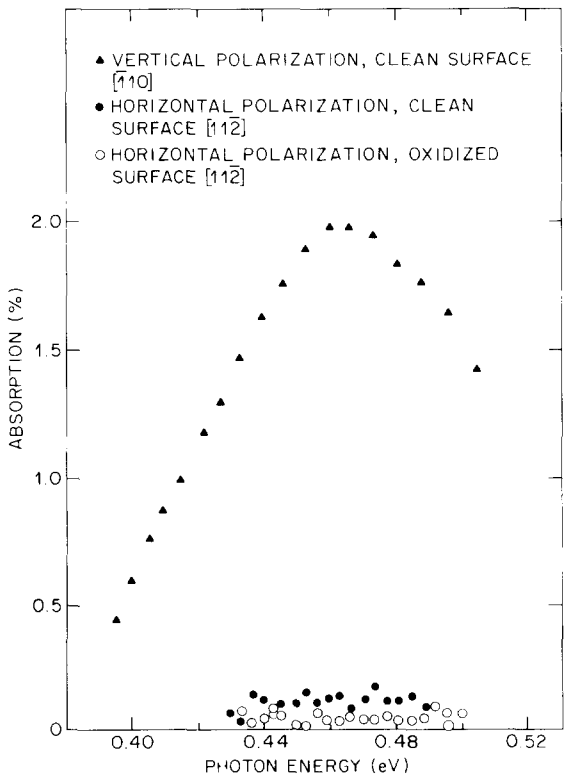

Fig. 41. Si(111)-2×1 surface-state absorption spectrum obtained by photothermal displacement spectroscopy. Saturation oxidation was obtained after ~1 h at 10^{-7} Torr oxygen to use as reference (with permission from ref. [233]).

the surface state optical absorption was also performed to investigate the electron–phonon interactions at the Si(111)-(2 × 1) and Ge(111)-(2 × 1) surfaces and the kinetics of the annealing phase transitions from a (2 × 1) to a (7 × 7) structure on Si(111) and from a (2 × 1) to a (2 × 8) structure on Ge(111) [232,362]. Since the optical absorption is a very local probe of the surface structure, as the absorption center contains at most a few atoms, it is a complementary tool to LEED and other diffraction techniques to study the kinetics of surface phase transitions. In fact, the ability to monitor phase transitions with laser techniques (with PTDS, for example), i.e. with good time resolution (< 1 μs), is crucial for surface kinetics and is emphasized here because it will not be discussed in section 4.4.

4.2.2. Metals: clean W(100)

Electromagnetic radiation is partially absorbed upon reflection off a metal surface because the metal is not perfect (i.e. its conductivity is not infinite).

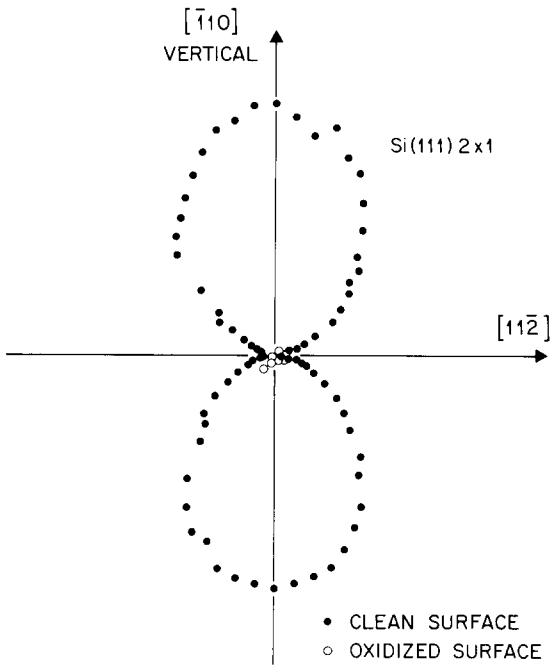

Fig. 42. Polarization dependence of peak surface absorption (0.468 eV) for Si(111)-(2×1) taken with photothermal displacement spectroscopy. Open circles are data points taken after oxidation of the cleaved surface. Similar results are found with reflectivity (see fig. 2 of ref. [354]) (with permission from ref. [233]).

This phenomenon is even more intuitive if we think of the emissivity of metals [164]. Such broadband absorption (or emission) is due to either free carrier scattering (FCS) or optical transitions (intra- or interband) within the optical skin depth. However, it has long been recognized that changes of the surface itself lead to changes in electronic absorption. Again, these effects may arise from modification of the surface electronic structure, altering the absorption by direct optical transitions, or of the surface scattering of the conduction electrons, usually described by the Fuchs' specularity parameter p, where $p = 1$ for specular and $p = 0$ for diffuse scattering [366]. For instance, resistivity measurements of very thin films as a function of gas adsorption have made it clear that structural and chemical changes occurring at the outermost layer can yield substantial changes in the resistivity [367–369]. It is therefore not surprising that substantial variations in the broadband reflectivity take place upon gas adsorption. These variations are reflected to a varying degree in the measured reflectance of all systems studied. Yet, it has been largely ignored so far.

For the H/W(100), however, Anderson et al. [370] and Restorff and Drew [371] noticed large changes in their reflectance spectra (0.6 to 6 eV) as a function of H coverage, which they attributed mostly to interband transitions that are produced or quenched by H chemisorption. Recently, Riffe et al. [372,373] have carried out a thorough study in the 1000 cm^{-1} region (0.125 eV) of H/W(100) using surface electromagnetic wave spectroscopy (SEWS). All these studies conclude that the clean W(100) surface is characterized by surface state absorption bands. In particular, Riffe et al. [372] invoke the presence of a 0.4 eV intrinsic surface state on the clean W(100) to explain the large changes they observe in the SEW absorption for $\theta < 0.42$ ML ($\theta = 2$ ML at saturation). The result of their study, restricted to the 1000 cm^{-1} region, is shown in fig. 43, where the measured change in α_{SEW} (see section 3.1.2) is plotted as a function of H coverage. Clearly, $\alpha(1033\ cm^{-1})$ decreases rapidly as $\theta \rightarrow 0.42$ ML. Since earlier photoemission [374–377] and field emission [378] studies have shown that a sharp surface state centered between 0.35 and 0.4 eV below E_F is completely quenched by 0.35 ML of hydrogen, Riffe et al. associate the decreasing SEW absorption to the disappearance of this surface state, the absorption of which is broad enough to give a substantial contribution at 1032 cm^{-1} (0.128 eV). They note that the Ic(2 × 2) phase obtained at $\theta = 0.42$ ML has the lowest SEW absorption in the 1000 cm^{-1} region and is therefore a good reference phase to examine the electronic absorption throughout the whole coverage range ($0 \rightarrow 2$ ML).

A similar study using *broadband* IRRAS was performed by Reutt et al. [379] and shows that, indeed, the Ic(2 × 2) surface is characterized by the highest reflectivity (lowest absorption) throughout the frequency range investigated (800–4000 cm^{-1}). They argue that, since this phase is well-ordered and devoid of surface state absorption, it is in fact the best reference phase to use for the broadband analysis of the reflectance spectra throughout the coverage range $\theta = 0$ to 2.0 ML. The result of the broadband IRRAS study for the clean W(100) at room temperature is shown in fig. 44, where the measured reflectance, using the Ic(2 × 2) phase as a reference, is plotted versus frequency. In these experiments, care was taken to maintain the sample temperature constant during the runs because the electronic absorption is a strong function of temperature [380]. The clean W(100) surface clearly exhibits a substantial broadband absorption with a maximum ($\Delta R/R \approx 0.7\%$) at 0.36 eV (2900 cm^{-1}) indicated by the double arrow labelled S.S.

This absorption is attributed to electronic transitions from filled surface states to empty states (above E_F) of the clean surface. Its width (~ 2000 cm^{-1}) is consistent with the 0.3 eV wide feature observed at 0.35 eV in field emission [378], which is rather narrow for an electronic state. It suggests that such states involve primarily d-electrons. Such localized electrons exhibit a small dispersion, resulting in narrow absorption profiles. Furthermore, as noted in section 2.2.1 (eq. (2.21)), for p-polarized radiation incident at $\theta \approx 85°$,

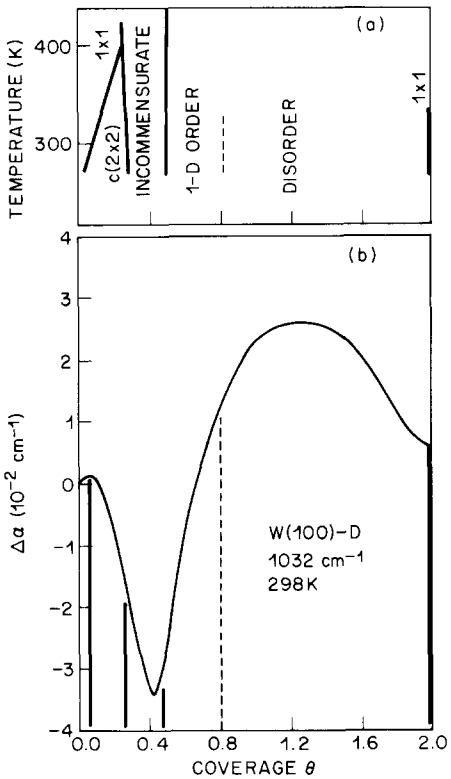

Fig. 43. (a) $T-\theta$ phase diagram determined by LEED (see fig. 26a). (b) Change in the SEW absorption, α_{SEW}, as a function of D coverage at 298 K and for a laser frequency of 1032 cm^{-1}. The coverage is determined from partial coverage thermal desorption assuming that $\theta = 2.0$ ML at saturation. The sharp dip occurs for the Ic(2×2) phase while the broad maximum is observed around 1.4 ML for the broad disordered "1×1" state (with permission from ref. [372]).

only electronic transitions involving the tangential component of the electric field are excited. Consequently, the surface state absorption must have xy or x^2-y^2 symmetry. The nature of the final state is obtained by invoking spin conservation and recognizing that ~ 0.1 eV radiation can only produce intraband transitions. The infrared absorption is therefore a result of electron–hole pair generation within surface states of d_{xy} or $d^2_{x^2-y^2}$ symmetry.

First principle calculations [381,382] and recent photoemission data [377,383,384] have considered in detail the origin of the surface states at $\bar{\Gamma}$ along the $\bar{\Sigma}$ line. In particular, the self-consistent scalar-relativistic linear-augmented-plane-wave calculations of Mattheiss and Hamann, including spin–orbit coupling, show the presence of strong surface states in the vicinity of E_F with x^2-y^2 symmetry along the $\bar{\Sigma}$ line (see figs. 6a and 9b of ref.

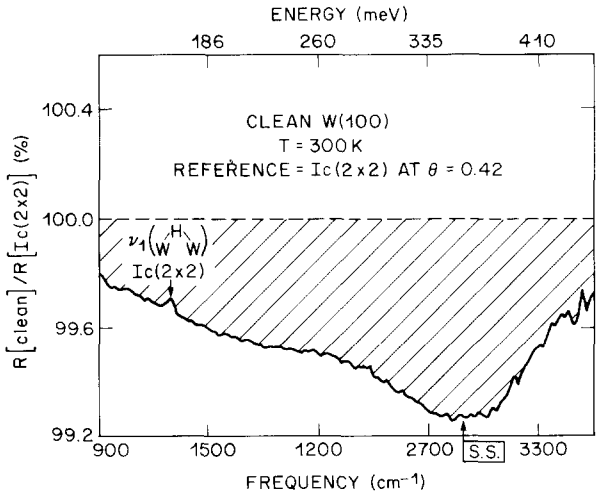

Fig. 44. Broadband reflectance absorption spectrum associated with the clean W(100) surface. The data were recordered at 300 K, using the H-induced Ic(2×2) phase as a reference ($\theta = 0.42$ ML). The data acquisition time is 10 s per spectrum and the resolution 16 cm^{-1}. The broadband peak around 2900 cm^{-1} at the point labelled S.S. corresponds to an absorption of the clean W(100) surface. The sharper, inverted peak at 1290 cm^{-1} corresponds to the ν_1 vibrational absorption of the reference phase, the Ic(2×2) (from ref. [379]).

[382]). The broad absorption in fig. 44 is therefore attributed to intraband transitions associated with these $d_{x^2-y^2}$ bands.

The excitation of these intraband transitions does not occur in a specular EELS experiment. Indeed, no broad feature similar to the infrared absorption shown in fig. 44 is present in EEL spectra of the clean W(100) surface [60,61,385–387]. The reason for this discrepancy is that specular EELS probes the ϵ_z component of the surface response [31] for losses both above and below the surface plane, in contrast to p-polarized SIRS that is sensitive only to $\epsilon_{x,y}$ for absorption below the surface plane of a *metallic* (large $|\epsilon|$) substrate (see end of section 3.1.1). Note that grazing incidence s-polarized reflectance spectra are two orders of magnitude less sensitive to the surface electronic absorption than p-polarized spectra (eqs. (3.11) and (3.12)). The above remarks are important to understand the dynamical results associated with H on W(100) and Mo(100) presented in section 4.3.2.2.

In summary, a strong infrared absorption arising from intraband transitions of surface states with $d_{x^2-y^2}$ symmetry appears to dominate the reflectance spectrum of clean W(100). Other processes, involving free carrier scattering (FCS) at the surface, have been ruled out mostly because they cannot account for the characteristic frequency dependence of the absorption shown in fig. 44. The latter is of course a small fraction ($\sim 0.7\%$) of the total electronic

absorption taking place upon reflection and dominated by bulk electron–phonon scattering within the skin depth region [388]. However, as will be apparent in section 4.3.2.2, it is large compared with the H vibrational absorption.

4.3. Dynamics

When the chemical nature and geometry of adsorbates at surfaces are well determined, then problems associated with the dynamics of such systems can be addressed. These include the dynamical interactions between adsorbate vibrations and substrate vibrations (phonons) or substrate electronic excitations (electron–hole pairs), as well as adsorbate–adsorbate interactions. Since most dynamical phenomena are manifested in the measured vibrational line shapes (when inhomogeneous broadening is negligible), several attempts to analyze line shapes in terms of such mechanisms have been carried out. Two classes of mechanisms have emerged as important: dephasing (phase relaxation) contributing to the line width without energy transfer (see section 2.5.2.1) and vibrational lifetime (energy relaxation) through electron–hole pair generation on metallic substrates (see section 2.5.2.2) and multiphonon excitation. In this section, we present a small subset of these studies selected for their tutorial value.

4.3.1. Phase relaxation: dephasing

4.3.1.1. CO on Ni(111) and Ru(001). Although CO on Pt(111) was the first system for which vibrational dephasing was observed and recognized [314], we review here CO on Ni(111) and Ru(001) because these systems have been analyzed in the same manner [135] and a coherent picture has been presented [389,390]. In particular, the difference between the two systems can be related to the different bonding configuration of the adsorbed CO, bridge-bonded on Ni(111) and linear-bonded on Ru(001).

On Ni(111), CO forms an ordered c(4 × 2) structure at saturation coverage ($\theta = 0.5$ ML) with all molecules in the bridge position (see fig. 45a). The LEED pattern becomes noticeably sharper below room temperature [391]. The peak position (wavenumber) and the width (FWHM) of the C–O stretch mode as a function of temperature, measured by Persson and Ryberg [392], are shown in fig. 46. Earlier measurements by Trenary et al. [393] gave much larger line widths and are therefore not considered here. The discrepancy between the two measurements has been discussed by Tobin [20]. Note that the frequency of the wavenumber *increases* with temperature, from 1898 cm^{-1} at 40 K to 1905 cm^{-1} at 300 K.

On Ru(001), CO forms an ordered $(\sqrt{3} \times \sqrt{3})R30°$ structure at $\theta = 0.33$ ML, with all the molecules in identical on-top sites [328]. This structure ensures the absence of temperature-induced changes in adsorption sites [314] or intensity transfer between different adsites [392]. The peak position (wave-

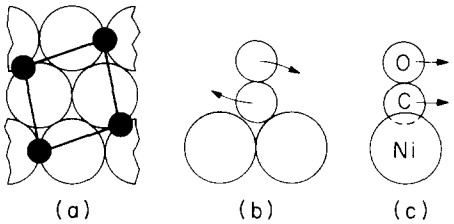

Fig. 45. (a) Position of the bridge-bonded CO molecules in the c(4×2) structure on Ni(111). (b) schematic representation of the frustrated rotation, and of (c) the frustrated translation (with permission from ref. [392]).

number) and width (FWHM) of the C–O stretch mode as a function of temperature are shown in fig. 47. Note that, in contrast to CO/Ni(111), the frequency of the wavenumber *decreases* with temperature, from 2027 cm^{-1} at 90 K to 2017 cm^{-1} at 420 K.

The analysis of the data is based on the phenomenological description presented in section 2.5.2.2 (eqs. (2.60) to (2.66)), for which three parameters are necessary to model the system: the frequency of the low frequency mode responsible for the dephasing (ω_0), the damping of this low frequency mode (η) and the frequency shift of the C–O stretch mode described by $\delta\omega = \hbar a/2m\Omega_0\omega_0$. Here a is a measure of the anharmonic coupling and Ω_0 the C–O stretch frequency. The solid curves in fig. 46 represent the theoretical

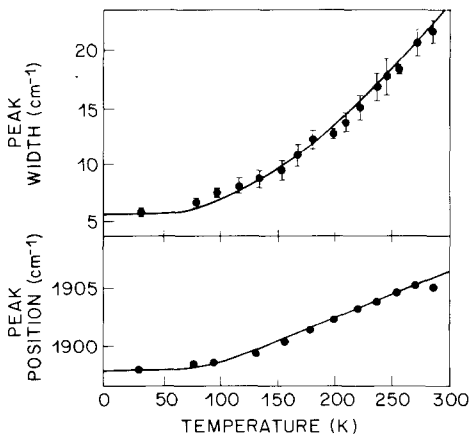

Fig. 46. Infrared-absorption peak position and width (FWHM) as a function of temperature for the internal C–O stretch vibrational mode of bridge-bonded CO on Ni(111). The solid lines are theoretical calculations as described in section 2.5.2.2. In the calculation, $\omega_0 = 235$ cm^{-1}, $\delta\omega = \eta = 20$ cm^{-1}, $\alpha_e = 3$ $Å^3$, $\alpha_v = 0.17$ $Å^3$, and $U_0 = 0.35$ $Å^{-1}$ (see section 2.5.2) (with permission from ref. [389]).

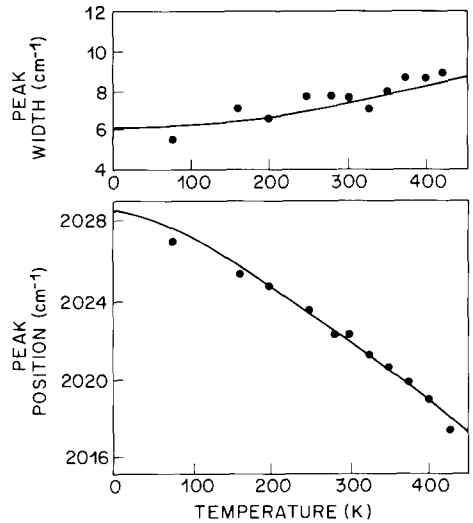

Fig. 47. Infrared-absorption peak position and width (FWHM) as a function of temperature for the internal C–O stretch vibrational mode of on-top bonded CO on Ru(001). The lines are theoretical calculations as described in section 2.5.2.2. In the calculation, $\omega_0 = 105$ cm^{-1}, $\delta\omega = -6$ cm^{-1}, and $\omega = 6$ cm^{-1} (with permission from ref. [389]).

results obtained with $\omega_0 = 235$ cm^{-1}, $\eta = 20$ cm^{-1} and $\delta\omega = 20$ cm^{-1}, and taking into account dipole–dipole interactions. The frequency ω_0 is close to the frequency predicted by Richardson and Bradshaw [394] for the frustrated rotational mode (see fig. 45b), $\omega_0 = 184$ cm^{-1}. In contrast, the frustrated translation (see fig. 45c) is estimated to be 76 cm^{-1}. Therefore, Persson and Ryberg [392] argue that the main contribution to the dephasing process is the anharmonic coupling of the CO stretch to the frustrated rotational mode. They further argue that direct coupling to the substrate phonons is negligible [135]. The relatively strong damping ($\eta = 20$ cm^{-1}) is consistent with the fact that the frustrated rotational mode is lower than the maximum phonon frequency on Ni, $\omega_{\text{phonon}}^{\text{max}} \approx 295$ cm^{-1} [395].

The data of fig. 47, for CO on Ru(001), are fitted with $\omega_0 = 105$ cm^{-1}, $\eta = 6$ cm^{-1} and $\delta\omega = -6$ cm^{-1}, including dipole–dipole interactions. The value of ω_0 suggests that the frustrated translation parallel to the surface must be responsible for the dephasing process. The other substrate–CO modes have been measured by EELS and are much higher in frequency: 445 cm^{-1} for the Ru–CO stretch and 410 cm^{-1} for the Ru–CO bend (frustrated rotation). Theoretical estimates by Richardson and Bradshaw [394] for CO on Ni(001) gave 437 cm^{-1} for the Ni–CO stretch, 411 cm^{-1} for the Ni-CO bend, and 82 cm^{-1} for the frustrated translation. Hoffmann and Persson also argue that the

value $\eta = 6$ cm^{-1} for the damping of the frustrated translation is consistent with an elastic continuum model.

A potential problem in fitting the data to extract these three parameters is the strong influence of dipole–dipole interactions. Indeed, causality [114,389] requires that the frequency shift of a mode wavenumber be of the same magnitude as the increase in line width *in the absence of any dipole–dipole interactions*. Clearly, this is not the case for CO on Ru(001) (fig. 47) where the line shift is much larger than the increase of the line width. An experimental check on the effects of dipole–dipole coupling was recently performed for CO on Ru(001) by Hoffmann using isotopic mixtures. In the isotopic dilution limit, the line width of the CO stretch mode increases in accordance with theory [396], thus supporting the present model.

The above description of the dynamics of CO on Ru(001) and Ni(111) is appealing due to its simplicity. For the bridge site, the frustrated rotation is much softer (184 cm^{-1}) than for the on-top site (411 cm^{-1}) [394]. Since the former is still below the highest phonon frequency of the Ni(111) substrate it is accessible as an exchanging mechanism. Moreover, the strongly antibonding character of the $2\pi^*$ orbitals with respect to the C–O bond for the bridge site accounts for the strong dephasing behavior with $\delta\omega > 0$. In contrast, the on-top site of CO on Ru(001) displays much weaker back-bonding. As a result, the C–O stretch has a high frequency. Coupling to the frustrated translation, which takes the CO molecule towards the bridge site, tends to lower the frequency of the CO stretch, i.e. $\delta\omega < 0$.

However, the problems associated with the above modelling stem precisely from its simplicity. The assumption that only one mode contributes dominantly to the dephasing process may not always be justified, particularly when that mode is below the maximum phonon frequency of the substrate. As with most parametrized models, the question of uniqueness remains open. For CO on Ni(111) and Ru(001), a fair amount of supporting evidence strengthens the arguments. Nonetheless, as pointed out by Tobin [20], the large discrepancy between Ryberg's and Trenary's data suggests that temperature inhomogeneous broadening remains a strong possibility for most of the line width studies. Further advances will come when a complete mapping (energy and symmetry) of the surface phonons and low frequency adsorbate–substrate mode is available from other measurements, such as inelastic He scattering [397].

4.3.1.2. Si(100)-(2×1)H. The monohydride phase is a particularly good system to investigate the contribution of vibrational phase relaxation (pure dephasing) to the vibrational line width because:

(1) It can be prepared in a single *stable* phase (see table 7), i.e. where adsorbed H is only present on the surface in a monohydride configuration (no H at steps or defects), which remains stable over a wide range of temperatures

(40 to 600 K). Diffusion is also negligible over the range investigated (40 to 500 K). Practically, these factors guarantee that the inhomogeneous contributions to the line width have a *negligible temperature dependence* (see caption of fig. 48 for the experimental determination of the inhomogeneous broadening).

(2) Large variations in line width were observed over a relatively small temperature range (150–500 K) with no changes in H concentration.

(3) The Si–H stretch mode (~ 2100 cm^{-1}) is well removed from the substrate phonons (≤ 500 cm^{-1}), requiring the excitation of 4 to 5 phonons for energy transfer. Moreover, there are no electronic excitations allowed in this frequency region. Consequently, lifetime broadening is expected to be negligible.

(4) A complete ab initio description is available (see sections 2.4.2 and 4.1.5) and was found to provide an accurate description of the geometry and vibrational parameters for the monohydride structure. In particular, accurate force fields for the diagonal and off-diagonal stretch and bend motions including non-negligible cubic and quartic terms were calculated, thus describing the non-linear coupling to the Si lattice from first principles.

(5) The Si–Si force constants of the underlying substrate have previously been obtained by extending the valence force model to Si(100) and found to reproduce well the bulk and surface phonon spectra [398].

As a result, the temperature dependence of the Si–H stretch line width could be modelled by molecular-dynamics simulations (section 2.5.1). While such simulations usually rely on fitted parameters, they could in this case be performed completely *a priori*, and in full dimensionality (32 atom Si slab, with 16 H atoms). The most serious drawback of such simulations, i.e. the classical treatment, was alleviated by means of novel stochastic methods [108] to introduce quantum effects.

Two types of molecular-dynamics calculations were carried out, one to obtain vibrational lifetimes and another to simulate infrared absorption spectra. The lifetime calculations were performed in the following way: The classical mechanical equations of motion were numerically integrated for the 44 atom slab of H and Si atoms. In addition to the force fields described above, friction and Gaussian white-noise random forces were applied to the edge atoms of the slab to account for energy flow between the slab and the missing remainder of the solid. One quantum of energy, at the theoretically calculated stretch frequency (2300 cm^{-1}), was initially deposited in the symmetric stretch frequency of each H–Si–Si–H unit ($K = 0$ mode) and the remainder of the positions and momenta were chosen from a proper Boltzmann distribution. The trajectory was then integrated and the decay of energy of the Si–H stretch modes monitored as a function of time. Energy relaxation was found to be so slow that even for the longest trajectories integrated, 2.6×10^{-10} s, less than 1% of the energy in the Si–H stretch modes was

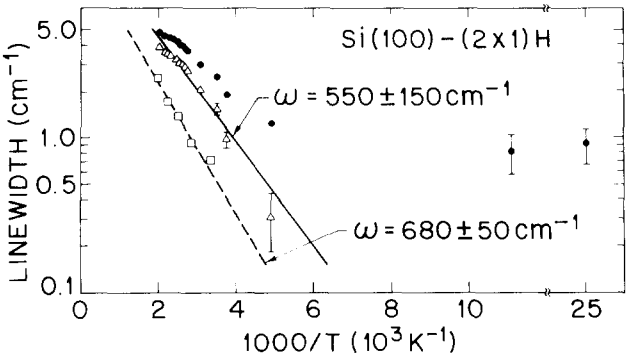

Fig. 48. Experimental line widths (solid circles) obtained from a Lorentzian fit to the data and proper deconvolution of the apodized resolution function. The error bars associated with the solid dots represent the reproducibility after different sample preparations (± 0.25 cm^{-1}). The open triangles are obtained by subtracting the inhomogeneous contribution from the experimental line widths, determined by analyzing the results of different preparation procedures. The open squares are the calculated line widths. Statistical uncertainty of calculated points is ± 0.4 cm^{-1}. The straight lines are least-squares fit to the calculated points (dashed) and the corrected experimental points (solid) (from ref. [108]).

dissipated. Similar results were obtained for the antisymmetric stretch. Thus, only a rough estimate of the vibrational lifetime of the Si–H stretch can be made, $\tau_H > 2 \times 10^{-8}$ s. When all H atoms were replaced by D atoms, using the same force fields, vibrational lifetimes were shortened sufficiently to calculate more reliable estimates ranging from $\tau_D = (1.0 \pm 0.5) \times 10^{-9}$ s at 500 K to $\tau_D = (3.0 \pm 1.5) \times 10^{-9}$ s at 0 K. Thus, it appears that the vibrational lifetime contributes negligibly to the observed infrared line widths for the Si–H and Si–D stretch modes ($\sim 10^{-3}$ cm^{-1} for H and $\sim 10^{-2}$ cm^{-1} for D).

The next molecular-dynamics calculation was a direct simulation of the IR spectrum using eq. (2.49) of section 2.5.1. The results are shown in fig. 48 (open squares) and compared to the experimentally determined line widths (closed circles). At low temperatures, the experimental line widths level off at about 0.9 cm^{-1}. This residual line width varies from sample to sample and with sample preparation in a manner consistent with inhomogeneous broadening. Therefore, an approximate homogeneous part of the line width (fig. 48, triangles) has been obtained by subtracting the 0.9 cm^{-1} inhomogeneous contribution. The calculated widths are in reasonable accord with the adjusted experimental widths, particularly with regard to temperature dependence. In fact, the agreement achieved is remarkable for a theory with no adjustable parameters. The discrepancies of about a factor of 2 could easily result from approximations inherent in the semiclassical simulation technique and/or inaccuracies in the ab initio force field. Furthermore, experimental and theoretical line widths for the Si–D stretch in Si(100)-(2 × 1)D are in equally

good agreement. Finally, it was found that dipole–dipole interactions make a negligible contribution to both the line width and lifetime.

The results suggest that the major contribution to the dephasing is the anharmonic coupling between the Si–H stretch and the Si–H bend modes, manifested by the slope of the straight-line fit through the calculated points of fig. 48 (open squares). When converted to wavenumbers, the slope is $\sim 680 \pm 50$ cm^{-1}, in close agreement with the 700 cm^{-1} (theoretical) activation energy for exciting the bending mode. Note that the slope of a straight-line fit through the adjusted experimental points of fig. 48 (triangles) yields an activation energy of 550 ± 150 cm^{-1}, in at least rough accord with the experimental bending frequency of 635 cm^{-1} [340].

In closing, we note that, because the silicon substrate lattice was taken to be harmonic, the simulations made no predictions on line shifts (a 4.1 cm^{-1} red shift is measured from 40 to 500 K for H). The anharmonic extension of the calculations is important as shifts can come from several mechanisms, including dephasing, thermal expansion and energy transfer mechanisms. Nevertheless, it appears that dynamical information can be obtained from line shape analysis in favorable cases. As data are compiled for a number of different systems for which the *structure is well-known* and for which inhomogeneous broadening can be ruled out, interesting dynamical information will be obtained. Using the present calculations as a bench mark, it appears that the vibrational lifetime of an atomic adsorbate on semiconductors is long enough (10^{-7} to 10^{-9} s) that *direct* measurements of the lifetimes using tunable pulsed lasers may be possible.

4.3.2. Energy relaxation: electron–hole pair excitation

4.3.2.1. Weak breakdown of adiabaticity: CO on Cu(100). The phenomenological treatment of the coupling of an adsorbate vibration to the substrate electronic structure usually assumes a flat density of states for the electrons across the Fermi level. This assumption is reasonable for most systems and has been applied to investigate the case of CO on Cu(100). In contrast to CO on Ni(111), Pt(111) or Ru(001), Ryberg found that on Cu(100) the CO stretch line width is temperature independent [118], at least between 20 and 130 K, which excludes dephasing and phonon mechanisms. In Ryberg's work, the poor fit obtained with a purely Gaussian function (see fig. 49a) was used as the sole argument to rule out inhomogeneous broadening. The reader is referred to Tobins' review for a discussion of inhomogeneous broadening [20].

Neglecting inhomogeneous broadening, Crljen and Langreth [131] fit Ryberg's data for the c(2 × 2) ordered phase of CO on Cu(100) [118], using eq. (2.54) in section 2.5.2.1, the result of which is shown in fig. 49a. Then, using the results of previous isotopic mixture experiments [399], they obtain the parameters associated with a *single* CO on the Cu(100) surface, and derive the

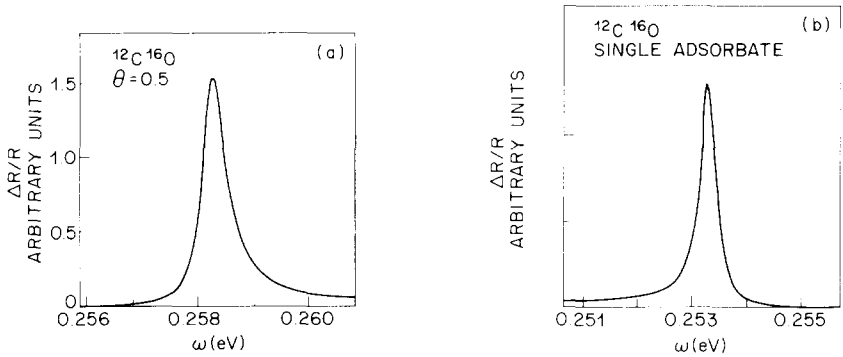

Fig. 49. Plot of the absorptance, $\Delta R/R$: (a) fit to Ryberg's data [118] for the ordered layer [c(2×2) structure] of CO on Cu(100) according to eq. (2.54) (see section 2.5.2.1); (b) calculated for a *single* CO on a Cu(100) surface (with permission from ref. [131]).

absorption spectrum plotted in fig. 49b. They find that the dipole–dipole interaction between the adsorbed CO molecules causes the tail of the line to go from the low energy side of the resonant frequency for a single oscillator to the high energy side for the collective mode. Such a sensitivity to coverage is a sharp reminder of problems associated with line shape analysis of strong dipole modes at surfaces.

Crljen and Langreth have also applied the coherent-potential approximation (CPA) [131] to calculate the line shape and resonant frequency for an isotopic mixture and for an incomplete CO monolayer. They find the isotopic mixture results in good agreement with the data [117], indicating that the line width is to a significant degree a measure of the lifetime of the vibration due to the electron–hole pair mechanism. However, the CPA-derived coverage results do not reproduce the data [399], indicating either that the CPA is not appropriate or that chemical effects play an important role in this system [131].

In closing, we note that the strongest confirmation that the line width is indeed dominated by lifetime broadening will come from direct T_1 measurements, using picosecond laser spectroscopy. From the value of the measured line width, $\Delta\tilde{\nu} = 4.6\ \mathrm{cm}^{-1}$, a *lower* limit on the lifetime is placed at 2.3 ps, a time scale accessible to time-resolved experiments [229]. In fact, preliminary results on supported Pt set an *upper* limit for CO vibrational lifetime to 10–20 ps.

4.3.2.2. Strong breakdown of adiabaticity: H on W(100) and Mo(100). In contrast to CO on metals, for which only weak coupling to electron–hole pairs may occur, the H-saturated W(100) surface gives a clear example of *strong* coupling with a large breakdown of adiabaticity. Indeed, one of its vibrational

modes is *only* detectable because it is *strongly* coupled to the substrate electronic excitations. Moreover, the density of electronic states is strongly peaked in energy, leading to a strong coupling.

The H-saturated phase is one of the best characterized surface structures. The coverage has been determined absolutely by MeV ion microanalysis [400] to be $(2.0 \pm 0.2) \times 10^{15}$ H/cm^2, i.e. 2 H per W surface atom. Using MeV ion channeling, Stensgaard et al. [400] determined that there is no measurable lateral displacement of the W surface atoms (< 0.05 Å) at saturation, i.e., H forces the W surface back into registry with the W bulk. A bulk-like arrangement of the top W layer is consistent with all the LEED data [332].

The chemisorption geometry for the hydrogen was elucidated by EELS. First, Adnot and Carette [385] showed, by means of H_2, D_2 and HD exposure experiments, that hydrogen was completely dissociated. Shortly thereafter, Ho

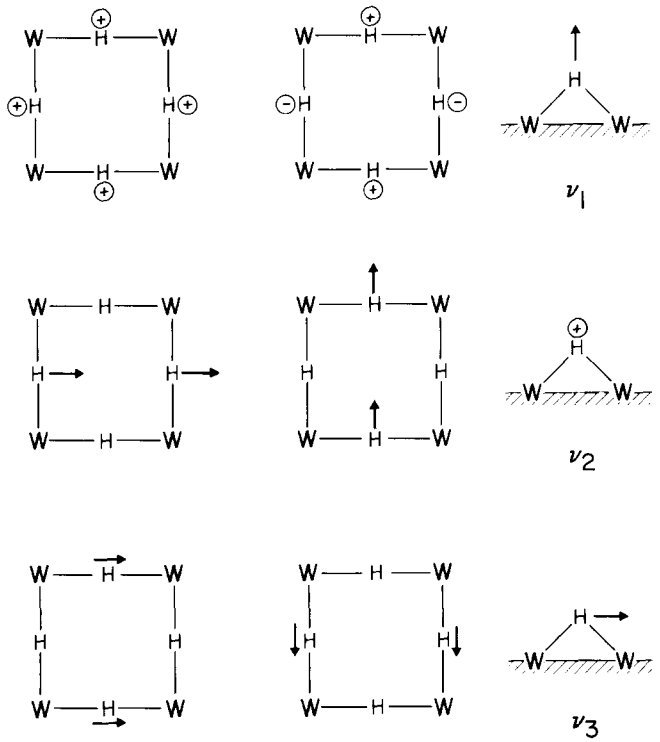

Fig. 50. Schematic representation of the six lattice modes associated with H in bridge position. Because there are 2 H per unit cell, there are two modes associated with each H displacement. These modes are degenerate for the ν_2 and ν_3 vibrations. For the ν_1 vibration, only the in-phase mode (top left) is infrared active. The out-of-phase (or optic) mode may have been observed by EELS in impact scattering [387] (from ref. [327]).

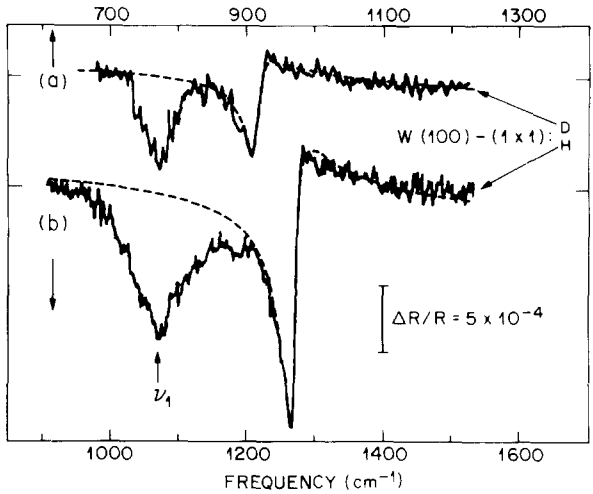

Fig. 51. Vibrational spectra of D and H on W(100) at saturation (10 L exposure). The resolution is (a) 4 cm^{-1} and (b) 2 cm^{-1}. A linear background subtraction was used to remove the broad nonvibrational background (see text). The dashed lines are the fits using the line shape function given in eq. (2.54) and the parameters listed in table 8 (from ref. [62]).

et al. [61] detected three normal modes by means of both dipole and impact scattering. The assignment of these modes led to the bridge site geometry. The combined results of the coverage determination, the MeV ion channeling data and the local geometry as determined by EELS suggest that H forms a well-ordered two-dimensional lattice as shown in fig. 50.

Among all the fundamental vibrational modes shown in fig. 50, only the in-phase symmetric stretch (ν_1), where all the H move up and down together (top left of fig. 50), is dipole allowed. The out-of-phase (or optic) ν_1 mode is forbidden [387], as are the two degenerate wag (ν_2) modes and the two degenerate asymmetric stretch (ν_3) modes. The observation by IRRAS of a vibrational feature at 1269 cm^{-1} *in addition to* the in-phase symmetric stretch ν_1 at 1069 cm^{-1} [62] was therefore surprising (see fig. 51), particularly as no such loss feature was evident in all the specular EEL spectra. Furthermore, similar IRRAS observations have recently been made for the H-saturated Mo(100) surface, where an absorption feature at 1302 cm^{-1} is seen *in addition to* the ν_1 mode absorption at 1016 cm^{-1} [379,401]. Again, specular EELS shows no loss at 1302 cm^{-1} [402]. The raw spectra (i.e. without background subtraction) are shown in fig. 52 and the data summarized in table 8 [379].

The vibrational feature at 1269 cm^{-1} on W(100)-(1 × 1)H and at 1302 cm^{-1} on Mo(100)-(1 × 1)H has been assigned to the first overtone ($2\nu_2$) of the wag mode (ν_2) [62,327,403]. Indeed, the first overtone of the wag is dipole allowed [404]. On W(100), the dipole-forbidden ν_2 mode has been identified by

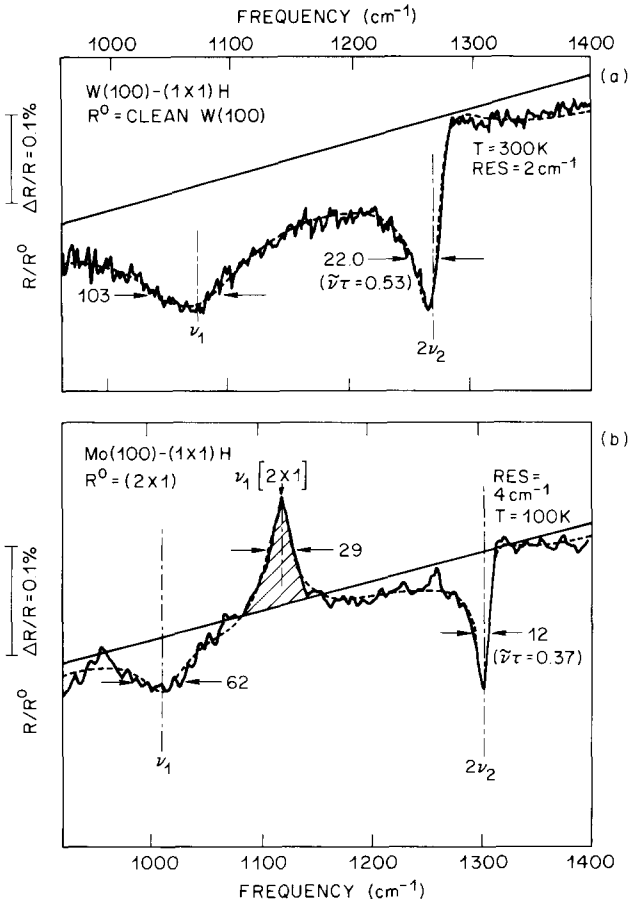

Fig. 52. Raw reflectance spectra of (a) W(100)-(1×1)H at $T = 300$ K, using a clean W(100) surface as reference, and of (b) Mo(100)-(1×1)H at $T = 100$ K, using the Mo(100)-(2×1)H phase as reference (see phase diagram in fig. 26b). The dashed lines are the result of a linear least-squares fit and the solid lines denote the linear position of the fit, which represents the electronic part of the absorption. The parameters are listed in table 8 (from ref. [379]).

off-specular EELS at $\tilde{\nu}_2 = 645$ cm^{-1} [61] so that the 1269 cm^{-1} feature is at twice that frequency with ~ 1.5% anharmonicity. In the case of the Mo(100)-(1 × 1)H system, the assignment is based mostly on an analogy with the W(100)-(1 × 1)H system and similar conclusions are reached [401].

The simplicity of the W(100)-(1 × 1)H system has attracted a number of theoretical studies [57,58,405]. In particular, the recent self-consistent LAPW calculations of Biswas and Hamann [57] (see table 3 in section 2.4.1) make it possible to estimate the adiabatic dynamic dipole moment associated with the

Table 8
Spectroscopic constants (in cm^{-1} unless noted otherwise) determined for the H-saturated surfaces Mo(100) and W(100)

Substrate	Mode	T (K)	$\tilde{\nu}_0$	FWHM (Γ)	ASYM ($\tilde{\nu}_0\tilde{\tau}$)	e^*/e
Mo(100)	ν_1	100	1016(4)	65(5)	–	0.039(2)
		245	1002(6)	72(10)	–	0.033(4)
	$2\nu_2$	100	1302(1)	12.2(5)	0.37(4)	0.024(1)
		245	1300(1)	18(1)	0.40(4)	0.023(2)
W(100)	ν_1	100	1079(3)	47(5)	–	
		300	1069(2)	103(8)	–	0.059(2)
	$2\nu_2$	100	1272(1)	18.5(10)	0.54(3)	
		300	1269(1)	22(1)	0.53(3)	0.036(2)

For W(100)-(1×1)D at 300 K, the $2\nu_2$ mode is characterized by $\tilde{\nu}_0 = 915$ cm^{-1}, FWHM = 25 cm^{-1} and $\tilde{\nu}_0\tilde{\tau} = 0.41$. $\tilde{\tau}$ is in cm.

wag overtone. From the lack of work function change ($d\phi/dz < 0.025$ a.u.) upon translating the H atom along the wag motion, an *upper* limit is set on the effective charge of the $2\nu_2$ mode: $[e^*(2\nu_2)/e^*(\nu_1)] < 0.4$. Since the $2\nu_2$ mode is not detected by EELS, a much lower value of the purely vibrational (adiabatic) $e^*(2\nu_2)$ is expected. A more precise calculation may in fact set a much lower limit. However, even this upper limit for $e^*(2\nu_2)$ falls short of the measured value (see table 8): $[e^*(2\nu_2)/e^*(\nu_1)] = 0.6$. It is clear, therefore, that the origin of the $2\nu_2$ feature is non-adiabatic [401].

In fact, the asymmetry of the $2\nu_2$ mode for both W(100)-(1 × 1)H and Mo(100)-(1 × 1)H is a strong indication that the $2\nu_2$ level is interacting with a continuum. Reutt et al. [401] have argued that the only possible continuum is the electronic excitation of the substrate electrons. It should be stressed that the observed asymmetry is not the result of dispersion asymmetry encountered for modes of thicker films with a strongly dispersive index of refraction [406].

The clue as to the origin of the electronic absorption continuum came from an analysis of the broadband absorption, as was done in section 4.2.2 for the clean W(100) surface. For the H/W(100) system, the Ic(2 × 2) phase ($\theta = 0.42$ ML) was used as reference (see section 4.2.2). For the H/Mo(100) system (see phase diagram in fig. 26b), a careful analysis showed that the highest reflectivity occurs at the onset of the $(z \times 2) + c(2 \times 2)$ phase (i.e. $\theta \approx 0.6$ ML where $z = 4$), referred to as $(z \times 2)$ for short. In their paper, Reutt et al. argue that any intrinsic surface state must also be quenched by the time the $(z \times 2)$ pattern develops and that the $(z \times 2)$ is in fact a good reference phase to analyze the electronic absorption at saturation coverage [401]. Using the Ic(2 × 2) and $(z \times 2)$ phases as reference, the reflectances of W(100)-(1 × 1)H and Mo(100)-(1 × 1)H are plotted in fig. 53, respectively. Both (1 × 1) phases

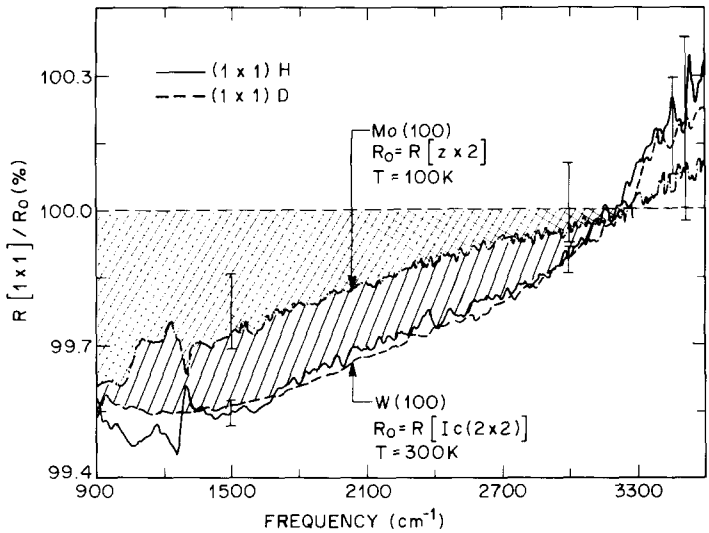

Fig. 53. Broadband reflectance absorption spectra of Mo(100)-(1×1)H (dot-dashed line) and W(100)-(1×1)H (solid line), determined using the Mo(100)-(z×2)H and W(100)-Ic(2×2)H as reference, respectively. The corresponding absorption for the deuterated phase on W(100) is shown in dashed line. The cross-hatched area for Mo and ruled and cross-hatched area for W represent additional electronic absorption by the H-saturated phases (from ref. [401]).

have substantial electronic absorption below 3000 cm^{-1} with respect to the reference phases. The two important observations are that (1) the absorption increases with decreasing energy for the (1 × 1) phases on both W(100) and Mo(100), and (2) the relative absorption of W(100)-(1 × 1)H is larger than that of Mo(100)-(1 × 1)H.

The frequency dependence was used by Reutt et al. to rule out possible contributions by free carrier scattering (FCS), as previously invoked by Riffe et al. [372]. Indeed, changes in specularity ($\Delta p \neq 0$) would lead to an opposite (and much weaker) frequency dependence. Instead, the strength and frequency dependence of the absorption can be well accounted for by the presence of surface electronic states in the vicinity of E_F at saturation. The absorption is centered around 1200 cm^{-1} (0.15 eV) on the W(100)-(1 × 1)H surface and lower on the Mo(100)-(1 × 1)H. The relatively narrow width (0.25 eV) of these absorption bands is again suggestive of d-states. Following the same reasoning as in section 4.2.2, Reutt et al. conclude that these absorption bands involve intraband transitions of states with d_{xy} or $d_{x^2-y^2}$ symmetry. In this case, however, d_{xy} states are favored as explained below.

Among the various theoretical calculations, the results of Richter and Wilkins [405] explicitly show the presence of surface states with d_{xy} symmetry (e.g. at $\bar{\Gamma}$ and $\bar{X}$), located in the immediate vicinity of E_F (≤ 0.1 eV). Such

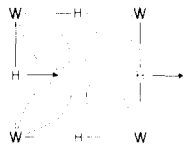

Fig. 54. Schematic representation of the electronic surface states (dashed lines) to which H can couple during the wag motion. These states have xy symmetry (z direction is perpendicular to the surface) and do not participate in the bonding of hydrogen.

states, schematically shown in fig. 54, are not altered by H adsorption (assuming an unreconstructed surface prior to adsorption) or by H vibration within the symmetry plane (xz or yz), because they do not participate in the bonding. However, they can couple to the wag motion because the latter breaks the mirror symmetry. In contrast the bonding states, to which the symmetric (ν_1) and asymmetric (ν_3) stretch modes couple strongly, are all located well below E_F (> 1 eV).

The observation of the surface state absorption is key to the detection of the $2\nu_2$ feature. In fact, this feature can be viewed as an interference on top of the strong electronic absorption, arising from a *strong* coupling of the wag motion to the sharply peaked electronic structure. That is, in the generalized polarizability expression given in eq. (2.54) in section 2.5.2.1, the dipole moment associated with the nuclear motion, μ^i, is negligible compared to that of the electronic response μ^e. However, the coupling strength, expressed as $\omega\tau$ in eq. (2.54) is large, leading to a strong asymmetry (see table 8). The above description is consistent with all the experimental observations as summarized below:

(1) Specular EEL spectra do not show a broad loss feature corresponding to the excitation of the d_{xy} states because only ϵ_z can be probed. Consequently, the $2\nu_2$ interference feature is absent from the loss spectra.

(2) The $2\nu_2$ mode is not seen at lower coverages, both on W(100) and Mo(100). In fact, its observation is correlated only with the additional electronic absorption present at saturation. We note that the d_{xy} states are strongly affected by the W or Mo reconstruction along the $\langle 10 \rangle$ direction at lower coverages and intraband transitions can no longer be excited.

(3) The $2\nu_2$ feature is not observed with grazing incidence s-polarized reflection because, as shown in eq. (2.20) and discussed at the end of section 3.1.1, the sensitivity to the *electronic* absorption below the surface plane is two orders of magnitude lower than for grazing incidence p-polarization.

(4) For both W(100) and Mo(100), the narrow widths of the $2\nu_2$ features compared to those of the ν_1 absorption bands (see table 8) are also consistent with this picture if dephasing through very low frequency substrate modes is responsible for the large width of the ν_1 bands. Indeed, the ν_1 frequency is shifted by 200–300 cm^{-1} as the W or Mo substrate reconstructs (see section

4.1.4). However, as soon as the W or Mo top layer departs from its unreconstructed bulk-like arrangement, the absorption by d_{xy} surface states vanishes. Consequently, low frequency fluctuations of the surface will decrease the strength of the surface state absorption so that the dephasing broadening of the $2\nu_2$ mode cannot be observed. Dephasing-induced broadening is small, as evidenced by the lack of temperature dependence of the $\omega\tau$ parameter (see table 8).

(5) The width and asymmetry of the $2\nu_2$ feature are smaller on Mo than on W(100). As shown in fig. 53, the density of electronic states is smaller on Mo(100) leading to a weaker absorption. It is therefore probable that the coupling is weaker, accounting for the narrower line width (longer lifetime) and smaller asymmetry parameter (see table 8).

(6) The unusual isotope dependence of the line width, asymmetry and strength on W(100) [62] is also indicative of a strong breakdown of adiabaticity. Indeed, the small-ω expansion originally used by Langreth [130] in evaluating these parameters is not valid when the electronic spectral density varies rapidly near E_F [407].

The implications of this work are two-fold. On the one hand, the vibrational lifetime of the $2\nu_2$ vibration can be extracted fairly accurately from the data, on the other, general remarks for vibrations involving parallel motion can be made. First, since the asymmetry parameters are insensitive to temperature (see table 8), the line shape appears to be dominated by the dynamics of the interference process. In particular, dephasing contribution to the line width is small. Consequently, the line widths extracted from the fits at 100 K (lowest temperature investigated) can be used to get a *close* lower bound for the vibrational lifetimes, yielding $\tau \geq 0.9$ ps for H on W(100) and $\tau \geq 0.6$ ps for H on Mo(100).

Second, this work suggests that, if non-adiabatic coupling is suspected for a vibrational mode involving parallel motion, then a measurable electronic absorption should be present in grazing incidence p-polarized spectra. For instance, Persson [408] recently suggested that the O–O stretch of O_2 chemisorbed on Pt(111) is likely to be damped via excitation of electron–hole pairs, because of a small asymmetry in the data [144]. Since the O–O stretch should couple to states with tangential symmetry and since these states participate in the bonding, a distinctive broadband absorption is expected to be associated with the O_2 covered layer. Further experiments are needed to investigate this point.

4.4. Kinetics

The importance of kinetic phenomena at surfaces hardly needs substantiation. From the kinetics of phase transitions on solid surfaces [409] to the kinetics of interface reactions [410], non-equilibrium phenomena are occupy-

ing the mind of surface scientists more and more. Not surprisingly, the time resolution of spectroscopic techniques is being improved to investigate surface kinetics [1]. Vibrational spectroscopy is particularly appropriate because it can monitor the time evolution of chemically well-identified species. In particular, advances in EEL spectrometers [411] have contributed to a number of kinetic studies [1].

Surface infrared spectroscopy distinguishes itself from EELS as a probe of surface kinetics in two respects. First, it can monitor surface reactions at high pressures, an important feature to understand the possible dominance of minority reactions at high pressures. Second, its high resolution makes it possible to infer important structural changes involving the adsorbates, such as domain formation, occupation of step and/or defect sites, and variation of adsorbate–adsorbate separation, particularly relevant for mixed surface species. In this section, therefore, we discuss recent results of time-resolved SIRS at relatively high pressures and possibilities to monitor adsorbate reconfiguration and diffusion in real time.

4.4.1. Surface reactions at high pressures

4.4.1.1. Self-sustained oscillations in CO oxidation rate on Pt. An early example of kinetic studies is the work of Burrows et al. [412,413] on the oscillatory CO oxidation reaction on Pt. The phenomenon of self-sustained reaction rate oscillations for metal-catalyzed oxidations has been documented for a large number of systems, including the oxidation of H_2, CO and hydrocarbons on Pt, Pd, Ir, Rh, and Ni catalysts in pressures from sub-millitorr to atmosphere. One of the interesting kinetic features is the long oscillation period, ranging from a minute to several hours, presumably associated with some slow surface process.

The primary emphasis of Burrow's work was to obtain direct experimental evidence for this slow surface process during the reaction rate, a worthwhile endeavor in view of the large number of possible theoretical models and the only one real-time experimental study [414]! The generally accepted reaction involves the adsorption of both CO and dissociated oxygen:

$$CO + * \rightleftarrows CO_{ads},$$

$$O_2 + 2* \rightleftarrows 2\,O_{ads},$$

$$CO_{ads} + O_{ads} \rightarrow CO_2 + 2*.$$

But the origin of the slow process, regulating the total number of available active sites, was not known.

The kind of information available in a broadband IRRAS experiment is shown in fig. 55b. The top trace is obtained by integrating the absorption band of the stretching mode of gas-phase CO_2 at 2336 cm^{-1}. (The total

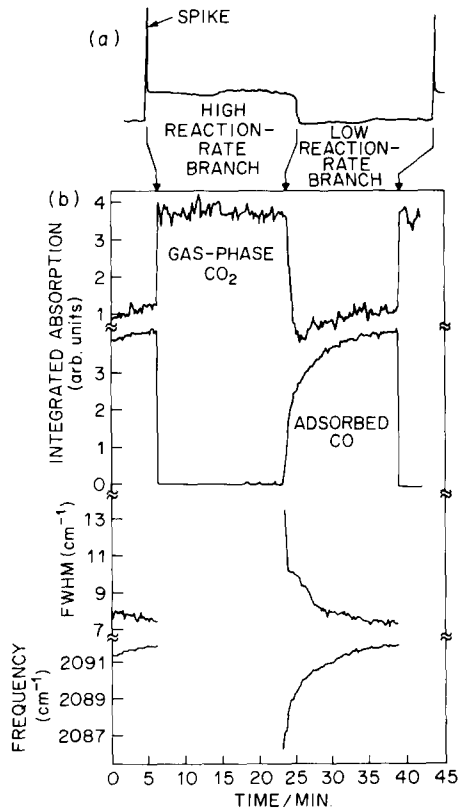

Fig. 55. (a) Single isothermal oscillation period, showing the output of a fast resistance controller (5 ms response time) used to maintain the Pt foil temperature constant. This signal is proportional to the reaction rate [412]. The sample is maintained at 540 K in 30 Torr of flowing $CO/O_2/He$ mixture in proportions 0.5%/49%/50.5%. (b) Spectral features as a function of time for the oscillation: (top) integrated absorption from gas-phase carbon dioxide; (middle) integrated absorption from adsorbed CO; (bottom) band width and frequency of the adsorbed CO band (from refs. [3,412]).

ambient pressure, mostly oxygen, is ~ 100 Torr.) The second trace is a result of the adsorbed CO band integration. The last two traces give details of the CO stretch line shape and wavenumber as a function of time. All these data points are acquired with 4 cm^{-1} resolution and every 6 s (10 scans averaging). Clearly, this time resolution is adequate to monitor the relatively slow changes taking place at the surface.

The most striking feature of fig. 55 is the low level of adsorbed CO during the high reaction rate branch of the cycle. This indicates a high reaction efficiency for adsorbed CO in this branch, because CO must adsorb before

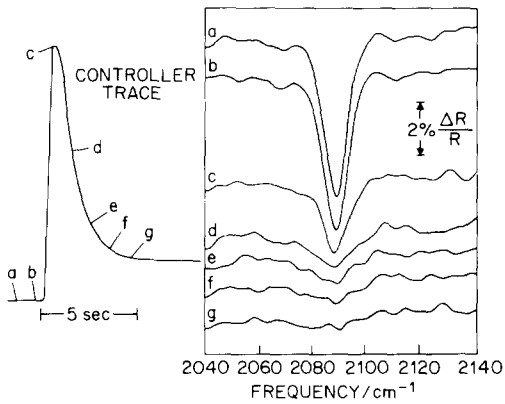

Fig. 56. Reaction ignition (spike), showing resistance controller trace and individual, 600 ms spectra collected at times shown. The reaction conditions are the same as for fig. 55 (from ref. [3]).

oxidizing. Since the CO_2 production rate is high, the adsorption rate must also be high. In contrast, the relatively slow rise in CO coverage during the low reaction-rate branch, especially in the later part of the branch, gives the first indication that the slow step driving the oscillations involved a slow variation in the number of surface sites available for CO adsorption.

Another striking feature of the oscillations is the "spike" at the ignition, or transition from low- to high-rate branch. Fig. 56 shows the spike for a typical cycle at an expanded time scale, and single-scan, 600 ms IR spectra collected during the spike. Once the ignition starts, the signal from adsorbed CO goes below the noise level in less than 3 s, while the spike itself lasts nearly 5 s. Combined with indirect spectral evidence that the oxygen coverage increases *during* the spike [3,413], these observations indicate that the spike (or enhanced reaction rate) is due to a relatively high product of *both* CO and O concentrations.

Moreover, the peak frequency remains approximately constant during the spike, while the integrated absorption of the peak decreases. This suggests that during the spike, the chemisorbed CO remains compressed into islands, as compared to the high-to-low reaction-rate branch transition, where the larger frequency shift indicates that CO initially adsorbs into more dispersed sites on the surface.

Burrows et al. proceeded to investigate the state of the surface at each stage of the oscillations by quenching the Pt sample and titrating it with CO, as described in ref. [413]. The results indicated a slow deactivation, in the high reaction-rate branch, of the surface sites that are active towards CO adsorption, and a slow recovery of these sites in the low reaction-rate branch. The nature of the blocking species was then uncovered by simultaneous AES and IRRAS studies. It was found that, contrary to accepted models, surface oxide

did not drive the oscillations. Instead, the appearance and removal of carbon at the surface was directly correlated to the period of the oscillations.

4.4.1.2. Hydrogen-assisted CO dissociation during methanation reaction on Ru(001). In their work, Hoffmann and Robbins [142] investigated whether the dissociation of CO during the well-accepted Fischer–Tropsch reaction:

$CO \rightarrow CO_{ads} \rightarrow C_{ads} + O_{ads}$,

$C_{ads} + 4\,H \rightarrow CH_4$,

$O_{ads} + 2\,H \rightarrow H_2O$,

is the rate-limiting step and whether hydrogen promotes this reaction. In particular, they monitored the CO stretch absorption band for CO adsorbed on Ru(001) under methanation conditions, with pure CO (2.5 Torr) and $CO : H_2$ mixtures (2.5 Torr each). In the case of pure CO, a relatively high reaction temperature of 650 K is required to observe a decrease in C–O stretch intensity, which indicates dissociation of CO. In the presence of hydrogen, the reaction occurs on a considerably faster time scale and requires a lower reaction temperature of 500 K. The rates of these reactions can be obtained by plotting the normalized logarithmic decrease in total CO coverage as a function of reaction time, as shown in figs. 57 and 58. The linear dependence in both cases indicates first-order reactions. Variation as a function of the reaction temperature (fig. 57) shows that CO dissociation is activated on Ru(001) with an activation energy of 20 kcal. From the plots in figs. 57 and 58, turn-over frequencies of 3×10^{-4} s^{-1} for CO (650 K) and 3×10^{-2} s^{-1} for $CO + H_2$ (500 K) are obtained. The presence of hydrogen thus increases the dissociation rate of CO by more than two orders of magnitude.

Hoffmann and Robbins suggest that the effect of hydrogen in the dissociation of CO is due to the reaction of hydrogen with oxygen from dissociated

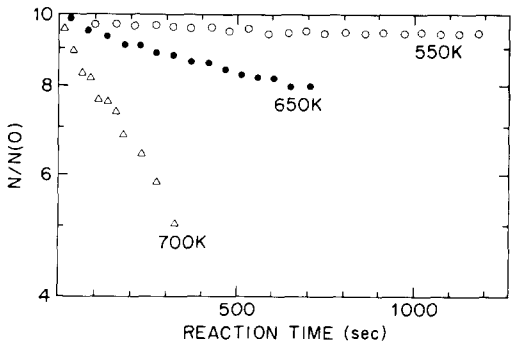

Fig. 57. Decrease of the total CO coverage versus reaction time for CO/Ru(001) at 2.5 Torr and various reaction temperatures. The linear behavior of $\ln(\theta/\theta_0)$ versus time indicates that this reaction is first order over a wide range of CO coverage (with permission from ref. [142]).

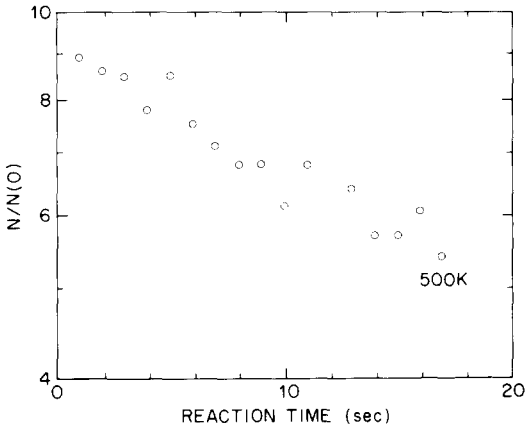

Fig. 58. Decrease of the total CO coverage in the presence of hydrogen at a reaction temperature of 500 K and 1:1 $CO:H_2$ ratio, indicating an increase of the reaction rate of more than two orders of magnitude compared to pure CO (cf. fig. 57) (with permission from ref. [142]).

CO to form water (last step in the reaction scheme). Water is a major reaction product in methanation over ruthenium and preliminary data [415] indicate that this reaction is very fast ($(5–25)\times 10^{-2}$ s^{-1} at 500 K). At higher temperatures both CO dissociation and recombination can occur, hydrogen can act as scavenger and remove oxygen via water formation to prevent the recombination of CO in favor of CO dissociation.

The decrease in CO intensity is due to the build-up of carbon on the surface. It is well known in the catalysis literature that the dissociation of CO in the absence of hydrogen causes CO disproportionation, which produces CO_2 as gas-phase product and surface carbon, i.e. $2CO \rightarrow CO_2(g) + C_{ads}$. This reaction scheme is confirmed also for Ru(001) with post-reaction spectroscopy. Oxygen titration of the remaining surface carbon exhibits features in the thermal desorption spectrum characteristic of carbidic carbon, which is considered a reactive form of carbon in the methanation of CO [416].

The observation that the decrease of the C–O stretching band occurs at constant frequency is also significant. It indicates that in spite of a decrease in total CO coverage, the *local coverage of the CO layer remains constant*. Just as in the previous example, this fact made it possible to use the integrated area of the absorption band as a measure of the total CO coverage. It is also indicative of island formation so that, under reaction conditions, carbon forms islands on Ru(001).

4.4.2. Adsorbate reconfiguration and diffusion

4.4.2.1. Temperature programmed IRRAS on Ni(100). In the previous two examples, the data is acquired rapidly ($\sim$ 100 ms) over a broad spectral range

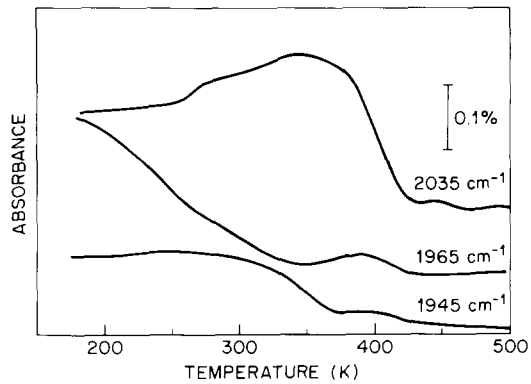

Fig. 59. Temperature programmed IRRA spectra (single frequency) of CO on Ni(100), starting from a CO-saturated surface at 190 K and ramping the temperature at 1 K/s. The top curve (2035 cm^{-1}) is assigned to CO adsorbed on top positions, the middle curve (1965 cm^{-1}) to CO adsorbed at symmetric bridge sites (high density), and the bottom curve (1945 cm^{-1}) to isolated CO adsorbed at bridge sites (with permission from ref. [418]).

by means of fast-scanning interferometers. However, kinetic data can also be obtained with dispersive instruments by monitoring an absorption band (at a fixed frequency) as a function of time. With such a restriction, a time resolution of ~ 10 ms has been achieved by Benziger et al. [417], who have used this set-up in conjunction with temperature programmed treatment to study the phase transformation of CO on Ni(100) and the structure of adsorbed intermediates formed during the reaction of acetic acid on Ni(100).

An example of the data is shown in fig. 59, where the absorption monitored at 2035, 1965 and 1945 cm^{-1} is plotted versus temperature during a heating cycle. From steady-state spectroscopic studies, Benziger and Schoofs [418] have assigned these three frequencies to on-top CO (2035 cm^{-1}), bridge-site and isolated CO (1945 cm^{-1}) and bridge-site CO with high packing density (1965 cm^{-1}). The data in fig. 59 are taken as evidence for a population of the on-top sites before desorption.

Another example is shown in fig. 60a. The absorption corresponding to the CH_3COOH monomer symmetric (1438 cm^{-1}) and asymmetric (1603 cm^{-1}) stretches is plotted as a function of sample temperature [419]. These modes are schematically depicted with double-sided arrows next to the center unit in fig. 60b, labelled S.S. and A.S. for the symmetric and antisymmetric stretch modes, respectively. The increase of the symmetric stretch absorption above 240 K, with the corresponding decrease of the asymmetric stretch absorption, is interpreted as the loss of a H to form bridge-bonded monodentate acetate (CH_3COO) adsorbed with its axis normal to the surface. The subsequent decrease of the symmetric stretch intensity at 320 K, while the asymmetric

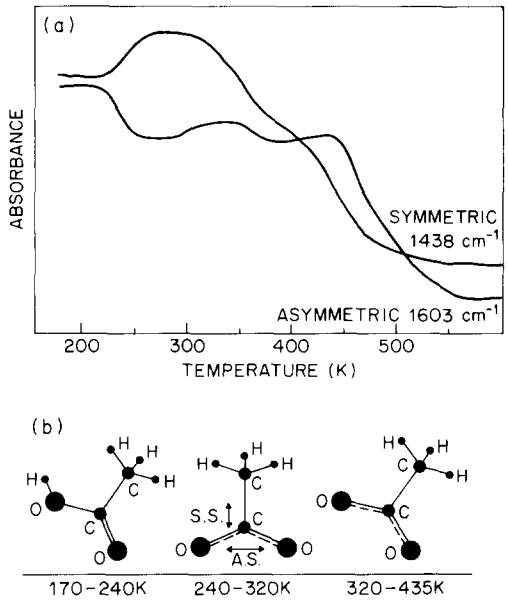

Fig. 60. (a) Temperature programmed IRRA spectra (single frequency) of adsorbed acetic acid monomer (CH_3COOH). (b) Proposed reaction and structure of monomer during heating (with permission from ref. [419]).

stretch intensity increases slightly, is taken as an indication of the formation of a monodentate acetate as a precursor to decomposition.

It must be pointed out that the most serious problem associated with the spectroscopic kinetic measurements presented above (including section 4.4.1) is the assumption that the integrated intensity of an adsorbate mode is linearly proportional to the coverage or state of that adsorbate. Such a linear relationship is an exception rather than a rule and must be confirmed independently and rigorously. Additional problems associated with the single-frequency monitoring of the last example stem from the fact that the electronic absorption of the surface changes as a function of temperature, reconstruction and adsorbate coverage (see section 4.1.5.2 for example). In fact, broadband absorption changes occurring upon O adsorption on Pt were used by Burrows et al. [413] to study oxygen adsorption during oscillations! Consequently, careful calibrations at many different frequencies are necessary before conclusions can be drawn. Such calibrations require a high level of reproducibility of *all* experimental parameters. Finally, even with a perfect calibration, transient phenomena may not be clearly interpretable due to transient extraneous effects that cannot be calibrated.

4.4.2.2. CO diffusion on Pt(111). Time-resolved infrared spectroscopy can also be used to monitor the time evolution of specific chemical species

subsequent to a disturbance that is fast compared to the time required to achieve an equilibrium configuration. In general, a temperature-jump perturbation produced by conventional thermal heating is slow compared to the corresponding surface processes. However, lasers could be used to prepare the surface in a non-equilibrium state. Alternatively, a coverage-jump perturbation is an attractive idea and is being developed to investigate diffusion-limited processes.

In such a θ-jump experiment, a pulsed molecular beam is required to deposit a measurable amount of molecules (0.01 to 0.1 ML) in a fraction of a millisecond, i.e. faster than the time resolution of the infrared spectrometer. For example, if a few percent of a CO monolayer is deposited randomly on a stepped Pt(111) surface, the chemisorbed molecules will initially be distributed uniformly (i.e. mostly on terraces), and the corresponding IRRA spectrum will be dominated by the terrace CO stretch mode at 2089 cm^{-1} (see section 4.1.3). However, since the CO molecules are more strongly bound at steps, they will diffuse to the nearby steps, giving rise to a new CO stretch mode around 2064 cm^{-1}. Since the time evolution of the IRRAS spectra is related to the diffusion on the (111) terraces, the diffusion barrier can be extracted from a series of time-resolved runs as a function of temperature, if *a proper treatment of the vibrational integrated intensities* is performed. That is, the dipole–dipole interactions and the electronic polarizability associated with the CO stretch must be measured in separate steady-state experiments, and used in modelling the spectral time evolution.

Such experiments can be carried out either with dispersive instruments with multi-channel detection or with interferometers. At the time of this review, several groups are developing such systems but no results have appeared yet. It is clear, however, that these experiments are technologically feasible [420]. More importantly, the information available from such studies is unique. For instance, diffusion measurements by SIRS are not hindered by the problems associated with other techniques. Indeed, field emission techniques using fluctuation spectroscopy [421,422] do not distinguish the chemical identity of the diffusing species and are subject to high field effects. Laser desorption techniques [423] measure macroscopic diffusion for which the role of defects may be dominant. Finally, helium diffraction techniques depend on understanding the long-range order and cannot distinguish easily between different chemical species. Consequently, diffusion measurements by SIRS are important and complementary, although they too are subject to modelling.

For fast-scanning interferometers, the time resolution is set by the repeat time between mirror scans, approximately 18 ms for 16 cm^{-1} resolution. However, the implementation of the method developed by Mantz to study events that can be reproducibly repeated is possible and should increase the time resolution to the data acquisition and digitization time between data points, i.e. $\sim 20\ \mu s$ [276,424]. The method is as follows: the first point of the

interferogram is taken as the event is initiated at the surface ($t = 0$), then the subsequent points of the scan are collected ($t = 1 \rightarrow i$) during one time period. These points are sent to time-bin #1. The next series of points ($i + 1 \rightarrow 2i$) are then collected and sent to time-bin #2. And so forth until the scan is over. So, for an interferogram with n points, $k = n/i$ time-bins are created. The next scan starts after a delay Δt (usually equal to the time necessary to accumulate i data points) with respect to the surface event at $t = 0$. The first i points of the interferogram are therefore sent to time-bin #2, and so on. The process must be repeated k times to fill all the time-bins with $n = ki$ points. In this manner, high resolution spectra can be obtained with good time resolution (~ 100 μs). The success of this method rests on the perfect reproducibility of the event and has not yet been demonstrated for surface studies.

5. Conclusions and outlook

Surface infrared spectroscopy has grown mature enough that its real and serious problems are becoming more apparent. The last section (selected examples) should have made it clear that many of the conclusions drawn from SIRS studies are not straightforward and several aspects are not understood. For instance, the detailed interpretation of the vibrational spectra (including missing bands) for the simple system of CO on Pt(111) is not complete [425], particularly for stepped surfaces and alkali-covered surfaces. The geometrical information (e.g. dimer length variation) inferred from analysis of the H symmetric stretch wavenumber on W(100) and Mo(100) has a 50% uncertainty (section 4.1.4.2). The ability of the technique to measure experimentally the orientation of molecular bonds, such as Si–H on Si(100), is very unreliable (see end of section 4.1.5.1), i.e. the data can merely be used as a test of the theoretically derived structure. Our understanding of surface electronic absorption in the infrared region is poor, although such absorption is important to the spectroscopy in general. The whole field of line shape analysis is still based on shaky grounds. Inhomogeneous broadening remains in general a very large component of the line width. A number of *different* mechanisms can all give rise to temperature, isotopic and coverage dependences. Finally, the use of vibrational mode intensity to determine the surface coverage, a critical step for all kinetic studies, is subject to several problems that cannot always be solved adequately.

Yet, progress has been made and SIRS has contributed respectably to the field of surface science, mostly because recent SIRS studies have tended to consider the problems listed above and have relied on a more multi-technique approach than earlier studies. Advances in theory have also added to the value of vibrational data, particularly for the thorough and quantitative analysis of H adsorption on metal and semiconductor surfaces. Moreover, the develop-

ment of the field has benefited greatly from input from other fields such as gas-phase spectroscopy, laser spectroscopy, molecular beam spectroscopy and chemical vapor deposition. In fact, some growing areas in SIRS rely heavily on such new technology.

There are three general areas where surface infrared spectroscopy is likely to make an impact: (1) in situ studies of catalytic (metals) and chemical vapor deposition (semiconductors) processes, (2) studies of dynamics at surfaces (e.g. vibrational energy transfer), and (3) studies of kinetics at surfaces (e.g. diffusion). All these rely on the properties that are specific to SIRS: high resolution, polarization properties, time resolution and compatibility with high pressures.

Beside the examples given in section 4.4.1 involving catalytic processes, in situ studies of semiconductor surfaces have recently been initiated in an effort to understand the fundamentals of chemical vapor deposition. For example, the recent study of the laser-induced decomposition of $Fe(CO)_5$ on Si(111) using multiple internal reflections has contributed to uncovering the mechanism and energetics of the process [426]. SIRS studies of chemically prepared silicon surfaces have pointed out the relevance of hydride formation to the very low measured surface recombination velocity [427]. As a result, several groups are incorporating SIRS to their experimental apparatus for in situ monitoring and exciting new results should appear soon.

Direct measurements of vibrational lifetimes are about to be performed for adsorbates on single crystal surfaces with picosecond laser spectroscopy. The pump–probe technique implemented by Cavanagh et al. [229] has proven useful to monitor the transient response of metal carbonyls, in particular metal carbonyl compounds, such as $Co_4(CO)_{12}$. An example of the data is shown in fig. 61 where the transient bleaching of the CO stretch mode at 2075 cm^{-1} is plotted as a function of probe delay times. The data cannot be described by a single exponential decay, but rather by a slow decay (427 ± 44 ps) and a fast decay (40 ± 12 ps). Cavanagh et al. suggest that the rapid decay corresponds to intermode (intra-molecular) relaxation followed by the slower population decay. While such multi-component decay processes are expected, the $Co_4(CO)_{12}$ data provide a case where the time scales of the processes are readily separable. Recently, the same group has lowered the fractional noise level in their pump–probe experiment to 4×10^{-4} [428], which should be sufficient to detect the bleaching of CO on single crystal metallic samples. Also, as mentioned in section 3.3.1.2, the sum generation technique is an attractive alternative to the one-color pump–probe technique for vibrational lifetime measurements. However, line shape analysis may still remain the only viable approach for *weak* vibrational modes on *metal* surfaces. It is therefore expected that it will continue be an active part of SIRS.

Kinetic measurements will certainly be a growing area of SIRS because such phenomena are an intrinsic aspect of all surface studies, and yet are very

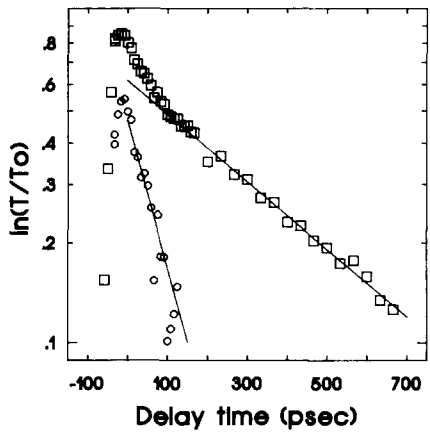

Fig. 61. Transient response of the CO stretch mode (E symmetry in C_{3v} point group) at 2075 cm^{-1} measured by IR-pump–IR-probe technique (mole fraction $= 1.4 \times 10^{-4}$). The open squares are the total bleaching signal and the straight line a fit of the long time data giving $T_1 = 437$ ps. The residuals between this fit and the observed transient are shown in smaller circles in the lower trace. The straight line fit of those data points yields $T_1 = 40$ ps (with permission from ref. [229]).

poorly understood. The combination of pulsed-molecular beams or pulsed-laser beams with time-resolved SIRS will make it possible to monitor non-equilibrium dynamics such as molecular motion and reactions at surfaces in a manner very complementary to time-resolved EELS, laser desorption techniques and field emission studies. While multichannel detection will improve the spectral response of time-resolved dispersive instrument, the implementation of Mantz's time-resolved technique for repetitive processes will improve the time resolution of interferometers. With such developments in sight, the prospect is good for new understanding of surface transients. In addition to experimental and theoretical efforts in new directions, the field is also ready for more widespread and systematic studies of *different* systems, involving a variety of adsorbates and substrates and many types of bonding mechanisms (physisorption, chemisorption). However, to carry out such studies, a stronger effort by researchers in different fields is necessary. It is hoped that this review will motivate the increasing use and development of surface infrared spectroscopy to further our understanding of surface phenomena.

Acknowledgements

This review was made possible thanks to the help of many colleagues, each one adding a new dimension to this work. In particular, the author is grateful for many stimulating discussions with R.G. Tobin, D.M. Riffe, M.D. Stiles, V.M. Bermudez, F.M. Hoffmann, A.L. Harris, L. Rothberg, G.S. Higashi, M.

Trenary, R.R. Cavanagh, J.E. Reutt, D.J. Doren, and V.A. Burrows. Substantial input on the theory section was provided by D.R. Hamann, J.C. Tully, K. Raghavachari, M.S. Hybertsen and P. Nordlander. The author is grateful to A.M. Bradshaw and E. Schweizer for sending their review article prior to publication.

Glossary of acronyms and abbreviations

ADC	Analog-to-digital converter
AES	Auger electron spectroscopy
APP	Avalanche periodic photodetector
ARUPS	Angle-resolved ultraviolet photoemission spectroscopy
CPA	Coherent-potential approximation
EAM	Embedded atom method
EELS	Electron energy loss spectroscopy
EMT	Effective medium theory
ER	External reflection
ES	Emission spectroscopy
ESDIAD	Electron-stimulated-desorption-ion-angular-distribution
FCS	Free carrier scattering
FWHM	Full width at half maximum
IABS	Inelastic atom beam scattering
IRRAS	Infrared reflection–absorption spectroscopy
LAPW	Linear augmented plane wave
LEED	Low energy electron diffraction
LDF	Local density functional
MIR	Multiple internal reflection
NEXAFS	Near-edge X-ray absorption fine structure
PAS	Photoacoustic spectroscopy
PDS	Photostimulated desorption spectroscopy
PEM	Photoelastic modulator
PEW	Plane electromagnetic wave
PTDS	Photothermal displacement spectroscopy
PZT	Piezoelectric transducer
RAS	Reflection–absorption spectroscopy
RMS	Root mean square
SEWS	Surface electromagnetic wave spectroscopy
SEXAFS	Surface extended X-ray absorption fine structure
SIRS	Surface infrared spectroscopy
SVS	Surface vibrational spectroscopy
UHV	Ultra-high vacuum
UPS	Ultraviolet photoelectron spectroscopy
XPS	X-ray photoelectron spectroscopy

References

[1] W. Ho, J. Phys. Chem. 91 (1987) 766.
[2] S. Pons, J. Electron Spectrosc. Related Phenomena 45 (1987) 303.
[3] V.A. Burrows, J. Electron Spectrosc. Related Phenomena 45 (1987) 41.
[4] P.L. Richards and R.G. Tobin, Infrared Spectroscopy of Adsorbates on Metals: Direct Absorption and Emission, in: Vibrational Spectroscopy of Molecules on Surfaces, Eds. J.T. Yates and T.E. Madey (Plenum, New York, 1987) pp. 417–463.
[5] J.F. Durana and J.D. McDonald, J. Chem. Phys. 64 (1967) 2518.
[6] G.E. Becker and G.W. Gobeli, J. Chem. Phys. 38 (1963) 2942.
[7] Y.J. Chabal, Surface Sci. 168 (1986) 594.
[8] S.A. Francis and A.H. Ellison, J. Opt. Soc. Am. 49 (1959) 131.
[9] D.L. Allara, Macromolecules 11 (1978) 1215;
M.D. Baker and M. Chesters, in: Vibrations at Surfaces, Eds. R. Caudano, J.-M. Gilles and A.A. Lucas (Plenum, New York, 1982) p. 289.
[10] Z. Schlesinger and A.J. Sievers, Surface Sci. 102 (1981) L29.
[11] D.L. Allara, D. Teicher and J.F. Durana, Chem. Phys. Letters 84 (1981) 20.
[12] G.N. Zhizhin, E.A. Vinogradov, M.A. Moskalova and V.A. Yakovlev, Appl. Spectrosc. Rev. 18 (1982–83) 171.
[13] C.K.N. Patel and A.C. Tam, Rev. Mod. Phys. 53 (1981) 517.
[14] M.A. Olmstead, N.M. Amer, S. Kohn, D. Fournier and A.C. Boccara, Appl. Phys. A32 (1983) 41.
[15] F.M. Hoffmann, Surface Sci. Rept. 3 (1983) 107.
[16] P. Hollins and J. Pritchard, Progr. Surface Sci. 19 (1985) 275.
[17] B.E. Hayden, Reflection Absorption Infrared Spectroscopy, in: Vibrational Spectroscopy of Molecules on Surfaces, Eds. J.T. Yates and T.E. Madey (Plenum, New York, 1987) pp. 265–344.
[18] A.M. Bradshaw and E. Schweizer, Infrared Reflection–Absorption Spectroscopy of Adsorbed Molecules, in: Advances in Spectroscopy: Spectroscopy of Surfaces, Ed. R.E. Hester (Wiley, New York, 1988).
[19] H. Ueba, Progr. Surface Sci. 22 (1986) 181.
[20] R.G. Tobin, Surface Sci. 183 (1987) 226.
[21] N.V. Richardson and N. Sheppard, Normal Modes at Surfaces, in: Vibrational Spectroscopy of Molecules on Surfaces, Eds. J.T. Yates and T.E. Madey (Plenum, New York, 1987) pp. 1–48.
[22] L.H. Little, Infrared Spectra of Adsorbed Molecules (Academic Press, New York, 1966).
[23] M.L. Hair, Infrared Spectroscopy in Surface Chemistry (Dekker, New York, 1967).
[24] A.T. Bell, Infrared Spectroscopy of High-Area Catalytic Surfaces, in: Vibrational Spectroscopy of Molecules on Surfaces (Plenum, New York, 1987) pp. 105–134.
[25] J.B. Marion, Classical Electromagnetic Radiation (Academic Press, New York, 1965).
[26] R.G. Greenler, J. Chem. Phys. 44 (1966) 310.
[27] J.D.E. McIntyre and D.E. Aspnes, Surface Sci. 24 (1971) 417.
[28] M.J. Dignam and M. Moskovits, Symp. Faraday Soc. 4 (1970) 208.
[29] M.J. Dignam and M. Moskovits, J. Chem. Soc. Faraday II. 69 (1973) 65.
[30] Y.J. Chabal, Vibrational Properties of Semiconductor Surfaces and Interfaces, in: Semiconductor Interfaces: Formation and Properties, Eds. G. LeLay and J. Derrien, Springer Proc. Phys. Vol. 22 (1987) 301 (Springer, Berlin, 1987).
[31] H. Ibach and D.L. Mills, Electron Energy Loss Spectroscopy and Surface Vibrations (Academic Press, New York, 1982).
[32] R.G. Greenler, J. Vacuum Sci. Technol. 12 (1975) 1410.
[33] N.J. Harrick, Internal Reflection Spectroscopy (Wiley, New York, 1967); 2nd printing by Harrick Scientific Corporation, Ossining, NY, 1979, pp. 42–44.

[34] F. Wooten, Optical Properties of Solids (Academic Press, New York, 1972) pp. 42–51.
[35] G.D. Mahan and A.A. Lucas, J. Chem. Phys. 68 (1978) 1344.
[36] Ref. [31], pp. 93–98.
[37] P. Chiaradia, Optical Properties of Surfaces and Interfaces, in: Semiconductor Interfaces: Formation and Properties, Eds. G. Lelay and J. Derrien, Springer Proc. Phys. Vol. 22 (1987) 290 (Springer, Berlin, 1987).
[38] P.J. Feibelman, Progress Surface Sci. 12 (1982) 287.
[39] A. Bagchi and A.K. Rajagopal, Solid State Commun. 31 (1979) 127.
[40] A. Bagchi, R.G. Barrera and A.K. Rajagopal, Phys. Rev. B33 (1979) 4824.
[41] M.A. Olmstead, Surface Sci. Rept. 6 (1986) 159.
[42] A. Selloni, P. Marsella and R. Del Sole, Phys. Rev. B33 (1986) 8885.
[43] A. Selloni and R. Del Sole, Surface Sci. 168 (1986) 35.
[44] W.L. Mochan and R.G. Barrera, Phys. Rev. Letters 56 (1986) 2221.
[45] P. Hohenberg and W. Kohn, Phys. Rev. 136 (1964) B864.
[46] W. Kohn and L.J. Sham, Phys. Rev. 140 (1965) A1133.
[47] O.K. Andersen, Phys. Rev. B12 (1975) 3060.
[48] L.F. Mattheiss and D.R. Hamann, Phys. Rev. B33 (1986) 823.
[49] For a history of pseudopotentials, see G.B. Bachelet, D.R. Hamann and M. Schlüter, Phys. Rev. B26 (1982) 4199.
[50] D.R. Hamann, J. Electron Spectrosc. Related Phenomena 44 (1987) 1.
[51] J.A. Appelbaum and D.R. Hamann, Phys. Rev. Letters 34 (1975) 806.
[52] P.J. Feibelman, Phys. Rev. Letters 58 (1987) 2766; Phys. Rev. B35 (1987) 2626.
[53] U. Backes and H. Ibach, Solid State Commun. 40 (1981) 575.
[54] P.J. Feibelman and D.R. Hamann, Surface Sci. 179 (1987) 153.
[55] M.A. Barteau, J.Q. Broughton and D. Menzel, Surface Sci. 133 (1983) 443.
[56] H. Conrad, R. Scala, W. Stenzel and R. Unwin, J. Chem. Phys. 81 (1984) 6371.
[57] R. Biswas and D.R. Hamann, Phys. Rev. Letters 56 (1986) 2291.
[58] M. Weinert, A.J. Freeman and S. Ohnishi, Phys. Rev. Letters 56 (1986) 2295.
[59] M.R. Barnes and R.F. Willis, Phys. Rev. Letters 41 (1978) 1729.
[60] J.P. Woods and J.L. Erskine, Phys. Rev. Letters 55 (1985) 2595.
[61] W. Ho, R.F. Willis, and E.W. Plummer, Phys. Rev. Letters 40 (1978) 1463.
[62] Y.J. Chabal, Phys. Rev. Letters 55 (1985) 845.
[63] P.J. Feibelman and D.R. Hamann, Surface Sci. 182 (1987) 411.
[64] A.M. Baró, H. Ibach and H.D. Bruchmann, Surface Sci. 88 (1979) 384.
[65] L.J. Richter and W. Ho, Phys. Rev. B36 (1987) 9797.
[66] J.E. Reutt, Y.J. Chabal and S.B. Christman, J. Vacuum Sci. Technol. (June/July 1988).
[67] D.R. Hamann and P.J. Feibelman, Phys. Rev. B37 (1988) 3847.
[68] L.J. Richter and W. Ho, J. Vacuum Sci. Technol. A5 (1987) 453.
[69] D. Tománek, S.G. Louie and C.-T. Chan, Phys. Rev. Letters 57 (1986) 2594.
[70] C. Nyberg and C.G. Tengstal, Phys. Rev. Letters 50 (1983) 1680.
[71] M. Weinert and J.W. Davenport, Phys. Rev. Letters 54 (1985) 1547.
[72] C. Umrigar and J.W. Wilkins, Phys. Rev. Letters 54 (1985) 1547.
[73] S. Andersson, Chem. Phys. Letters 55 (1978) 185.
[74] S.R. Chubb and W.E. Pickett, Phys. Rev. Letters 58 (1987) 1248.
[75] P.J. Feibelman and D.R. Hamann, Surface Sci. 173 (1986) L582.
[76] P.J. Feibelman and D.R. Hamann, Surface Sci. 186 (1987) 460.
[77] A. Redondo and W.A. Goddard III, J. Vacuum Sci. Technol. 21 (1982) 344.
[78] W.J. Hehre, L. Radon, P.V.R. Schleyer and J.A. Pople, Ab Initio Molecular Orbital Theory (Wiley, New York, 1986).
[79] Y.J. Chabal and K. Raghavachari, Phys. Rev. Letters 53 (1984) 282.
[80] J.A. Pople, R. Krishnan, H.B. Schlegal and J.S. Binkley, Int. J. Quantum Chem. Symp. 13 (1979) 225; 15 (1981) 269.

[81] K. Raghavachari, J. Chem. Phys. 81 (1984) 2717.
[82] R. Krishnan, M.J. Frisch and J.A. Pople, J. Chem. Phys. 72 (1980) 4244, and references therein.
[83] T.H. Upton and W.A. Goddard III, Phys. Rev. Letters 46 (1981) 1635; CRC Crit. Rev. Solid State Mater. Sci. 10 (1981) 261.
[84] T.H. Upton and W.A. Goddard III, Phys. Rev. Letters 42 (1979) 472.
[85] C.W. Bauschlicher and P.S. Bagus, Phys. Rev. Letters 52 (1984) 200.
[86] C.W. Bauschlicher and P.S. Bagus, Phys. Rev. Letters 54 (1985) 349.
[87] I.P. Batra, P.S. Bagus and K. Hermann, Phys. Rev. Letters 52 (1984) 384.
[88] J.K. Nørskov, Phys. Rev. B20 (1979) 446.
[89] J.K. Nørskov and N.D. Lang, Phys. Rev. B21 (1980) 2136.
[90] P. Nordlander, S. Holloway and J.K. Nørskov, Surface Sci. 136 (1984) 59.
[91] O.K. Andersen, in: The Electronic Structure of Complex Systems, NATO Advanced Study Institute, Eds. W. Temmerman and P. Phariseau (Plenum, New York, 1982).
[92] M.J. Puska, R.M. Nieminen, M. Manninen, B. Chakraborty, S. Holloway and J.K. Nørskov, Phys. Rev. Letters 51 (1983) 1081.
[93] C.M. Mate and G.A. Somorjai, Phys. Rev. B34 (1986) 7417.
[94] P. Nordlander and S. Holmström, Surface Sci. 159 (1985) 443.
[95] M.S. Daw and M.I. Baskes, Phys. Rev. B29 (1984) 6443.
[96] O. Gunnarsson and H. Hjelmberg, Phys. Scripta 11 (1975) 97.
[97] D. Newns, Phys. Rev. 178 (1969) 1123.
[98] T. Fondén, J. Idiodi, P. Johnsson, B.I. Lundqvist, A. Mällo and S. Papadia, unpublished.
[99] S.A. Adelman and B.J. Garrison, J. Chem. Phys. 65 (1976) 3751.
[100] J.D. Doll and D.R. Dion, J. Chem. Phys. 65 (1976) 3762.
[101] J.C. Tully, J. Chem. Phys. 73 (1980) 1975.
[102] J.C. Tully, Acc. Chem. Res. 14 (1981) 188.
[103] A. Nitzan and J.C. Tully, J. Chem. Phys. 78 (1983) 3959.
[104] J.C. Tully, J. Electron Spectrosc. Related Phenomena 45 (1987) 381.
[105] D.W. Noid, M.L. Koszykowski and R.A. Marcus, J. Chem. Phys. 67 (1977) 404.
[106] P.H. Berens and K.R. Wilson, J. Chem. Phys. 74 (1981) 4872.
[107] J.E. Adams, J. Chem. Phys. 84 (1986) 3589.
[108] J.C. Tully, Y.J. Chabal, K. Raghavachari, J.M. Bowman and R.R. Lucchese, Phys. Rev. B31 (1985) 1184.
[109] W.H. Miller and C.W. McCurdy, J. Chem. Phys. 69 (1978) 5163.
[110] U. Landman, R.N. Barnett, C.L. Cleveland and P. Nordlander, in: Tunneling, Eds. J. Jortner and B. Pullman (Reidel, Dordrecht, 1986) p. 269; and to be published.
[111] B.N.J. Persson and M. Persson, Solid State Commun. 36 (1980) 175; Surface Sci. 97 (1980) 609.
[112] B.N.J. Persson and R. Ryberg, Phys. Rev. Letters 48 (1982) 549.
[113] B. Hellsing and M. Persson, Phys. Scripta 29 (1984) 360, and references therein.
[114] J.W. Gadzuk and A.C. Luntz, Surface Sci. 144 (1984) 429, and references therein.
[115] R. Ryberg, Chem. Phys. Letters 83 (1981) 423. Note that the line widths reported here and in ref. [112] are dominated by inhomogeneities (see ref. [116]).
[116] R. Ryberg, J. Chem. Phys. 82 (1985) 567.
[117] R. Ryberg, Surface Sci. 114 (1982) 627.
[118] R. Ryberg, Phys. Rev. B32 (1985) 2671.
[119] S. Chiang, R.G. Tobin, P.L. Richards and P.A. Thiel, Phys. Rev. Letters 52 (1984) 648; S. Chiang, R.G. Tobin and P.L. Richards, J. Vacuum Sci. Technol. A2 (1984) 1069.
[120] J.C. Ariyasu, D.L. Mills, K.G. Lloyd and J.C. Hemminger, Phys. Rev. B28 (1983) 6123; B30 (1984) 504.
[121] G.P. Brivio and T.B. Grimley, J. Phys. C10 (1977) 2331.

[122] H. Metiu, J. Chem. Phys. 68 (1978) 1453;
H. Metiu and W.E. Palke, J. Chem. Phys. 69 (1978) 2574;
T. Maniv and H. Metiu, J. Chem. Phys. 72 (1980) 1996.
[123] P. Apell, Phys. Scripta 24 (1981) 795.
[124] J.W. Gadzuk, Phys. Rev. B24 (1981) 1651.
[125] H. Ueba, J. Chem. Phys. 77 (1982) 3759.
[126] B.N.J. Persson and N.D. Lang, Phys. Rev. B26 (1982) 5409.
[127] M. Persson and B. Hellsing, Phys. Rev. Letters 49 (1982) 662.
[128] B. Hellsing, M. Persson and B.I. Lundqvist, Surface Sci. 126 (1983) 147.
[129] P. Apell, Solid State Commun. 47 (1983) 615.
[130] D.C. Langreth, Phys. Rev. Letters 54 (1985) 126.
[131] Z. Crljen and D.C. Langreth, Phys. Rev. B35 (1987) 4224.
[132] R.S. Sorbello, Phys. Rev. B32 (1985) 6294.
[133] H. Morawitz, Phys. Rev. Letters 58 (1987) 2778.
[134] S. Van Smaalen and T.F. George, J. Chem. Phys. 87 (1987) 7307.
[135] B.N.J. Persson, J. Phys. C17 (1984) 4741.
[136] Z.Y. Zhang and D.C. Langreth, Phys. Rev. Letters 59 (1987) 2211.
[137] M.V. Klein, Localized Modes and Resonance States in Alkali Halides, in: Physics of Color Centers, Ed. W.B. Fowler (Academic Press, New York, 1968) pp. 514–530.
[138] R.G. Greenler, J. Chem. Phys. 50 (1969) 1963.
[139] R.G. Greenler, Japan. J. Appl. Phys. Suppl. 2(2) (1974) 265.
[140] Y.J. Chabal, E.E. Chaban and S.B. Christman, J. Electron Spectrosc. Related Phenomena 29 (1983) 35.
[141] J.C. Campuzano and R.G. Greenler, Rev. Sci. Instr. 52 (1981) 678.
[142] F.M. Hoffmann and J.L. Robbins, J. Electron Spectrosc. Related Phenomena 45 (1987) 421.
[143] W. Erley, J. Electron Spectrosc. Related Phenomena 44 (1987) 65.
[144] N.D.S. Canning and M.A. Chesters, J. Electron Spectrosc. Related Phenomena 29 (1983) 69.
[145] M.H. Greenblatt, Rev. Sci. Instr. 29 (1958) 738.
[146] G. Martin, Rev. Sci. Instr. 34 (1963) 707.
[147] T.P. Vogl, R.O. McIntosh and M. Garbuny, Rev. Sci. Instr. 36 (1965) 1439.
[148] M.M. Eisenstadt, Rev. Sci. Instr. 38 (1967) 134.
[149] R.W. Roberts, J.F. Harrod and H.A. Poran, Rev. Sci. Instr. 38 (1967) 1105.
[150] L.J. Schkolnick, Rev. Sci. Instr. 39 (1968) 122.
[151] S.E. Hannum, W.C. Mateyka, G.G. Possley and W.H. Smith, Rev. Sci. Instr. 40 (1969) 1254.
[152] W.W. Roepke, Rev. Sci. Instr. 41 (1970) 243.
[153] M. Kottle and R.G. Greenler, Rev. Sci. Instr. 42 (1971) 1235.
[154] P.E. Wierenga, G.J. Mollenhorst and A.T.B. Wikkering, Rev. Sci. Instr. 49 (1977) 408.
[155] T.J. Manuccia, J.R. Peele and C.E. Geosling, Rev. Sci. Instr. 52 (1981) 1857.
[156] P. Hollins and J. Pritchard, J. Vacuum Sci. Technol. 17 (1980) 665.
[157] D. Douglas Berger, Rev. Sci. Instr. 53 (1982) 1619.
[158] C. Damerow and W. Erley, J. Vacuum Sci. Technol. A5 (1987) 2974.
[159] H.G. Tompkins, in: Methods of Surface Analysis, Ed. A.W. Czanderna (Elsevier, New York, 1975) ch. 10, pp. 447–481.
[160] J. Pritchard, in: Moderne Verfahren der Oberflächenanalyse, Dechema Monogr. 78 (1975) 231.
[161] J. Pritchard and T. Catterick, in: Experimental Methods in Catalytic Research, Vol. 3, Eds. R.B. Anderson and P.T. Dawson (Academic Press, New York, 1976).
[162] R. Ryberg, J. Phys. Colloq. 44 (1983) C10–421.
[163] L.D. Landau and E.M. Lifshitz, Electrodynamics of Continuous Media (Pergamon, Oxford, 1960) pp. 279–284.
[164] A.J. Sievers, J. Opt. Soc. Am. 68 (1978) 1505, and references therein.

[165] B. Donovan, Elementary Theory of Metals (Pergamon, Oxford, 1967) pp. 215–227.
[166] J. Zenneck, Ann. Phys. 23 (1907) 846.
[167] A. Sommerfeld, Ann. Phys. 28 (1909) 665.
[168] G.N. Zhizhin, M.A. Moskaleva, E.V. Shomina and V.A. Yakovlev, in: Surface Polaritons, Eds. V.M. Agronovich and D.L. Mills (North-Holland, New York, 1982) pp. 93–143.
[169] A.D. Boardman, Electromagnetic Surface Modes (Wiley, New York, 1982).
[170] D.L. Mills and E. Burstein, Rept. Progr. Phys. 37 (1974) 817.
[171] R.W. Wood, Phys. Rev. 48 (1935) 928.
[172] U. Fano, J. Opt. Soc. Am. 31 (1941) 213.
[173] R.H. Ritchie, E.T. Arakawa, J.J. Cowan and R.N. Hamm, Phys. Rev. Letters 21 (1968) 1530.
[174] A. Otto, Z. Phys. 216 (1968) 398.
[175] E. Kretschmann and H. Raether, Z. Naturforsch. A23 (1968) 2135.
[176] R.J. Bell, R.W. Alexander and C.A. Ward, Surface Electromagnetic Wave Spectroscopy, in: Vibrational Spectroscopies for Adsorbed Species, Eds. A.T. Bell and M.L. Hair, ACS Symp. Ser. 137 (1980) 99.
[177] J. Schoenwald, E. Burstein and J.M. Elson, Solid State Commun. 12 (1973) 185.
[178] G.N. Zhizhin, M.A. Moskaleva, E.I. Firsov, E.V. Shomina, V.A. Yakovlev and V.I. Grigos, Soviet Phys. JETP 52 (1980) 282.
[179] G.N. Zhizhin, V.A. Sychugov, V.I. Silin and V.A. Yakovlev, Opt. Commun. 50 (1984) 141.
[180] G.N. Zhizhin, N.N. Morozov, M.A. Moskaleva, A.A. Sigarev, E.V. Shomina, V.A. Yakovlev and V.I. Grigos, Opt. Spectrosc. (USSR) 48 (1980) 102.
[181] J. Schoenwald and E. Burstein, in: Proc. Taormina Conf. on Polaritons, Ed. E. Burstein (Pergamon, New York, 1974) p. 139.
[182] J.D. McMullen, Solid State Commun. 17 (1975) 331.
[183] D.A. Bryan, D.L. Begley, K. Bhasin, R.W. Alexander, R.J. Bell and R. Gerson, Surface Sci. 57 (1976) 53.
[184] D.L. Begley, R.W. Alexander, C.A. Ward, R. Miller and R.J. Bell, Surface Sci. 81 (1979) 245.
[185] G.N. Zhizhin, M.A. Moskaleva, E.V. Shomina and V.A. Yakovlev, Soviet Phys. Solid State 21 (1979) 1630.
[186] G.N. Zhizhin, M.A. Moskaleva, E.V. Shomina and V.A. Yakovlev, Fiz. Met. Metalloved. 50, N3 (1980).
[187] Y.J. Chabal and A.J. Sievers. Appl. Phys. Letters 32 (1978) 90.
[188] Y.J. Chabal and A.J. Sievers, J. Vacuum Sci. Technol. 15 (1978) 639.
[189] Y.J. Chabal and A.J. Sievers, Phys. Rev. B24 (1981) 2921.
[190] M.A. Chesters, S.F. Parker and V.A. Yakovlev, Opt. Commun. 55 (1985) 17.
[191] Z. Schlesinger, B.C. Webb and A.J. Sievers, Solid State Commun. 39 (1981) 1035.
[192] E.S. Koteles and W.H. McNeill, Intern. J. Infrared Millimeter Waves 2 (1981) 361.
[193] Z. Schlesinger and A.J. Sievers, Solid State Commun. 43 (1982) 671.
[194] Z. Schlesinger and A.J. Sievers, Phys. Rev. B26 (1982) 6444.
[195] Y.J. Chabal and A.J. Sievers, Phys. Rev. Letters 44 (1980) 944.
[196] D.M. Riffe, L.M. Hanssen, A.J. Sievers, Y.J. Chabal and S.B. Christman, Surface Sci. 161 (1985) L559.
[197] Z. Schlesinger and A.J. Sievers, Appl. Phys. Letters 36 (1980) 409.
[198] V.A. Yakovlev, V.A. Sychugov and A.A. Khakimov, Soviet J. Quantum Electron. 13 (1983) 364.
[199] L.M. Hanssen, D.M. Riffe and A.J. Sievers, Opt. Letters 11 (1986) 782.
[200] R.E. Collin, Field Theory of Guided Waves (McGraw-Hill, New York, 1960) pp. 453–507.
[201] M.J.D. Low, J. Catalysis 4 (1965) 719.
[202] M.J.D. Low and I. Coleman, Spectrochim. Acta 22 (1966) 369.

[203] P.R. Griffiths, Chemical Infrared Fourier Transform Spectroscopy (Wiley, New York, 1975) ch. 12, pp. 308–329.
[204] D. Kember and N. Sheppard, Appl. Spectrosc. 29 (1975) 496.
[205] L.M. Gratton, S. Paglia, F. Scattaglia and M. Cavallini, Appl. Spectrosc. 32 (1978) 310.
[206] B. Jonson, B. Rebenstorf, R. Larrson and M. Primet, Appl. Spectrosc. 40 (1986) 798.
[207] J.F. Blanke and J. Overend, Spectrochim. Acta 32A (1976) 1383.
[208] P.L. Richards and L.T. Greenberg, in: Infrared and Millimeter Waves, Ed. K.J. Button (Academic Press, New York, 1982) pp. 149–207.
[209] H. Ibach, Surface Sci. 66 (1977) 56. Note that all reported values of e^*/e are too low by a factor of $\sqrt{2}$ as explained in A.M. Baró, H. Ibach and H.D. Bruchmann, Surface Sci. 88 (1979) 384.
[210] R.G. Tobin, S. Chiang, P.A. Thiel and P.L. Richards, Surface Sci. 140 (1984) 393.
[211] R.G. Tobin and P.L. Richards, Surface Sci. 179 (1987) 387.
[212] N.J. Harrick, Phys. Rev. Letters 4 (1960) 224.
[213] J. Fahrenfort, Spectrochim. Acta 17 (1961) 698.
[214] F.M. Mirabella and N.J. Harrick, Internal Reflection Spectroscopy: Review and Supplement (Harrick, Ossining, NY, 1985).
[215] P.A. Wilks and T. Hirschfeld, Appl. Spectrosc. Rev. 1 (1967) 99.
[216] G.L. Haller, R.W. Rice and Z.C. Wan, Catalysis Rev.-Sci. Eng. 13 (1976) 259.
[217] N.J. Harrick, Appl. Opt. 4 (1965) 1664.
[218] K.H. Beckmann, Surface Sci. 3 (1965) 314; 5 (1966) 187.
[219] K.H. Beckmann and N.J. Harrick, J. Electrochem. Soc. 118 (1971) 614.
[220] N.J. Harrick, Phys. Rev. Letters 125 (1962) 1165.
[221] B.D. McCombe, R.T. Holm and D.E. Schafer, Solid State Commun. 32 (1979) 603.
[222] W.C.M. Claassen and J. Dieleman, An In Situ Infrared Study of the Interaction of Oxygen and Fluorine Plasmas with Si and SiO_2 Surfaces, Topical Meeting on Microphysics of Surfaces, Beams and Adsorbates, Tech. Digest Ser. 1987, Vol. 9 (Optical Society of America, Washington, DC, 1987).
[223] A.C. Tam, Pulsed Laser Photoacoustic and Photothermal Detection, in: Photoacoustic and Thermal Wave Phenomena in Semiconductors (North-Holland, New York, 1987) pp. 176–198.
[224] S.R.J. Brueck, T.F. Deutsch and D.E. Oates, Appl. Phys. Letters 43 (1983) 157.
[225] F. Träger, H. Coufal and T.J. Chuang, Phys. Rev. Letters 49 (1982) 1720.
[226] G.S. Higashi and L.J. Rothberg, Appl. Phys. Letters 47 (1985) 1288.
[227] L.J. Rothberg, M. Bernstein and K.S. Peters, J. Chem. Phys. 79 (1983) 2569.
[228] L.J. Rothberg, J. Chem. Phys. 91 (1987) 3467.
[229] R.R. Cavanagh, E.J. Heilweil and J.C. Stephenson, J. Electron Spectrosc. Related Phenomena 45 (1987) 31.
[230] S. Ameri, E.A. Ash, V. Neumann and C.R. Petts, Electron. Letters 17 (1981) 337.
[231] M.A. Olmstead and N.M. Amer, J. Vacuum Sci. Technol. B1 (1983) 751.
[232] M.A. Olmstead and N.M. Amer, Phys. Rev. B33 (1986) 2564.
[233] M.A. Olmstead and N.M. Amer, Phys. Rev. Letters 52 (1984) 1148; Phys. Rev. B29 (1984) 7048.
[234] M.J.D. Low, Appl. Spectrosc. 40 (1986) 1011.
[235] J.R. Stevenson, H. Ellis and R. Barlett, Appl. Opt. 12 (1973) 2884.
[236] P. Meyer and D. Pettigrand, Rev. Phys. Appl. 11 (1976) 661.
[237] P. Lagarde, Infrared Phys. 18 (1978) 395;
P. Meyer and P. Lagarde, J. Phys. (Paris) 37 (1976) 1387.
[238] J.R. Stevenson and J.M. Cathcart, Nucl. Instr. Methods 172 (1980) 367.
[239] W.D. Duncan and G.P. Williams, Appl. Opt. 22 (1983) 2914.
[240] J. Schwinger, Phys. Rev. 70 (1946) 798; 75 (1949) 1912.

[241] A.A. Sokolov and I.M. Ternov, Synchrotron Radiation (Pergamon, Oxford, 1968).
[242] J. Yarwood, T. Shuttelworth, J.B. Hasted and T. Nanba, Nature 312 (1984) 742.
[243] E. Schweizer, J. Nagel, W. Braun, E. Lippert and A.M. Bradshaw, Nucl. Instr. Methods A239 (1985) 680.
[244] V.M. Bermudez, R.L. Rubinovitz and J.E. Butler, J. Vacuum Sci. Technol. (June/July 1988).
[245] J.E. Butler, V.M. Bermudez and J.L. Hylden, Surface Sci. 163 (1985) L708;
V.M. Bermudez, J.L. Hylden and J.E. Butler, J. Electron Spectrosc. Related Phenomena 38 (1986) 143.
[246] V.M. Bermudez and V.H. Ritz, Appl. Opt. 17 (1978) 542.
[247] J.L. Wragg, H.W. White and L.F. Sutcu, Rev. Sci. Instr. 59 (1988) 89; Phys. Rev. B37 (1988) 2508.
[248] D.K. Lambert, Phys. Rev. Letters 50 (1983) 2106.
[249] D.K. Lambert, J. Vacuum. Sci. Technol. B3 (1985) 1479.
[250] D.K. Lambert, J. Electron Spectrosc. Related Phenomena 30 (1983) 59.
[251] F.M. Hoffmann, N.J. Levinos, B.N. Perry and P. Rabinowitz, J. Electron Spectrosc. Related Phenomena 38 (1986) 153; Phys. Rev. B33 (1986) 4309.
[252] P. Rabinowitz, A. Stein, R. Brickman and A. Kaldor, Appl. Phys. Letters 35 (1979) 739.
[253] X.D. Zhu, H. Suhr and Y.R. Shen, Phys. Rev. B35 (1987) 3047.
[254] J.H. Hunt, P. Guyot-Sionnest and Y.R. Shen, Chem. Phys. Letters 133 (1987) 189.
[255] P. Guyot-Sionnest, J.H. Hunt and Y.R. Shen, Phys. Rev. Letters 59 (1987) 1597.
[256] A.L. Harris, C.E.D. Chidsey, N.J. Levinos and D.N. Loiacono, Chem. Phys. Letters 141 (1987) 350.
[257] D.R. Mattson, Appl. Spectrosc. 32 (1978) 335.
[258] P.R. Griffiths, R.G. Greenler and N. Sheppard, Appl. Spectrosc. 31 (1977) 448.
[259] P.R. Griffiths, H.J. Sloane and R.W. Hannah, Appl. Spectrosc. 31 (1977) 485.
[260] D.H. Chenery and N. Sheppard, Appl. Spectrosc. 32 (1978) 79.
[261] W.G. Golden, D.D. Saperstein, M.W. Severson and J. Overend, J. Phys. Chem. 88 (1984) 574.
[262] W.G. Golden, D.S. Dunn and J. Overend, J. Catalysis 71 (1981) 395.
[263] M.A. Chesters, S.F. Parker and R. Raval, Surface Sci. 165 (1986) 179.
[264] P.R. Griffiths and J.A. de Haseth, Fourier Transform Infrared Spectrometry, Vol. 83 of Chemical Analysis Ser., Eds. P.J. Elving and J.D. Winefordner (Wiley, New York, 1986) ch. 7.
[265] W.H. Steel, Interferometry (Cambridge Press, Cambridge, 1967).
[266] R.J. Bell, Introductory Fourier Transform Spectroscopy (Academic Press, New York, 1972).
[267] J. Chamberlain, G.W. Chantry and N.W.B. Stone, The Principle of Interferometric Spectroscopy (Academic Press, New York, 1979).
[268] M.J. Dignam and M.D. Baker, J. Vacuum Sci. Technol. 21 (1982) 80; Appl. Spectrosc. 35 (1981) 186.
[269] Ref. [264], p. 261.
[270] L.A. Nafie and M. Diem, Appl. Spectrosc. 33 (1979) 130.
[271] L.A. Nafie, E.D. Lipp and C.G. Zimba, Proc. Soc. Photo-Opt. Instr. Eng. 289 (1981) 457.
[272] L.A. Nafie and D.W. Vidrine, in: Fourier Transform Spectroscopy: Applications to Chemical Systems, Vol. 3, Eds. J.R. Ferraro and L.J. Basile (Academic Press, New York, 1982).
[273] H. Bar-Lev, Infrared Phys. 7 (1967) 93.
[274] L. Genzel, H.R. Chandrasekhar and J. Kuhl, Opt. Commun. 18 (1976) 381.
[275] P.R. Griffiths, Appl. Spectrosc. 31 (1977) 284.
[276] A.W. Mantz, Appl. Opt. 17 (1978) 1347.
[277] R.J. Keyes, Ed., Optical and Infrared Detectors, Vol. 19 of Topics in Applied Physics (Springer, Berlin, 1977) chs. 2–5.
[278] R.H. Kingston, in: Detection of Optical and Infrared Radiation, Vol. 10 of Springer Series in Optical Sciences, Ed. D.L. Mac Adam (Springer, Berlin, 1978).

[279] Ref. [264], pp. 209–217.
[280] See, e.g., D.J. Frankel, C. Yu, J.P. Harbison and H.H. Farrell, J. Vacuum Sci. Technol. B5 (1987) 1113.
[281] Y.J. Chabal, Phys. Rev. Letters 50 (1983) 1850.
[282] Y.J. Chabal, G.S. Higashi and S.B. Christmann, Phys. Rev. B28 (1983) 4472.
[283] H. Ibach, H. Hopster and B. Sexton, Appl. Surface Sci. 1 (1977) 1;
H. Ibach and S. Lehwald, J. Vacuum Sci. Technol. 15 (1978) 407.
[284] H. Steininger, H. Ibach and S. Lehwald, Surface Sci. 117 (1982) 685.
[285] L.L. Kesmodel, L.H. Dubois and G.A. Somorjai, Chem. Phys. Letters 56 (1978) 267; J. Chem. Phys. 70 (1979) 2180.
[286] M.R. Albert, L.G. Sneddon, W. Eberhart, F. Greuter, T. Gustafsson and E.W. Plummer, Surface Sci. 120 (1982) 19.
[287] J.A. Horsley, J. Stohr and R.J. Koestner, J. Chem. Phys. 83 (1985) 3146.
[288] P. Skinner, M.L. Howard, L.A. Oxton, S.F.A. Kettle, D.B. Powell and N. Sheppard, J. Chem. Soc. Faraday Trans. II, 77 (1981) 1203.
[289] This behavior is consistent, however, with the geometry of fig. 19 as discussed by B.J. Bandy, M.A. Chesters, D.I. James, G.S. McDougall, M.E. Pemble and N. Sheppard, Phil. Trans. Roy Soc. (London) A318 (1986) 141.
[290] M.A. Chesters and E.M. McCash, Surface Sci. 187 (1987) L639.
[291] I.J. Malik, M.E. Brubaker, S.B. Mohsin and M. Trenary, J. Chem. Phys. 87 (1987) 5554.
[292] D.C. McKean, Spectrochim. Acta A29 (1973) 1559;
B.B. Lal, M. Diem, P.L. Polavarapu, M. Oboodi, T.B. Freeman and L.A. Nafie, J. Am. Chem. Soc. 104 (1982) 3336.
[293] B.E. Hayden, K. Prince, D.P. Woodruff and A.M. Bradshaw, Surface Sci. 133 (1983) 589; Phys. Rev. Letters 51 (1983) 475.
[294] R. Ryberg, Phys. Rev. Letters 49 (1982) 1579; Phys. Rev. B31 (1985) 1545.
[295] M.A. Chesters and E.M. McCash, Spectrochim. Acta, in press.
[296] G. Herzberg, Molecular Spectra and Molecular Structure: II Infrared and Raman Spectra of Polyatomic Molecules (Van Nostrand, New York, 1945) p. 419.
[297] G.J. Kerley, J. Chem. Soc. Faraday Trans. II, 82 (1986) 41.
[298] R. Kaplan, Surface Sci. 93 (1980) 145.
[299] F. Meyer, Surface Sci. 27 (1971) 107.
[300] K. Fujiwara and H. Ogata, Surface Sci. 86 (1979) 700;
K. Fujiwara, Surface Sci. 108 (1981) 124; J. Chem. Phys. 75 (1981) 5172.
[301] H. Ibach, H. Wagner and H.D. Bruchmann, Solid State Commun. 42 (1982) 457;
H. Ibach, H.D. Bruchmann and H. Wagner, Appl. Phys. A29 (1982) 113.
[302] S. Ciraci and H. Wagner, Phys. Rev. B27 (1983) 5180.
[303] D. Schmeisser, F.J. Himpsel and G. Hollinger, Phys. Rev. B27 (1983) 7813.
[304] D. Schmeisser, Surface Sci. 137 (1984) 197;
W. Ranke and D. Schmeisser, Surface Sci. 149 (1984) 485;
W. Ranke, D. Schmeisser and Y.R. Ying, Surface Sci. 152/153 (1985) 1103.
[305] H. Kobayashi, T. Kubota, M. Onchi and M.N. Shijima, Phys. Letters A95 (1983) 345;
J.A. Schaefer, J. Anderson and G.J. Lapeyre, J. Vacuum Sci. Technol. A3 (1985) 1443;
F. Stucki, J. Anderson, G.J. Lapeyre and H.H. Farrell, Surface Sci. 143 (1984) 84;
J.A. Schaefer, F. Stucki, D.J. Frankel, W. Goepel and G.J. Lapeyre, J. Vacuum Sci. Technol. B2 (1984) 359.
[306] Y.J. Chabal, Phys. Rev. B29 (1984) 3677.
[307] Y.J. Chabal and S.B. Christman, Phys. Rev. B29 (1984) 6974.
[308] Y.J. Chabal, J. Vacuum Sci. Technol. A3 (1985) 1448.
[309] P.A. Thiel and J.E. Madey, Surface Sci. Rept. 7 (1987) 211.
[310] R.A. Shigeishi and D.A. King, Surface Sci. 58 (1976) 379.

[311] H. Steininger, S. Lehwald and H. Ibach, Surface Sci. 123 (1982) 264.
[312] E. Schweizer, M. Tüshaus and A.M. Bradshaw, to be published.
[313] R.G. Tobin, R.B. Phelps and P.L. Richards, Surface Sci. 183 (1987) 427.
[314] B.E. Hayden and A.M. Bradshaw, Surface Sci. 125 (1983) 767.
[315] J.W. Gadzuk, J. Opt. Soc. Am. B4 (1987) 201.
[316] T.S. Jones, S. Holloway and J.W. Gadzuk, Surface Sci. 184 (1987) L431.
[317] B.E. Hayden, K. Kretzschmar, A.M. Bradshaw and R.G. Greenler, Surface Sci. 149 (1985) 394.
[318] R.G. Greenler, F.M. Leibsle and R.S. Sorbello, Phys. Rev. B32 (1985) 8431.
[319] F.M. Leibsle, R.S. Sorbello and R.G. Greenler, Surface Sci. 179 (1987) 101.
[320] B. Poelsema, L.K. Verheij and G. Comsa, Phys. Rev. Letters 49 (1982) 1731.
[321] P. Hollins and J. Prichard, in: Vibrational Spectroscopies for Adsorbed Species, Eds. A.T. Bell and M.L. Hair, ACS Symp. Ser. 137 (1980) 51–74;
P. Hollins, K.J. Davies and J. Prichard, Surface Sci. 138 (1984) 74;
P. Hollins, Spectrochim. Acta, in press.
[322] R.G. Greenler, K.D. Bursch, K. Kretzschmar, R. Klauser, A.M. Bradshaw and B.E. Hayden, Surface Sci. 152/153 (1985) 338.
[323] R.G. Greenler, F.M. Leibsle and R.S. Sorbello, J. Electron Spectrosc. Related Phenomena 39 (1986) 195.
[324] R.G. Greenler, K.D. Bursch and J.P. Stec, to be published.
[325] F.M. Hoffmann and J. Paul, J. Chem. Phys. 86 (1987) 2990.
[326] F.M. Hoffmann and J. Paul, J. Chem. Phys. 87 (1987) 1857.
[327] Y.J. Chabal, J. Electron Spectrosc. Related Phenomena 38 (1986) 159.
[328] H. Pfnür, D. Menzel, F.M. Hoffmann, A. Ortega and A.M. Bradshaw, Surface Sci. 93 (1980) 431.
[329] A. Ortega, F.M. Hoffmann and A.M. Bradshaw, Surface Sci. 119 (1982) 79.
[330] M.E. Brubaker and M. Trenary, J. Chem. Phys. 85 (1986) 6100; J. Electron Spectrosc. Related Phenomena 44 (1987) 47.
[331] M. Grunze, P.H. Kleban, W.N. Unertl and F. Rys, Phys. Rev. Letters 51 (1983) 582.
[332] P.J. Estrup and J. Anderson, J. Chem. Phys. 45 (1966) 2254;
R.A. Barker and P.J. Estrup, J. Chem. Phys. 74 (1981) 1442;
D.A. King and G. Thomas, Surface Sci. 92 (1980) 201;
R.A. Barker and P.J. Estrup, Phys. Rev. Letters 41 (1978) 1307.
[333] G. Ehrlich, in: Structure of Surfaces, Eds. M.A. Van Hove and S.Y. Tong (Springer, Berlin, 1985) pp. 375;
H.W. Fink and G. Ehrlich, Phys. Rev. Letters 52 (1984) 1532; Surface Sci. 150 (1985) 419;
T.T. Tsong and R. Casanova, Phys. Rev. B24 (1981) 3063;
T.L. Einstein, in: Chemistry and Physics of Solid Surfaces, Vol. 2, Ed. R. Vanselow (Springer, Berlin, 1979) pp. 181;
H. Dreysse, D. Tomanek and K.H. Bennemann, Surface Sci. 173 (1986) 538;
J.P. Muscat, Phys. Rev. B33 (1986) 8136;
K.H. Lau and W. Kohn, Surface Sci. 65 (1977) 607.
[334] Y.J. Chabal, S.B. Christman, J.J. Arrecis, J.A. Prybyla and P.J. Estrup, J. Electron Spectrosc. Related Phenomena 44 (1987) 17.
[335] J.A. Prybyla, P.J. Estrup and Y.J. Chabal, J. Vacuum Sci. Technol. A5 (1987) 791.
[336] J.A. Prybyla, P.J. Estrup, S.C. Ying, Y.J. Chabal and S.B. Christman, Phys. Rev. Letters 58 (1987) 1877; and to be published.
[337] J.J. Arrecis, Y.J. Chabal and S.B. Christman, Phys. Rev. B33 (1986) 7906.
[338] Ref. [396], p. 168.
[339] J.W. Chung, K. Evans-Lutterodt, E.D. Specht, R.J. Birgeneau, P.J. Estrup and A.R. Kortan, Phys. Rev. Letters 59 (1987) 2192.

[340] F. Stucki, J.A. Schaefer, J.R. Anderson, G.J. Lapeyre and W. Göpel, Solid State Commun. 47 (1983) 795.
[341] Y.J. Chabal and K. Raghavachari, Phys. Rev. Letters 54 (1985) 1055.
[342] L.C. Feldman, P.J. Silvermann and I. Stensgaard, Nucl. Instr. Methods 168 (1980) 589.
[343] Recent EELS work claims that complete dihydride formation is achieved [L. Papagno, X.Y. Shen, J. Anderson, G. Schirripa Spagnolo and G.J. Lapeyre, Phys. Rev. B34 (1986) 7188]. Higher exposures and lower sample temperatures may account for the formation of some dihydride in the EELS experiment. However, as pointed out in section 4.1.5.2, complete dihydride formation is chemically unstable.
[344] R.E. Schlier and H.E. Farnsworth, J. Chem. Phys. 30 (1959) 917.
[345] D. Haneman, Phys. Rev. 121 (1961) 1093.
[346] K.C. Pandey, Phys. Rev. Letters 47 (1981) 1913.
[347] G. Chiarotti, S. Nannarone, R. Pastore and P. Chiaradia, Phys. Rev. B4 (1971) 3398.
[348] T.J. Himpsel, P. Heimann, T.-C. Chiang and D.E. Eastman, Phys. Rev. Letters 45 (1980) 1112;
S. Brennan, J. Stöhr, R. Jaeger and J.E. Rowe, Phys. Rev. Letters 45 (1980) 1414.
[349] G. Chiarotti, G. Del Signore and S. Nannarone, Phys. Rev. Letters 21 (1968) 1170.
[350] G. Chiarotti, P. Chiaradia and S. Nannarone, Surface Sci. 49 (1975) 315.
[351] P. Chiaradia and N. Nannarone, Surface Sci. 54 (1976) 547.
[352] P. Chiaradia, G. Chiarotti, S. Nannarone and P. Sassaroli, Solid State Commun. 26 (1978) 813.
[353] P. Chiaradia, G. Chiarotti, S. Selci and Z. Zhu, Surface Sci. 132 (1983) 62.
[354] P. Chiaradia, A. Cricenti, S. Selci and G. Chiarotti, Phys. Rev. Letters 52 (1984) 1145.
[355] S. Nannarone, P. Chiaradia, F. Ciccacci, R. Memeo, P. Sassaroli, S. Selci and G. Chiarotti, Solid State Commun. 33 (1980) 593.
[356] S. Selci, P. Chiaradia, F. Ciccacci, A. Cricenti, N. Sparvieri and G. Chiarotti, Phys. Rev. B31 (1985) 4096; Phys. Rev. Letters 56 (1986) 2411.
[357] G.A. Bootsma and F. Meyer, Surface Sci. 14 (1969) 52.
[358] R. Dorn, H. Lüth and H. Ibach, Surface Sci. 42 (1974) 583.
[359] G. Quentel and R. Kern, Surface Sci. 135 (1983) 325.
[360] M. Büchel and H. Lüth, Surface Sci. 50 (1975) 451;
J. Clabes, M. Henzler, Phys. Rev. B21 (1980) 625;
W. Kuhlmann and M. Henzler, Surface Sci. 99 (1980) 45.
[361] J. Assmann and W. Mönch, Surface. Sci. 99 (1980) 34;
M. Henzler, J. Appl. Phys. 40 (1969) 3758;
W. Müller and W. Mönch, Phys. Rev. Letters 27 (1971) 250.
[362] M.A. Olmstead and N.M. Amer, in: Proc. 17th Intern. Conf. on the Physics of Semiconductors (Springer, New York, 1985) p. 21.
[363] J. Bokor, R. Storz, R.R. Freeman and P.H. Bucksbaum, Phys. Rev. Letters 57 (1986) 881.
[364] J.E. Rowe, H. Ibach and H. Froitzheim, Surface Sci. 48 (1975) 44;
J.E. Rowe, Solid State Commun. 15 (1975) 1505;
H. Froitzheim, H. Ibach and D.L. Mills, Phys. Rev. B11 (1975) 4980;
H. Lüth, A. Ritz and R. Matz, Solid State Commun. 46 (1983) 343; Surface Sci. 132 (1983) 46;
N.J. DiNardo, J.E. Demuth, W.A. Thompson and Ph. Avouris, Phys. Rev. B31 (1985) 4077;
J.E. Demuth, R. Imbihl and W.A. Thompson, Phys. Rev. B34 (1986) 1330;
N.J. DiNardo, W.A. Thompson, A.J. Schell-Sorokin and J.E. Demuth, Phys. Rev. B34 (1986) 3007.
[365] R. Del Sole and A. Selloni, Solid State Commun. 50 (1984) 825; Phys. Rev. B30 (1984) 883.
[366] K. Fuchs, Proc. Cambridge Phil. Soc. 34 (1938) 100.
[367] J.W. Geus, in: Chemisorption and Reactions on Metallic Films, Ed. J.R. Anderson (Academic Press, New York, 1971) p. 327, and references therein.

[368] P. Wissman, in: Springer Tracts in Modern Physics, Vol. 77, Ed. G. Höhler (Springer, New York, 1975), and references therein.
[369] M. Watanabe and A. Hiratuka, Surface Sci. 86 (1979) 398.
[370] J. Anderson, G.W. Rubloff, M.A. Passler and P.J. Stiles, Phys. Rev. B10 (1974) 2401.
[371] J.B. Restorff and H.D. Drew, Surface Sci. 88 (1979) 399.
[372] D.M. Riffe, L.M. Hanssen and A.J. Sievers, Phys. Rev. B34 (1986) 692.
[373] D.M. Riffe, L.M. Hanssen and A.J. Sievers, Surface Sci. 176 (1986) 679.
[374] E.W. Plummer and R.D. Young, Phys. Rev. B1 (1970) 2088.
[375] B.J. Waclawski and E.W. Plummer, Phys. Rev. Letters 29 (1972) 783.
[376] B. Feuerbacher and B. Fitton, Phys. Rev. Letters 29 (1972) 786.
[377] S.-L. Weng, E.W. Plummer and T. Gustafsson, Phys. Rev. B18 (1978) 1718.
[378] L.W. Swanson and L.C. Crouser, Phys. Rev. Letters 16 (1966) 389; Phys. Rev. 163 (1967) 622.
[379] J.E. Reutt, Y.J. Chabal and S.B. Christman, Phys. Rev. B, submitted.
[380] For free carrier scattering mechanisms, the measured $\Delta R/R$ is roughly proportional to τ^{-1}, i.e. proportional to the metal resistivity ρ. For tungsten, the conductivity ρ varies from 0.85 to 4.95 $\mu\Omega$ cm between 100 and 300 K [A. Kannuluik, Proc. Roy. Soc. 141 (1933) 159]. In general, the temperature dependence is stronger than linear for the range of temperature investigated.
[381] M. Posternak, H. Krakauer, A.J. Freeman and D.D. Koelling, Phys. Rev. B21 (1980) 5601.
[382] L.F. Mattheiss and D.R. Hamann, Phys. Rev. B29 (1984) 5372.
[383] J.C. Campuzano, D.A. King, C. Somerton and J.E. Inglesfield, Phys. Rev. Letters 45 (1980) 1649.
[384] M.I. Holmes and T. Gustafsson, Phys. Rev. Letters 47 (1981) 443.
[385] A. Adnot and J.-D. Carette, Phys. Rev. Letters 39 (1977) 209.
[386] J.P. Woods and J.L. Erskine, J. Vacuum Sci. Technol. A4 (1986) 1414.
[387] J.L. Erskine, J.P. Woods, A.D. Kulkarni and F.W. de Wette, J. Electron Spectrosc. Related Phenomena 44 (1987) 27.
[388] F.J. Blatt, Physics of Electronic Conduction in Solids (McGraw-Hill, New York, 1968) pp. 183–196.
[389] B.N.J. Persson, F.M. Hoffman and R. Ryberg, Phys. Rev. B34 (1986) 2266.
[390] F.M. Hoffmann and B.N.J. Persson, Phys. Rev. B34 (1986) 4354.
[391] W. Erley, H. Wagner and H. Ibach, Surface Sci. 80 (1979) 612.
[392] B.N.J. Persson and R. Ryberg, Phys. Rev. Letters 54 (1985) 2119.
[393] M. Trenary, K.J. Uram, F. Bozso and J.T. Yates, Surface Sci. 146 (1984) 269.
[394] N.V. Richardson and A.M. Bradshaw, Surface Sci. 88 (1979) 255.
[395] R.J. Birgenau, J. Cordes, G. Dolling and A.D.B. Woods, Phys. Rev. 136 (1964) A1339.
[396] B.N.J. Persson and F.M. Hoffmann, J. Electron Spectrosc. Related Phenomena 45 (1987) 215; J. Chem. Phys. 88 (1988) 3349.
[397] A.M. Lahee, J.P. Toennies and Ch. Wöll, Surface Sci. 177 (1986) 371.
[398] R.R. Lucchese and J.C. Tully, Surface Sci. 137 (1983) 570.
[399] B.N.J. Persson and R. Ryberg, Phys. Rev. B24 (1981) 6954.
[400] I. Stensgaard, L.C. Feldman and P.J. Silverman, Phys. Rev. Letters 42 (1979) 247; L.C. Feldman, P.J. Silverman and I. Stensgaard, Surface Sci. 87 (1979) 410.
[401] J.E. Reutt, Y.J. Chabal and S.B. Christman, J. Electron Spectrosc. Related Phenomena 44 (1987) 325.
[402] F. Zaera, E.B. Kollin and J.L. Gland, Surface Sci. 166 (1986) L149.
[403] Y.J. Chabal, J. Vacuum. Sci. Technol. A4 (1986) 1324.
[404] Ref. [31], p. 188.
[405] R. Richter and J.W. Wilkins, Surface Sci. 128 (1983) L190.
[406] Ref. [33], pp. 76–81.

[407] Z.Y. Zhang and D.C. Langreth, submitted to Phys. Rev. B15.
[408] B.N.J. Persson, Chem. Phys. Letters 139 (1987) 457.
[409] See., e.g., Ber. Bunsenges. Phys. Chem. 90 (1986) 183–321.
[410] See., e.g., Kinetics of Interface Reactions, Vol. 8 of Springer Series in Surface Science, Eds. M. Grunze and H.J. Kreuzer (Springer, Berlin, 1987).
[411] W. Ho, J. Vacuum Sci. Technol. A3 (1985) 1432;
S. Kevan and L.H. Dubois, Rev. Sci. Instr. 55 (1984) 10.
[412] V.A. Burrows, S. Sundaresan, Y. J. Chabal and S.B. Christman, Surface Sci. 160 (1985) 122.
[413] V.A. Burrows, S. Sundaresan, Y.J. Chabal and S.B. Christman, Surface Sci. 180 (1987) 110.
[414] G. Ertl, P.R. Norton and J. Rustig, Phys. Rev. Letters 49 (1982) 177;
R. Imbihl, M.P. Cox and G. Ertl, J. Chem. Phys. 84 (1986) 3519, and references therein.
[415] F.M. Hoffmann, private communication.
[416] R.D. Kelley and D.W. Goodman, Surface Sci. 123 (1982) L743.
[417] J.B. Benziger, R.E. Preston and G.R. Schoofs, Appl. Opt. 26 (1987) 343.
[418] J.B. Benziger and G.R. Schoofs, Surface Sci. 171 (1986) L401.
[419] E.W. Scharpf and J.B. Benziger, J. Phys. Chem. 91 (1987) 5531.
[420] J.E. Reutt and Y.J. Chabal, unpublished.
[421] R. Gomer and A. Auerbach, Surface Sci. 167 (1986) 493.
[422] R. Gomer, Appl. Phys. A39 (1986) 1.
[423] C.H. Mak, B.G. Koehler, J.L. Brand and S.M. George, J. Chem. Phys. 87 (1987) 2340.
[424] A.W. Mantz, Appl. Spectrosc. 30 (1976) 459.
[425] H. Ueba, Surface Sci. 188 (1987) 421.
[426] J.R. Swanson, C.M. Friend and Y.J. Chabal, J. Chem. Phys. 87 (1987) 5028.
[427] E. Yablonovitch, D.L. Allara, C.C. Chang, T. Gmitter and T.B. Bright, Phys. Rev. Letters 57 (1986) 249;
V.A. Burrows, Y.J. Chabal, G.S. Higashi and S.B. Christman, unpublished.
[428] R.R. Cavanagh, private communication.